# PAIR-BREAKING IN SUPERCONDUCTIVITY

By

Elisabeth J. Nicol, B.Sc., M.Sc.

*A Thesis*

*Submitted to the Faculty of Graduate Studies*

*in Partial Fulfilment of the Requirements*

*for the Degree*

*Doctor of Philosophy*

McMaster University

September 1991

# PAIR-BREAKING IN SUPERCONDUCTIVITY

DOCTOR OF PHILOSOPHY(1991)
(PHYSICS)

McMASTER UNIVERSITY
Hamilton, Ontario

TITLE: Pair-breaking in superconductivity

AUTHOR: Elisabeth J. Nicol,
B.Sc. (Mount Allison University),
M.Sc. (McMaster University)

SUPERVISOR: Dr. J.P. Carbotte

NUMBER OF PAGES: ix, 263

# ABSTRACT

We have examined within Eliashberg theory the effect of several pair-breaking mechanisms on superconducting properties. Many predictions are made, some of which have recently been confirmed experimentally.

First, we present the strong coupling theory of the thin film critical current. Predictions for the temperature dependence of this property are made for the cases of strong inelastic scattering, spin fluctuations, and magnetic and non-magnetic impurity scattering.

We next examine the recently proposed marginal Fermi liquid theory, which has been shown to account for the unusual normal state properties of the high $T_c$ superconductors. Here we have calculated several superconducting properties in this model. The most important result arising from this work is the effect of the gapping of the spectrum of fluctuations. This produces a drop in the quasiparticle damping rate below $T_c$ and a peak in the low frequency temperature dependent conductivity. These predictions have been recently confirmed by several experiments. Also, in the frequency dependent optical conductivity, no absorption is predicted up until $4\Delta$ in the clean limit. The experimental observation of a lack of Holstein structure in the ratio of the superconducting to normal state optical conductivity is explained.

Several electromagnetic properties of superconductors are calculated with the inclusion of spin fluctuations and paramagnetic impurities. Predictions are made for the optical conductivity in the clean limit with magnetic impurity scattering. In this latter case, the Holstein structure will be reduced from the pure case and absorption will occur below $2\Delta$.

Finally, we have examined a model for a spin glass superconductor which leads to a temperature dependent scattering rate. Within this model several thermodynamic and electrodynamic properties have been examined, giving results which might be confirmed by experiment. Reentrant behaviour is predicted for a certain choice of parameters.

*To my mother,*
*June Elizabeth Dwyer*

# ACKNOWLEDGEMENTS

I wish to thank my supervisor, Dr. Jules Carbotte, for his guidance and encouragement. He is an outstanding example of a fine physicist, teacher, and friend, and has profoundly influenced my approach to physics and teaching. His physical insight, generosity of nature, and joyful enthusiasm have made working with him a pleasure. I could not ask for a better supervisor.

The interest shown in my work by my supervisory committee was very much appreciated. Members of this committee were: Dr. J. Greedan, Dr. C. Kallin, Dr. D.W. Taylor, and Dr. T. Timusk. In particular, Dr. David Taylor has been extremely kind to agree to be on my committee and to take upon himself the task of diligently eradicating my thesis of all errors by a very thorough reading before its submission.

I am fortunate to be indebted to many people for communications and discussions. With regard to the work on critical currents, I thank Dr. K. Maki (USC) and Dr. Thomas R. Lemberger (Ohio State). I would especially like to thank Dr. Ewald Schachinger (Graz) for little lessons sent by e-mail and technical assistance with the development of my programs. In addition, Ewald has provided moral support and encouragement.

My knowledge of optical conductivity has benefitted greatly from discussions with Dr. Tom Timusk, Dr. Dave Tanner (Florida), and Dr. Doug A. Bonn (UBC). Tom Timusk has in particular been a very supportive and enthusiastic collaborator. Dave Tanner aided in my understanding of microwave conductivity through the two-fluid model. I thank Doug Bonn for his excellent hospitality while visiting the University of British Columbia under the auspices of the CIAR and allowing me to reproduce his unpublished data in this thesis. He has also been the sole supporter and encourager of my long term interest in heavy fermions. On the theoretical side, Dr. N.E. Bickers (USC) and Dr. J. Swihart (Indiana) have also answered many questions that I addressed to them about their calculations.

With regard to my work on marginal Fermi liquid theory, I am very grateful to Dr. Peter B. Littlewood (AT&T) for communications and also for his support. I thank him for sending me copies of his and Dr. Nuss's work in advance of publication. Dr. Peter Entel (Duisberg), a recent visitor to our

group, has also kept me on my toes with constant cross-examination about marginal Fermi liquid theory and optical conductivity in general.

The faculty of the physics department have been quite helpful: in particular, Drs. Kallin, Sprung, Sutherland, and Pudritz have allowed me time on their computers, so that much of this work could be completed. Catherine Kallin has also been very helpful with regard to discussions pertaining to optical conductivity calculations. And Ralph Pudritz has been very supportive and I have appreciated the interest that he has shown in my work and the time that he has spent listening to my jumbled but enthusiastic explanations of my latest result.

Several present and former students in our group have been very helpful to my progress, namely, Richard Akis, Chao Jiang, Dr. Frank Marsiglio, Dr. Walter Stephan, and Dr. Peter Williams. In particular, Frank was a fantastic office companion and made me memorize the Eliashberg equations while I was still a particle theorist. His enthusiasm and support were invaluable to me and we had many long hours of excellent discussions. He has also read and offered comments on much of this thesis. My work on spin glasses follows that of Walter Stephan who has provided a subroutine to make this possible. Richard Akis has also contributed a numerical subroutine used in my work. Much of the work on paramagnons follows in the footsteps of Peter Williams.

I thank my good friend and fellow physicist, Maureen Reedyk, for constant companionship, good discussions, lots of tea, attending art school with me, and the experience of transferring liquid Helium at one o'clock in the morning.

Several post doctoral fellows have been my lunch companions: Dr. Michael Prohammer (Austria), Dr. Henrik Jensen (NORDITA), and Dr. Andrew Brass (Manchester). They have both encouraged my progress in physics and kept me internationally literate. In particular, I thank Henrik Jensen for his hospitality in Copenhagen. In this regard, I also thank Dr. Masa Toyama for his hospitality in Kyoto, which allowed me to attend the LT18 conference, and more recently Dr. N. Tsuda's hospitality in Tokyo in providing us with accommodation in an apartment belonging to the Science University of Tokyo. I wish I could mention by name all the international visitors that

I have met through the theory group at McMaster, but I can only thank them collectively for gracing my dining table and expanding my horizons with their conversations.

Some of the programs used in this work were written by former students, Dr. Johanna Daams, Dr. Frank Marsiglio, and Dr. Boza Mitrović (also a kind supporter who tolerated my faulty navigation around Kyoto), maintained and translated into C by Dr. Ewald Schachinger. John Benjamins is to be thanked for patiently restoring accidentally deleted files and keeping the computers running.

My one-man fan club, Dr. Robert L. Hawkes (Mt. Allison) gave me my first experience of physics research as a summer student and has been a great supporter ever since. He has enthusiastically followed my career and taken a special interest in my teaching activities (himself the winner of every teaching award offered in Canada).

Finally, I wish to thank my perfect companion, John Macfarlane, for *everything*.

My research has been funded in part by the Natural Sciences and Engineering Research Council (NSERC) in the form of a post-graduate scholarship, the Canadian Institute for Advanced Research (CIAR), a Harry Lymann Hooker Scholarship, a D.G. Burns Scholarship, and the Yates fund.

# Table of Contents

# Chapter 1

# Introduction

The field of superconductivity has had a rich and illustrious history. From the original discovery of a zero resistance state in mercury below the temperature of 4.19 K in the laboratory of H.K. Onnes in 1911 [Onnes (1911)], to the discovery of oxide superconductors by Bednorz and Müller in 1986 [Bednorz and Müller (1986)], the study of superconductivity has produced one of the most exact theories in physics, many unusual phenomena, novel technological applications, and several Nobel prizes have recorded the achievements of physicists in this area.

"Supermagnetivity" might have been another possible descriptive name for this phenomenon, because a superconducting material that exhibits zero resistance below a characteristic transition temperature $T_c$, also expels all magnetic flux from its body as it is cooled below $T_c$ in a magnetic field. It becomes a perfect diamagnet. It is this phenomenon that results in the popular demonstrations for the public of a magnet (or even a person on

top of a magnet!) levitated above a superconductor. Meissner and Ochsenfeld discovered this important characteristic of superconductors in 1933 [Meissner and Ochsenfeld (1933)].

Early theoretical descriptions of superconductors were phenomenological theories by several people [Gorter and Casimir (1934a,b); London (1948,1950); Ginzburg and Landau (1950)]. Gorter and Casimir modelled the superconductor by a two-component fluid, one of normal electrons and one of superconducting electrons. These theories were reasonably successful at describing some of the thermodynamic [Gorter and Casimir (1934a,b)] and electromagnetic [London (1948,1950); Ginzburg and Landau (1950)] phenomena but were rather unsatisfying as they provided no description of a microscopic mechanism. A clue to the underlying mechanism was found with the discovery of what is now known as the isotope effect [Maxwell (1950); Reynolds *et al.* (1950)]. This effect involves a change in transition temperature $T_c$ upon changing the mass of the ions in the lattice through isotopic replacement. This led to the realization that the lattice of ions was somehow involved in the superconductivity. This was independently suggested by Fröhlich [Fröhlich (1950)]. Shortly after this time, Cooper (1956) showed that two electrons (normally repulsive to each other due to their like charges) could form a bound state under a very weak attractive interaction in the presence of a filled Fermi sea. These electrons were later named Cooper pairs. The major achievement in the search for a microscopic theory came when Bardeen, Cooper and Schrieffer (BCS) (1957) used a product wavefunction of overlapping Cooper pairs to calculate many of the thermodynamic and electrodynamic properties of superconductors.

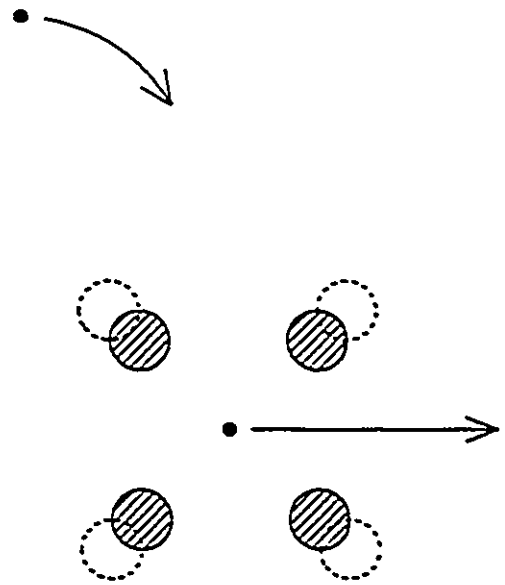

Figure 1.1 A simple real space picture illustrating the effective attraction between electrons in a superconductor. An electron (shown as the black dot) polarizes the lattice of positively charged ions (shaded circles) off their equilibrium positions (unshaded circles). The electron quickly moves on. However, the ions respond slowly, remaining polarized as a region of net postive charge, which attracts another electron (at the top of the diagram). This forms an effective attraction between two electrons.

The mechanism of pairing of the Cooper pair is now known to be the Fröhlich or electron-phonon interaction. This interaction is schematically depicted in real space in Fig. 1.1. To achieve attraction between two electrons is very simple in this qualitative picture. A conduction electron in the metal attracts the positively charged ions causing a polarization of the ion lattice around the electron. The electron is moving very fast with the Fermi velocity and the heavy, sluggish ions respond very slowly to the electron's presence. Hence, by the time the polarization is complete and the ions displaced off their equilibrium positions towards the electron's apparent position, the electron has moved away. In the mean time, another conduction electron "sees"

this region of net positive charge and by virtue of the Coulomb potential, is attracted towards this region. This forms an effective pairing between the two electrons which may actually be separated by a distance of the order of $10^4$ Å. This is a simple qualitative picture. The pairing actually occurs in momentum space as shown by the Feynman diagram of Fig. 1.2 where an electron interacts with a phonon (a quantum of lattice vibration) which in turns couples to another electron, pairing an electron of momentum $\vec{k}$ and spin $\uparrow$ with an electron of momentum $-\vec{k}$ and spin $\downarrow$. In real space the separation of the electrons can be quite large, as indicated above, and it is defined as the coherence length $\xi_o$. As there are approximately $10^{22}$ electrons/cm$^3$ in a metal and this distance is so large, this can only imply that in real space the pairs overlap. This is what qualitatively gives the zero resistance. Normal electrical resistance arises from individual electrons scattering off impurities or defects in the metal and hence being lost from the net current. In the superconducting state the electrons are all bound together in this complicated overlapping manner and hence it is difficult to scatter by an impurity a single electron as it is tied to the rest through phase coherence of the wavefunction. The result is that there is no degradation of the electrical current.

Another feature of the superconducting state is the energy gap. To pluck an electron out of this many body condensate would cost an energy $\Delta$, where $\Delta$ is the energy gap between the ground state and the excitations of the system.

Zero resistance and flux expulsion are not the only characteristics of superconductors; there are many changes in the thermodynamic and electromagnetic properties of a superconductor that can be found discussed in many texts [Schreiffer (1964); Parks (1969); Rickhayzen (1965,1980); Tinkham

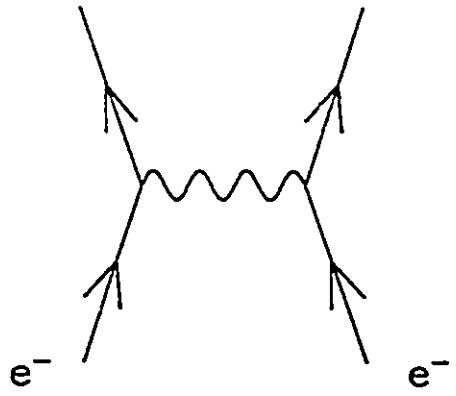


Figure 1.2 A Feynman diagram for the scattering of two electrons (straight lines) through the exchange of a phonon (wavy line).

(1975); Abrikosov, Gor'kov and Dzyaloshinski (1963); Fetter and Walecka (1971); Mahan (1981); etc.], including elementary solid state textbooks [Kittel (1986); Ashcroft and Mermin (1976)]. We will describe in this thesis only those properties for which we explicitly perform calculations.

BCS calculated many of these properties and achieved qualitative agreement with experiment. For this amazing feat, they received the Nobel prize. However, although this theory captured the essence of the mechanism of superconductivity, it gave only universal numbers for several properties, *i.e.*, all materials were predicted to have the same value for a particular property. The agreement was excellent for a material like aluminum but materials such as lead and mercury did not agree quantitatively with the theory.

This led to the theories of Migdal (1958) and Eliashberg (1960) for the normal state and superconducting state, respectively. The essential modification that they added to BCS theory was to include the response of the

lattice correctly. In BCS theory, the interaction potential was treated as a constant within a rim of $2\hbar\omega_D$ around the Fermi surface and zero otherwise. In Migdal-Eliashberg theory, the full details of the electron-phonon interaction were included. This implies a frequency-dependent interaction, where certain phonon frequencies could be more effective than others for pairing. This interaction is entirely material-dependent. In addition, as long as the interaction energy is less than the Fermi energy, then Migdal (1958) argued that this theory is exact to all orders in the electron-phonon interaction. From this theory, which is summarized in Appendix A, a complicated set of non-linear equations arise that require numerical solution. They depend on two parameters, $T_c$, and $\alpha^2F(\omega)$, the electron-phonon spectral density function. These two parameters are taken from experiment and the theory is used to calculate all other properties. Excellent *quantitative* agreement is achieved to within a few percent, for all conventional materials [Carbotte (1990)]. This is probably the most exact theory we have in condensed matter physics and it is very impressive. This theory forms the basis for the investigations of this thesis.

Only a brief, incomplete and qualitative outline of the history of superconductivity and some of its theoretical developments has been sketched here. No mention has been made of some of the more exotic forms of superconductivity, such as, organic superconductors, heavy fermion compounds, etc. or of some of the brilliant theoretical achievements, such as the Josephson effect (as predicted by Brian Josephson in 1962 [Josephson (1962,65)] and who was subsequently awarded the Nobel prize).

The scope of this thesis is quite broad. The topics range from critical currents to spin glasses. These subjects will be introduced in the subsequent chapters. The main unifying theme of these rather different aspects of theoretical superconductivity is that of "pair-breaking". As discussed, the superconducting state is a superposition of paired electrons (Cooper pairs) of $(\vec{k}\uparrow, -\vec{k}\downarrow)$. The destruction of the superconducting state is very important from an applications point of view and also from the information that it can provide us on the stability of the superconducting state in the presence of magnetic fields, currents, or as clues to new exotic mechanisms in unconventional materials. The breaking of Cooper pairs is the mechanism by which the superconductivity is destroyed. This can occur by increasing the temperature so that the electrons can be thermally excited out of the state, but also by other pair-breaking mechanisms. For instance, the electrons are paired by $(\uparrow, \downarrow)$ and a magnetic field that would tend to align the spins along the direction of the field, $(\uparrow, \uparrow)$, say, would destroy the pairing. Magnetic impurities tend to spin-flip scatter the electrons as do spin-density fluctuations (paramagnons) and hence pairing is destroyed. Other pair-breaking effects can arise from an applied current which shifts the energies of the electrons and hence, large enough currents can give enough energy to the electrons to excite them out of the superconducting state. These are some of the pair-breaking mechanisms examined in this thesis.

Chapter 2 examines the critical currents in thin film superconductors – the last mechanism mentioned above, and presents results for strong-coupling theory (Eliashberg theory) without impurities and with normal or magnetic impurities. Chapters 3 and 4 discuss the novel marginal Fermi

liquid theory which has been proposed as a theory of the new high temperature superconductors. The pair-breaking mechanism in this case involves spin density fluctuations but in a rather different ground state. Chapter 5 records some studies of the effect of paramagnetic impurities and paramagnons, (static and dynamic pair-breaking, respectively) on several electromagnetic properties of superconductors. Chapter 6 is an extensive chapter on thermodynamic and electromagnetic properties of intrinsic spin glass superconductors, where the essential feature is pair-breaking similar to that of paramagnetic impurities but now the effective paramagnetic impurity is temperature-dependent. Chapter 7 forms a conclusion to this thesis and the appendices supplement the material in the chapters. Appendix A, in particular, contains the necessary mathematical introduction to Eliashberg theory.

# Chapter 2

# Critical Currents in Thin Film Superconductors

## 2.1 INTRODUCTION

The critical current of a superconductor is the maximum current that can be carried by the metal without it reverting to the normal state. Although there are many mechanisms which limit the current-carrying capacity of a superconductor, such as motion of the flux lattice, the theoretically highest attainable current is limited finally by the pair-breaking of the superconducting state induced by the current itself. Usually, the upper limit on the critical current of a type I superconductor, where no vortex lattice forms, is given by the Silsbee current, *i.e.*, the current that produces a magnetic field at the surface of the material which is equal to the thermodynamic critical magnetic field, $H_c$. However, in a thin film, the energy associated with this magnetic field is reduced in comparison to the kinetic energy associated with the current itself, by a factor of the order of the sample's cross-sectional area

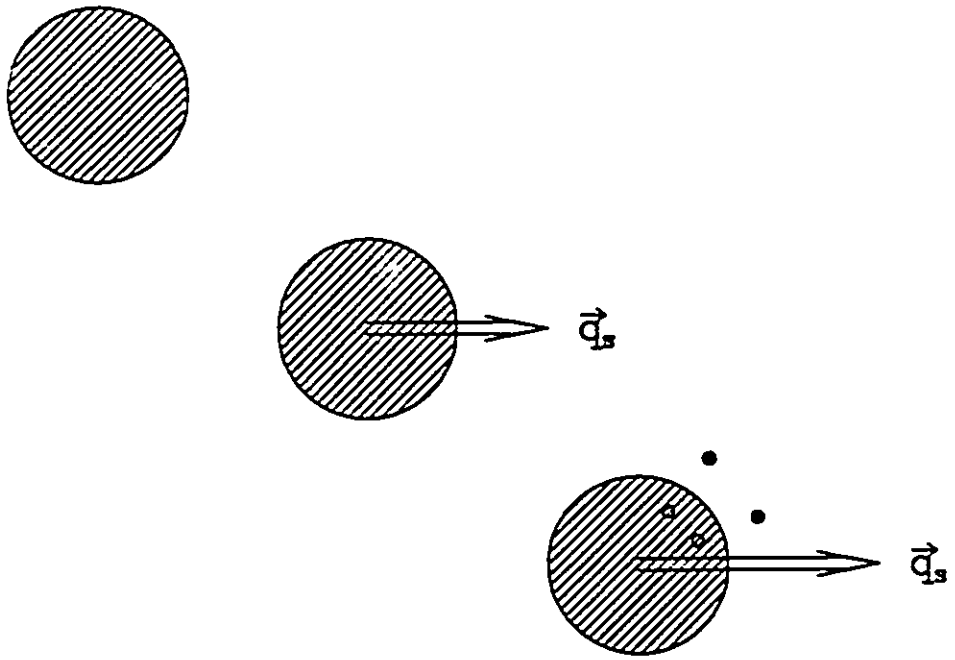


Figure 2.1 A schematic representation of velocity-depairing. The top shaded circle represents the quiescent superconducting condensate of Cooper pairs with no applied current. The second picture shows the condensate shifted in momentum space by an applied momentum $\vec{q}_s$. The third frame shows, under increased $\vec{q}_s$, the excitation of electrons out of the superconducting state by their increased kinetic energy exceeding that necessary to bind them to the condensate.

divided by the square of the penetration depth [Tinkham (1975)]. Hence, samples smaller in dimension than the penetration depth will have a critical current that is limited by the velocity-depairing of the superconducting state.

A simple schematic picture to illustrate this velocity-depairing is given in Fig. 2.1. First, we start with the superconducting condensate of Cooper pairs in its ground state with no applied momentum. This is schematically represented by the shaded circle. Then in the second part of the picture, we apply a current with momentum $\vec{q}_s$. This shifts the condensate in momentum space by an amount $q_s$ in the direction of $\vec{q}_s$. As the condensate

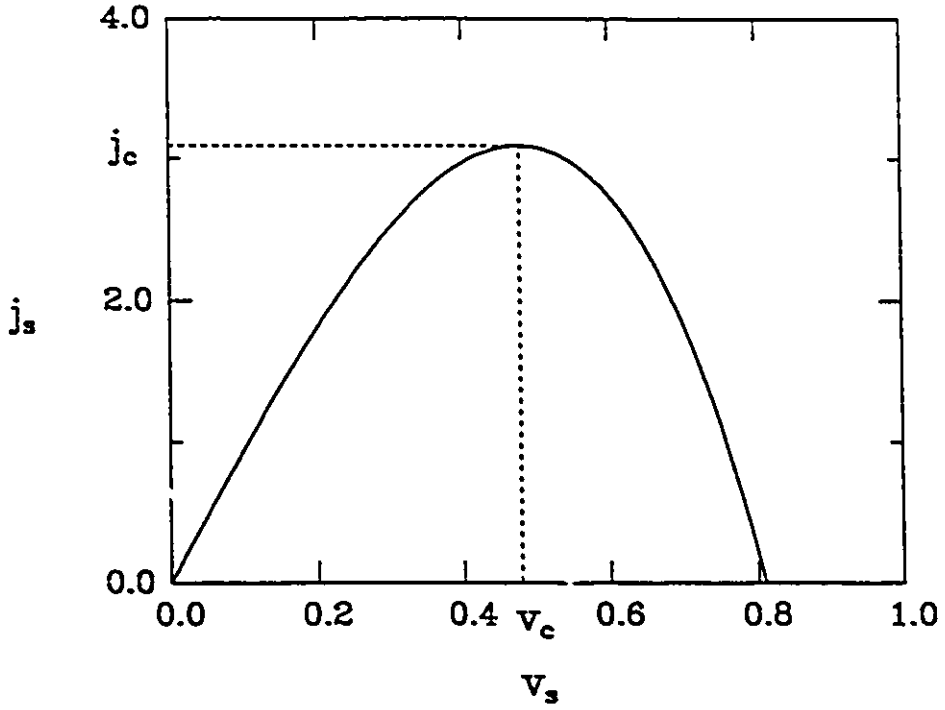


Figure 2.2 The superfluid current density $j_s$ as a function of the applied velocity $v_s = q_s/m$, in arbitrary units, for $T = 0.9T_c$. The critical current density $j_c$ is defined as the maximum in this curve, which occurs at a critical velocity $v_c$. This curve was numerically calculated from BCS theory.

is formed of Cooper pairs of electrons $(\vec{k}\uparrow, -\vec{k}\downarrow)$, where $\vec{k}$ is the momentum and $\uparrow$ represents the electron spin being $+1/2$, the pairs become shifted to $(\vec{k}+\vec{q}_s\uparrow, -\vec{k}+\vec{q}_s\downarrow)$. The quasiparticle energy now has a term proportional to $\vec{k}\cdot\vec{q}_s$ and a higher order term proportional to $q_s^2$. This latter term can be neglected for small $q_s$. Hence, the net effect of the applied current is to shift the quasiparticle energy by $\vec{k}\cdot\vec{q}_s$. When upon increasing $q_s$, as shown in the third part of Fig. 2.1, this term becomes of the order of the energy gap, $\Delta$, the binding energy of the electron to the condensate, the electrons begin to depair and there is a rapid destruction of the superconducting state, with the sample finally reverting to the normal phase.

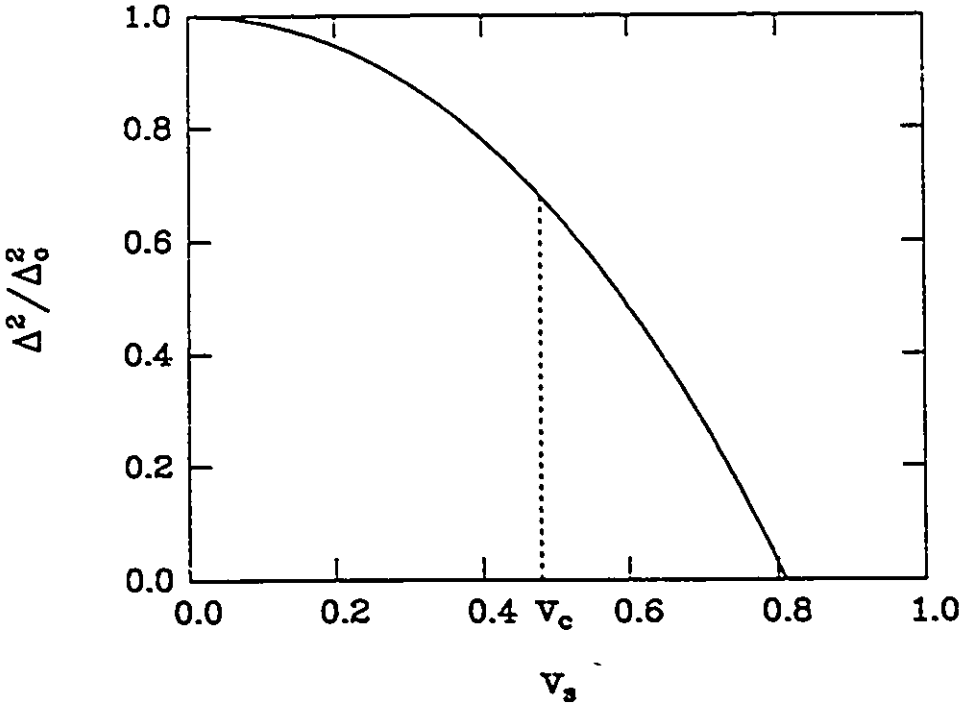


Figure 2.3 The order parameter squared normalized to its zero velocity value as a function of the applied velocity $v_s = q_s/m$, in arbitrary units, corresponding to Fig. 2.2.

The applied current density $j_s$ for the process is drawn in Fig. 2.2, as a function of of the superfluid velocity $v_s$, which is related to $q_s$ by $v_s = q_s/m$. The current rises linearly with increasing velocity, as $j_s = nev_s$, where $n$ is the electron density and $e$ is the charge, until depairing begins to set in and then the slope decreases due to electrons being lost from the condensate. The maximum in this curve is defined as the critical current density, $j_c$, the maximum attainable current. It occurs at a critical velocity $v_c$.

In Fig. 2.3, we show the corresponding order parameter $\Delta$, normalized by its value in the absence of the applied momentum, as a function of $v_s$. Here, we plot the squared quantity merely to make the correspondence to the well-known Ginzburg-Landau result, where an expansion of the free energy in the square of the order parameter occurs [Tinkham, (1975)].

This pair-breaking current was first calculated by Ginzburg (1956) who found the temperature-dependence of the critical current density, $j_c$, near $T_c$ to be $j_c = j_o(1 - T/T_c)^{3/2}$, where $j_o$ is an impurity-dependent coefficient later refined in Ginzburg-Landau theory [Gor'kov (1959, 1960)]. $T$ is the temperature and $T_c$, the critical temperature of a superconductor. Further investigations of the pair-breaking current [Rogers (1960); Bardeen (1962); Parameter (1962); Parameter and Berton (1964); Maki (1963, 1964)] were carried out for $j_c$ as a function of temperature in the clean ($l \gg \xi_o$) and dirty ($l \ll \xi_o$) limits finally culminating in a paper by Kupriyanov and Lukichev (1980) where they numerically calculated $j_c(T)$ from the Eilenberger equations [Eilenberger (1968)] for arbitrary elastic scattering. (The Eilenberger equations are a real-space formulation of Eliashberg-type equations, useful for properties where the order parameter may vary in space.) Thus, the temperature-dependence of the critical current with arbitrary normal impurity scattering has been calculated for a BCS superconductor.

Experimental verification of the BCS theory has been shown in the clean [Glover and Coffey (1964); Hunt (1966); Andratskii *et al.* (1974); Skocpol (1976)] and dirty [Romijn *et al.* (1982)] limits for Sn and Al thin films, respectively. Measurements are quite difficult and must be performed on samples with dimensions that are small compared with the electromagnetic penetration depth $\lambda$ and the BCS coherence length $\xi_o$. This is necessary to achieve uniform current flow and to suppress the formation of vortices. Also, measurements are difficult very far from $T_c$ as many of these constraints break down due to their temperature dependence. Romijn *et al.* (1982) have given a good discussion of these points.

More recent interest in inelastic scattering in the high temperature superconductors resulted in an attempt by Lemberger and Coffey (1988) to incorporate inelastic scattering in an approximate way in the usual BCS theory for $j_c$. They predicted that inelastic scattering would suppress $j_c$ near $T_c$. This motivated us to re-examine the problem within the formalism of the Eliashberg theory of strong coupling superconductivity which naturally incorporates inelastic scattering through the electron-boson spectral function $\alpha^2F(\omega)$.

In Section 2.2, we present the strong coupling Green's function in the presence of a uniform current and use it to calculate the superfluid current density, $j_s$, and the accompanying equations for the order parameter. From these equations we calculate the critical current as a function of temperature and impurity content for both non-magnetic and magnetic impurities, and our results are presented in Section 2.3. Also in Section 2.3, we present functional derivative calculations which confirm and give insight into our previous results. In Section 2.4, we present a strong coupling correction formula for $j_c$ near $T_c$ in the pure limit as a function of a single parameter and in Section 2.5, we examine the asymptotic limit of $j_c$, where the mass renormalization parameter tends to infinity. We summarize our conclusions in Section 2.6.

## 2.2 THEORY

Under the application of a small momentum $\tilde{q}_s$ to the superconducting condensate in zero magnetic field, Rogers (1960) has shown that there will be no appreciable change in the BCS ground state wavefunction and

that the superconducting condensate will simply be shifted from a condensate of pairs of momentum $\vec{k}\uparrow$ and $-\vec{k}\downarrow$ to one of pairs of $\vec{k}+\vec{q}_s\uparrow$ and $-\vec{k}+\vec{q}_s\downarrow$ and that the quasiparticle excitation energy will shift by $\vec{v}\cdot\vec{q}_s$ where $\vec{v}=\vec{p}/m=\hbar\vec{k}/m$. Maki (1969) has given the BCS Green's function for the current carrying state as

$$G_{\omega_n,\vec{q}_s}(\vec{p})=(i\omega_n-\vec{v}\cdot\vec{q}_s+\xi\rho_3+\Delta\rho_1\sigma_2)^{-1} \quad , \tag{2.1}$$

where $\xi=p^2/2m-\mu$, with $\mu$ the chemical potential, $\Delta$ is the superconducting order parameter and $\omega_n$ are the finite temperature ($T$) Matsubara frequencies, $\omega_n=\pi T(2n-1)$, $n=0,\pm1,\pm2,\ldots$. The Green's function here is the Nambu-Gor'kov Green's function in four-by-four matrix notation where the $\rho_i$ and $\sigma_i$ are the Pauli matrices operating on the electron-hole and spin spaces, respectively, and $\rho_1\sigma_2$ is a tensor product. In this notation, the equation for the BCS order parameter $\Delta$ is given as [Maki (1969)]

$$\Delta=-VT\sum_{n=-\infty}^{\infty}\int\frac{d^3p}{(2\pi)^3}\mathrm{Tr}[\rho_1\sigma_2 G_{\omega_n,\vec{q}_s}(\vec{p})] \quad , \tag{2.2}$$

where V is the constant pairing potential and Tr is the trace of the matrix. The supercurrent density $\vec{j}_s$ induced in a thin film superconductor in zero magnetic field is [Maki (1969)]

$$\vec{j}_s=\frac{eT}{m}\sum_{n=-\infty}^{\infty}\int\frac{d^3p}{(2\pi)^3}\mathrm{Tr}[\vec{p}\,G_{\omega_n,\vec{q}_s}(\vec{p})] \quad , \tag{2.3}$$

with $e$, the electron charge, and $m$, the electron mass. We generalize these results to the case of strong coupling theory by using the strong coupling Green's function, as it is modified in the presence of a uniform current, in the formula for the current above and in the standard Eliashberg equations for the order parameter. Following the usual development of strong coupling

theory [Allen and Mitrović (1982); see also Appendix A], the Green's function is

$$G_{\omega_n,\vec{q}_s}(\vec{p}) = (i\tilde{\omega}_n - \vec{v}\cdot\vec{q}_s + \xi\rho_3 + \tilde{\Delta}_n\rho_1\sigma_2)^{-1} \tag{2.4}$$

and the equation for the current is derived from Eq.(2.3) by performing the trace and the energy integral:

$$\vec{j}_s = \frac{3eN}{2k_F}\pi T \sum_{n=-\infty}^{\infty}\int_{-1}^{1} dz \frac{i(\tilde{\omega}_n - isz)z}{\sqrt{(\tilde{\omega}_n - isz)^2 + \tilde{\Delta}_n^2}}\hat{q}_s \quad , \tag{2.5}$$

where $s = v_F q_s = k_F q_s/m$, $\hat{q}_s$ is a unit vector in the direction of $\vec{q}_s$, $N$, the electronic density and $k_F$, the Fermi momentum. Likewise, the standard Eliashberg equations for the order parameter and renormalized frequencies of the superconducting state are also modified and are given as

$$\tilde{\Delta}_n = \pi T \sum_{m=-\infty}^{\infty}[\lambda(n-m) - \mu^*\theta(\omega_c - |\,\omega_m\,|)]\int_{-1}^{1}\frac{dz}{2}\frac{\tilde{\Delta}_m}{\sqrt{(\tilde{\omega}_m - isz)^2 + \tilde{\Delta}_m^2}}$$
$$+ \pi(t^+ - t^-)\int_{-1}^{1}\frac{dz}{2}\frac{\tilde{\Delta}_n}{\sqrt{(\tilde{\omega}_n - isz)^2 + \tilde{\Delta}_n^2}} \tag{2.6}$$

and

$$\tilde{\omega}_n = \omega_n + \pi T \sum_{m=-\infty}^{\infty}\lambda(n-m)\int_{-1}^{1}\frac{dz}{2}\frac{\tilde{\omega}_m - isz}{\sqrt{(\tilde{\omega}_m - isz)^2 + \tilde{\Delta}_m^2}}$$
$$+ \pi(t^+ + t^-)\int_{-1}^{1}\frac{dz}{2}\frac{\tilde{\omega}_n - isz}{\sqrt{(\tilde{\omega}_n - isz)^2 + \tilde{\Delta}_n^2}} \quad . \tag{2.7}$$

Where,

$$\lambda(n-m) \equiv \lambda(i\omega_m - i\omega_n) \equiv \int_0^{\infty}\frac{2\nu\alpha^2F(\nu)}{\nu^2 - (i\omega_m - i\omega_n)^2}d\nu \tag{2.8}$$

and $\tilde{\Delta}_n \equiv \tilde{\Delta}(i\omega_n) = Z(i\omega_n)\Delta(i\omega_n)$ and $\tilde{\omega}_n = Z(i\omega_n)\omega_n$. The normal impurity scattering rate, $t^+$, is defined as $1/(2\pi\tau_N)$ and the paramagnetic impurity scattering rate, $t^-$, is defined as $1/(2\pi\tau_p)$, where $\tau_p$ is the spin-flip lifetime and $\tau_N$ is the normal impurity scattering time. Note that with $s = 0$ in

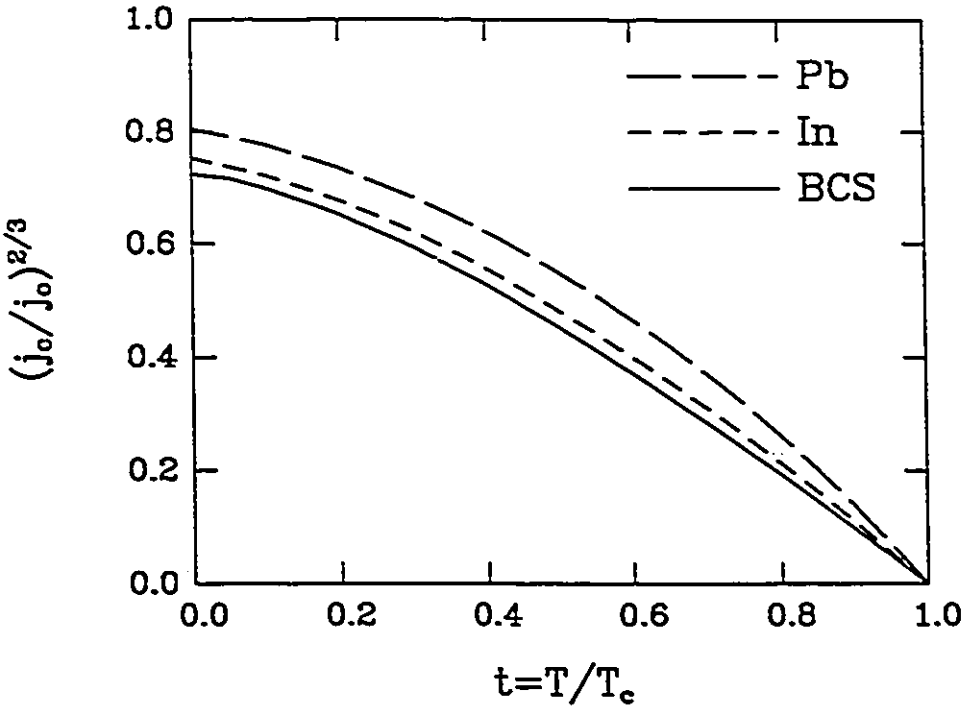


Figure 2.4 The temperature dependence of the critical current density on the clean limit for the materials indicated in the figure. Aluminum followed the BCS curve and is not shown. Tin fell in between the BCS curve and that for indium, and mercury also followed closely the curve for Pb. These two curves are also not shown for the purposes of clarity. Indium is representative of intermediate coupling and Pb, of strong coupling. Strong inelastic scattering from the phonons is seen to always increase $j_c$ above the BCS result.

Eqs. (2.6) and (2.7) we recover the usual Eliashberg equations with impurity scattering.

We numerically solve Eqs. (2.5)-(2.7) self-consistently for a value of $q_s$ which maximizes $j_s$. This value of $j_s$ is then defined, in the usual manner, to be the critical current density, $j_c$.

## 2.3 NUMERICAL RESULTS

In this section we present the results for numerical solution of the equations just presented in the previous section using known $\alpha^2 F(\omega)$ spectra

of type I superconductors derived from tunneling experiments. In Fig. 2.4, we display $(j_c/j_o)^{2/3}$, in the clean limit ($t^+ = t^- = 0$), versus the reduced temperature, $t = T/T_c$, for the materials indicated. Indium is representative of intermediate coupling and lead, of strong coupling. Aluminum is not shown but the curve followed the universal BCS curve almost exactly. The curve for tin fell in between that for Al and In, and mercury fell almost on top of the Pb curve, and hence we have omitted these curves for clarity. Here, $j_o$ is the temperature-independent coefficient of the Ginzburg-Landau result near $T_c$, *i.e.*, , $j_c = j_o(1-t)^{3/2}$, where $j_o = 8eN\pi T_c/(3mv_F\sqrt{7\zeta(3)})$. There is an increase in the critical current over the BCS result for strong coupling superconductors showing that inelastic scattering increases the critical current rather than decreases it as previously proposed by Lemberger and Coffey (1988). We will discuss this result later on.

Bardeen (1962) has given two phenomenological forms for the temperature dependence of $j_c$ near $T_c$. He gives $j_c(t) = j_o[(1-t^2)(1+t^2)]^{1/2}$ and $j_c(t) = j_o(1-t^2)^{3/2}$. When, as in Fig. 2.4, it is difficult to distinguish the curves for different materials, it is common to define a deviation function, where a phenomenological result is subtracted from the actual calculated quantity, and this deviation is plotted as a function of $t$ or $t^2$. A plot of the deviation function is useful for showing the fine details of how the curves for different materials differ from one another and for comparing with the phenomenological models. Such plots are shown in Fig. 2.5 for the two phenomenological results of Bardeen, above. Notice that the numerical results are always below these phenomenological forms and that there is some crossover between the curves at low temperatures. But near $T_c$, where the phenomenological forms

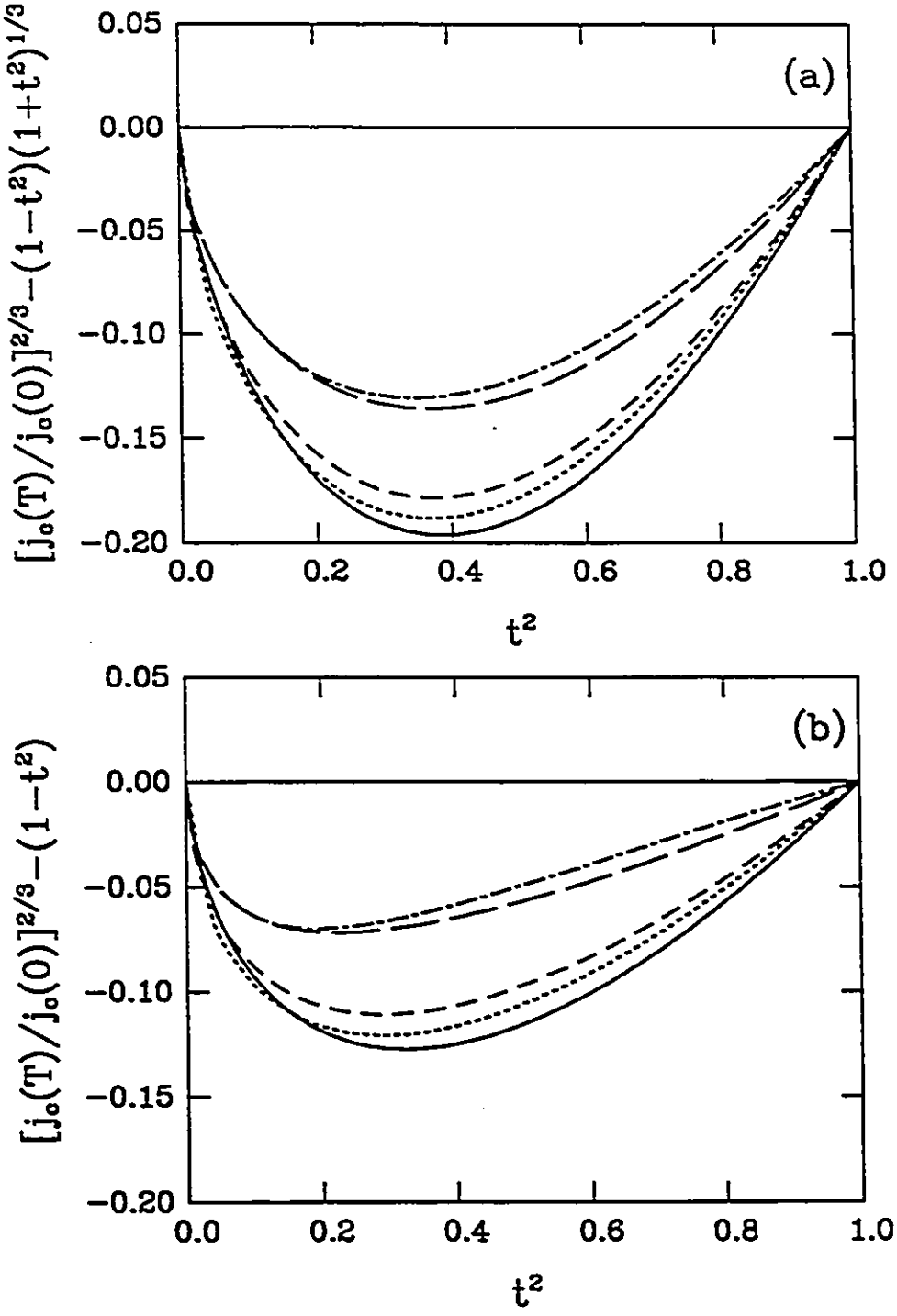


Figure 2.5 Deviation functions for several materials as a function of $t^2$. Curves are drawn for Pb (— - —), Hg (— — —), In (- - -), Sn (- - - -), and BCS (solid line). In (a), the phenomenological form is $j_c(t) = j_o[(1-t^2)(1+t^2)]^{1/2}$, and in (b), it is $j_c(t) = j_o(1-t^2)^{3/2}$.

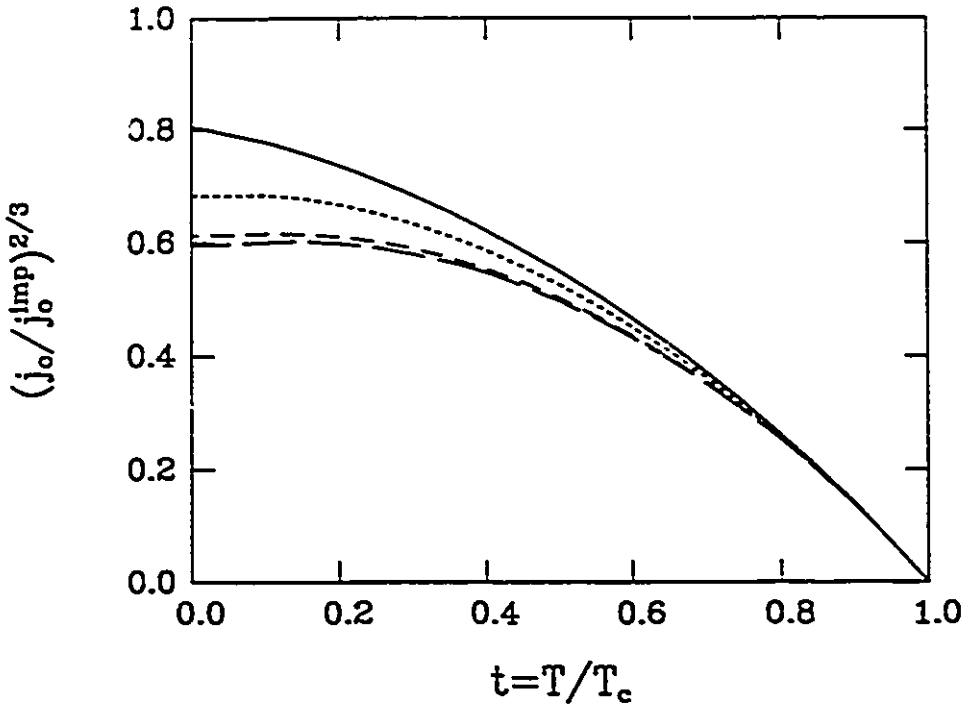


**Figure 2.6** The temperature dependence of the critical current density in Pb for various amounts of normal impurity scattering: $t^+$ = 100 meV (— — —), 10 meV (– – –), 1 meV (- - - -) and the pure limit (solid line). Normal impurities decrease the critical current until saturation is reached in the dirty limit ($t^+ \approx 100$ meV). Here, $(j_o^{imp})^{2/3} \equiv -T_c \frac{dj_c^{2/3}}{dT}|_{T_c}$.

have their greatest validity, the curves for the different materials increase in magnitude towards zero in increasing order of their degree of strong coupling.

In Fig. 2.6, we show the effect of normal impurities for a selected material, Pb. In qualitative agreement with the BCS results [Kupriyanov and Lickichev (1980)], as the impurity scattering rate is increased the critical current decreases until, in the dirty limit, it saturates. Note that in this figure we have normalized all curves by $(j_o^{imp})^{2/3} \equiv -T_c \frac{dj_c^{2/3}}{dT}|_{T_c}$ to remove the material-dependent constants. Recall, that in the clean limit, we normalized by $j_o^{2/3}$ which is equivalent to $-T_c \frac{dj_c^{2/3}}{dT}|_{T_c}$.

The effect of paramagnetic impurities on Pb is shown in Fig. 2.7. We have shown the curves in two ways as paramagnetic impurities cause a reduction in $T_c$ as well. In Fig. 2.7(a), we display the curves as they start from their effective reduced temperatures ($T_{co}$ is the $T_c$ without any $t^-$), normalized by $(j_o^{imp})^{2/3} \equiv -T_c \frac{dj_c^{2/3}}{dT}|_{T_c}$ and in Fig. 2.7(b), we show curves where $t = T/T_{co}$ and $(j_o^{imp})^{2/3} \equiv -T_{co} \frac{dj_c^{2/3}}{dT}|_{T_c}$. We notice a surprising result: paramagnetic impurity scattering causes an increase in the temperature-dependent part of the critical current over the clean limit result as the temperature is lowered.

To confirm these results, we calculate the functional derivatives which give the differential change in the property $(j_c/j_o)^{2/3}$ for an infinitesimal addition of weight at a frequency $\Omega$ in the spectral function, $\alpha^2F(\omega)$. This is drawn schematically in Fig. 2.8, where the $\alpha^2F(\omega)$ spectrum for Pb is shown augmented by an infinitesimal delta function at a frequency $\Omega$. Formally, the functional derivative is defined as

$$\frac{\delta Q}{\delta \alpha^2 F(\Omega)} = \lim_{\epsilon \to 0} \frac{Q\left[\alpha^2 F(\omega) + \epsilon \delta(\omega - \Omega)\right] - Q\left[\alpha^2 F(\omega)\right]}{\epsilon} \tag{2.9}$$

where $Q$ in this case is $(j_c/j_o)^{2/3}$. This was also calculated numerically and we present results for the Pb spectrum only, as the results are similar for the other materials.

In Fig. 2.9, we show the functional derivative for pure Pb for several temperatures. There are several interesting things to notice. First, the functional derivative is mostly positive, except at low frequencies, with a maximum and then going to zero at higher frequencies. This illustrates that moving weight from any region of the spectral function to the frequency of the maximum in the functional derivative will increase the property. Adding

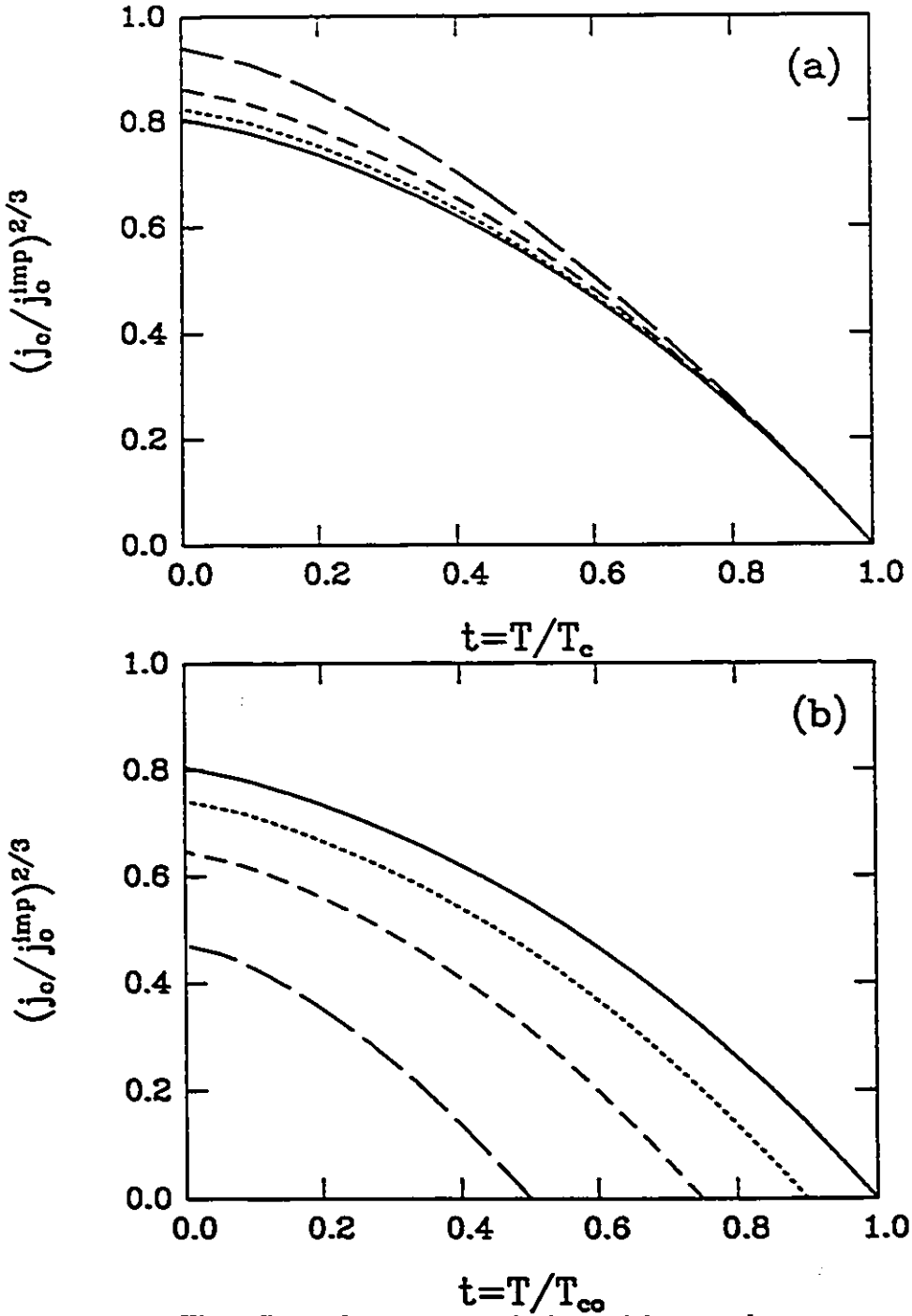


**Figure 2.7** The effect of paramagnetic impurities on the temperature dependence of the critical current for the material, Pb. Shown are curves for $t^- = 0.188$ meV (— — —), 0.102 meV (– – –), 0.042 meV (- - - -), and the pure limit (solid line) corresponding to reduced $T_c$'s of $T_c/T_{co} = 0.5$, 0.75, 0.9, and 1, respectively. In (a), the critical current is plotted as a function of $T/T_c$, with $(j_o^{imp})^{2/3} \equiv -T_c \frac{dj_c^{2/3}}{dT}|_{T_c}$, and in (b) it is plotted as a function of $T/T_{co}$, with $(j_o^{imp})^{2/3} \equiv -T_{co} \frac{dj_c^{2/3}}{dT}|_{T_c}$, to exhibit, in the latter case, the reduction in $T_c$ with increasing paramagnetic impurity scattering.

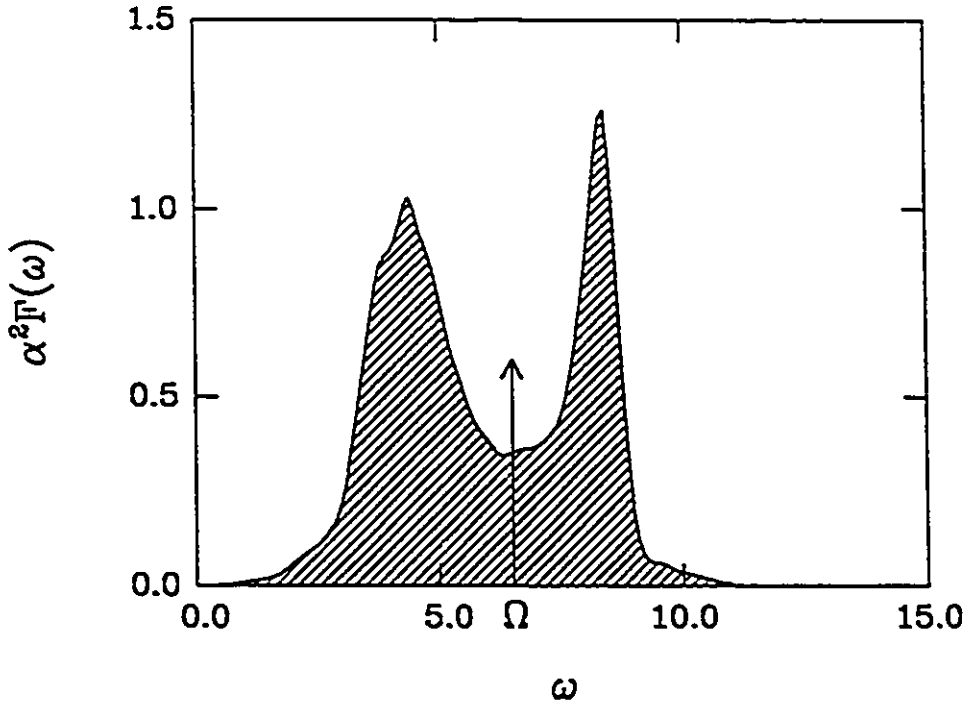


Figure 2.8 A schematic representation of the concept of a functional derivative. The $\alpha^2F(\omega)$, in this case, that for Pb, is augmented by an infinitesimal delta function at $\omega = \Omega$ and the change that occurs in the property is calculated.

spectral weight at any frequency will enhance $j_c$ except at very low frequencies where the functional derivative is negative. In this region, adding weight decreases $j_c$ which is in perfect agreement with the results for normal impurities because low frequency phonons mimic static impurities and from Fig. 2.6, we see that this should decrease $j_c$ as it does. Another point to notice is that the overall magnitude of the functional derivative decreases with temperature and this reflects the fact that absolute value of the slope of the curves in Fig. 2.4 is decreasing as the temperature is lowered. This is simply the inelastic scattering freezing out at lower temperatures. Recall that the inelastic scattering here refers to electron-phonon scattering.

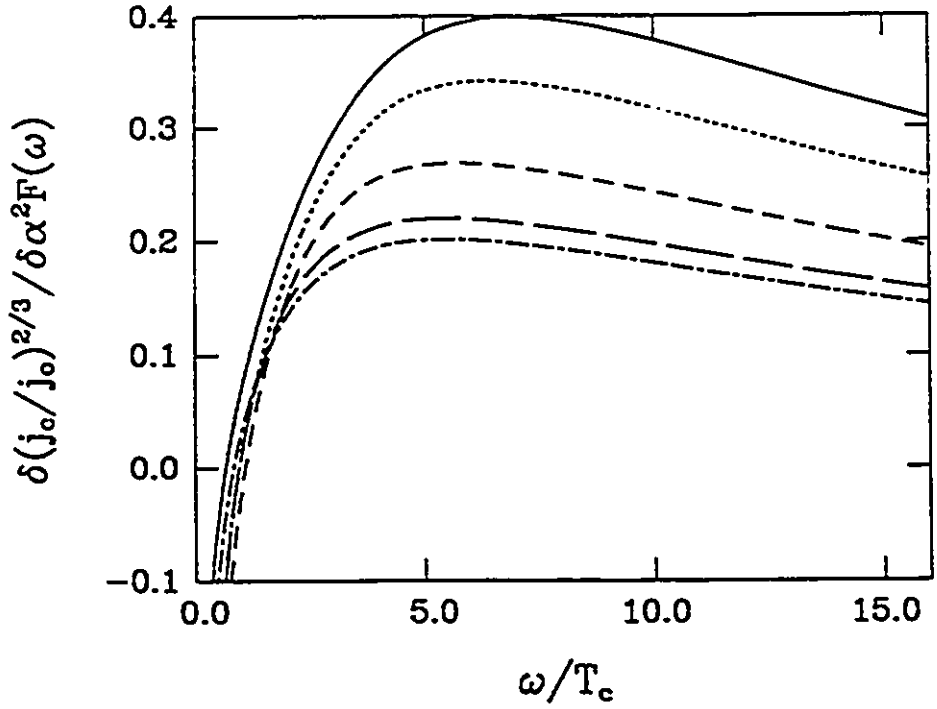


**Figure 2.9** The functional derivative of the critical current for pure Pb versus $\omega/T_c$ for the reduced temperature $t = 0.9$ (solid line), 0.75 (- - - -), 0.5 (– – –), 0.25 (— — —), and 0.1 (— - — -).

Finally, in Fig. 2.10, we display functional derivatives for different impurity content. The upper frame shows the results for normal impurities. Notice that the overall decrease in magnitude of the curves with increasing impurites is similar to the decreases in the curves of Fig. 2.6. The features of the curves are the same as in Fig. 2.9 but now the negative tail at lower frequencies is starting to shift inward towards the origin with increasing impurity scattering and is finally non-existent in the dirty limit as the critical current has saturated and no further impurity scattering can reduce the current further. The second frame illustrating the effect of paramagnetic impurities has similar features as the others. Again the increasing magnitude of the curves with impurity content is similar to the increasing magnitude of the curves in Fig. 2.7. The shape and negative low frequency tail follow

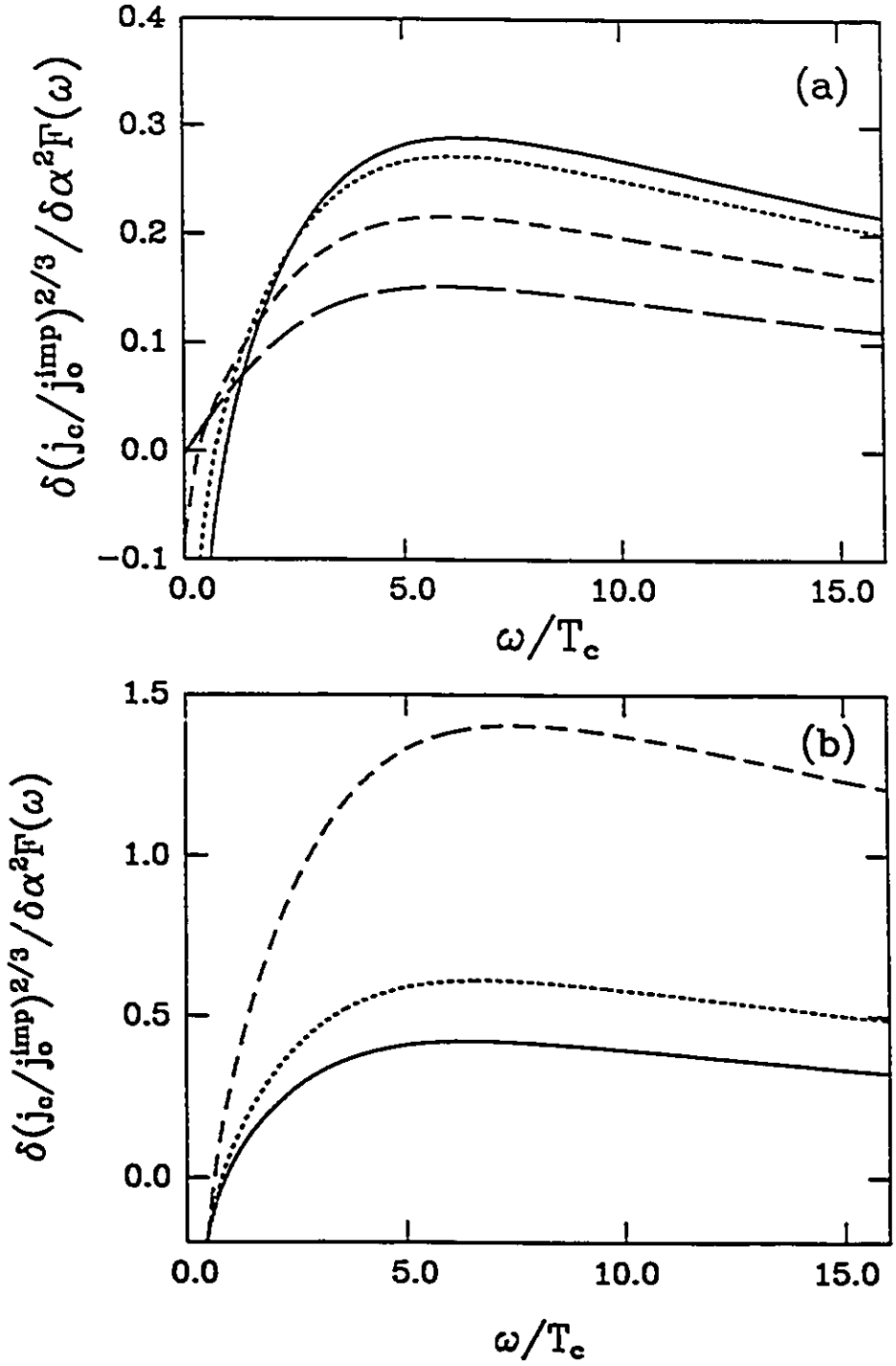


**Figure 2.10** (a) The functional derivative for Pb at $T/T_c = 0.75$ versus $\omega/T_c$ for several values of $t^+$: 0 meV (solid line), 1 meV (- - - -), 10 meV (— — —) and 100 meV (— — — —). Notice that in the dirty limit ($t^+ \approx 100$ meV), there remains no negative low frequency tail as the system has saturated and no additional impurity scattering can cause a reduction in $j_c$. (b) The functional derivative for Pb in the case of added paramagnetic impurities: $t^- = 0.188$ meV (solid line), 0.102 meV (- - - -) and 0.042 meV (— — —).

from the same discussion as the other curves and it is only the change in magnitude that is of interest here.

## 2.4 STRONG COUPLING CORRECTION FORMULA

After the manner of Marsiglio and Carbotte (1986) and Marsiglio (1988), we develop a formula giving the strong coupling correction to the clean limit Ginzburg-Landau result near $T_c$, in terms of the strong coupling parameter $T_c/\omega_{\ln}$, where $\omega_{\ln}$ is the characteristic Allen-Dynes frequency of $\alpha^2F(\omega)$ defined as [Allen and Dynes (1975)]:

$$\omega_{\ln} = \exp\left[\frac{2}{\lambda}\int_0^\infty d\omega\,\frac{\alpha^2F(\omega)}{\omega}\ln\omega\right] \quad . \tag{2.10}$$

Performing the integrals over $z$ and expanding in powers of $\tilde{\Delta}_m/\tilde{\omega}_m$ and $s/\tilde{\omega}_m$, as $\Delta_m$ and $s$ are small near $T_c$, Eqs. (2.6) and (2.7) become:

$$\tilde{\Delta}_n \simeq \pi T\sum_{m=-\infty}^{\infty}\int_0^\infty \frac{d\nu\,2\nu\,\alpha^2F(\nu)}{\nu^2+(\omega_m-\omega_n)^2}\frac{\tilde{\Delta}_m}{|\,\tilde{\omega}_m\,|}\left(1-\frac{\tilde{\Delta}_m^2}{2\tilde{\omega}_m^2}-\frac{1}{3}\frac{s^2}{\tilde{\omega}_m^2}\right) \tag{2.11}$$

and

$$Z_s(n) \simeq 1+\frac{\pi T}{\omega_n}\sum_{m=-\infty}^{\infty}\int_0^\infty \frac{d\nu\,2\nu\,\alpha^2F(\nu)}{\nu^2+(\omega_m-\omega_n)^2}\frac{\tilde{\omega}_m}{|\,\tilde{\omega}_m\,|}\left(1-\frac{\tilde{\Delta}_m^2}{2\tilde{\omega}_m^2}\right) \quad , \tag{2.12}$$

where we have kept terms only to $\mathcal{O}(\tilde{\Delta}_m^2)$ and $\mathcal{O}(s^2)$. We have set $t^+$ and $t^-$ equal to zero for the clean limit and have taken $\mu^* = 0$ for simplicity, realizing that some of the effects of $\mu^*$ will already be included in $T_c$ which is taken from experiment. We now use a step function approximation [Marsiglio and Carbotte (1986); Marsiglio (1988)] for $\Delta(\omega_n)$ and $Z(\omega_n)$ of the form:

$$\Delta(\omega_n) = \begin{cases} \Delta_o(T) & , \quad |\,\omega_n\,| < \omega_o \\ \Delta_\infty & , \quad |\,\omega_n\,| > \omega_o \end{cases} , \tag{2.13a}$$

$$Z(\omega_n) = \begin{cases} Z_o(T) & , \quad |\,\omega_n\,| < \omega_o \\ 1 & , \quad |\,\omega_n\,| > \omega_o \end{cases} , \tag{2.13b}$$

where $\omega_c$ is several times the maximum phonon frequency. We also assume that $T_c \ll \omega_{ln} \ll \omega_c$, where $\omega_{ln}$ is the characteristic Allen-Dynes frequency of $\alpha^2F(\omega)$ given in Eq. (2.10). In this approximation Eqs. (2.11) and (2.12) become:

$$\tilde{\Delta}_n = \pi T \sum_{m=-N_c+1}^{N_c} \int_0^\infty \frac{d\nu\, 2\nu\, \alpha^2F(\nu)}{\nu^2 + (\omega_m - \omega_n)^2} \frac{\tilde{\Delta}_c}{|\tilde{\omega}_m|}\left(1 - \frac{\tilde{\Delta}_c^2}{2\tilde{\omega}_m^2} - \frac{1}{3}\frac{\bar{s}^2}{\tilde{\omega}_m^2}\right) \qquad (2.14)$$

and

$$Z_S(n) = Z_N(n) + \frac{\pi T}{\omega_n} \sum_{m=-N_c+1}^{N_c} \int_0^\infty \frac{d\nu\, 2\nu\, \alpha^2F(\nu)}{\nu^2 + (\omega_m - \omega_n)^2} \mathrm{sgn}(\omega_m)\left(-\frac{1}{2}\frac{\tilde{\Delta}_c^2}{\tilde{\omega}_m^2}\right) \quad , \qquad (2.15)$$

where $N_c = \frac{\omega_c}{2\pi T} + \frac{1}{2}$. Note that $\Delta_\infty$ can be replaced by zero in Eq. (2.13a) as $\Delta_\infty$ can be shown to be proportional to $\mu^*$, which we have taken to be zero. These two equations can be written as:

$$\Delta_c Z_S(n) = \int_0^\infty 2\nu\, d\nu\, \alpha^2F(\nu)\Delta_c\left[P_1 + Q_1 - \frac{\Delta_c^2}{2}(P_2 + Q_2) - \frac{1}{3}\bar{s}^2(P_2 + Q_2)\right] \qquad (2.16)$$

and

$$Z_S(n) = Z_N(n) + \int_0^\infty d\nu\, 2\nu\, \alpha^2F(\nu)\left[-\frac{1}{2}\Delta_c^2(U_1 + V_1)\right] \quad , \qquad (2.17)$$

where, by folding the sums to the domain $[1, \infty]$ and replacing $N_c$ by infinity as the convergence is sufficiently rapid, we have extracted the following sums:

$$U_i \equiv 4\pi T \sum_{m=1}^{\infty} \frac{1}{\omega_m^{2i-1}} \frac{1}{(\omega_m^2 + \omega_n^2 + \nu^2)^2} \quad , \qquad (2.18a)$$

$$V_i \equiv 4\pi T \sum_{m=1}^{\infty} \frac{1}{\omega_m^{2i-1}} \frac{4\omega_m^2\omega_n^2}{(\omega_m^2 + \omega_n^2 + \nu^2)^4} \quad , \qquad (2.18b)$$

$$P_i \equiv 2\pi T \sum_{m=1}^{\infty} \frac{1}{\omega_m^{2i-1}} \frac{1}{\omega_m^2 + \omega_n^2 + \nu^2} \quad , \qquad (2.18c)$$

$$Q_i \equiv 2\pi T \sum_{m=1}^{\infty} \frac{1}{\omega_m^{2i-1}} \frac{4\omega_m^2\omega_n^2}{(\omega_m^2 + \omega_n^2 + \nu^2)^3} \quad . \qquad (2.18d)$$

We have also used the notation $\tilde{s} = s/Z_s(i\omega_n) \simeq s/(1+\lambda)$. These sums can be evaluated in terms of digamma functions and to $\mathcal{O}(1/\nu^4)$ they are, for small $n$, in particular for $n = 1$,

$$Q_1 = \frac{(\pi T)^2}{\nu^4} \quad , \tag{2.19a}$$

$$P_1 = \frac{1}{\nu^2}\ln\frac{1.13\nu}{k_BT} - \frac{(\pi T)^2}{\nu^4}\left(\ln\frac{1.13\nu}{k_BT} - \frac{1}{2}\right) - \frac{1}{6}\frac{(\pi T)^2}{\nu^4} \quad , \tag{2.19b}$$

$$P_2 = \frac{7}{4}\frac{\zeta(3)}{(\pi T)^2}\frac{1}{\nu^2} - \frac{7}{4}\zeta(3)\frac{1}{\nu^4} - \frac{1}{\nu^4}\ln\frac{1.13\nu}{k_BT} \quad , \tag{2.19c}$$

$$U_1 = \frac{2}{\nu^4}\left(\ln\frac{1.13\nu}{k_BT} - \frac{1}{2}\right) \quad , \tag{2.19d}$$

The rest, including $Q_2$ and $V_1$, are to higher order and are not kept as $T_c \ll \nu$. Here, $\zeta(x)$ is the Riemann zeta function.

Substituting Eq. (2.17) into Eq. (2.16), we can arrive at the simple form of

$$1 = F(T) + \Delta_o^2 G(T) + \frac{2}{3}\tilde{s}^2 H(T) \quad , \tag{2.20}$$

where we define

$$F(T) \equiv \frac{\lambda}{1+\lambda}\ln\frac{1.13\omega_o}{k_BT} - \frac{\bar{\lambda}-\tilde{\lambda}}{1+\lambda} - \frac{(\pi T)^2}{1+\lambda}[a(T) - \frac{4}{3}b] \quad , \tag{2.21a}$$

$$G(T) \equiv -\frac{7}{8}\frac{\zeta(3)}{(\pi T)^2}\frac{\lambda}{1+\lambda} + \frac{7}{8}\zeta(3)\frac{b}{1+\lambda} - \frac{b}{2}\frac{1}{1+\lambda} + \frac{3}{2}\frac{a(T)}{1+\lambda} \quad , \tag{2.21b}$$

and

$$H(T) \equiv -\frac{7}{8}\frac{\zeta(3)}{(\pi T)^2}\frac{\lambda}{1+\lambda} + \frac{7}{8}\zeta(3)\frac{b}{1+\lambda} + \frac{1}{2}\frac{a(T)}{1+\lambda} \quad , \tag{2.21c}$$

with the following moments of $\alpha^2F(\nu)$:

$$a(T) \equiv \int_0^\infty \frac{2\nu\alpha^2F(\nu)}{\nu^4}\ln\frac{1.13\nu}{k_BT}\,d\nu \quad , \tag{2.22a}$$

$$b \equiv \int_0^\infty \frac{2\nu\alpha^2F(\nu)}{\nu^4}\,d\nu \quad , \tag{2.22b}$$

$$\bar{\lambda} \equiv \int_0^\infty \frac{2\nu\alpha^2 F(\nu)}{\nu^2} \ln \frac{\omega_o + \nu}{\nu} d\nu \quad , \tag{2.22c}$$

$$\tilde{\lambda} \equiv \int_0^\infty \frac{2\nu\alpha^2 F(\nu)}{\nu^2} \ln \frac{\omega_o + \nu}{\omega_o} d\nu \quad , \tag{2.22d}$$

and

$$\int_0^\infty \frac{2\nu\alpha^2 F(\nu)}{\nu^2} \ln \frac{1.13\nu}{k_B T} d\nu = \lambda \ln \frac{1.13\omega_o}{k_B T} - (\bar{\lambda} - \tilde{\lambda}) \quad . \tag{2.23}$$

For $\omega_o \gg \nu$, $\tilde{\lambda} \approx 0$. Note that $F(T_c) = 1$ gives a $T_c$ equation with strong coupling corrections.

Now examining Eq. (2.5) for the superfluid current density, we can integrate by parts to find

$$j_s = \frac{3eN}{m} \pi T \sum_{n=-\infty}^{\infty} \int_{-1}^{1} dz \frac{z^2 \Delta_n^2}{[(\omega_n - i\bar{s}_n z)^2 + \Delta_n^2]^{3/2}} \vec{q}_s \quad . \tag{2.24}$$

Neglecting $\bar{s}_n z$ and $\Delta_n^2$ in the denominator relative to $T$:

$$j_s = \frac{eN}{m} \pi T_c \sum_{n=-\infty}^{\infty} \frac{\Delta_n^2}{|\omega_n|^3} \vec{q}_s \quad . \tag{2.25}$$

Using the step-function approximation,

$$j_s = \frac{eN}{m v_F} \frac{2}{(\pi T_c)^2} \frac{7}{8} \zeta(3) \Delta_o^2 \bar{s} \quad . \tag{2.26}$$

Substituting $\Delta_o$ from Eq. (2.20) into Eq. (2.26) yields

$$j_s = \frac{eN}{m v_F} \frac{2}{(\pi T_c)^2} \frac{7}{8} \zeta(3) \left[ \frac{1 - F(T)}{G(T_c)} - \frac{2}{3} \frac{H(T_c)}{G(T_c)} \bar{s}^2 \right] \bar{s} \quad . \tag{2.27}$$

Taking $dj_s/d\bar{s} = 0$ gives the critical value of $\bar{s}$, $\bar{s}_c$, that maximizes $j_s$:

$$\bar{s}_c^2 = \frac{1}{2} \left( \frac{1 - F(T)}{H(T_c)} \right) \quad , \tag{2.28}$$

and $j_c \equiv j_s(\bar{s}_c)$ gives

$$\begin{aligned} j_c &= \frac{eN}{m v_F} \frac{2}{(\pi T_c)^2} \frac{7}{8} \zeta(3) \frac{2}{3\sqrt{2}} \frac{[1 - F(T)]^{3/2}}{G(T_c)\sqrt{H(T_c)}} \quad , \\ &= j_{oo} \frac{[1 - F(T)]^{3/2}}{G(T_c)\sqrt{H(T_c)}} \quad , \end{aligned} \tag{2.29}$$

where $j_{oo} \equiv 7\zeta(3)cN/(6\sqrt{2}mv_F(\pi T_c)^2)$.

Now $a(T_c)$ and $b$ can be evaluated to be [Marsiglio (1988)]:

$$a(T_c) = \frac{\alpha_1}{\omega_{\ln}^2}\lambda \ln\frac{1.13\omega_{\ln}}{k_B T_c} \quad , \tag{2.30a}$$

$$b = \frac{\alpha_2}{\omega_{\ln}^2}\lambda \quad , \tag{2.30b}$$

where $\alpha_1$ and $\alpha_2$ are constants compensating for averaging over the spectrum using the mean value theorem of calculus. Using the fact that $F(T_c) = 1$,

$$\begin{aligned} F(T) &= 1 + \frac{\lambda}{1+\lambda}\ln\frac{T_c}{T} \quad , \\ &\simeq 1 + \frac{\lambda}{1+\lambda}(1-t)\left[1 + 2\pi^2\alpha_1\left(\frac{T_c}{\omega_{\ln}}\right)^2 \ln\frac{1.13\omega_{\ln}}{k_B T_c}\right. \\ &\qquad \left. - \pi^2\left(\alpha_1 + \frac{8}{3}\alpha_2\right)\left(\frac{T_c}{\omega_{\ln}}\right)^2\right] \end{aligned} \tag{2.31a}$$

and

$$G(T_c) = -\frac{7}{8}\frac{\zeta(3)}{(\pi T_c)^2}\frac{\lambda}{1+\lambda} + \frac{7}{8}\zeta(3)\frac{\alpha_2}{\omega_{\ln}^2}\frac{\lambda}{1+\lambda} - \frac{1}{2}\frac{\alpha_2}{\omega_{\ln}^2}\frac{\lambda}{1+\lambda} + \frac{3}{2}\frac{\alpha_1}{\omega_{\ln}^2}\frac{\lambda}{1+\lambda}\ln\frac{1.13\omega_{\ln}}{k_B T_c} \quad , \tag{2.31b}$$

$$H(T_c) = -\frac{7}{8}\frac{\zeta(3)}{(\pi T_c)^2}\frac{\lambda}{1+\lambda} + \frac{7}{8}\zeta(3)\frac{\alpha_2}{\omega_{\ln}^2}\frac{\lambda}{1+\lambda} + \frac{1}{2}\frac{\alpha_1}{\omega_{\ln}^2}\frac{\lambda}{1+\lambda}\ln\frac{1.13\omega_{\ln}}{k_B T_c} \quad , \tag{2.31c}$$

where $t = T/T_c$. Substituting Eq. (2.31) into Eq. (2.29) and expanding in terms of the small parameter, $T_c/\omega_{\ln}$, leads to a form for $j_c$, near $T_c$, of

$$\begin{aligned} \left(\frac{j_c}{j_{oo}}\right)^{2/3} &= \frac{1 - F(T)}{[G^2(T_c)H(T_c)]^{1/3}} \quad , \\ &\simeq \frac{8(\pi T_c)^2}{7\zeta(3)}(1-t)\left[1 + \left(\frac{T_c}{\omega_{\ln}}\right)^2 a_1 \ln\frac{\omega_{\ln}}{a_2 T_c}\right] , \end{aligned} \tag{2.32}$$

or finally,

$$\left|\frac{d(j_c/j_o)^{2/3}}{dt}\right|\Bigg)_{t=1} = 1 + a_1\left(\frac{T_c}{\omega_{\ln}}\right)^2 \ln\left(\frac{\omega_{\ln}}{a_2 T_c}\right) \quad , \tag{2.33}$$

where $a_1$ and $a_2$ are constants related to particular moments of the $\alpha^2F(\omega)$ spectrum, $T_c/\omega_{\ln} \ll 1$, and $j_o = 8eN\pi T_c/(3mv_F\sqrt{7\zeta(3)})$.

As in previous work, due to the approximations made, we prefer to fit this form (*i.e.*, $a_1$ and $a_2$) to the calculated values for several materials to obtain a correction formula in terms of a single parameter. We find that a reasonable fit to the numerical data is given by

$$\left|\frac{d(j_c/j_o)^{2/3}}{dt}\right|_{t=1} = 1 + 21.2\left(\frac{T_c}{\omega_{\ln}}\right)^2 \ln\left(\frac{\omega_{\ln}}{2.3T_c}\right) \quad . \tag{2.34}$$

Here, we have used the slopes at $T_c$ for the curves of several type I materials, some of which are shown in Fig. 2.4, and their known values of $T_c/\omega_{\ln}$ and we have also used several Einstein spectra with different $T_c/\omega_{\ln}$ values to aid in fitting the function. Fig. 2.11 shows the slope at $T_c$ for several type I materials (solid dots) and Einstein spectra (open circles). The fit of Eq. (2.34) is shown as the solid curve and represents the theoretical data well. Deviations from a single curve will result due to the detailed shape of the $\alpha^2F(\omega)$ spectrum and the specific value of $\mu^*$, which are not fully accounted for in Eq. (2.34), but the general trend is well-described by a single parameter, $T_c/\omega_{\ln}$, using this formula. Note, that the BCS result of a slope of 1 is recovered in the limit of $T_c/\omega_{\ln} \to 0$.

## 2.5 THE ASYMPTOTIC LIMIT NEAR $T_c$ IN THE ONE-GAP MODEL

To investigate whether strong coupling will always increase $j_c$ near $T_c$ in the clean limit, we can examine the unphysical asymptotic limit of $\lambda \to \infty$

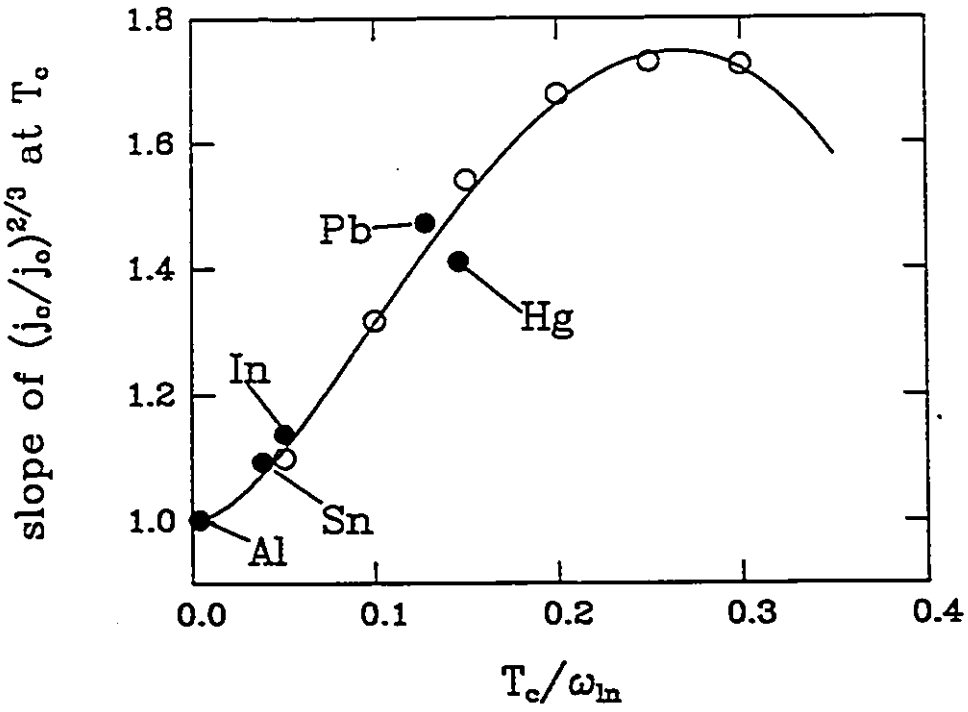


Figure 2.11 The absolute value of the slope of $(j_c/j_o)^{2/3}$ at $T_c$ in the clean limit as a function of a single strong coupling parameter $T_c/\omega_{ln}$ for the materials indicated in the figure. The open circles are Einstein spectra with $\mu^* = 0$. The curve corresponds to Eq. (2.34) of the text.

following the procedure of Marsiglio *et al.* . (1989, 1990) and Marsiglio and Carbotte (1990). Substituting Eq. (2.12) into Eq. (2.11) yields

$$\Delta_n + \frac{\pi T}{\omega_n}\Delta_n \sum_{m=-\infty}^{\infty} \lambda(n-m)\frac{\omega_m}{|\,\omega_m\,|}\left(1-\frac{\Delta_m^2}{2\omega_m^2}\right) = \pi T \sum_{m=-\infty}^{\infty} \lambda(n-m)\frac{\Delta_m}{|\,\omega_m\,|}\left(1-\frac{\Delta_m^2}{2\omega_m^2}-\frac{1}{3}\frac{\bar{s}_m^2}{\omega_m^2}\right), \quad (2.35)$$

where $\bar{s}_m \equiv s/Z_s(m)$. Separating out the $n = m$ term explicitly,

$$\Delta_n + \frac{\pi T}{\omega_n}\Delta_n\lambda(0)\frac{\omega_n}{|\,\omega_n\,|}\left(1-\frac{\Delta_n^2}{2\omega_n^2}\right) + \frac{\pi T}{\omega_n}\Delta_n \sum_{m\neq n} \lambda(n-m)\frac{\omega_m}{|\,\omega_m\,|}\left(1-\frac{\Delta_m^2}{2\omega_m^2}\right)$$

$$= \pi T\lambda(0)\frac{\Delta_n}{|\,\omega_n\,|}\left(1-\frac{\Delta_n^2}{2\omega_n^2}-\frac{1}{3}\frac{\bar{s}_n^2}{\omega_n^2}\right) + \pi T \sum_{m\neq n} \lambda(n-m)\frac{\Delta_m}{|\,\omega_m\,|}\left(1-\frac{\Delta_m^2}{2\omega_m^2}-\frac{1}{3}\frac{\bar{s}_m^2}{\omega_m^2}\right). \quad (2.36)$$

With the exception of the $\lambda(0)$ term coupled with $\tilde{s}_m^2$, the other $\lambda(0)$ terms cancel with the result:

$$\Delta_n = \pi T \sum_{m \neq n} \lambda(n-m)\left(\Delta_m - \frac{\omega_m}{\omega_n}\Delta_n\right)\left[\frac{1}{|\omega_m|}\left(1 - \frac{1}{2}\frac{\Delta_m^2}{\omega_m^2}\right)\right]$$
$$- \frac{1}{3}\pi T \lambda(0)\frac{\Delta_n}{|\omega_n|}\frac{\tilde{s}_n^2}{\omega_n^2} - \frac{1}{3}\pi T \sum_{m \neq n} \lambda(n-m)\frac{\Delta_m}{|\omega_m|}\frac{\tilde{s}_m^2}{\omega_m^2} \quad . \tag{2.37}$$

For convenience, we will use a delta function for the spectral function, $\alpha^2 F(\nu) \equiv A\delta(\nu - \omega_E)$, with position at the Einstein frequency, $\omega_E$, and area, $A$. With this choice, $\lambda(n-m)$ of Eq. (2.8) becomes

$$\lambda(m-n) = \frac{2\omega_E A}{\omega_E^2 + (\omega_m - \omega_n)^2} \quad . \tag{2.38}$$

And for $n = m$, $\lambda(0) = 2A/\omega_E$.

As we are interested in the asymptotic limit of $\lambda \to \infty$, when we examine $\lambda(n-m)$ for $n \neq m$, as shown in Eq. (2.38), for $\lambda \to \infty$, we can neglect $\omega_E$ in the denominator (*i.e.*, $\lambda = 2A/\omega_E$ and we fix $A$ and let $\omega_E \to 0$) provided $n \neq m$ and $\omega_E \ll 2\pi T$. So $\lambda(n-m)$ becomes:

$$\lambda(n-m) = \frac{2\omega_E A}{(\omega_n - \omega_m)^2} \quad . \tag{2.39}$$

We use Eq. (2.39) and take advantage of the symmetries of $\Delta(-n) = \Delta(n+1)$ and $\omega(-n) = -\omega(n+1)$ to fold the sums over to the [1,∞] domain and find that

$$\Delta_n = \pi T \omega_E A \sum_{m=1}^{\infty} \frac{2}{(2\pi T)^2}\left\{\left[\frac{1-\delta_{n,m}}{(m-n)^2} + \frac{1}{(m+n-1)^2}\right]\Delta_m\right.$$
$$\left. - \left[\frac{1-\delta_{n,m}}{(m-n)^2} - \frac{1}{(m+n-1)^2}\right]\Delta_n\frac{\omega_m}{\omega_n}\right\}\left[\frac{1}{\omega_m} - \frac{1}{2}\frac{\Delta_m^2}{\omega_m^3}\right] - \frac{1}{3}\pi T\lambda(0)\Delta_n\frac{\tilde{s}_n^2}{\omega_n^3}$$
$$- \frac{1}{3}\pi T \omega_E A \sum_{m=1}^{\infty} \frac{2}{(2\pi T)^2}\left\{\left[\frac{1-\delta_{n,m}}{(m-n)^2} + \frac{1}{(m+n-1)^2}\right]\Delta_m\frac{\tilde{s}_m^2}{\omega_m^3}\right. . \tag{2.40}$$

Now to obtain a rough approximation, we assume that $\Delta(n = 1) = \Delta(T)$ and that all other gaps are zero. This is known as the one-gap model. For $m = n = 1$:

$$\Delta(T) = \Delta(T)\frac{\omega_E A}{2\pi T}\left[\frac{1}{\omega_1} - \frac{\Delta^2(T)}{\omega_1^3}\right] - \frac{1}{3}\pi T\lambda(0)\frac{\Delta(T)}{\omega_1}\frac{\bar{s}_1^2}{\omega_1^2} - \frac{1}{3}\Delta(T)\frac{\omega_E A}{2\pi T}\frac{\bar{s}_1^2}{\omega_1^3} \quad , \quad (2.41)$$

or

$$1 = \frac{\omega_E A}{2\pi T}\left[\frac{1}{\pi T} - \frac{\Delta^2(T)}{(\pi T)^3}\right] - \frac{1}{3}\lambda(0)\frac{\bar{s}_1^2}{(\pi T)^2} - \frac{1}{3}\frac{\omega_E A}{2\pi T}\frac{\bar{s}_1^2}{(\pi T)^3} \quad , \quad (2.42)$$

Note that the sum to infinity of the $\Delta_n$ term is zero for $1/\omega_m$ term in the square brackets as the terms cancel in pairs. Solving for $\Delta^2(T)$:

$$\Delta^2(T) = (\pi T)^2 - 2\frac{(\pi T)^4}{\omega_E A}\left[1 + \frac{1}{3}\lambda(0)\frac{\bar{s}_1^2}{(\pi T)^2} + \frac{1}{3}\frac{\omega_E A}{(\pi T)^4}\bar{s}_1^2\right] \quad . \quad (2.43)$$

We now substitute Eq. (2.43) into Eq. (2.25) for the superfluid current density near $T_c$ to find

$$\begin{aligned} j_s &= \frac{eN}{mv_F}\frac{1}{(\pi T_c)^2}\Delta(T)\bar{s}_1 \\ &= \frac{eN}{mv_F}\frac{1}{(\pi T_c)^2}\left[(\pi T)^2 - 2\frac{(\pi T)^4}{\omega_E A} - \frac{2}{3}\frac{(\pi T)^2}{\omega_E A}\left(\lambda(0) + \frac{\omega_E A}{(\pi T)^2}\right)\bar{s}_1^2\right]\bar{s}_1 \quad . (2.44) \end{aligned}$$

Applying $dj_s/d\bar{s}_1 = 0$ to find the critical value of $\bar{s}_c$ gives

$$\bar{s}_c^2 = \frac{\omega_E A}{2(\pi T)^2}\frac{1}{\lambda(0) + \omega_E A/(\pi T)^2}\left[(\pi T)^2 - 2\frac{(\pi T)^4}{\omega_E A}\right] \quad . \quad (2.45)$$

And $j_c \equiv j_s(\bar{s}_c)$ is

$$j_c = \frac{eN}{mv_F}\frac{2}{3\sqrt{2}}\sqrt{\frac{\omega_E A}{\lambda(0) + \omega_E A/(\pi T_c)^2}}\left[1 - 2\frac{(\pi T)^2}{\omega_E A}\right]^{3/2} \quad . \quad (2.46)$$

Using $\pi T_c = \sqrt{(A\omega_E/2)}$, derived from Eq. (2.42) with $\Delta$ and $s$ equal to zero, we arrive at

$$\begin{aligned} j_c &= \frac{eN}{mv_F}\frac{2}{3\sqrt{2}}\sqrt{\frac{2}{\lambda(0) + 2}}\pi T_c(1 - t^2)^{3/2} \quad , \\ &\simeq \frac{eN}{mv_F}\frac{4}{3}\pi T_c\sqrt{\frac{2}{\lambda(0) + 2}}(1 - t)^{3/2} \quad . \quad (2.47) \end{aligned}$$

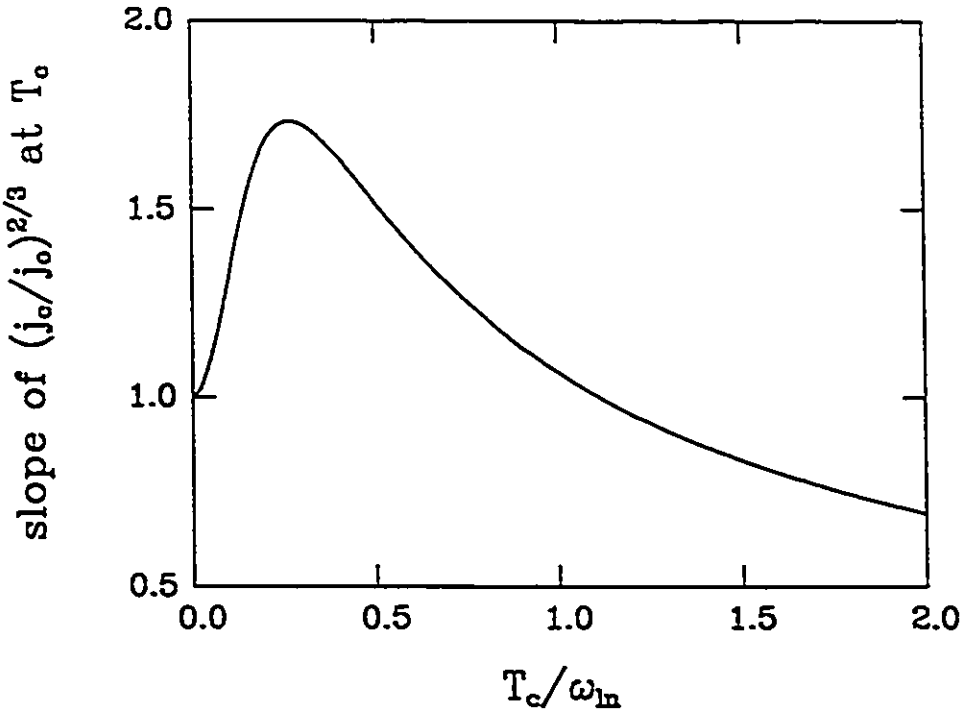


**Figure 2.12** The absolute value of the slope of $(j_c/j_o)^{2/3}$ at $T_c$ in the clean limit as a function of the strong coupling parameter $T_c/\omega_{ln}$ for Einstein spectra with $\mu^* = 0$. In the very strong coupling regime, the slope decreases and falls below the BCS value of 1. At $T_c/\omega_{ln} \sim 4$, this curves joins up with our analytic asymptotic form.

Now as $\lambda = 2A/\omega_E$, and hence $\pi T_c = \sqrt{\lambda}\omega_E/2$

$$j_c \simeq \frac{eN}{mv_F}\frac{2\sqrt{2}}{3}\omega_E(1-t)^{3/2} \quad , \quad \lambda \to \infty. \tag{2.48}$$

If we write Eq. (2.47), as $(j_c/j_o)^{2/3}$, where $j_o$ is defined at the end of Section IV, then

$$\left|\frac{d(j_c/j_o)^{2/3}}{dt}\right|_{t=1} \simeq \left(\frac{7\zeta(3)}{2}\right)^{1/3}\frac{1}{\lambda^{1/3}} \quad , \quad \lambda \to \infty. \tag{2.49}$$

Thus, for very strong coupling, the slope of $(j_c/j_o)^{2/3}$ should reduce and eventually fall below the BCS value. To verify this behaviour, we used an Einstein spectrum to numerically calculate the slope near $T_c$ for large values of $T_c/\omega_{ln}$. In Fig. 2.12, we display our results. For $T_c/\omega_{ln} \ll 1$, the

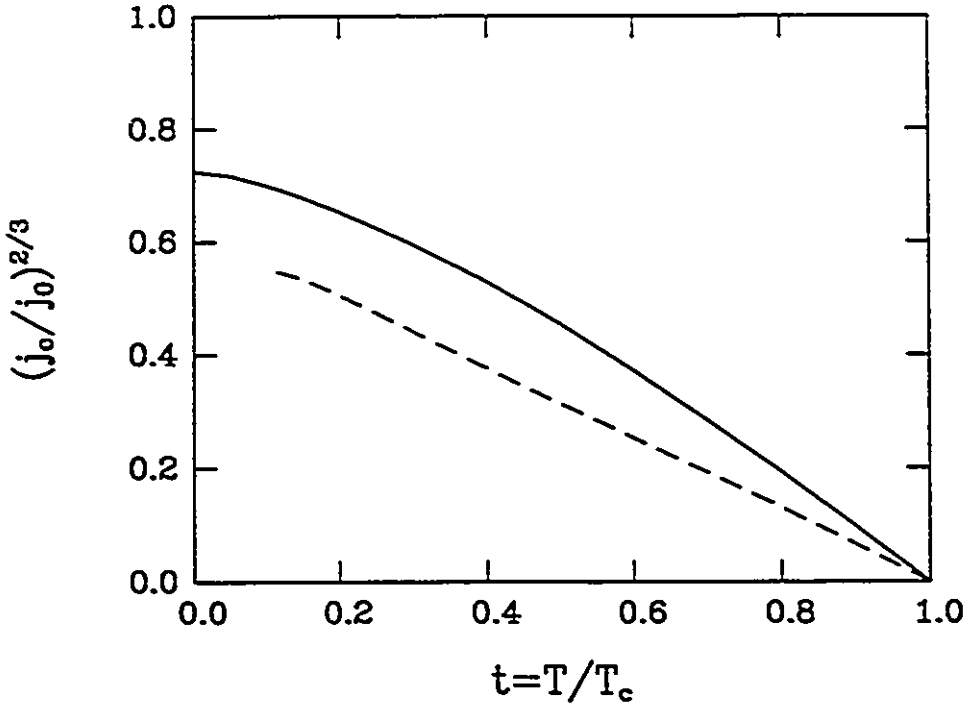


**Figure 2.13** The temperature dependence of the critical current density for an Einstein spectrum with $T_c/\omega_{ln} = 2.0$ and $\mu^* = 0$ (dashed curve). Plotted for comparison is the BCS result (solid line). Extremely strong inelastic scattering can reduce the critical current.

curve agrees with the form found in Section IV. The slope then turns over at a value of $T_c/\omega_{ln} \sim 0.26$ and begins to decrease, falling below BCS for values of $T_c/\omega_{ln} > 0.6$. We found that the numerical curve joined up with our analytical asymptotic form (Eq. (2.49)) at a $T_c/\omega_{ln} \sim 4$.

In Fig. 2.13, we display the temperature dependence of $(j_c/j_o)^{2/3}$ in the very strong coupling regime for $T_c/\omega_{ln} = 2.0$ (dashed curve). We notice that the slope of the curve near $T_c$ is below the BCS curve (plotted as the solid curve for comparison) and that the temperature dependence is nearly linear down to low temperatures.

The values of the inelastic scattering rate used by Lemberger and Coffey (1988) correspond to values of $T_c/\omega_{ln} < 0.25$ and this is in the regime

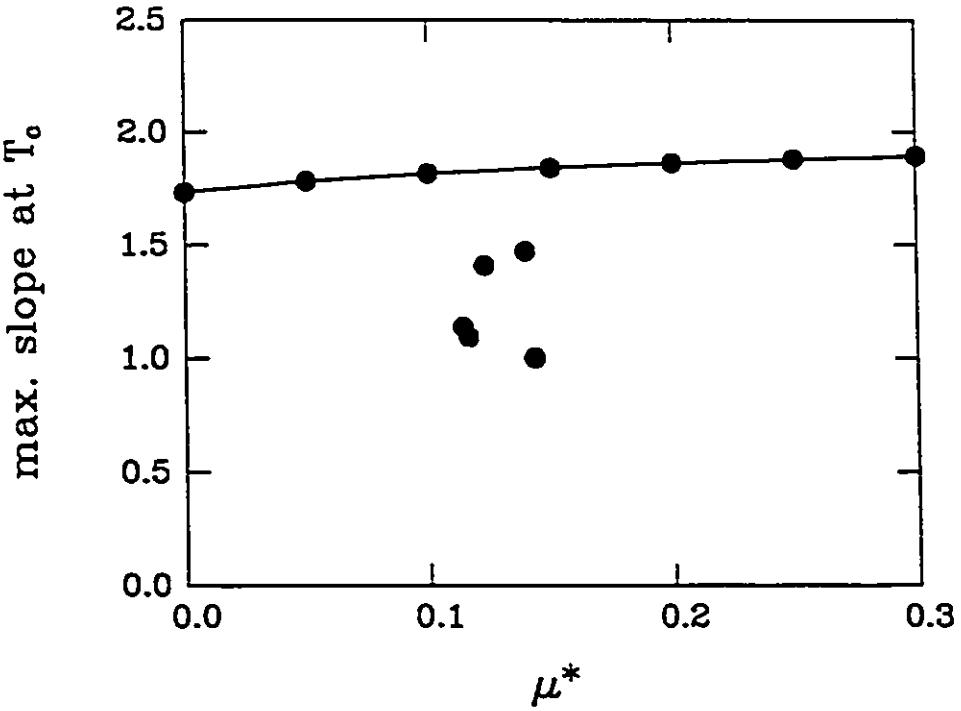


Figure 2.14 Maximum slope at $T_c$ obtainable for different values of $\mu^*$. The curve drawn through the solid dots represents an upper bound on the slope near $T_c$ obtainable in Eliashberg theory. The solid dots below this curve are the results of numerical calculations for the real materials shown in Fig. 2.11.

where $j_c$ is increased by inelastic scattering, contrary to their results. However, they do capture the essence of very strong inelastic scattering when with their approximate form they find a decrease in $j_c$. This only occurs for extreme strong coupling which is not in the parameter region that they considered quantitatively. The shape of the temperature dependence that we find is rather different from what they propose, as we observe a linear temperature dependence for $j_c^{2/3}$ (see Fig. 2.13), whereas their curves exhibit an upward curvature.

The maximum in the curve of Fig. 2.12 motivates us to place an upper bound on the maximum slope near $T_c$ for the critical current, obtainable from Eliashberg theory. This is shown as the solid curve in Fig. 2.14, where

we have plotted the maximum value obtainable for the slope (the peak in Fig. 2.12) for different values of $\mu^*$, shown as solid dots on the curve. The solid dots below the curve are the values for the type I materials used in our calculations. The real materials fall well below the theoretical maximum or upper bound.

## 2.6 CONCLUSIONS

We have calculated the pair-breaking critical current of a thin film superconductor in zero magnetic field for several type I superconductors. It is found that strong inelastic scattering increases $j_c$ contrary to a previous suggestion [Lemberger and Coffey (1988)]. This result would at first seem to be opposite to what one would expect, however, the inelastic scattering has two aspects: one is the real processes which scatter electrons and decrease the current and the other is the virtual processes which enter the pairing equation and enhance the stability of the superconducting state. And in this case, the virtual processes are enhancing the pairing. This is illustrated and confirmed by the functional derivatives, as discussed in Section 2.3. We have also calculated the effect of impurities, both magnetic and nonmagnetic, on $j_c$ and have found an increase and a decrease in the critical current as a function of temperature for each type of impurity, respectively. Finally, we have presented a strong coupling correction formula as a function of a single parameter $T_c/\omega_{\ln}$ and examined the very strong coupling regime where the critical current finally begins to decrease and go below the BCS result, confirming this with a calculation of $j_c$ in the asymptotic limit of $\lambda \to \infty$. From this work we can place an upper bound on the slope of $j_c^{2/3}$ near $T_c$ within Eliashberg theory.

We are unaware of any experiments for $j_c(T)$ on strongly coupled superconductors or on ones containing paramagnetic impurities. Thus, many of our results await experimental verification.

# Chapter 3

# Marginal Fermi Liquid Theory I

## *Various Properties*

In this chapter, we will discuss a novel theory, marginal Fermi liquid theory, that has been proposed [Varma (1989); Varma *et al.* (1989)] as a possible explanation for the high temperature superconductivity in the copper oxide compounds. It has been claimed [Varma (1989); Varma *et al.* (1989)] that this theory adequately describes the unusual normal state properties of the copper oxides. We apply this theory here to calculate several superconducting properties to determine if there could be possible agreement between theory and experiments performed on these materials. First, however, before discussing the nature of a "marginal" Fermi liquid, it will be necessary to introduce some of the concepts of Fermi liquid theory. After this introduction, we present the phenomenological marginal Fermi liquid model that we use and describe results for the gap ratio, isotope effect, London penetration depth, and dc Josephson current. In the next chapter, we present calculations of the optical conductivity.

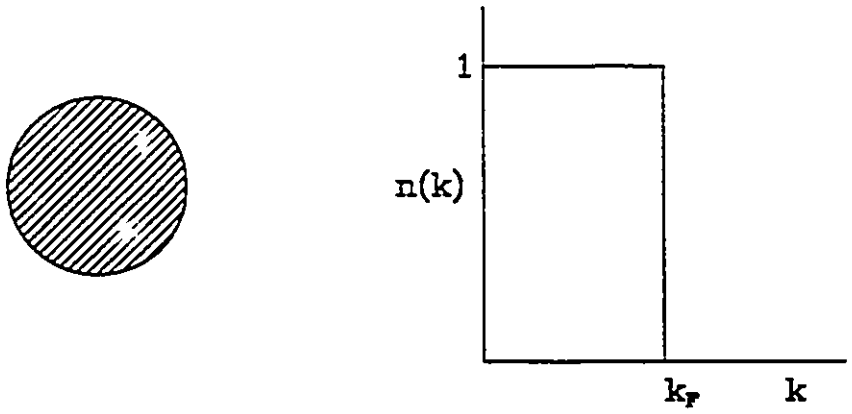


Figure 3.1 Picture of a free Fermi gas of electrons at $T = 0$. On the left we show the momentum states of the electrons in momentum space, with all states occupied up to the radius of a sphere given as $k_F$. On the right is the corresponding momentum occupation function, $n(k)$.

## 3.1 FERMI LIQUID THEORY

Fermi liquid theory has a long history with applications to the theory of metals and $He^3$. As several books and reviews exist on the topic [for example, Pines and Nozières (1966); Wilkins (1980)], we wish only to summarize some of the essential features necessary to understand what is meant by a Fermi liquid and further discuss a "marginal" Fermi liquid.

At zero temperature, if there were no interactions between electrons, we would have a free Fermi gas of electrons, where all momentum states below $k_F$ (the Fermi momentum) would be occupied with electrons ($\uparrow\downarrow$) for each state and all states unoccupied above $k_F$. This is schematically pictured on the left in Fig. 3.1. On the right, we show the corresponding single spin momentum occupation function $n(k)$, which is unity up until $k_F$ and zero thereafter. The presence of this sharp discontinuity in the occupation number at $k_F$ is then described as a Fermi surface. An elementary excitation of this

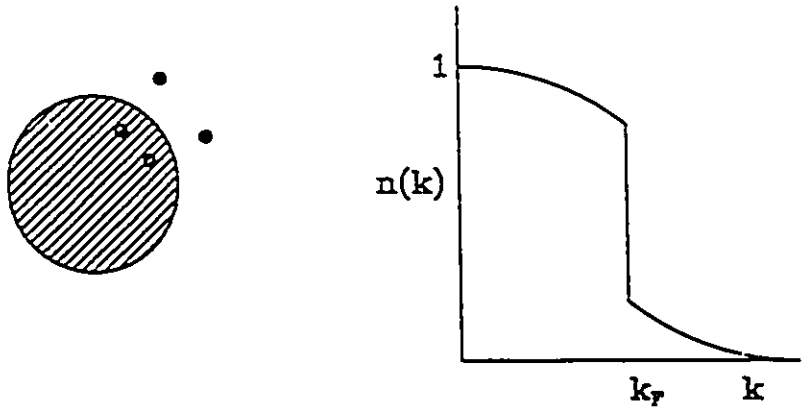


Figure 3.2 Picture of a interacting sea of electrons at $T = 0$. On the left is the momentum states of the electrons in momentum space, where some electrons occupy states outside the free Fermi sea leaving holes behind. On the right is the corresponding momentum occupation function $n(k)$, which is smeared around the Fermi surface at $k_F$.

system is to promote an electron to a momentum $k > k_F$ and leave behind a hole in the Fermi sea. This is referred to as a hole-particle pair.

For a normal metal, the electrons interact with each other via the Coulomb potential and the situation is a very complicated many body problem. In general, though, because of the Coulomb interactions (or correlation effects), electrons with momentum $k < k_F$ will spend some time outside the Fermi sea with momentum $k > k_F$, as exhibited schematically in Fig. 3.2. This causes a smearing in the momentum occupation distribution with states just above $k_F$ now occupied and some just below $k_F$ unoccupied (Fig. 3.2). However, there will still remain a finite jump at $k_F$ which we will denote as $z_k(\omega)$. For the non-interacting free Fermi gas, $z_k(\omega) = 1$ and due to correlations $z_k(\omega) < 1$ and varies as $(1+\lambda)^{-1}$, where $\lambda$ is a measure of the strength of the correlations in the system. It has been proven within perturbation theory [Luttinger and Nozières (1962a,b)] that even in the limit of $\lambda \to \infty$, a finite

jump in the momentum occupation function at $k_F$ still exists and as long as it exists, there is still a Fermi surface.

To describe the complicated interacting many-body system is a very difficult problem, but fortunately, all that needs to be known for most properties of interest is information about the elementary excitations of the system. This problem was first tackled by Landau (1956,1957) in his now-famous description of liquid $He^3$ as a liquid of fermions (and hence the name Fermi liquid). In his theory, the ground state can be very complicated, but if an extra particle is added of energy $E_k$ with $k > k_F$ just above the Fermi surface, the excitation can be described in terms of the energy measured with respect to the Fermi surface. Therefore, low-lying excited states of a complicated ground state can be mapped back to the elementary excitations of the non-interacting system in one-to-one correspondence. The excitations of the real system are now called quasiparticles (or quasiholes, in the opposite case) and can be described in terms of the plane wave states of the non-interacting system, with an effective mass $m^* = (1 + \lambda)m$. These quasiparticles still have between them a residual interaction. If one were to decompose this quasiparticle state, one would find that it is a superposition of all the elementary bare electron-hole pair states of the non-interacting system. The net result is that through this mapping we can revert back to describing the system in terms of single particle states but with renormalized quantities, such as the effective mass, above.

This is very important for the problem of superconductivity as the correlation energies of a metal are of the order of eV, whereas, the condensation energy of the superconducting state is of the order of meV. In this case, one might wonder how the superconductivity will occur in the presence

of such an overwhelming correlation energy. The resolution to this problem requires that one use Fermi liquid theory to fold the correlation energy into the renormalized mass of the quasiparticles so that the superconductivity occurs due to the weak attraction between long-lived quasiparticles in the presence of a filled Fermi sea of quasiparticles [Schrieffer (1964)]. In the conventional theory of superconductivity, the quasiparticles interact through a residual Coulomb repulsion (not accounted for by Fermi liquid theory) and the attractive exchange of virtual phonons.

Now we will discuss Fermi liquid theory in a more quantitative manner and point out some of its predictions. Our discussion follows those of Wilkins (1980) and Allen and Mitrović (1982). For the non-interacting sea of electrons at $T = 0$, an added particle representing an excitation of momentum $\vec{k}$ has a well-defined energy $E_k$ and an infinite lifetime. In the fully interacting system, on the other hand, the interactions can shift the single particle energies $\epsilon_k$, which are measured with respect to the Fermi level, and also cause scattering between quasiparticles. This causes the quasiparticle to have a finite lifetime for occupation of a state $(\vec{k}, \sigma)$. The shift in energy is given in terms of the many-body self-energy $\Sigma(\tilde{E}_k)$

$$\tilde{E}_k = \epsilon_k + \Sigma(\tilde{E}_k) \quad , \tag{3.1}$$

where $\Sigma(\tilde{E}_k)$ is a complex function. For the quasiparticle picture to remain valid the damping must be small and hence the imaginary part must be small with respect to the real part. If

$$\tilde{E}_k \equiv \Re e\tilde{E}_k - \frac{i\hbar}{2\tau(\tilde{E}_k)} \quad , \tag{3.2}$$

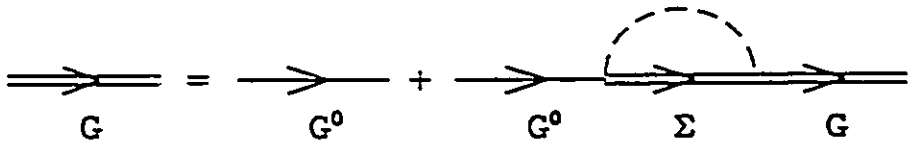


Figure 3.3 Dyson's equation. The single straight line represents the non-interacting Green's function and the double line, the fully interacting Green's function. The dashed line is a boson propagator, such as a phonon.

where $1/\tau(\tilde{E}_k)$ is the damping rate, then $\tau$ can be evaluated (in this assumption) at the real value of $\tilde{E}_k$, *i.e.*, if $E_k = \Re e\tilde{E}_k$ then $\tau(\tilde{E}_k) = \tau(E_k)$. The choice of sign here indicates that the state evolves in time as $\exp[-i\tilde{E}_k t]$ and thus decays as a function of time.

Hence, we can write the excitation energy $E_k = \Re e\tilde{E}_k$ as

$$E_k = \epsilon_k + \Re e\Sigma(\vec{k}, E_k + i\Gamma_k) \tag{3.3}$$

and the lifetime as

$$\frac{\hbar}{2\tau_k} = -\Gamma_k = \Im m\Sigma(\vec{k}, E_k + i\Gamma_k) \approx \Im m\Sigma(\vec{k}, E_k + i0^+) \quad , \tag{3.4}$$

in general.

Now to discuss the kink in the momentum distribution which indicates the existence of a Fermi surface, we must define the spectral weight $z_k(\omega)$. To do this we must examine how the single particle Green's function is changed in the presence of interactions. In a fully interacting system, the single particle Green's function is given by Dyson's equation (Fig. 3.3)

$$G(\vec{k},\omega) = G^\circ(\vec{k},\omega) + G^\circ(\vec{k},\omega)\Sigma(\vec{k},\omega)G(\vec{k},\omega) \tag{3.5}$$

or

$$G(\vec{k},\omega) = \frac{G^{\circ}(\vec{k},\omega)}{1 - G^{\circ}(\vec{k},\omega)\Sigma(\vec{k},\omega)} \tag{3.6}$$

$$= \frac{1}{G^{\circ -1}(\vec{k},\omega) - \Sigma(\vec{k},\omega)} \quad . \tag{3.7}$$

where the single particle Green's function in the noninteracting case, $G^{\circ}(\vec{k},\omega)$ is given as

$$G^{\circ}(\vec{k},\omega) = \frac{1}{\omega - \epsilon_k + i0^+} \quad , \tag{3.8}$$

where single particle energies are located at the poles of the Green's function, $\omega = \epsilon_k$. This non-interacting Green's function Fourier transforms into an undamped travelling wave in real space. Hence, the fully renormalized single particle Green's function is

$$G(\vec{k},\omega) = \frac{1}{\omega - \epsilon_k - \Sigma(\vec{k},\omega)} \quad . \tag{3.9}$$

Now in this case the poles of the Green's function occur at the quasiparticle energies

$$E_k = \Re e\{\omega\} = \epsilon_k + \Re e[\Sigma(\vec{k}, E_k + i\Gamma_k)] \tag{3.10}$$

and are shifted away from the real axis into the imaginary plane by the amount of the quasiparticle damping

$$\Im m\{\omega\} = \frac{\hbar}{2\tau_k} = \Im m\Sigma(\vec{k}, E_k + i\Gamma_k) \quad . \tag{3.11}$$

Near the Fermi surface the damping is small and hence we can Taylor expand the denominator of Eq. (3.9, [Allen and Mitrović (1982)]. Letting $\Re e\{\Sigma(\vec{k},\omega)\} = \Sigma_1(\vec{k},\omega)$ and $\Im m\{\Sigma(\vec{k},\omega)\} = \Sigma_2(\vec{k},\omega)$,

$$\omega - \epsilon_k - \Sigma(\vec{k},\omega) = \omega - \epsilon_k - \Sigma_1(\vec{k},\omega) - i\Sigma_2(\vec{k},\omega)$$

$$\simeq \omega - \epsilon_k - \left[\Sigma_1(\vec{k},0) + \omega\frac{\partial\Sigma_1}{\partial\omega}\bigg|_{\omega=0}\right] - i\Sigma_2(\vec{k},\omega) \tag{3.12}$$

$$\simeq \omega\left(1 - \frac{\partial\Sigma_1}{\partial\omega}\bigg|_{\omega=0}\right) - [\epsilon_k + \Sigma_1(\vec{k},0)] - i\Sigma_2(\vec{k},\omega) \quad . \tag{3.13}$$

Then the pole occurs at $\omega_o$ given by

$$\omega_o = E_k - \frac{ih}{2\tau_k} \quad . \tag{3.14}$$

where

$$E_k = \left(1 - \frac{\partial \Sigma_1}{\partial \omega}\bigg|_{\omega=0}\right)^{-1} [\epsilon_k + \Sigma_1(\vec{k},0)] \tag{3.15}$$

and

$$\frac{h}{2\tau_k} = -\left(1 - \frac{\partial \Sigma_1}{\partial \omega}\bigg|_{\omega=0}\right)^{-1} \Sigma_2(\vec{k},E_k) \quad . \tag{3.16}$$

For low temperatures in problems like the electron-phonon problem, $\Sigma_1(\vec{k},0)$ is small but $\partial\Sigma_1/\partial\omega$ can be large ($\sim 1$). This latter quantity is called the mass enhancement parameter $\lambda_k$,

$$\lambda_k \equiv -\frac{\partial \Sigma_1}{\partial \omega}\bigg|_{\omega=0} \quad . \tag{3.17}$$

The quasiparticle "residue" or spectral weight is defined to be $z_k$, where

$$z_k^{-1}(\omega = 0) = 1 - \frac{\partial \Sigma_1}{\partial \omega}\bigg|_{\omega=0} = 1 + \lambda_k \tag{3.18}$$

and $z_k(0)$ is a measure of the size of the discontinuity in the momentum distribution at $k_F$. The fact that it is non-zero defines a Fermi surface and ensures that Fermi liquid theory holds. Note also that $z_k$ is a measure of how much plane wave mixture is left in the single particle Green's function:

$$G(\vec{k},\omega) = \frac{1}{\omega - \epsilon_k - \Sigma(\vec{k},\omega)} = \frac{z_k}{\omega - E_k + i\Gamma_k} + G^{incoh} \quad , \tag{3.19}$$

where $G^{incoh}$ refers to the incoherent part of the Green's function.

Fermi liquid theory automatically predicts several things. One example of this is the temperature dependence of the electrical resistivity. This quantity depends on the scattering rate for electrons at the Fermi surface. At

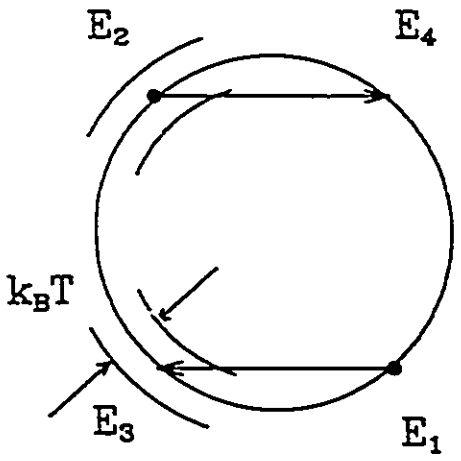


**Figure 3.4** Schematic of the scattering between two electrons (black dots) in Fermi liquid theory, leading to a $T^2$ resistivity.

zero temperature in the quasiparticle picture there will be a filled Fermi volume with all N electron states occupied and one single excited electron with $E_1 > E_F$. Now, following the argument given by Ashcroft and Mermin (1976), for there to be a scattering event, an electron with $E_2 < E_F$ must scatter with this excited particle, each scattering to energies $E_3$ and $E_4$ which must by the Pauli exclusion principle be greater than $E_F$ (unoccupied states). But at T=0, if $E_1 = E_F$, energy conservation ($E_1 + E_2 = E_3 + E_4$) can only occur for $E_2 = E_3 = E_4 = E_F$ where there is no phase space for the process to occur. Hence, the lifetime of the excited state is infinite at $T = 0$. At finite $T$, there is now a smearing of the distribution about $E_F$ on the scale of $k_BT$ and the choice of $E_2$ will be within the range of $k_BT$. The final scattered $E_3$ will also vary within $k_BT$ but $E_4$ will now be fixed by the conservation law and hence

the scattering rate goes as $(k_B T)^2$. This is depicted schematically in Fig. 3.4. Likewise, if the energies of the particles can vary within an energy shell of the Fermi surface, similar arguments for $E_1 > E_F$ will lead to frequency dependence of the scattering rate varying as $\omega^2$, where $\omega = E_1 - E_F$, or in general $1/\tau \sim a\omega^2 + bT^2$. There are other properties which also exhibit characteristic behaviour in Fermi liquid theory but we have chosen to illustrate this one here as it is central to our discussion in the following section.

## 3.2 MARGINAL FERMI LIQUID THEORY

As discussed, Fermi liquid theory gives definite predictions about the behaviour of certain physical quantities. Most notable is that the resistivity is predicted to vary with temperature as $T^2$. One of the first obvious features of the new high temperature superconducting copper oxide compounds was that their temperature-dependent resistivity curves varied as $T$. In general, the unusual normal state properties of these materials seem to point to a scattering rate that is linear in frequency $\omega$ and linear in temperature $T$. Evidence like this strongly indicated that these materials could not be described by the conventional Fermi liquid picture in which the conventional electron-phonon theory of superconductivity is imbedded. This led to rather exotic proposals for the mechanism of superconductivity in these systems, such as, anyons [Laughlin (1988)], spin bags [Schrieffer *et al.* (1988)] resonating valence bonds [Anderson (1987)], etc. However, more recent data from angle-resolved photoemission experiments [Arko *et al.* (1989); Campuzano *et al.* (1990); Imer *et al.* (1989)], which are capable of measuring the Fermi surface of a material, showed that, indeed, these materials have a Fermi surface. This at first appeared to be in conflict with other experiments which

indicated that Fermi liquid-like properties were not evident. With mounting evidence for a Fermi surface accumulating from photoemission experiments, it appeared that the more exotic theories that provide for no such surface had to be dispensed with and some alternative sought. This gave support to the idea of a "marginal" Fermi liquid. Essentially, this is a theory that yields a Fermi surface in the weakest possible sense of the definition but otherwise does not make the same predictions as Fermi liquid theory.

To quantify this idea, recall that the quasiparticle residue $z_k(\omega)$, which characterizes the jump at $k_F$ and hence indicates the presence of a Fermi surface when $z_k(\omega = 0)$ is non-zero, depends on the real part of the self-energy. Now if

$$\Sigma_1(\vec{k},\omega) \sim \omega \ln\left|\frac{\omega}{\omega_c}\right| \quad , \tag{3.20}$$

where $\omega_c$ is a high energy cutoff, then

$$\frac{\partial\Sigma_1(\vec{k},\omega)}{\partial\omega} = \ln\left|\frac{\omega}{\omega_c}\right| + 1 \quad , \tag{3.21}$$

or

$$\left.\frac{\partial\Sigma_1}{\partial\omega}\right|_{\omega=E_k} = \ln\left|\frac{E_k}{\omega_c}\right| + 1 \quad , \tag{3.22}$$

and hence,

$$z_k^{-1} = 1 - \left.\frac{\partial\Sigma_1}{\partial\omega}\right|_{\omega=E_k} = -\ln\left|\frac{E_k}{\omega_c}\right| = \ln\left|\frac{\omega_c}{E_k}\right| \quad , \tag{3.23}$$

or

$$z_k = \frac{1}{\ln|(\omega_c/E_k)|} \quad . \tag{3.24}$$

Now when a quasiparticle is on the Fermi surface $E_k = 0$ and $z_k \to 0$. Hence, the jump in the distribution tends to zero, but in a very weak way (*i.e.*, logarithmically), and thus a Fermi surface just barely remains in the weakest sense. However, from the self-energy of Eq. (3.20), all other properties of the

Table 3.1

| Fermi Liquid Theory | Marginal Fermi Liquid Theory |
|---|---|
| $\Re e\Sigma \sim \omega$ | $\Re e\Sigma \sim \omega \ln(x/\omega_c)$, with $x = \max(\mid \omega \mid, T)$ |
| $\Im m\Sigma \sim \omega^2$ | $\Im m\Sigma \sim x$, with $x = \max(\mid \omega \mid, T)$ |
| $\tau(\omega \to 0) \to \infty$ | $\tau(\omega \to 0) \to \infty$ |
| $z_k = 1/(1+\lambda) \leq 1$ | $z_k \sim (\ln \omega)^{-1} \to 0$ as $\omega \to 0$ |

theory have non-Fermi liquid-like behaviour. This is one way of defining a marginal Fermi liquid and presumably alternative definitions could be found. The linear-$T$ and linear-$\omega$ scattering rate experimentally observed in the high $T_c$ copper-oxide superconductors will arise if $\Sigma_2$ is equal to

$$\frac{1}{2\tau_k} = \Sigma_2 \propto x, \quad \text{where} \quad x = \mid \omega \mid \quad \text{or} \quad T. \tag{3.25}$$

In Table 3.1, we contrast some fundamental quantities of Fermi liquid theory with those resulting from the particular marginal Fermi liquid defined here. Note that there are still well-defined quasiparticles with an infinite lifetime at the Fermi surface, but that the self-energy function is quite different and will give rise to different physics.

Unfortunately, to develop an expression for such a self-energy from a microscopic theory is a more difficult task. Although a microscopic theory has yet to be fully developed, several microscopic models have been proposed which have some of the features of this phenomenological marginal Fermi liquid [Anderson (1990); Nagaosa and Lee (1990); Schmitt-Rink *et al.* (1989); Virosztek and Ruvalds (1990); Ruvalds and Virosztek (1991); Orenstein *et al.* (1990)] and a scaling theory has been given [Zimanyi and Bedell (1991)].

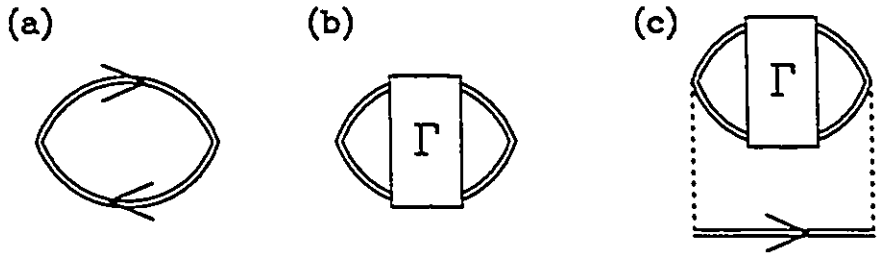


Figure 3.5 The Feynman diagram for the particle-hole susceptibility $\chi(\vec{q},\omega)$ (a) without vertex corrections and (b) with vertex corrections. The form of the polarizability in Eq. (3.26) is postulated to arise from bound states in the vertical particle-particle channel of the vertex function $\Gamma$. (c) The electron self-energy due to this susceptibility, where the dashed lines represent a coupling $g$.

Rather than take such an approach, another possibility is to assume a phenomenological model and should it work, then one would search for a microscopic description of the phenomenology after the fact. This is the approach taken by Varma *et al.* (1989) and by ourselves. Should the phenomenological theory succeed, this would give impetus towards setting this theory on a microscopic foundation. But before such effort is expended it would be useful to see if the phenomenological theory can stand the test of experiment.

## 3.3 A PHENOMENOLOGICAL MARGINAL FERMI LIQUID THEORY

Varma *et al.* (1989) postulated that in the copper-oxide system there are charge and spin density fluctuations of the electronic system. These fluctuations lead to a polarizability of the electronic medium that would renormalize the electron through the self-energy. Such a polarizability is drawn

in terms of a Feynman diagram in Fig. 3.5. This is simply analogous to the electron-phonon interaction with the phonon line being replaced by the polarizability (Fig. 3.5). Their proposal for this polarizability is as follows:

$$\Im m P(\vec{q},\omega) \sim \begin{cases} -N(0)\omega/T & , \quad \text{for } |\omega| < T \quad , \\ -N(0)\,\mathrm{sgn}\,\omega & , \quad \text{for } |\omega| > T \quad , \end{cases} \tag{3.26}$$

where $N(0)$ is the single particle density of states at the Fermi energy. The form of this polarizability is postulated to come from the vertex corrections in the particle-hole susceptibility shown in Fig. 3.5.

The self-energy that arises from applying the Feynman rules to Fig. 3.5 is given as

$$\Sigma(\vec{q},\omega) \sim g^2 N^2(0) \left( \omega \ln \frac{x}{\omega_c} - i\frac{\pi}{2} x \right) \quad , \tag{3.27}$$

where $x = \max(|\omega|, T)$. The parameter $\omega_c$ is taken to be some high energy cutoff on the polarizability and $g$ is a coupling constant at the vertex of the electron interacting with the polarization bubble. As this has the form that we have previously hinted at, we find that

$$z_k \sim \frac{1}{\ln |\omega_c / E_k|} \tag{3.28}$$

and the quasiparticle lifetime is still infinite at the Fermi surface, *i.e.*,

$$\frac{1}{2\tau_k} = \frac{\pi}{2} E_k \quad \text{which as} \quad E_k \to 0, \quad \tau_k \to \infty \quad . \tag{3.29}$$

And as mentioned, this form of the scattering rate guarantees a scattering rate $1/\tau$ which has the form:

$$\frac{1}{\tau} \sim a\omega + bT \quad . \tag{3.30}$$

From our qualitative arguments in section 3.1, it is difficult to see how this dependence could arise. For instance, if the Fermi surface is smeared in temperature by $k_B T$, it is not clear why there would be a restriction on $k_2$ or

$k_3$ such that only one factor of $T$ may come into the scattering rate. One possibility occurs in the nested Fermi liquid theory of Virosztek and Ruvalds (1990), where, due to the nesting of the two-dimensional Fermi surface, there is only one factor of $T$ and the other factor is the temperature-independent bandwidth. However, it is the scattering rate dependence in Eq. (3.30) that is manifested in the normal state properties of the copper oxides giving them novel normal state behaviour.

As this proposed polarizability appears to be successful in describing the normal state properties, it is worthwhile to examine its predictions for the superconducting state to see if this theory could truly be a candidate for the theory of the high temperature superconductors.

Kuroda and Varma initiated this effort by considering the properties of an s-wave, spin singlet superconductor, where the equations are formally similar to the Eliashberg equations for phonons and paramagnons (see Appendix A and Chapter 5). For numerical convenience, they model the polarizability of Eq. (3.26) by

$$\Im m P(\omega) \sim \begin{cases} -N(0)\tanh(\omega/2T) \quad , & \text{for } |\omega| < \omega_c \quad , \\ 0 \quad , & \text{for } |\omega| > \omega_c \quad , \end{cases} \tag{3.31}$$

Hence, the Eliashberg equations are now given as

$$\tilde{\Delta}_n = \pi T \sum_m \lambda^-(m-n) \frac{\tilde{\Delta}_m}{\sqrt{\tilde{\omega}_m^2 + \tilde{\Delta}_m^2}} + \pi t^+ \frac{\tilde{\Delta}_n}{\sqrt{\tilde{\omega}_n^2 + \tilde{\Delta}_n^2}} \tag{3.32}$$

and

$$\tilde{\omega}_n = \omega_n + \pi T \sum_m \lambda^+(m-n) \frac{\tilde{\omega}_m}{\sqrt{\tilde{\omega}_m^2 + \tilde{\Delta}_m^2}} + \pi t^+ \frac{\tilde{\omega}_n}{\sqrt{\tilde{\omega}_n^2 + \tilde{\Delta}_n^2}} \quad , \tag{3.33}$$

where $\omega_n = (2n+1)\pi T$ with $n = 0, \pm 1, \pm 2, \ldots$ and $\pi t^+ \equiv 1/(2\tau)$ with $\tau$ the residual scattering rate. In Eqs. (3.32) and (3.33), we have neglected the

Coulomb pseudopotential and $\lambda(n-m)$ is given in terms of the electron–exchange-boson spectral density $\alpha^2F(\omega)$ for any boson exchange process of interest,i.e., phonons, plasmons, charge fluctuations etc., by

$$\lambda^+ = \lambda^- = \lambda(n-m) = \int_0^\infty \frac{2\omega\,\alpha^2F(\omega)}{\omega^2+(\omega_n-\omega_m)^2}\,d\omega \quad . \tag{3.34}$$

In the marginal Fermi liquid model, an essential feature is the coupling to both charge and spin fluctuations as described by Kuroda and Varma (1990). In this case the charge degrees of freedom, which are pair-creating, couple to the superconducting electrons through a dimensionless coupling $\lambda_\rho$ while coupling to spin is described by $\lambda_\sigma$. The modifications of Eqs. (3.32) and (3.33) are made by replacing $\lambda^-(m-n)$ by $(\lambda_\rho-\lambda_\sigma)F(m-n)$ and $\lambda^+(m-n)$ by $(\lambda_\rho+\lambda_\sigma)F(m-n)$ where from the above approximation

$$F(m-n) = \frac{1}{\pi}\int_{2\Delta(T)}^{\omega_c} \frac{2\omega\tanh(\frac{\omega}{2T})}{\omega^2+(\omega_m-\omega_n)^2}\,d\omega \quad . \tag{3.35}$$

Kuroda and Varma (1990) report results for $T_c$, $2\Delta/k_BT_c$, and $\Delta C/\gamma T_c$, and Williams and Carbotte (1990) report results for $\Delta C/\gamma T_c$ and $T_c\Delta C'/\Delta C$. Recent work has been done on the de Haas-van Alphen effect by Wasserman *et al.* (1991), and Littlewood and Varma (1991) have done calculations for optical conductivity, tunnelling, NMR relaxation rate, thermal conductivity, and photoemission spectra.

In this theory, there are three parameters $\omega_c$, $\lambda_\rho$, and $\lambda_\sigma$. Choosing $T_c$ determines $\lambda_\rho$ and hence we are left with two parameters. We prefer to work with a quantity $g$ defined as

$$g = \frac{\lambda_\rho-\lambda_\sigma}{\lambda_\rho+\lambda_\sigma} \quad , \tag{3.36}$$

which is a measure of the amount of coupling to spin fluctuations in the model. A value of $g=1$ corresponds to no spin fluctuations.

Notice, that in the spectral function a lower cutoff is applied at $2\Delta(T)$. In the normal state $\Delta(T) = 0$ and the integral is as usual, but in the superconducting state a gap opens up in the excitation spectrum and as, in this case, the electrons that contribute to the polarizability are also those that superconduct, a gap of $2\Delta$ must also appear in the lower end of the spectral function. This is because it would take an energy of $2\Delta$ to liberate a pair of bound electrons that could contribute to the fluctuations. This feature leads to novel behaviour which will be reported in the next chapter.

Some of the unusual features of this spectrum compared with that of conventional electron-phonon theory are the self-consistent lower cutoff in the superconducting state, the temperature dependence of the spectral density and the flat featureless spectrum extending to very high frequencies. It is the same spectrum (except for coupling strength) for both the charge and spin fluctuations (unlike phonons and parmagnons where the two spectra can be different). Note, that no theory has been derived for the momentum dependence of the marginal Fermi liquid and this is assumed to be a smooth function which causes no problems [Kuroda and Varma (1990)].

## 3.4 THE GAP RATIO

The solution of Eqs. (3.32) and (3.33) require numerical iteration for $\tilde{\Delta}(i\omega_n)$ and $\tilde{\omega}(i\omega_n)$. As the temperature-dependent gap $\Delta(T)$ must be solved for self-consistently, a value of $\Delta(T) = 0$ is initially assumed and for fixed $T_c$, $g$, and $\omega_c$, the equations are iterated to obtain $\tilde{\Delta}_o(i\omega_n)$ and $\tilde{\omega}_o(i\omega_n)$. These discrete quantities are then analytically continued by Padé approximants [Vidberg and Serene (1977); Mitrović *et al.* (1984); Carbotte *et al.* (1986)] to give the gap and renormalization function on the real frequency axis,

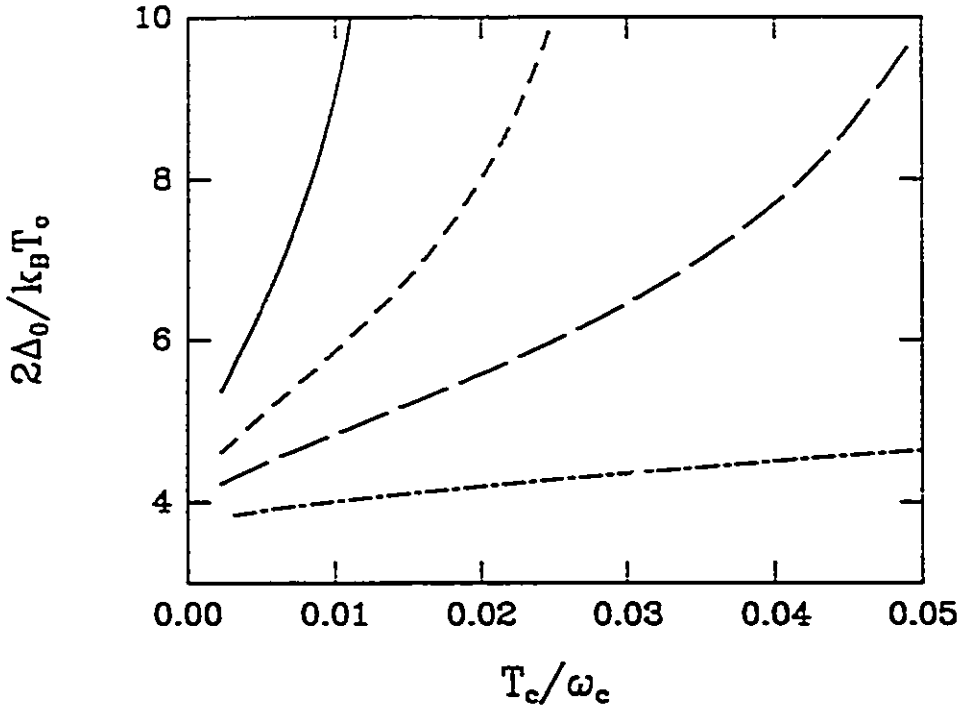


**Figure 3.6** The gap to critical temperature ratio $2\Delta_o/k_BT_c$ as a function of $T_c/\omega_c$ for four values of $g = 0.4$ (solid), 0.5 (short dashed), 0.6 (long dashed), 0.8 (dot-dashed).

$\Delta(\omega,T)$ and $Z(\omega,T)$, respectively. The gap edge $\Delta_o(T)$ is then defined to be $\Delta_o(T) = \Re e\Delta(\omega = \Delta_o(T),T)$. With this new value of $\Delta_o(T)$, the equations are iterated again for new solutions $\tilde{\Delta}_1(i\omega_n)$ and $\tilde{\omega}_1(i\omega_n)$ which are again analytically continued for the purposes of finding $\Delta_o(T)$, and this procedure is continued until $\Delta_o(T)$ stops changing to within a certain accuracy. We solved the equations at a reduced temperature of $T/T_c = 0.1$ which is sufficient for obtaining zero-temperature results.

In this manner, we obtained the curves of Fig. 3.6, where $2\Delta_o/k_BT_c$ is plotted as a function of $T_c/\omega_c$ for several values of $g$ the pair-breaking parameter. For small values of $g$ (larger pair-breaking), the gap ratio is found to be quite large and for all $g < 1$, $2\Delta_o/k_BT_c > 3.53$ (the BCS value). This is mainly due to the self-consistency of the solution for $\Delta(T)$. As the spectral

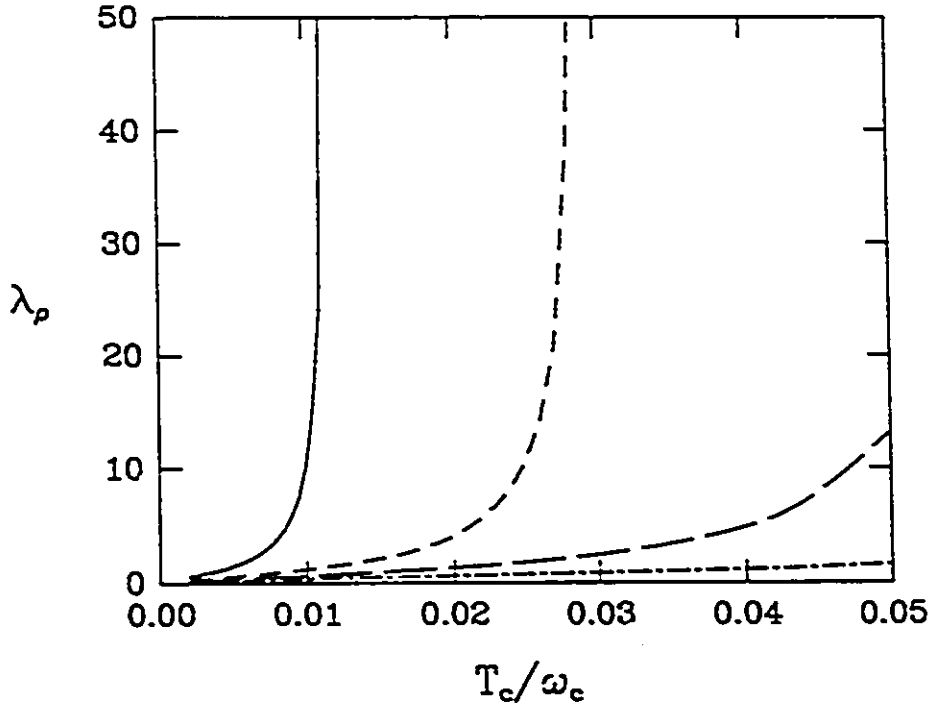


**Figure 3.7** The charge-fluctuation channel coupling $\lambda_\rho$ as a function of $T_c/\omega_c$ for four values of $g = 0.4$ (solid), 0.5 (short dashed), 0.6 (long dashed), 0.8 (dot-dashed).

function is gapped at the lower end, low frequency charge and spin fluctuations are removed. However, the spin fluctuations which are pair-breaking are more effective at low frequencies than the charge fluctuations, which are pair-enhancing, hence the overall effect is to remove more pair-breaking effects in the system and hence increase the stability of the condensate which is measured by the gap $\Delta_o$.

The gap in a fully oxygenated single crystal of $YBa_2Cu_3O_7$ has been reported to be of the order of $2\Delta_o/k_BT_c \simeq 8$ [Schlesinger *et al.* (1987); Collins *et al.* (1989); Schutzmann *et al.* (1989)] in far-infrared measurements. We see from our results that this value can be achieved for $g = 0.4$ with a cutoff $\geq 10\,000$ K, while for $g = 0.6$ it is $\geq 2500$ K. It is worth noting that similar

large values of $2\Delta_o/k_BT_c$ are also indicated in photoemission experiments on cuprate superconductors [Manzke *et al.* (1989); Imer *et al.* (1989); Olsen *et al.* (1989)].

Fig. 3.7 exhibits the coupling strength in the charge fluctuation channel, $\lambda_\rho$, as a function of $T_c/\omega_c$, for comparison with Fig. 3.6. It can be seen that as the gap ratio grows extremely large, the coupling to charge fluctuations diverges quickly to extremely large values. This is usually taken to be unphysical and one would not consider such a region of the model to be valid.

It should be pointed out that in our solution of the equations (in light of the fact that there is no microscopic theory and hence no defined prescription for the lower cutoff on the integral in Eq. (3.35)), we have used a sharp cutoff. Littlewood and Varma (1990,1991) in their calculations have used a joint density of states to apply a lower cutoff at $2\Delta_o$. We have found that this does not change the net results significantly.

Solving for $\Delta(T)$ at $T > 0$ is more difficult as Padé approximants are not reliable [Leavens and Ritchie (1985); Blaschke and Blocksdorf (1982)]. It was decided that the temperature dependence of $\Delta(T)$ would be taken to be the BCS temperature dependence, because it is well-known for strong coupling superconductors that the temperature dependence of the gap function does not deviate significantly from the BCS result. Assuming the Padé continuation to be accurate at finite temperature, self-consistent iteration produced a $\Delta_o(T)$ slightly above the BCS value with an instability in the

iterative technique near $T_c$. Hence, it was decided that for numerical convenience and with no significant change in the physics, that the BCS temperature dependence scaled by the self-consistent $\Delta(T = 0)$ was sufficient for finite temperature calculations.

## 3.5 THE ISOTOPE EFFECT

As mentioned in Chapter 1, the isotope effect was the first indication that the ion lattice is involved in the superconductivity. $T_c$ is observed to shift when the ions are replaced by an isotope. This points to the electron-phonon interaction as the mechanism for pairing and indeed within BCS theory $T_c$ is easily seen to depend on the ion mass $M_{ion}$ through the $T_c$ equation:

$$T_c = 1.13\omega_D \exp\left[-\frac{1}{N(0)V}\right] \tag{3.37}$$

$$\propto \frac{1}{\sqrt{M_{ion}}} \quad . \tag{3.38}$$

The isotope effect coefficient $\beta$ is then defined to be (assuming a monatomic lattice):

$$\beta \equiv -\frac{d\ln T_c}{d\ln M_{ion}} \quad . \tag{3.39}$$

From Eq. (3.38), $\beta = 0.5$ in BCS theory. However, within Eliashberg theory, this coefficient may be less than 0.5 and even negative due to a competition between the mass renormalization parameter $\lambda$ and the Coulomb pseudopotential $\mu^*$ which depends on the phonon frequency [Carbotte (1990)]. This is in agreement with experiment. However, Eliashberg theory also makes one definite statement about the isotope effect coefficient, which is the following: to have only an electron-phonon mechanism for the pairing and to require $\beta$ to be very small ($\lesssim 0.1$), the corresponding $T_c$ must only be a few Kelvins

[Carbotte (1990); Carbotte and Nicol (1991)]. Thus, if the pairing in the high temperature superconductors is to be ascribed to the electron-phonon interaction alone, the isotope effect coefficient should be observed to be about 0.5, and it is not.

The oxygen isotope effect in $YBa_2Cu_3O_7$ has been measured by many workers [Batlogg *et al.* (1987); Bourne *et al.* (1987a); Leary *et al.* (1987); Morris *et al.* (1988); Benitez *et al.* (1989); Yvon *et al.* (1989); Hoen *et al.* (1989); Franck *et al.* (1990)]. In all cases, it is found to be small and of the order of 0.05 with some values as high as 0.1 [Franck *et al.* (1990)]. Bourne *et al.* (1987b) find that the Ba and Cu isotope effect coefficient is essentially zero as do several other groups [Quan *et al.* (1988); Vasiliev *et al.* (1988a,b); Hidaka *et al.* (1988)]. Thus, the total isotope effect coefficient $\beta_{tot}$ is small, $\cong$ 0.05. Small values for the isotope effect have also been found in the Tl and Bi copper oxides as reviewed by Katayama-Yoshida *et al.* (1988). These results favour a non-phonon, electronic mechanism for the pairing in the high $T_c$ oxides although other interpretations, such as inhomogeneities [Phillips (1989,1991a,b)] and anharmonic phonons [Plakida (1991)], have been given.

More recently, new results by Crawford *et al.* (1990) in $La_{2-x}Sr_xCuO_4$ as a function of $x$ and by Franck *et al.* (1990b) in $Y_{1-x}Pr_xBa_2Cu_3O_7$ have revealed that the oxygen isotope coefficient $\beta_{ox} \equiv -d\ln T_c/d\ln M_{ox}$, with $M_{ox}$ the oxygen mass, can vary greatly with dopant $x$. By the time the critical temperature has been reduced to 30K, $\beta_{ox}$ is almost 0.5. This can be understood in terms of energy dependence of the electronic density of states near the Fermi energy on a scale of importance for superconductivity. Tsuei *et al.* (1990) use a van Hove singularity while Schachinger *et al.* (1990) employ a Lorentzian form for this energy dependence. For the specific case of

$Y_{1-x}Pr_xBa_2Cu_3O_7$ an alternative explanation has been given by Carbotte *et al.* (1991) in terms of the pair breaking effect of the Pr dopant. While it is not yet well understood what changes occur in the electronic and spin structure of $YBa_2Cu_3O_7$ when the yttrium is replaced by praseodymium [Ghamaty *et al.* (1991)], there is some evidence that the Pr ions act as ordinary paramagnetic impurities, strongly exchange-coupled to the holes in the $CuO_2$ planes. Other evidence suggests filling of mobile holes in the conducting plane by electrons donated by the substituted Pr. This would favour the energy dependent density of states $N(\epsilon)$ model in which the chemical potential shifts away from the peak in $N(\epsilon)$ with a corresponding increase in $\beta$.

In the marginal Fermi liquid model, the coupling between two electrons is via charge (attractive) and spin (repulsive) fluctuations and so it does not exhibit an isotope effect. To include this effect, an additional phonon contribution must be introduced. It is interesting to investigate whether large values and rapid variation of the isotope coefficient $\beta$ can be incorporated into this model without introducing a large phonon contribution. In this section, we extend the model to include a phonon contribution and investigate what limits are put on the electron-phonon mass renormalization by the constraint $\beta = 0.05$ in the stoichiometric $YBa_2Cu_3O_7$. We also investigate how the isotope effect increases when the critical temperature is reduced through an increase in spin fluctuations or a decrease in the charge fluctuations keeping, in all cases, the electron-phonon interaction fixed.

The Eliashberg equations [Eqs. (3.32) and (3.33)], with $t^+ = 0$, reduce at $T_c$ to

$$\Delta(i\omega_n)Z(i\omega_n) = \pi T_c \sum_m \lambda^-(m-n)\frac{\Delta(i\omega_m)}{|\omega_m|} \tag{3.40}$$

and

$$\omega_n Z(i\omega_n) = \omega_n + \pi T_c \sum_m \lambda^+(m-n)\mathrm{sgn}(\omega_m) \quad . \tag{3.41}$$

To add phonons to the marginal Fermi liquid model we need only to add to each of $\lambda^+(m-n) = (\lambda_\rho + \lambda_\sigma)F(n-m)$ and $\lambda^-(m-n) = (\lambda_\rho - \lambda_\sigma)F(n-m)$ a phonon contribution of the form of Eq. (3.34) with $\alpha^2F(\omega)$ being the electron-phonon spectral density. A feature of this extended marginal Fermi liquid model which should be noted is that both spin and charge fluctuations are determined by the same kernel $F(n-m)$ while the phonons are different in this respect. For the purpose of this work it will be sufficient to use a delta function model for the electron-phonon spectral density at a single Einstein energy $\omega_E$, *i.e.*,

$$\alpha^2F(\omega) = \frac{\omega_E\lambda_E}{2}\delta(\omega-\omega_E) \quad . \tag{3.42}$$

Here, $\lambda_E$ is the electron-phonon mass enhancement factor. This parameter is often taken to be a measure of the strength of the electron-phonon interaction.

To start, let us consider a pure phonon model consisting of a number of different modes $\omega_{Ei}$ with associated mass enhancement factor $\lambda_i$ where $\lambda_i = 2A_i/\omega_{Ei}$ for a spectral weight model $\alpha^2F(\omega) = \sum_i A_i\delta(\omega-\omega_{Ei})$. If we use a square well model [Allen and Mitrović (1982)] in Eqs. (3.40) and (3.41) with a constant gap value (a very rough approximation) we can get an interesting result for $T_c$, namely,

$$T_c = 1.13\left[\prod_i(\omega_{Ei})^{\frac{\lambda_i}{\lambda_{tot}}}\right]\left[e^{-\frac{1+\lambda_{tot}}{\lambda_{tot}}}\right] \quad , \tag{3.43}$$

which is not expected to be accurate but which has a suggestive form. If all the $\omega_{Ei}$'s are the same we recover the usual BCS result for $T_c$ which is

Table 3.2

| $i$ | $\omega_{Ei}$ | $\lambda_i$ | $\beta_i$ exact | $\beta_i$ approx. |
|---|---|---|---|---|
| 1 | 5 | 0.1 | 0.198 | 0.167 |
| 2 | 10 | 0.05 | 0.086 | 0.083 |
| 3 | 15 | 0.15 | 0.216 | 0.250 |
| total | | 0.3 | 0.5 | 0.5 |

$T_c = 1.13\omega_E \exp[-(1 + \lambda_{tot})/\lambda_{tot}]$ with $\lambda_{tot} \equiv \sum_i \lambda_i$. An interesting feature of Eq. (3.43), however, is that the partial isotope effect is

$$\beta_i \equiv -\frac{d\ln T_c}{d\ln M_i} = \frac{1}{2}\frac{\lambda_i}{\lambda_{tot}} \quad . \tag{3.44}$$

where we have associated a different mass $M_i$ with each $\omega_{Ei}$. On summing Eq. (3.44), we recover the well known result that $\beta_{tot} \equiv \sum_i \beta_i = 1/2$ for a pure phonon model. While we do not expect Eq. (3.44) to be very accurate, in Table 3.2 we show results for the $\beta_i$'s in a model with $T_c \cong 1$K, $\lambda_1 = 0.1$ ($\omega_{E1} = 5.0$ meV), $\lambda_2 = 0.05$ ($\omega_{E2} = 10.0$ meV), and $\lambda_3 = 0.15$ ($\omega_{E3} = 15.0$ meV). On comparing results from complete numerical solutions of Eqs. (3.40) and (3.41) with results from Eq. (3.44) we see good but not exact agreement. We have found that as the $\lambda_i$'s are increased, the agreement becomes much worse. Nevertheless, we can use Eq. (3.44) to illustrate some important points in the discussion of the our numerical results.

Suppose we now use an equation of the form of Eq. (3.43) for the extended marginal Fermi liquid model which includes a phonon contribution in addition to coupling in the pairing channel with charge (attractive) and spin (repulsive) fluctuations. It is

$$T_c = 1.13\omega_E^{\frac{\lambda_E}{\lambda_E+\lambda_-}}\omega_c^{\frac{\lambda_-}{\lambda_E+\lambda_-}}e^{-\frac{1+\lambda_E+\lambda_+}{\lambda_E+\lambda_-}} \quad , \tag{3.45}$$

from which it follows that

$$\beta = \frac{1}{2}\frac{\lambda_E}{\lambda_E + (\lambda_\rho - \lambda_\sigma)F(0)} \quad . \tag{3.46}$$

In Eq. (3.45), $\tilde{\lambda}^- \equiv \lambda^- F(0)$ and $\tilde{\lambda}^+ \equiv \lambda^+ F(0)$, where $F(0)$ is the $m = n$ term of Eq. (3.35) with $T = T_c$. Because the spin fluctuation contribution, $\lambda_\sigma$, enters with a minus sign in the denominator of Eq. (3.46) it is clear that including spin fluctuations will lead to an enhancement of the isotope effect over its value when they are neglected. A similar result was first obtained by Williams and Carbotte (1991) in a phonon-plus-paramagnon model, which corresponds closely to setting $\lambda_\rho = 0$ in Eq. (3.46). In this case $\beta > 1/2$ is possible. As in the work of Carbotte *et al.* (1991) on paramagnetic impurities, the isotope effect is affected by the presence of magnetic fluctuations. This makes it very interesting to investigate the effects of a small phonon contribution added to a dominant charge and spin contribution in the marginal Fermi liquid model.

In our numerical work, we start by imposing two constraints on the parameters of the theory, which are now $\lambda_\rho$, $\lambda_\sigma$, $\omega_c$, $\lambda_E$, and $\omega_E$. We will insist that $T_c \cong 90$K and $\beta \cong 0.05$. This is typical of the observed situation in stoichiometric $YBa_2Cu_3O_7$. This leaves three free parameters. Results do not depend much on $\omega_c$ and so we will fix this quantity at 200 meV. Further, we introduce a parameter $g \equiv (\lambda_\rho - \lambda_\sigma)/(\lambda_\rho + \lambda_\sigma)$ which is a measure of the admixture of charge to spin fluctuations in the marginal Fermi liquid model. Results will then be presented as a function of $g$ and $\omega_E$.

While it is not our aim here to present fits to experimental data, the reader should keep in mind the experimental data for $Y_{1-x}Pr_xBa_2Cu_3O_7$. As the praseodymium concentration $x$ is increased, the value of $T_c$ is observed to drop steadily from 96K in the stoichiometric compound. At the

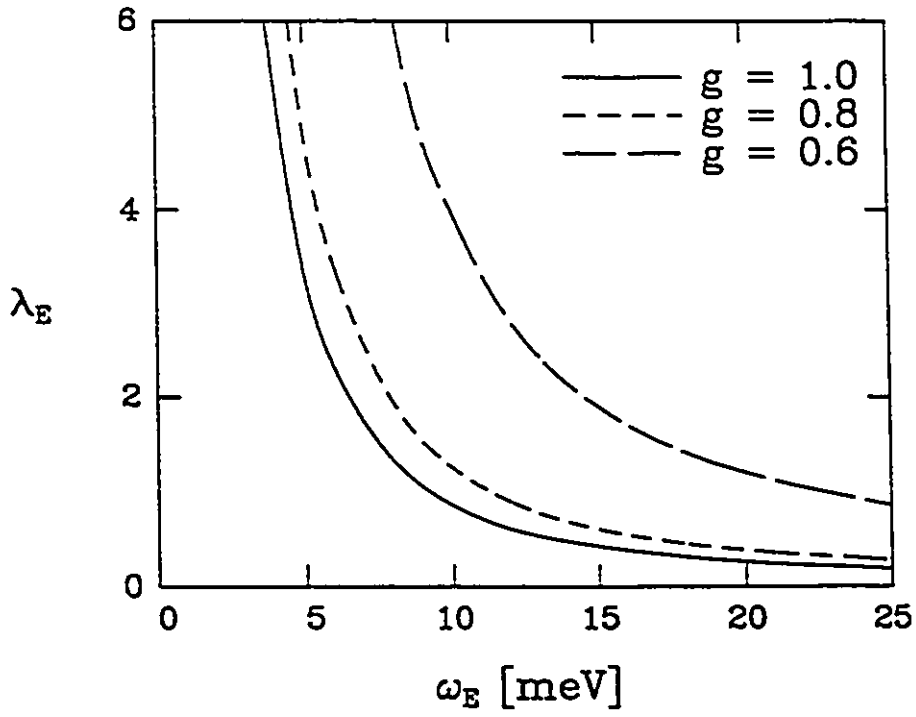


**Figure 3.8** The electron-phonon mass renormalization parameter $\lambda_E$ as a function of $\omega_E$ for different values of $g$, the admixture of charge and spin fluctuations in the extended marginal Fermi liquid model. These curves were calculated for $\omega_c = 200$ meV, $T_c = 90$K, and $\beta = 0.05$. $g = 1.0$ corresponds to no spin fluctuations.

same time the oxygen isotope coefficient $\beta_{ox}$ increases from 0.05 to a value around 0.45 at $T_c \cong 30$K. The questions we ask are how much or how little electron-phonon interaction is necessary in the extended marginal Fermi liquid model to obtain $\beta = 0.05$ in the stoichiometric compound? And, can the variation of $\beta$ with a change in $T_c$ in $Y_{1-x}Pr_xBa_2Cu_3O_7$ be understood, at least qualitatively, within this model?

In Fig. 3.8, we show values of the phonon mass renormalization parameter $\lambda_E$ as a function of the phonon energy $\omega_E$ for various values of $g$ for the stoichiometric compound. In all cases, the value of $\lambda_E$ required to achieve $\beta = 0.05$ and $T_c = 90$K is small when $\omega_E$ is large but grows substantially with decreasing Einstein frequency. Also at fixed $\omega_E$, the $\lambda_E$ value increases when

$g$ decreases, *i.e.*, when more spin fluctuations are introduced in the system. This means that the introduction of spin fluctuations allows for an increase in phonon contribution at fixed $T_c$ and $\beta$. Note that the difference between some ($g < 1$) and no ($g = 1$) spin fluctuations increases with a decrease in $\omega_E$ and can become very substantial. We can understand qualitatively this result from our Eq. (3.46), where increasing $\lambda_\sigma$ at fixed $\lambda_\rho$ must be compensated by an increase in $\lambda_E$ to maintain $\beta$ at 0.05.

While $\lambda_E$ may become large as $\omega_E$ is reduced, this does not imply that phonons make an ever increasing contribution to the value of $T_c$. In fact, in all cases shown in Fig. 3.8, introducing phonons increases $T_c$ above its value for the marginal Fermi liquid, acting alone, by no more than 5K. According to this measure the phonons are not very important. On the other hand, as we have just seen, the corresponding values of $\lambda_E$ can become quite large and such values are consistent with a very small isotope effect. For modest values of the spin fluctuation parameter $\lambda_\sigma$ this arises only when $\omega_E$ is very small and of the order of 5 meV. Coupling to mainly 5 meV phonons seems to us unlikely in oxide superconductors, for which the phonon spectrum can extend up to 100 meV [Renker *et al.* (1987,1988)]. In addition, large values of $\lambda_E$ are inconsistent with resistivity data [Gurvitch and Fiory (1987)].

With respect to the experimental data for $Y_{1-x}Pr_xBa_2Cu_3O_7$, it is of some interest to change the parameters in our model so as to decrease $T_c$ and see what effect this has on the corresponding $\beta$ value. Of course, the marginal Fermi liquid model is phenomenological and does not have, at the moment, a foundation in microscopic theory. Thus, we do not know how the three parameters $\lambda_\rho$, $\lambda_\sigma$, and $\omega_c$ might be changing with praseodymium doping. In the absence of such guidance we will consider three very simple

models for this change. In the first model we will keep $\lambda_\rho$ fixed and decrease $T_c$ by increasing the spin fluctuations. In a second, we simply reduce $\lambda_\rho$ and $\lambda_\sigma$ together by the same percentage amount. In the third, we will fix $\lambda_\sigma$ and reduce $\lambda_\rho$. In all cases, the phonon contribution is in no way changed. Note that in the first and third models important charge and spin fluctuations, respectively, remain even when $T_c$ becomes small and of the order of the value it would have with phonons alone, while in the second model the marginal Fermi liquid part of the interaction is gradually being phased out.

In Fig. 3.9(a), we show results for $\beta$ as a function of $T_c$ for an initial model in which $g = 1$ in the stoichiometric compound, *i.e.*, there are no spin fluctuations. The value of the critical temperature is then reduced by switching off $\lambda_\rho$ leaving the phonon contribution constant. As this is done $\beta$ increases towards a value of 0.5 which occurs exactly when the only contribution to the $T_c$ is from the phonons acting alone. One can see this behaviour in a qualitative manner from Eq. (3.46), where in the limit of $\lambda_\rho \to 0$ for $\lambda_\sigma = 0$, $\beta$ increases to 0.5. However, we stress that the crude approximations leading to Eq. (3.46) do not make it quantitatively correct (especially for large $T_c$'s and large $\lambda$'s). It is important to be aware that as $\lambda_\rho$ is decreased towards zero, the phonons with fixed $\omega_E$ and $\lambda_E$ make an increasing contribution to $T_c$ in absolute terms, *i.e.*, the effect of the phonons is non-linear and they are more effective in increasing $T_c$ the smaller the marginal Fermi liquid component. In Fig. 3.9(b), we show a similar calculation for $g = 0.6$. Here, the rise to $\beta = 0.5$ is much sharper mainly because of a larger electron-phonon contribution. These curves reflect the trend in the experimental data in a more quantitative manner but require $\lambda$'s that would violate those derived experimentally from resistivity measurements [Gurvitch and Fiory (1987)].

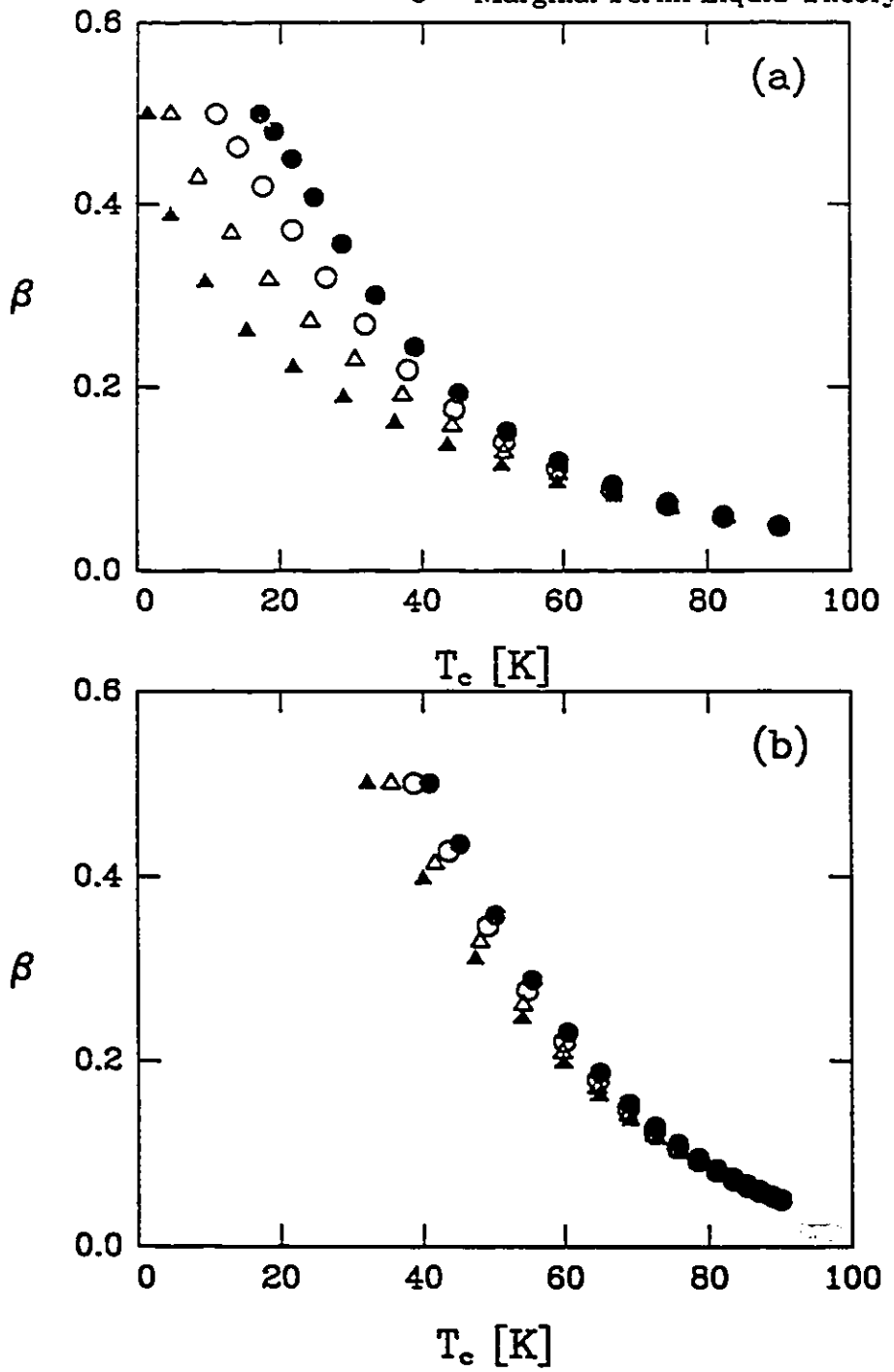


**Figure 3.9** (a) The isotope coefficient, $\beta$, as a function of $T_c$ for various phonon frequencies: $\omega_E = 5.0$ meV (solid dots), $\omega_E = 10.0$ meV (open circles), $\omega_E = 15.0$ meV (open triangles), and $\omega_E = 20.0$ meV (solid triangles). In this graph, $g = 1.0$ and the parameters in the extended marginal Fermi liquid model were chosen to give $\beta = 0.05$ at a $T_c$ of 90K, corresponding to the stoichiometric compound. $T_c$ was reduced by allowing the marginal Fermi liquid component to approach zero while keeping the phonon component fixed. $\beta$ rises in this case to the BCS value of 0.5 where only the phonon component remains. (b) Similar to (a) but with $g = 0.6$. Now the isotope coefficient $\beta$ rises more sharply to $\beta = 0.5$ due to a stronger phonon contribution.

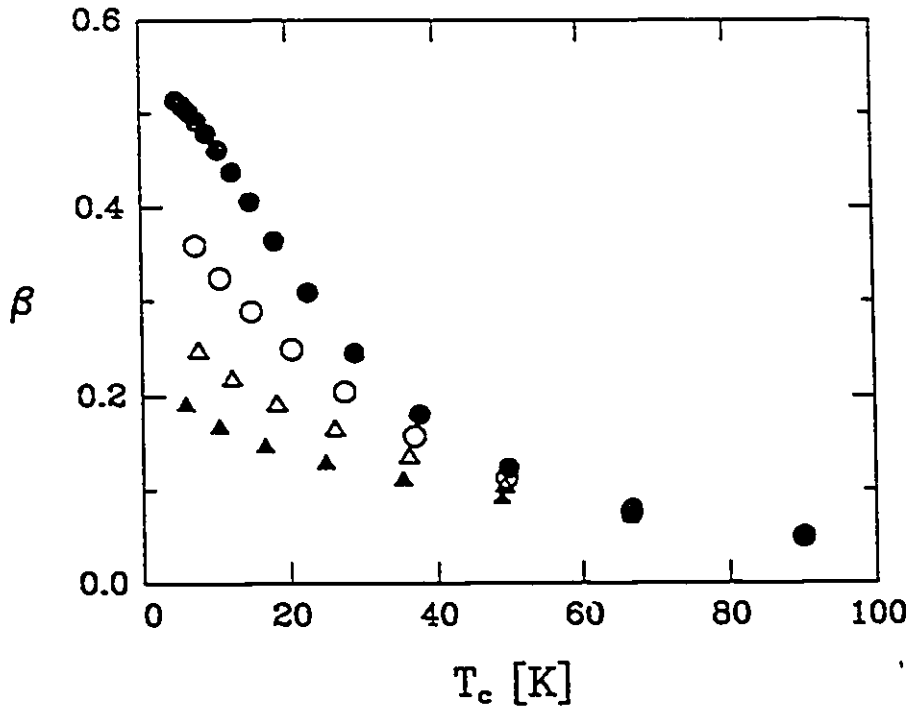


**Figure 3.10** $\beta$ as a function of $T_c$ for various phonon frequencies: $\omega_E$ = 5.0 meV (solid dots), $\omega_E$ = 10.0 meV (open circles), $\omega_E$ = 15.0 meV (open triangles), and $\omega_E$ = 20.0 meV (solid triangles). As in Fig. 2, marginal Fermi liquid parameters are chosen to give $\beta = 0.05$ at $T_c$ = 90K. Here $g = 1.0$ but curves for $g = 0.8$ and 0.6 were not very different. The model used for the reduction in $T_c$ was to fix $\lambda_\rho$ and increase the amount of spin fluctuations, $\lambda_\sigma$. This reduces $T_c$ and also allows for the possibility of $\beta$ exceeding the BCS value of 0.5, as exhibited by the $\omega_E = 5$ meV curve.

Very similar trends for the variation of $\beta$ with $T_c$ value are found when $\lambda_\rho$ is left fixed and the amount of spin fluctuations $\lambda_\sigma$ is increased so as to reduce $T_c$. Results are shown in Fig. 3.10. The rise in $\beta$ is more gradual than for Fig. 3.9 but we note that at the lowest temperatures $\beta$ can now be larger than 0.5, although not by much in the curves shown. This is not surprising since the value of $T_c$ is depressed due to spin fluctuations and thus the $T_c$ becomes small even though the charge fluctuations and the electron-phonon interaction remain large. Such a possibility is anticipated in the work of Carbotte *et al.* (1991) and Williams and Carbotte (1991). Again, referring

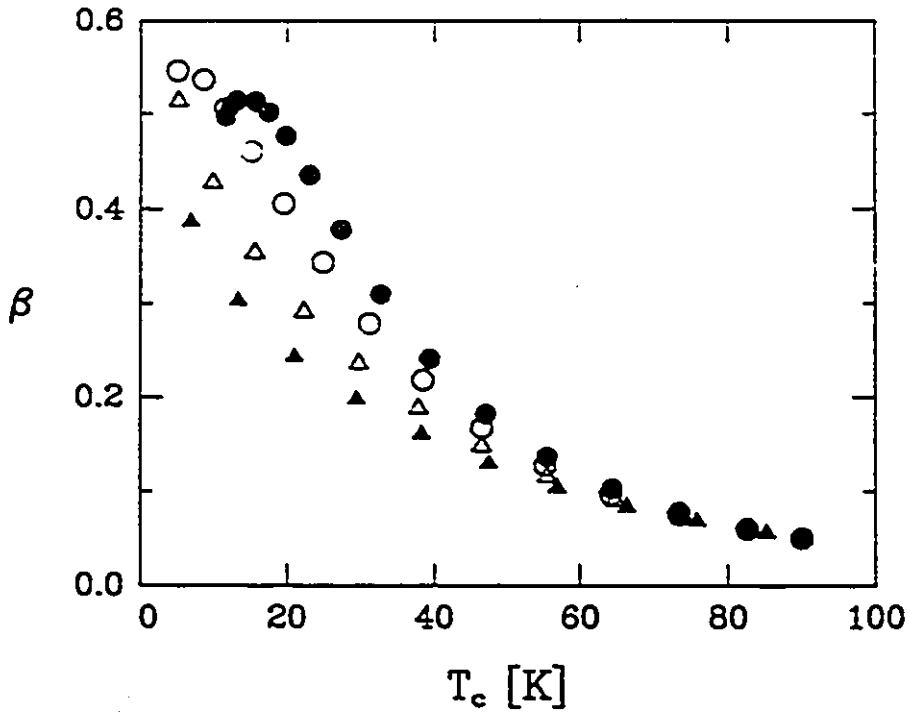


**Figure 3.11** $\beta$ as a function of $T_c$ for $g = 0.6$ and for various phonon frequencies: $\omega_E = 5.0$ meV (solid dots), $\omega_E = 10.0$ meV (open circles), $\omega_E = 15.0$ meV (open triangles), and $\omega_E = 20.0$ meV (solid triangles). As in Fig. 2, marginal Fermi liquid parameters are chosen to give $\beta = 0.05$ at $T_c = 90$K. The model used for the reduction in $T_c$ was to fix $\lambda_\sigma$ and decrease the amount of charge fluctuations, $\lambda_\rho$. This reduces $T_c$ and also allows for the possibility of $\beta$ exceeding the BCS value of 0.5, as exhibited by the $\omega_E = 5$, 10, and 15 meV curves.

to Eq. (3.46) for $\beta$, it is clear that an isotope coefficient > 1/2 can be achieved when $\lambda_\sigma > \lambda_\rho$.

Finally, Fig. 3.11 displays results for our third model, that of fixing $\lambda_\sigma$ and decreasing $\lambda_\rho$. The curves in this case fall in a region intermediate to the other two models and also exhibit an isotope effect coefficient that is greater than 1/2 for the same reasons mentioned above.

In relation to the $Y_{1-x}Pr_xBa_2Cu_3O_7$ experimental results, it is interesting to note that a good part of the observed rise to $\beta = 0.45$ at $T_c = 30$K can be understood simply on the basis of our simple model. In reality, of

course, something more complicated is at work. Two possible suggestions are pair-breaking and an energy dependence in the electronic density of states.

In conclusion, we have calculated the isotope effect coefficient in the marginal Fermi liquid model with an additional phonon contribution. We have found that a large value of $T_c$ with attendant small values of $\beta$ (of order 0.05) is consistent with a small value of the electron-phonon mass renormalization parameter $\lambda_E$ provided coupling is primarily to high energy phonons. For coupling to low energies the corresponding $\lambda_E$ values can be much larger although the total contribution to the enhancement in overall $T_c$ value is never greater than about 5K. Also as the amount of spin fluctuations in the system is increased, the corresponding value for $\lambda_E$ increases. This effect is small for large $\omega_E$ but can be very substantial for low values. Finally, we find that, if $T_c$ is reduced by either increasing the amount of spin fluctuations with all other parameters fixed, decreasing uniformly $\lambda_\rho$ and $\lambda_\sigma$ to zero, or decreasing $\lambda_\rho$ only, the isotope coefficient increases sharply towards a value of 1/2 or even above. The increase in $\beta$, however, is never large enough to explain presently available results for $Y_{1-x}Pr_xBa_2Cu_3O_7$ and, at the same time, remain consistent with the dc resistivity determination of $\lambda$.

## 3.6 THE LONDON PENETRATION DEPTH

The zero-frequency penetration depth is a measure of the distance scale on which a static magnetic field will penetrate into the superconductor. Although a superconductor has the property that it excludes all magnetic flux, at the superconducting surface screening currents are produced to provide the diamagnetism and it is in the surface layer that the field may still penetrate. For a semi-infinite plane the field $B$ would decay into the surface

from its free space value $B_o$ as $B = B_o \exp[-x/\lambda]$, where $\lambda$ is the penetration depth.

Calculations for electromagnetic properties, in general, are derived from a calculation of the response function $K(\vec{q},\omega)$ which is the linear response in Fourier transform space for the induced current density $j(\vec{q},\omega)$ due to a perturbing electromagnetic vector potential $A(\vec{q},\omega)$ [Nam (1967a,b); Scholten *et al.* (1977)]:

$$j_\mu(\vec{q},\omega) = -K_{\mu\nu}(\vec{q},\omega)A^\nu(\vec{q},\omega) \quad . \tag{3.47}$$

with the tensor notation referring to the three coordinate directions. More will be said about this response function in the next chapter when we treat finite frequency optical conductivity properties. The zero-frequency, temperature-dependent penetration depth for specular reflection is then given as [Nam (1967a,b)]:

$$\lambda(T) = \frac{2}{\pi}\int_0^\infty dq \frac{1}{q^2 + K(q,0)/4\pi} \quad . \tag{3.48}$$

The high $T_c$ copper oxides are Type II superconductors in the clean limit (*i.e.*, $\lambda \gg \xi(0)$, where $\xi(0)$ is the zero-temperature coherence length). This is called the London limit. In this limit, Nam (1967a,b) has evaluated $K(q,0)$ and obtained for the London penetration depth:

$$\lambda_L(T) = \left[\frac{4}{3}\pi N(0)e^2 v_F^2 T \sum_{n=1}^{\infty} \frac{\Delta_n^2}{Z_n(\omega_n^2 + \Delta_n^2)^{3/2}}\right]^{-1/2} \quad . \tag{3.49}$$

Following the numerical procedure outlined in Section 3.4 we have calculated the penetration depth from Eq. (3.49). The zero-temperature gap

$\Delta_o$ was iterated self-consistently but for numerical convenience $\Delta(T)$ was taken to have the BCS temperature dependence scaled by $\Delta_o$.

Figs. 3.12 and 3.13 display results for $g = 0.4$ and 0.5, and $g = 0.6$ and 0.8, respectively. Curves correspond to different values of $T_c/\omega_c$ as indicated in the figures. Also shown are curves for the two-fluid model $[\lambda_L(0)/\lambda_L(T)]^2 = 1 - t^4$ (second lowest solid curve) and the curve for the weak coupling BCS clean limit (lowest solid curve). The solid dots correspond to careful data from Pumpin *et al.* (1990) which follow the two-fluid curve. In general, magnetization experiments find a temperature dependence near the weak coupling BCS curve and muon spin relaxation ($\mu$SR) experiments tend to agree more with the two-fluid model. Sweeping $T_c/\omega_c$ from small to large values in this theory increases the height of the curves. Curves falling on and above the two-fluid result can also be achieved with ordinary strong coupling theory, and it is essentially the strong coupling effects from the spin fluctuation component that results in the behaviour seen here (see Chapter 5). However, no single curve describes the experimental data. Curves that give reasonably good agreement still overestimate the data at high temperatures and underestimate the data at low temperatures. The most recent experimental results by Anlage *et al.* (1991) indicate a temperature dependence conforming more to the marginal Fermi liquid like behaviour.

The constraints put on the parameters to obtain overlap between the experiment and our theory in these graphs would restrict the value of $2\Delta_o/k_BT_c$ to be greater than the BCS value of 3.53 but less than approximately 5. This is not as large as the suggested experimental value of 8 given by Schlesinger *et al.* (1987); however, Timusk *et al.* (1989) have pointed out

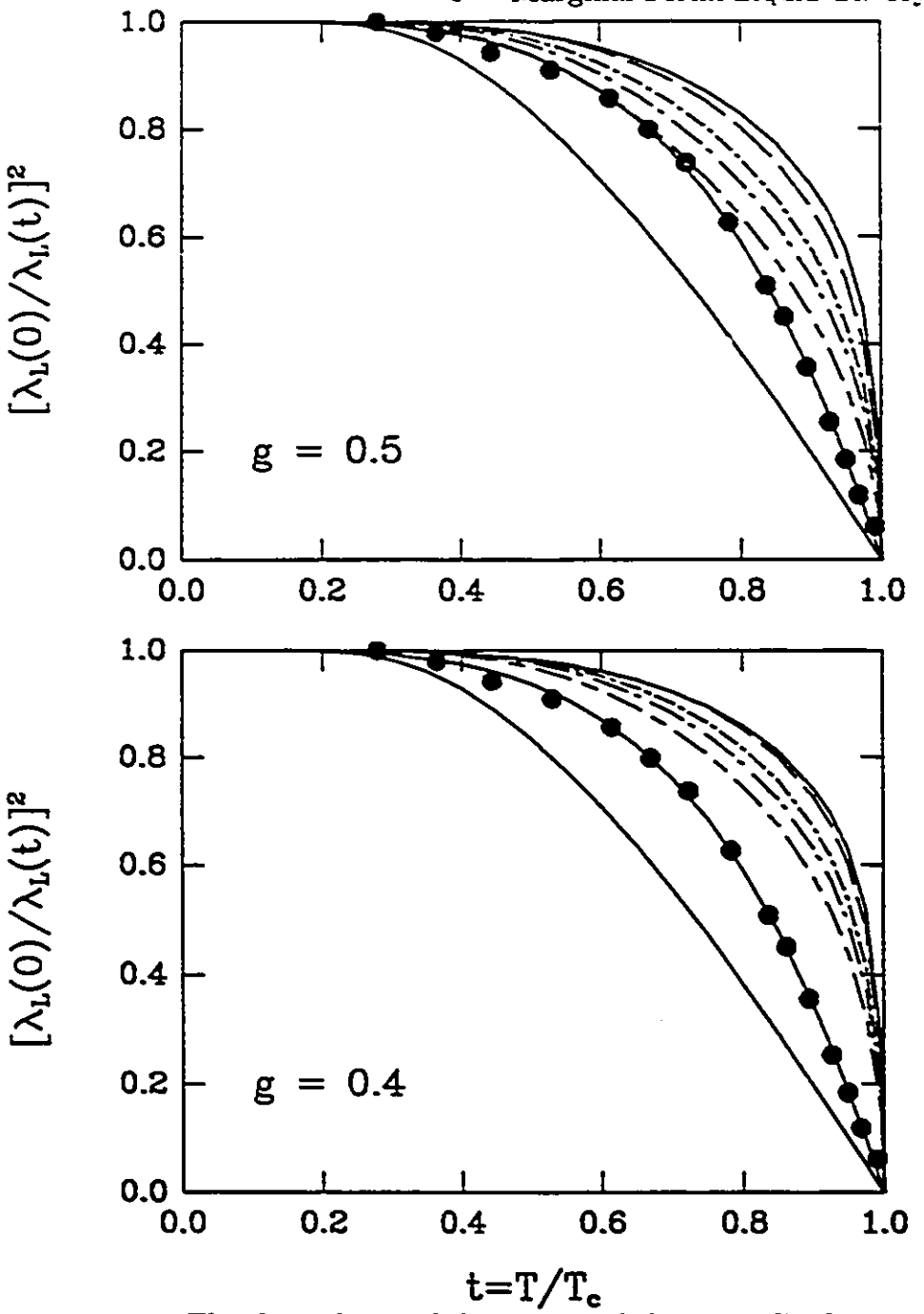


**Figure 3.12** The dependence of the square of the normalized penetration depth $\lambda_L(0)/\lambda_L(t)$ on reduced temperature $t$ for several values of $T_c/\omega_c$, namely, 0.0215 (solid line), 0.0144 (long dashed line), 0.0086 (dash-dotted line), 0.0057 (long dash-dotted line) and 0.0029 (long dash-short dashed line). Also shown are data (solid dots) and the two-fluid model results (solid line) which represent the data very well. Finally, the lowest solid curve is the BCS prediction shown for comparison. The top frame is for $g = 0.5$. The lower frame is for $g = 0.4$ with the $T_c/\omega_c$ values of 0.0108, 0.0086, 0.0057, and 0.0043, and 0.0029 for the upper five curves in descending order.

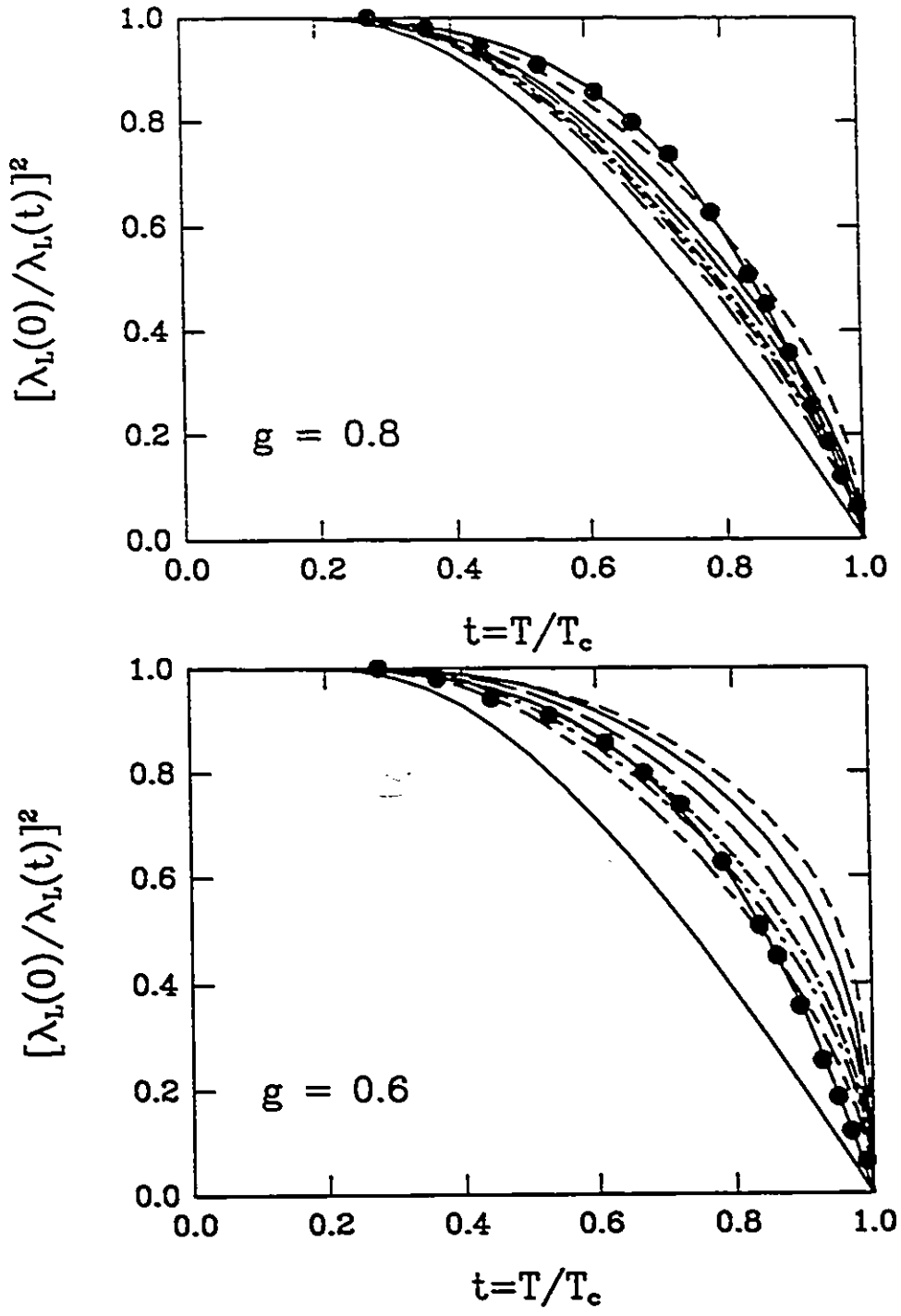


**Figure 3.13** Same as Fig. 3.12. The top frame is for $g = 0.8$ with $T_c/\omega_c$ values (in descending order of the curves) of 0.0431 (short dashed curve), 0.0215, 0.0144, 0.0086, 0.0057, and 0.0029. The lower frame is for $g = 0.6$ with same parameters as in the top frame.

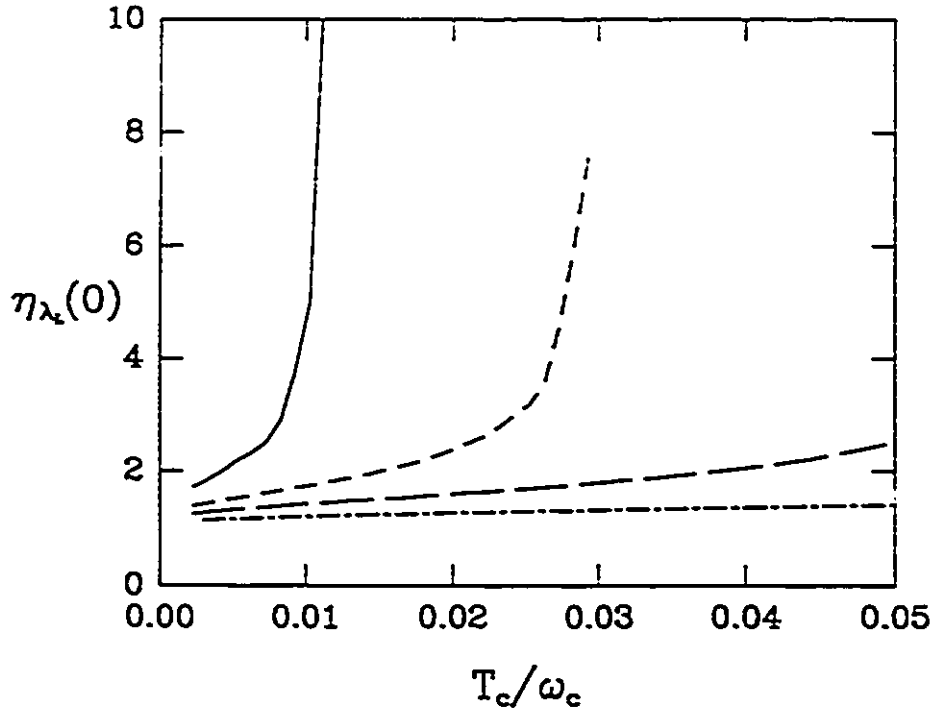


**Figure 3.14** The deviation of the zero-temperature London penetration depth $\lambda_L(0)$ from its BCS value as a function of $T_c/\omega_c$ for $g = 0.4$ (solid), 0.5 (short dashed), 0.6 (long dashed), 0.8 (dot-dashed).

that problems remain in the interpretation of the infrared data in terms of a large gap edge value.

On the other hand in $\mu$SR experiments by Lichti *et al.* (1989) on $R\mathrm{Ba_2Cu_3O_7}$ with $R$ = Eu, Gd, and Er, a temperature dependence considerably above that for the two-fluid model is observed. This is more consistent with $2\Delta_0/k_BT_c \sim 8$. It is, therefore, difficult at this time to draw firm conclusions from the data. However, our model is not inconsistent with the data.

In Fig. 3.14, we show the deviation of the zero-temperature London penetration depth $\eta_{\lambda_L}(0)$ from BCS as a function of $T_c/\omega_c$ for the same values of $g$ previously considered. By definition,

$$\lambda_L(0) \equiv \eta_{\lambda_L}\lambda_L^{\mathrm{BCS}}(0) \quad . \tag{3.50}$$

In Eq. (3.50). $\lambda_L^{BCS}(0)$ is calculated for a superconductor with $T_c$ = 11.6 K and with a $\delta$-function spectral density placed at a frequency $\omega_E$ = 200 meV. We see from Fig. 3.14 that $\eta_{\lambda_L}(0)$ is always greater than 1 in the range considered and that it shows a very strong increase around $T_c/\omega_c = 0.01$ for $g = 0.4$ and around 0.03 for $g = 0.5$. This reflects the unphysical increase in $\lambda_p$ in this range of parameters as shown in Fig. 3.7. The existence of this large correction to $\lambda_L(0)$ is hard to establish experimentally at this time because of uncertainties in the other parameters that enter the formula (3.49) for $\lambda_L(0)$.

## 3.7 THE dc JOSEPHSON CURRENT

It is of some interest to investigate the temperature dependence of the dc Josephson effect as predicted by the marginal Fermi liquid model since recent experiments by Mannhart *et al.* (1988) have reported anomalous behaviour for temperature dependence as well as absolute size of the intrinsic intra grain Josephson current. While a convincing explanation of the observed behaviour has, in fact, been put forward by Deutscher (1989) on the basis of inhomogeneity in the order parameter near grain boundaries, due to the short coherence length intrinsic to the CuO, other possible explanations are worth considering.

The critical dc Josephson current associated with a superconductor-insulator-superconductor tunnel junction is the limiting current that can flow through the junction. This dc current occurs at zero voltage bias as a result of the pair wavefunction "leaking" across the insulator barrier, allowing pairs of electrons to tunnel through the barrier. The ac Josephson current, which is not discussed here, is the result of the wavefunction on one side of the barrier having a different phase from that on the other side. Under a voltage bias, this

produces interference between the time evolution of the states on opposite sides of the junction and results in oscillations of the pair current across the junction, producing an ac current typically at microwave frequencies.

The dc Josephson current, at any temperature, is related to the local penetration depth $\lambda_l$. This may be evaluated from Eq. (3.48), in the case of small $q$ appropriate to a short mean free path $l$, to be [Nam (1967a,b)]:

$$\lambda_l = \left[\frac{8}{3}\pi N(0)e^2 v_F^2 \tau_N T \sum_{n=1}^{\infty} \frac{\Delta_n^2}{\omega_n^2 + \Delta_n^2}\right]^{-1/2} . \tag{3.51}$$

We will present the dc Josephson current normalized to its zero-temperature value which is given by [Nam (1967a,b); Akis and Carbotte (1990)]:

$$\frac{J_c(T)}{J_c(0)} = \left[\frac{\lambda_l(0)}{\lambda_l(T)}\right]^2 . \tag{3.52}$$

As before, we fix $\lambda_\rho$ to obtain a $T_c = 100$ K and plot results in terms of the two remaining parameters, $g$ the admixture of spin and charge fluctuations and $\omega_c$ the upper cutoff in the fluctuation spectrum.

In Figs. 3.15 and 3.16 we show results for the temperature variation of $J_c(T)/J_c(0)$ as a function of reduced temperature $t = T/T_c$. In the upper frame of Fig. 3.15, $g = 0.5$ and in the lower frame it is 0.4 while the corresponding numbers for Fig. 3.16 are 0.8 and 0.6, respectively. In Fig. 3.15 are, from top to bottom, $\omega_c = 400$ meV (solid curve), $\omega_c = 600$ meV (long dashed curve), $\omega_c = 1000$ meV (dash-dotted curve), $\omega_c = 1500$ meV (long dash-dotted curve), and $\omega_c = 3000$ meV (long dash-short dashed curve). The final solid curve is the BCS result shown for comparison. For $g = 0.4$, the corresponding values of $\omega_c$ are 800 meV, 1000 meV, 1500 meV, 2000 meV and 3000 meV. For $g = 0.8$ and $g = 0.6$, they are $\omega_c = 400$ meV, 600 meV, 1000 meV, 1500 meV, 3000 meV, with the additional dotted curve corresponding to 200 meV.

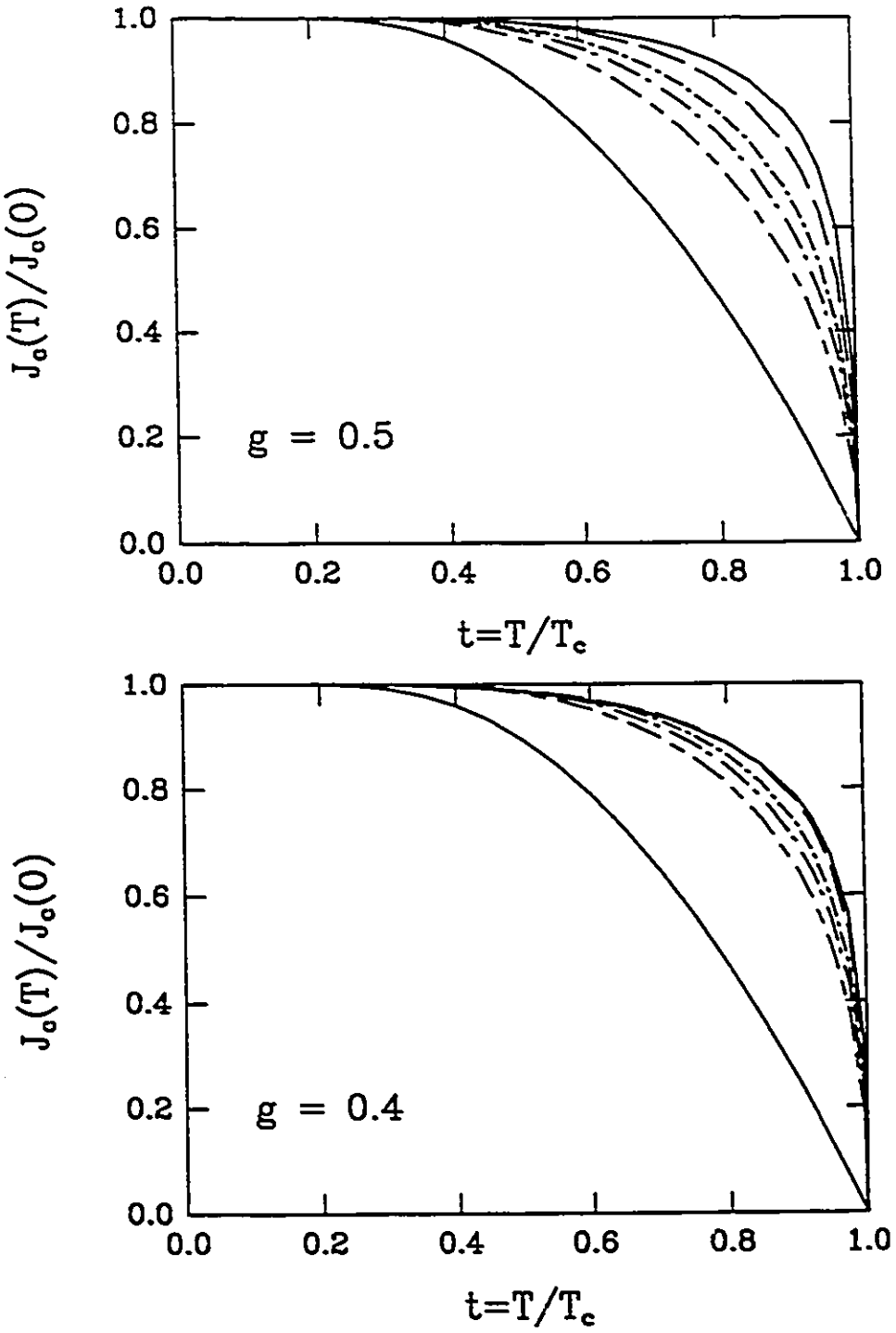


**Figure 3.15** The reduced dc Josephson current $J_c(T)/J_c(0)$ as a function of reduced temperature $t$ for $g = 0.4$ (lower frame) and $g = 0.5$ (upper frame). The various curves correspond to different values of the cutoff $\omega_c$ as described in the text. The lower solid curve is the BCS variation, included for comparison.

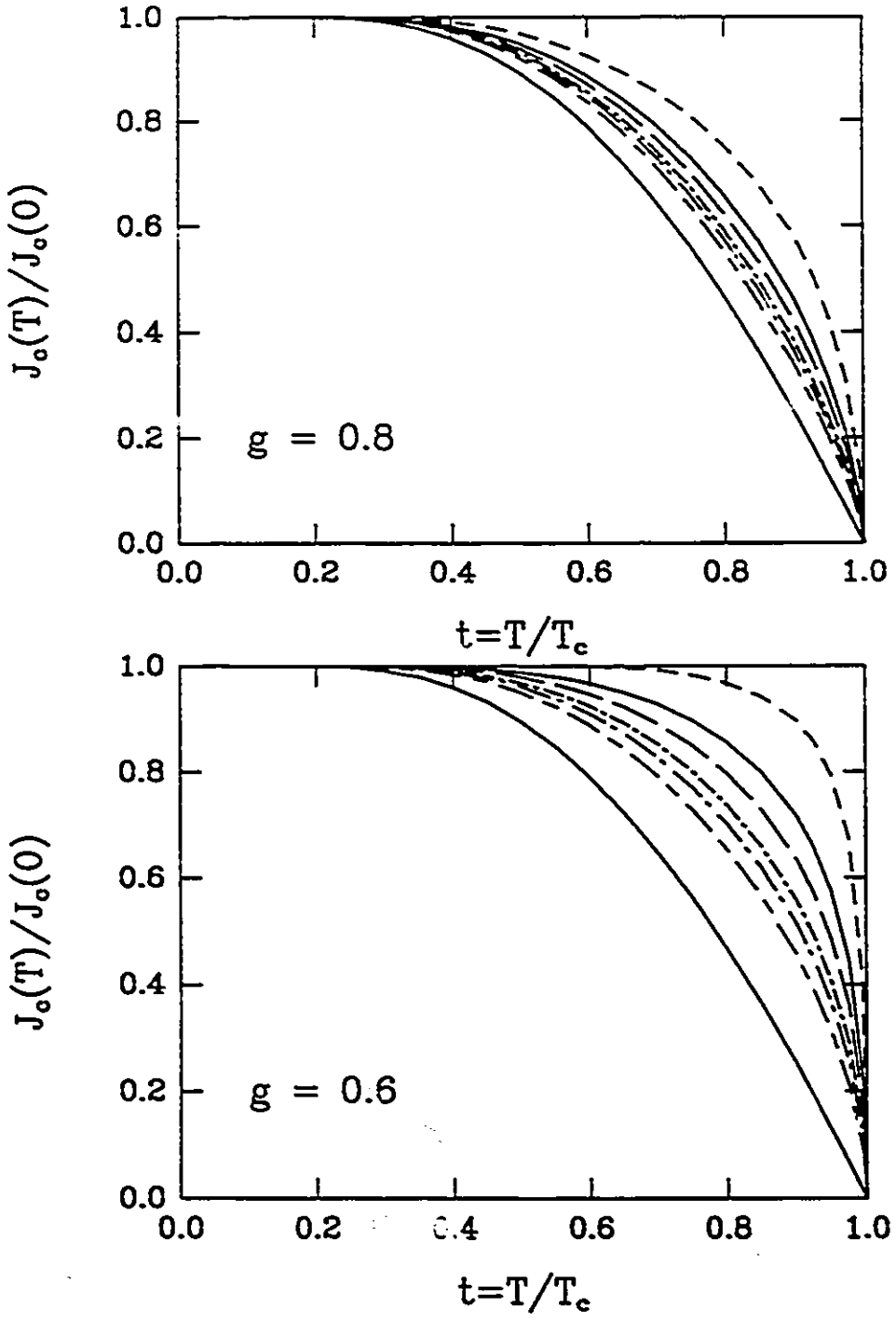


**Figure 3.16** Same as for Fig. 3.15 but the lower frame is for $g = 0.6$ and the upper frame is for $g = 0.8$.

It is clear on examination of these figures that in all cases considered the present model gives deviations from BCS behaviour which always fall above that curve. The variation for $g = 0.6$ and $\omega_c = 200$ meV (short dashed curve) is particularly striking and represents a dependence on reduced temperature which remains near 1 for all reduced temperatures below $\lesssim 0.8$ and then drops very rapidly towards zero as $T_c$ is approached. Such a variation is opposite to that observed in the experiment of Mannhart *et al.* (1988). According to Deutscher (1989), however, such data cannot be directly compared with the results of the present calculation since it is necessary to account for an inhomogeneous variation in the order parameter as the junction boundary is approached. When this is done, assuming a BCS superconductor, very good agreement with experiment is found. Since our results do not deviate very strongly from BCS they also should lead to good agreement with the experiment once inhomogeneities are accounted for, so that, present data are consistent with a marginal Fermi liquid model.

Another quantity of interest is the value of the Josephson current at zero temperature. This quantity depends, among other things, on the value of the barrier resistance. It is customary to present results in terms of BCS theory in which case $J_c \propto 1/\Delta_o$. We then write $J_c(0) = \eta_{J_c}(0) J_c^{BCS}(0)$ and so $\eta_{J_c}(0)$ is independent of the normal state material parameters of the junction. This quantity is plotted in Fig. 3.17 for various values of $g$ as a function of $T_c/\omega_c$. It is seen that $J_c(0)$ is reduced in our model from its BCS value $\eta_{J_c}(0) \lesssim 1$ but the reduction is far too small to explain on the basis of the present theory alone the order of magnitude reduction in current observed by Mannhart. The discussion of Deutscher (1989) is presumably applicable and inhomogeneous effects need to be introduced for comparison with data.

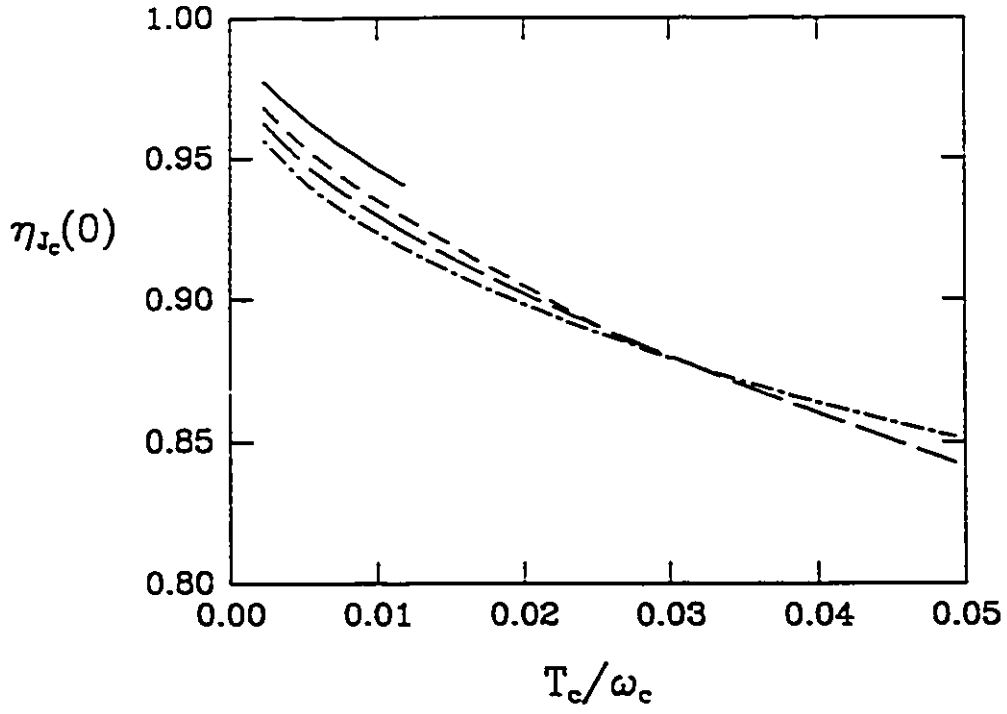


**Figure 3.17** The zero temperature dc Josephson current divided by its BCS value as a function of $T_c/\omega_c$ for various values of $g$, namely, $g = 0.4$ (solid curve), $g = 0.5$ (short dashed curve), $g = 0.6$ (long dash curve) and $g = 0.8$ (dash-dotted curve).

In conclusion, the temperature dependence of the dc Josephson current has been calculated in the marginal Fermi liquid model and found to deviate significantly from BCS with the current everywhere above the BCS prediction. In some cases, the temperature variation of the normalized dc current remains nearly 1 up to reduced temperature $t \lesssim 0.8$ and then drops very rapidly to zero. For fixed junction parameters the absolute magnitude of the current at $T = 0$ as found in our model is smaller than in BCS but not by an order of magnitude as observed recently. To have agreement with experiment it appears to be necessary to include the effect of the inhomogeneity in the order parameter around the junction boundary as described by Deutscher, whose calculations are based on an intrinsic BCS model for

the intragrain superconductivity. We expect that using a marginal Fermi liquid description instead will lead to results equally consistent with present experiments.

# Chapter 4

# Marginal Fermi Liquid Theory II

## *Optical Properties*

Since the discovery of the high $T_c$ copper oxide materials, the nature of the superconductivity has remained a mystery. It is generally acknowledged that the conventional electron-phonon mechanism for pairing cannot alone be responsible for the high $T_c$ observed in these materials. Due to the high value of $T_c$ and the novel normal state properties of these compounds, several other pairing theories have been proposed.

Experiments performed on the high $T_c$ superconductors have also been improving substantially due to: sample quality, availability of single crystals, and more systematic investigations of the entire family of copper oxides. In addition, the sophistication of the experiments is increasing, allowing for more detailed information to be obtained about several theoretical quantities. Thus, the situation is ripe for concrete tests of the various theories. On the theoretical side, it is important to investigate the consequences of a theory that would produce experimental signatures differentiating it

from other theories. In this way, one can eliminate unsuitable theories and hopefully discover the correct one for these materials.

To this end, in this chapter, we will discuss the results of calculations pertaining to the finite-frequency and temperature-dependent optical conductivity. With regard to the marginal Fermi liquid, very novel results have been obtained that are a result of the fluctuation spectrum developing a gap at low frequencies in the superconducting state.

Before presenting these striking results, we will give a simple introduction to optical absorption to illustrate the processes that we are considering and to aid in later discussions. We will follow this by some technical details about the calculation of optical conductivity illustrated by conventional strong coupling calculations. We then present calculations in the marginal Fermi liquid model of Varma *et al.* (1989) [see Chapter 3] of the zero-temperature conductivity, the quasiparticle damping rate, and the temperature-dependent conductivity, with emphasis, in the latter case, on the microwave region of the frequency spectrum.

## 4.1 INTRODUCTION

The low frequency conductivity, such as measured by microwave and far infrared experiments, has traditionally played an important role in the investigations of the superconducting state. This is due to the possibility of extracting, amongst other things, information about the energy gap (in conventional superconductors, such as Pb [Palmer and Tinkham (1968)]), and the quasiparticle damping rate. Infrared measurements on superconductors can yield important information on the excitation spectrum of the system in the energy range of a few times the energy gap $\Delta_o$, and are therefore very

important. Because of this, many experimental studies on the high $T_c$ oxides have now been published. These are too numerous to describe here and the reader is referred to the recent review of Timusk and Tanner (1989) for references and discussion. While there is, at present, a great deal of agreement among the various researchers as to experimental results, their interpretation remains controversial [Schlesinger *et al.* (1990); Kamarás *et al.* (1990)]. While some authors argue for the existence of a large gap $2\Delta_o/k_BT_c \sim 8$ [Schlesinger *et al.* (1990)], others reason that a gap cannot be seen in the clean limit [Kamarás *et al.* (1990)]. At higher energies the exact nature of the mid-infrared absorption is also not yet known [Kamarás *et al.* (1990)].

Recently, Lee, Rainer and Zimmermann (1989) have given a real frequency formulation of the optical conductivity, valid for any value of the mean free path. They have studied, within such a formalism, several possible models for the Eliashberg kernels which could possibly be applicable to the high $T_c$ oxides. They give results for pure phonon as well as combined phonon-plus-exciton models with particular emphasis placed on the Holstein effect. These processes reflect some of the details of the excitation spectrum involved. Complementary calculations using an imaginary frequency axis (Matsubara) formulation of the theory with final analytic continuation of the current-current correlation function using Padé approximants have been performed by Bickers *et al.* (1990). These conventional strong coupling calculations predict large changes in the infrared spectrum in the Holstein region when the materials become superconducting. There is general agreement among experimentalists that such structures are not observed in the infrared conductivity [Kamarás *et al.* (1990); Schlesinger *et al.* (1990)].

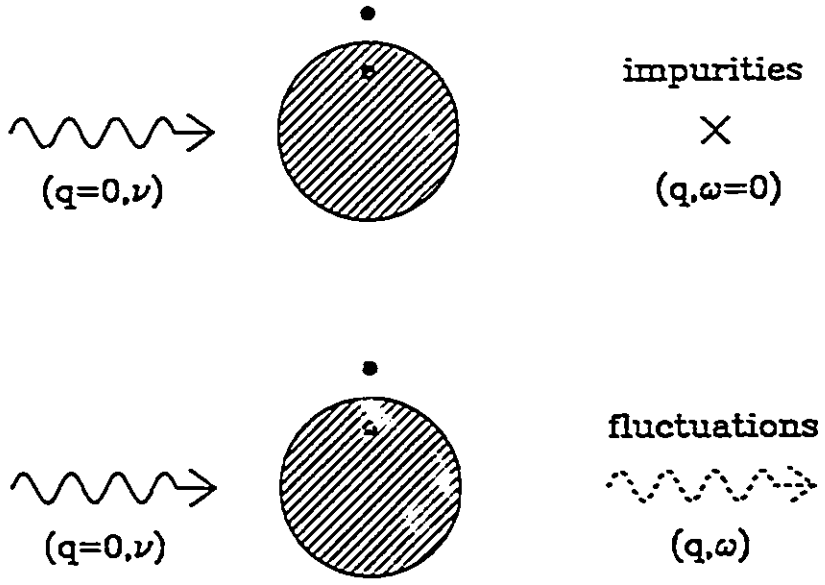


**Figure 4.1** A schematic diagram illustrating the absorption processes considered in this thesis. In the first process (top), a photon of energy $\nu$ is incident on a Fermi sea of electrons in a metal (the shaded sphere), creating a hole-particle pair. Energy and momentum are conserved by relaxing this process with impurity scattering, and hence, absorption occurs. This schematic corresponds to the optical conductivity in Fig. 4.2. In the second process (bottom), fluctuations, such as phonons, are available to relax the system and conserve energy and momentum. This process corresponds to Fig. 4.3.

Before displaying our results for the marginal Fermi liquid model, we will introduce the formalism necessary for calculating optical conductivity and reproduce the theoretical results of the two groups mentioned above to exhibit results typical of conventional strong coupling calculations. The optical conductivity that we will consider here involves two processes: impurity-assisted absorption and fluctuation-assisted absorption. These are illustrated schematically in Fig. 4.1. In the first case of impurity-assisted absorption, a photon of energy $\nu$ ($\hbar = 1$) and momentum $q = 0$ is incident on the sea of electrons in the metal (the shaded region here) and creates a hole-particle

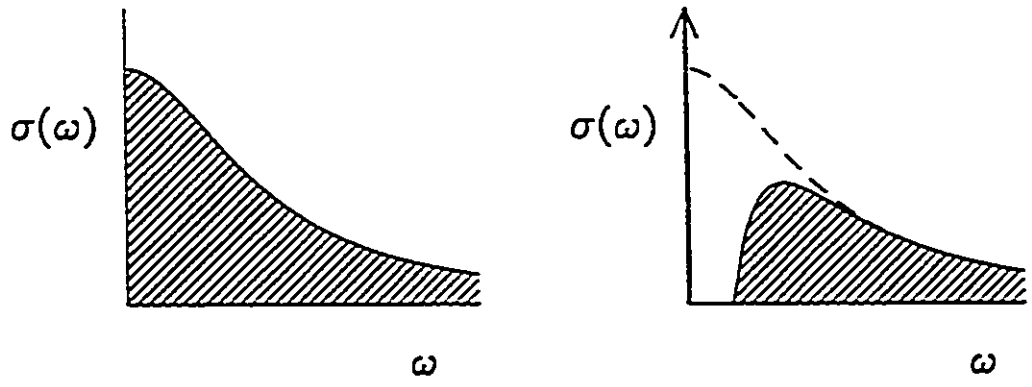


Figure 4.2 The real part of the optical conductivity $\sigma(\omega)$ due to impurity scattering. On the left is the conductivity in the normal state and on the right is the conductivity in the superconducting state. In the superconducting state, no absorption occurs until $\omega = 2\Delta$, at which point the conductivity rises up and eventually joins the normal state curve (dashed line). The missing area between the two curves is to be found in a delta function at $\omega = 0$.

pair which has both energy and momentum. However, this process alone does not conserve energy and momentum, and so impurities in the system allow this process to happen by absorbing the extra momentum but with no change in energy. Hence, absorption of light can occur in an impure system at any frequency of the incident light. The result of the absorption process is shown on the left in Fig. 4.2. This is simply the Drude conductivity given in many elementary solid state textbooks for the viscous damping of electrons in an applied electric field:

$$\sigma_1(\omega) = \frac{ne^2\tau}{m(1+\omega^2\tau^2)} = \frac{\omega_p^2\tau}{4\pi(1+\omega^2\tau^2)} \quad , \tag{4.1}$$

where $n$ is the density of electrons, $m$ the electron mass, and $\tau$ the scattering lifetime. [Note that the conductivity is a complex quantity but we are interested in this thesis only in the real part $\sigma_1(\omega)$.] In this curve, $\sigma_1(\omega = 0) = \omega_p^2\tau/(4\pi)$, where $\omega_p \equiv 4\pi ne^2/m$ is the plasma frequency, and the

half-width at half-maximum is the scattering rate $1/\tau$. In the superconducting state, the creation of an electron-hole pair cannot occur until a Cooper pair is liberated from the condensate and this places a threshold on the process of $2\Delta$. Hence, absorption does not occur until $2\Delta$, whereupon absorption occurs and quickly rises up to meet the normal state conductivity, as shown in Fig. 4.2 on the right. There are two sum rules of some importance here. The first sum rule states that the area under the curve shown on the left of Fig. 4.2 is given as [Tinkham (1975)]:

$$\int_0^\infty \sigma_1(\omega)d\omega = \frac{\omega_p^2}{8} \quad . \tag{4.2}$$

The second sum rule states that this area is conserved in the superconducting state [Ferrell and Glover (1958); Tinkham and Ferrell (1959)]:

$$\int_0^\infty [\sigma_{1S}(\omega) - \sigma_{1N}(\omega)]d\omega = 0 \tag{4.3}$$

and hence the area lost in the right side of Fig. 4.2 ends up in the zero-frequency delta function shown in Fig. 4.2 for the dc current associated with the superconducting condensate:

$$\sigma_{1S}(\omega = 0) = \frac{\pi n_s e^2}{2m}\delta(0) \quad , \tag{4.4}$$

where $n_s$ is the phenomenological two-fluid model density of superconducting electrons. [Note that in the two-fluid model the penetration depth, which is associated with the zero-frequency limit of the conductivity, is given as $\lambda_L^2 = mc^2/(4\pi n_s e^2)$.]

Another process of interest here is that associated with fluctuations (conventionally phonons). Again, light is incident upon the system creating an electron-hole pair. But now to conserve momentum, a fluctuation, such

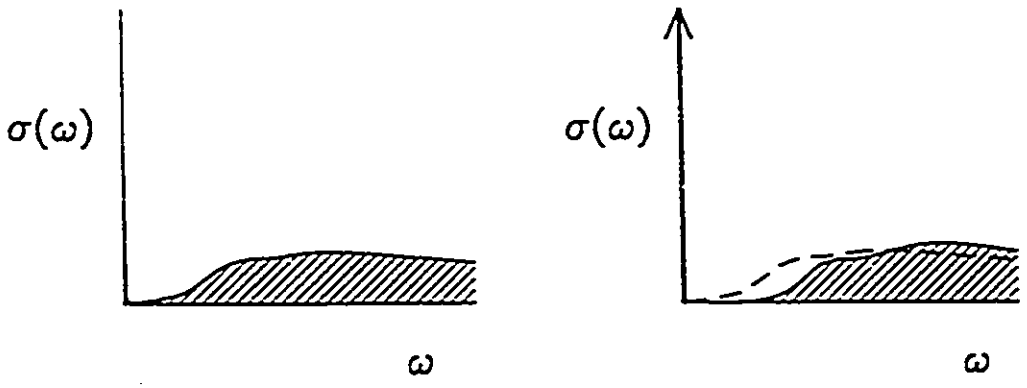


Figure 4.3 The optical conductivity in the normal (left) and superconducting (right) states, corresponding to the fluctuation-assisted absorption process described in the text and shown in the bottom of Fig. 4.1. Notice that the features associated with the fluctuation spectrum are shifted by $2\Delta$ in the superconducting state, where no absorption occurs until $\omega = 2\Delta$. The dashed curve on the right is the normal state conductivity for comparison.

as a phonon, is emitted (Fig. 4.1). This fluctuation conserves momentum but also has an energy associated with it, requiring overall energy conservation. Hence, this absorption process can only absorb at specific energies associated with the fluctuations in the system. This process, when phonons are involved, is also known as the Holstein process. Absorption from the spectrum for Pb (shown in Fig. 2.8) is shown in Fig. 4.3 and, as mentioned above, mimics the shape and weight of the fluctuation spectrum. In the superconducting state, again the absorption is gapped by $2\Delta$ and absorption occurs at $2\Delta+\omega$, where $\omega$ is the frequency of the fluctuation. Hence, the features in the left hand graph of Fig. 4.3 are shifted by $2\Delta$ in the graph on the right. These are the only two processes considered in this thesis.

These processes can be mathematically summarized in Fig. 4.4 by the Feynman diagram for the current-current correlation function $\Pi(i\nu_m)$ [referred to as $K(\vec{q},\omega)$ in Section 3.6], with the electron line renormalized

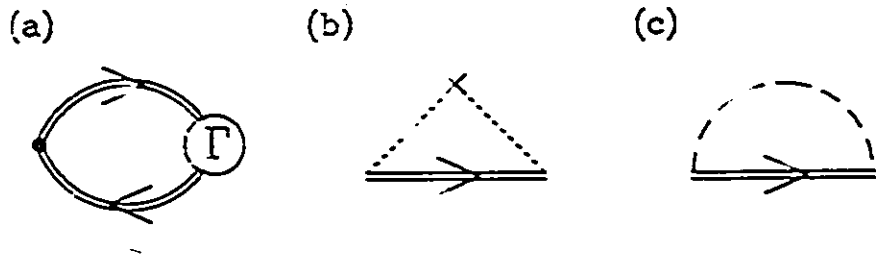


Figure 4.4 (a) The current-current correlation function $\Pi(i\nu_m)$ for the current response to an applied field. A current at the vertex corresponding to the black dot creates a hole-particle pair which recombines producing a current response at the other vertex. The electron lines are renormalized by (b) impurity scattering, where × represents the impurity and the dotted line the Coulomb interaction, and by (c) fluctuations (dashed line). The circle containing Γ represents possible vertex corrections to (a).

by the fluctuations and impurities. This is given in terms of the Green's functions [see Appendix A] as (Bickers *et al.* (1990))

$$\Pi(i\nu_m) = \frac{T}{N}\sum_{n\vec{k}} \mathrm{Tr}\frac{ek_x}{n} G(\vec{k}, i(\omega_n + \nu_m)) G(\vec{k}, i\omega_n)\Gamma_x \quad , \tag{4.5}$$

where the vertex function, that would contain higher order impurity and fluctuation ladder scattering processes, is taken in first order to be $\Gamma_x = ek_x/m$. This approximation is equivalent to the use of the usual $\alpha^2F(\omega)$ and quasiparticle scattering time $\tau$ instead of using the corresponding transport quantities, $\alpha^2_{tr}F(\omega)$ and $\tau_{tr}$ [Grimvall (1981)].

The conductivity $\sigma(\omega)$ is related to the real frequency axis analytic continuation of the current-current correlation function $\Pi(i\nu_m)$ which is known, within a Matsubara formalism, only at discrete boson frequencies $\nu_m = 2m\pi T$ where $m$ is integral and $T$ is the temperature. Specifically,

$$\sigma(\omega) = \frac{i}{\omega}\Pi(i\nu_m \rightarrow \omega + i0^+) \quad . \tag{4.6}$$

Referring to Bickers *et al.* (1990) for details, $\Pi(i\nu_m)$ is given in terms of the plasma frequency $\omega_p$, the Matsubara gaps $\tilde{\Delta}_n$ and renormalization factors $\tilde{\omega}_n$ by

$$\Pi(i\nu_m) = \frac{\omega_p^2}{4\pi} \pi T \sum_n S_{n,m} \tag{4.7}$$

with

$$S_{n,m} = \frac{\tilde{\omega}_n(\tilde{\omega}_n + \tilde{\omega}_{n+m}) + \tilde{\Delta}_n(\tilde{\Delta}_n - \tilde{\Delta}_{m+n})}{R_n P_{n,m}}$$

$$- \frac{\tilde{\omega}_{n+m}(\tilde{\omega}_{n-m} + \tilde{\omega}_n) + \tilde{\Delta}_{n+m}(\tilde{\Delta}_{n+m} - \tilde{\Delta}_n)}{R_{n+m} P_{n,m}} \quad ,$$

$$\text{for} \quad (m \neq 0, -2n-1),$$

$$= \tilde{\Delta}_n^2 / R_n^3 \quad , \qquad \text{for} \quad (m = 0),$$

$$= 1/R_n \quad , \qquad \text{for} \quad (m = -2n-1). \tag{4.8}$$

In equation (4.8), $R_n = \sqrt{\tilde{\omega}_n^2 + \tilde{\Delta}_n^2}$ and $P_{n,m} = \tilde{\omega}_n^2 - \tilde{\omega}_{n+m}^2 + \tilde{\Delta}_n^2 - \tilde{\Delta}_{n+m}^2$. $\tilde{\Delta}_n$ and $\tilde{\omega}_n$ are calculated from the Eliashberg equations given in Eqs. (3.32)-(3.34).

The model used by Bickers *et al.* (1990) for $\alpha^2 F(\omega)$ is that of a single truncated Lorentzian with peak position at $\omega_o$ and width $\Gamma_o$ and truncated at $\Gamma_c$, *i.e.*,

$$\alpha^2 F(\omega) \propto \left[ \frac{1}{(\omega - \omega_o)^2 + \Gamma_o^2} - \frac{1}{\Gamma_c^2 + \Gamma_o^2} \right] \quad , \quad |\omega - \omega_o| < \Gamma_c \quad ,$$

$$= 0 \quad , \qquad\qquad |\omega - \omega_o| > \Gamma_c \quad . \tag{4.9}$$

The parameters are $\omega_o = 50$ meV, $\Gamma_o = 5$ meV and $\Gamma_c = 3\Gamma_o = 15$ meV. In Fig. 4.5 we show our results for the ratio of the real part of the conductivity in the superconducting state divided by the normal state, $(\sigma_{1S}(\omega)/\sigma_{1N}(\omega))$. The same four impurity concentrations, $t^+ \equiv 1/(2\pi\tau) = 0.0$ (dotted curve), 0.796 meV (dashed curve), 7.96 meV (dashed-dotted curve), and 79.6 meV (solid

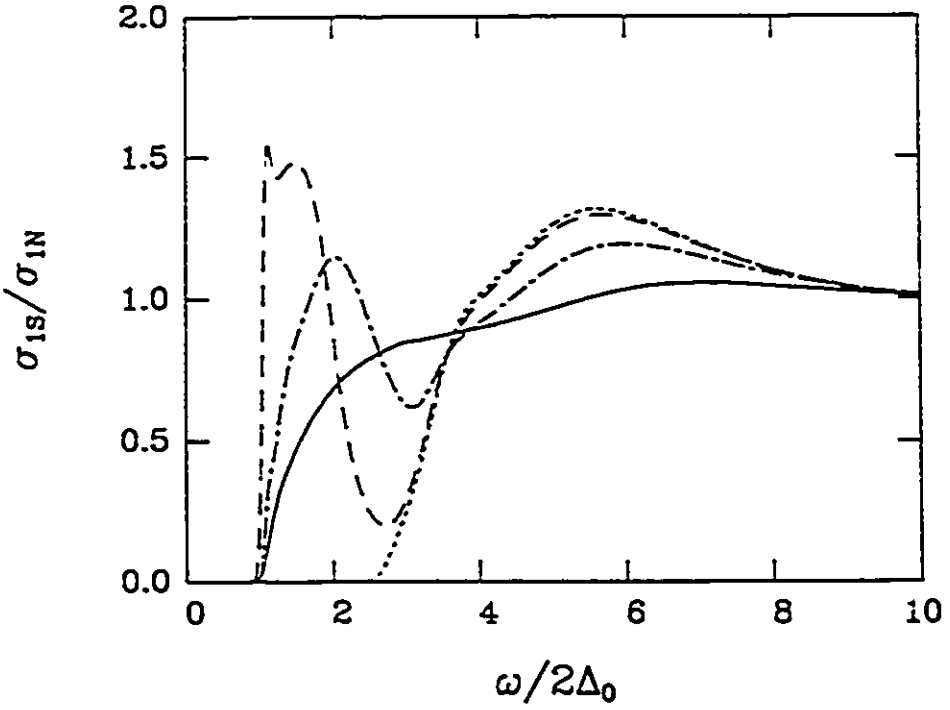


**Figure 4.5** The ratio of the real part of the conductivity in the superconducting state to that of the normal state as a function of frequency in units of twice the energy gap $\Delta_0$. Four impurity concentrations are considered as defined in the text. Except for the pure limit case the results are in excellent agreement with those of Bickers *et al.* (1990) obtained for the same phonon model and using the same Matsubara formulation of the conductivity.

curve) as considered by Bickers *et al.* (1990) are illustrated. These results are in excellent agreement with those of Bickers *et al.* (1990) except for the dotted curve. In our case, the curve begins to rise at a value of twice the gap plus the first excitation energy in the phonon spectrum. This must be so physically, since we are in the clean limit. Bickers *et al.* (1990) show only a pronounced dip at this energy and then absorption down to $2\Delta_0$ which cannot be correct and is probably an artifact of their analytic continuation technique [Vidberg and Serene (1977); Bickers (private communication)] using Padé approximants. Except for the problem just mentioned, there is excellent agreement for the other values of $t^+$. Notice that a conventional phonon model for the

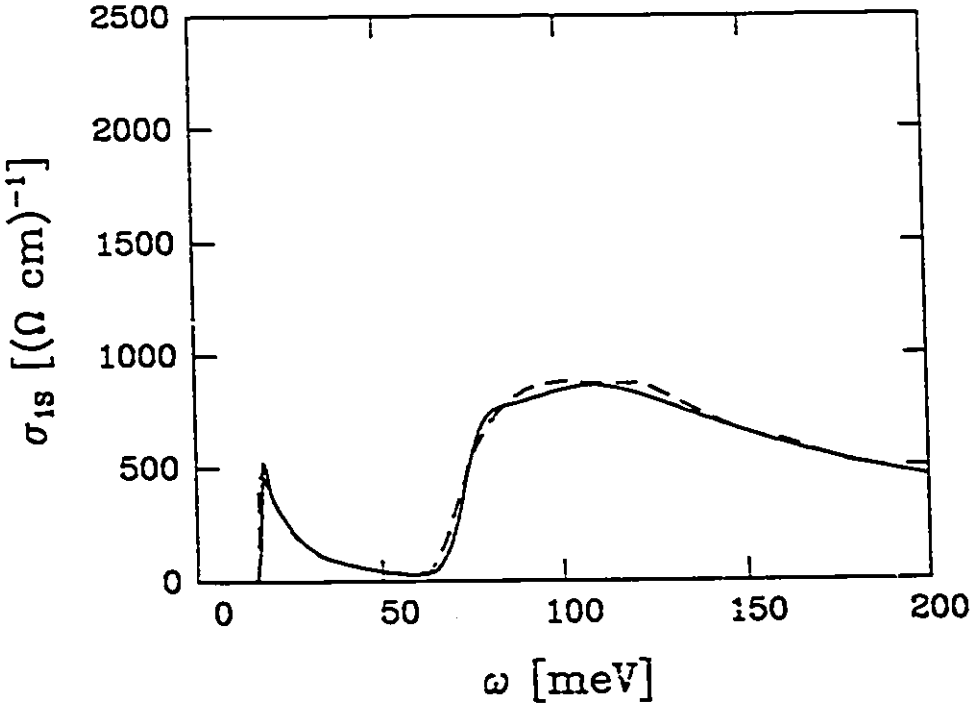


**Figure 4.6** A comparison of the real part of the conductivity in the superconducting state $\sigma_{1S}(\omega)$ in units of $(\Omega\,\mathrm{cm})^{-1}$ as a function of frequency $\omega$ in meV. The solid curve was obtained in this thesis using the imaginary frequency axis formulation for the conductivity, namely, Eqs. (4.6) to (4.8). The dashed curve shown for comparison is the result of Lee *et al.* (1989) for their model C, defined in the text, which they obtained from a real frequency axis formulation. The agreement between the two methods is very good.

fluctuations gives large Holstein structure in this ratio. This is not observed experimentally in the high $T_c$ oxides [Kamarás *et al.* (1990); Schlesinger *et al.* (1990)].

It is of importance to compare the results obtained for the conductivity $\sigma(\omega)$ using the imaginary axis formulation represented in Eqs. (4.6) to (4.8) with results of direct real axis calculations. Such a formulation, for arbitrary impurity content $t^+$, has been considered recently by Lee, Rainer and Zimmermann (1989). It involves formulas for $\sigma(\omega)$ that are mathematically very different from Eqs. (4.6) to (4.8) and makes use of the real frequency axis

version of the Eliashberg equations [Scalapino (1969)] instead of Eqs. (3.32)-(3.34). These are much more complicated to solve numerically but no analytic continuation [Vidberg and Serene (1977)] is needed to obtain $\sigma(\omega)$ so that Padé approximants can be avoided entirely. In Fig. 4.6 we compare results obtained in this work (solid line) with the real axis results of Lee, Rainer and Zimmermann (1989) (dashed line). The near exact agreement is impressive and gives us confidence to proceed and consider a marginal Fermi liquid in the next section. Note that the case considered in Fig. 4.6 is model C of Lee *et al.* (1989). In this model a delta function is used for the spectral density $\alpha^2F(\omega)$ with average phonon energy at 50 meV, the mass enhancement parameter $\lambda = 0.8$, the plasma frequency is 820 meV and the inverse scattering time is 1.05 meV with a $T_c$ value of 50K and a corresponding gap to critical temperature ratio, $2\Delta_o/k_BT_c$, of 3.9.

## 4.2 FREQUENCY-DEPENDENT OPTICAL CONDUCTIVITY AT $T = 0$

As a prescription has already been given for including the polarizability of Eq. (3.26) in the formalism for the Eliashberg equations [Kuroda and Varma (1990); Nicol *et al.* (1990, 1991); Nicol and Carbotte (1991a,b); Littlewood and Varma (1990, 1991)], we proceed to present results for our calculations of the optical conductivity in the marginal Fermi liquid model. These calculations were done by solving the imaginary axis gap equations in Eliashberg theory [Daams *et al.* (1981); Baquero *et al.* (1981); Zarate and Carbotte (1984); Daams and Carbotte (1981); Rainer and Bergmann (1974)] given in Eqs. (3.32)-(3.34) with the kernel of Eq. (3.26), to obtain the Matsubara gaps and frequencies which were then used in the Matsubara formula for

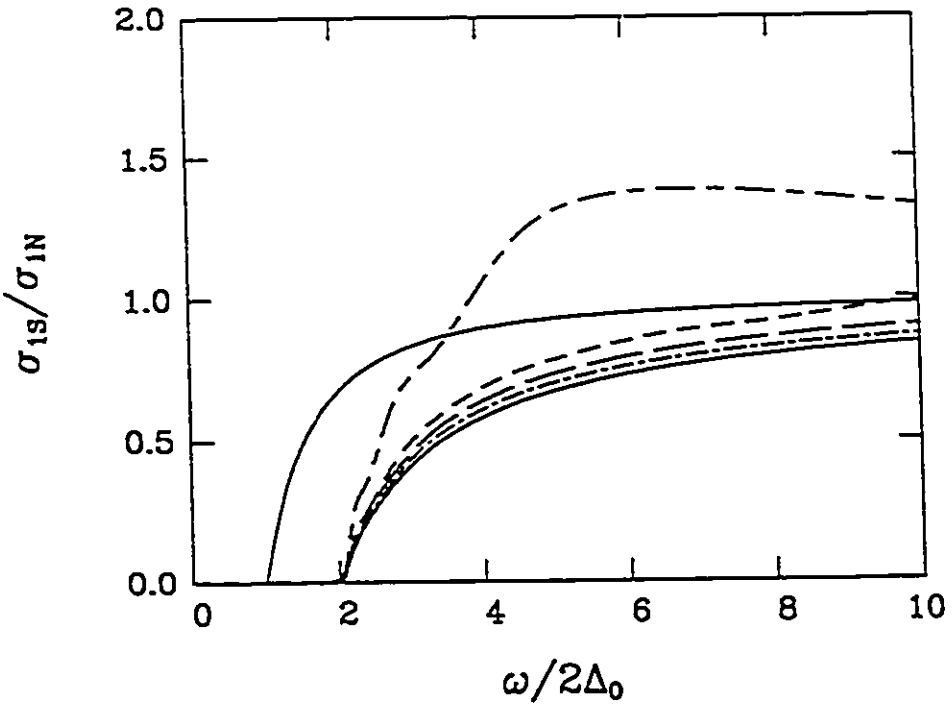


**Figure 4.7** The ratio of superconducting to normal state value of the real part of the conductivity $\sigma_1(\omega)$ as a function of frequency $\omega$ in units of twice the zero temperature energy gap $\Delta_o$. The solid curve starting at $2\Delta_o$ is the BCS dirty limit and is shown for comparison. The curves all start at $4\Delta_o$ and apply to the clean limit ($\gamma^+ = 0.0$). The solid curve is for a cutoff $\omega_c$ of 3000 meV while the others ending with the short-dashed-long-dashed curve are for $\omega_c$ = 1500 meV, 600 meV, 400 meV, and 200 meV, respectively. Only the last (short-dashed-long-dashed) curve, which corresponds to a gap ratio of $2\Delta_o/k_BT_c = 8.2$, shows significant deviations from BCS in the Holstein region.

the current-current correlation function (Eqs.(4.7)-(4.8)). An analytic continuation of the current-current correlation function was performed by Padé approximants [Vidberg and Serene (1977)] to obtain the optical conductivity given by Eq. (4.6). Our numerical calculations were performed for $T = 0.1T_c$, which is essentially $T = 0$. Similar calculations have been performed by Littlewood and Varma (1990, 1991).

In all the results to be presented in this section, the critical temperature is fixed at 100K. The two remaining parameters are the upper cutoff on

the fluctuation spectrum $\omega_c$ (Eq. (3.35)) and the relative admixture of the coupling to charge and spin ($g$). First, we present a series of results for the clean limit ($t^+ = 0$) with $g = 0.6$ as a function of cutoff $\omega_c$. These are presented in Fig. 4.7 where we have plotted the ratio of the real part of the conductivity in the superconducting state to that of the normal state $\sigma_{1S}(\omega)/\sigma_{1N}(\omega)$ as a function of frequency normalized to twice the zero temperature energy gap $\Delta_o$. Note that all the curves start at $\omega/2\Delta_o = 2$, i.e., at $4\Delta_o$, except for the BCS dirty limit case [Mattis and Bardeen (1958)] which, of course, starts at $2\Delta_o$ and is included only for comparison (solid curve starting at $2\Delta_o$). It is important to realize that the gap is to be calculated self-consistently. For a given value of $\Delta_o$ the spectrum in Eq. (3.35) becomes gapped and this effect is included by replacing the lower limit for the integral on $\omega$ in Eq. (3.35) by $2\Delta_o$ rather than zero. After each run, the lower cutoff is re-adjusted until the value of $\Delta_o$ no longer changes. The set of curves in Fig. 4.7 corresponds to a cutoff of 3000 meV (solid curve), 1000 meV (dashed-dotted curve), 600 meV (long dashed curve), 400 meV (short dashed curve), and 200 meV (long-dashed-short-dashed curve), $2\Delta_o/k_BT_c$ values of 4.3, 4.7, 5.1, 5.7, and 8.2, respectively, and $\lambda_\rho$ of 0.3, 0.6, 0.9, 1.5, and 6.4.

The observation from the figure, that, in all cases, the absorption in the clean limit starts at $4\Delta_o$ is consistent with the idea that absorption can only occur at $2\Delta_o$, the energy required to break a Cooper pair plus the lowest excitation energy for charge or spin fluctuations which also occur at $2\Delta_o$ in our model. This is reflected in the lower cutoff which we have applied self-consistently to the fluctuation spectrum. Note also that, even for a upper cutoff of 400 meV, a $\lambda_\rho = 1.54$ with corresponding value of $2\Delta_o/k_BT_c = 5.7$, the structure is small compared with its strength in a typical conventional strong

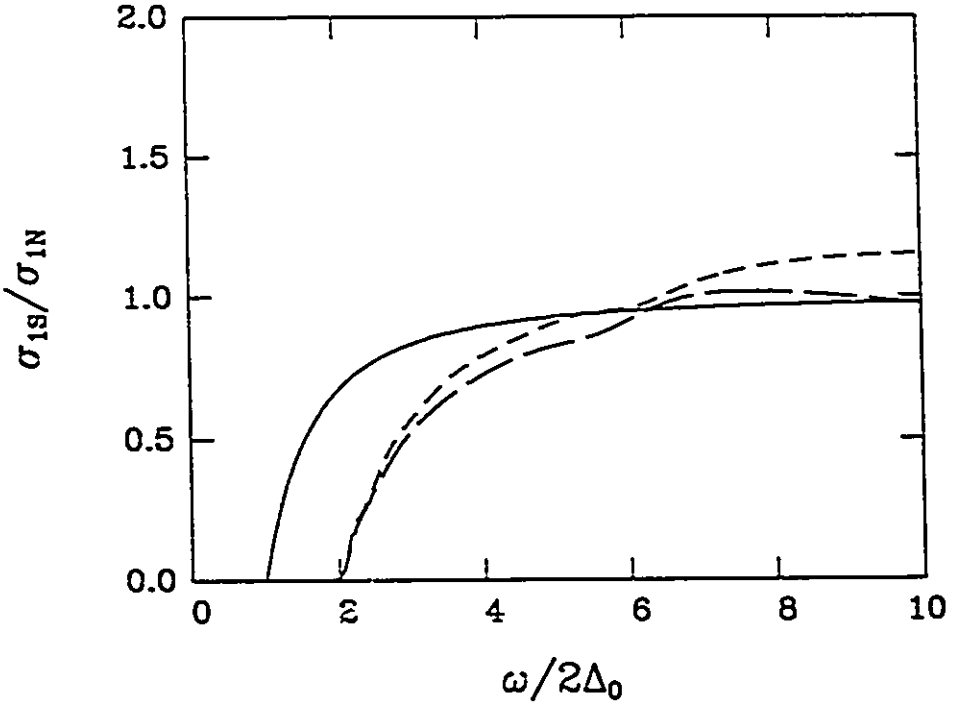


**Figure 4.8** The ratio of the real part of the conductivity in the superconducting state to its value in the normal state as a function of frequency in units of twice the zero temperature energy gap $\Delta_o$. The solid curve is for comparison and applies to the dirty BCS limit. The short dashed curve is for $2\Delta_o/k_BT_c = 8.5$, $\lambda_\rho = 5.27$, and $\omega_c = 400$ meV with $g = 0.5$ while the long dashed curve is for $2\Delta_o/k_BT_c = 4.5$, $\lambda_\rho = 1.25$, and $\omega_c = 200$ meV with $g = 0.8$. These curves start at $4\Delta_o$ since they apply to the clean limit and show relatively small structure in the Holstein region when compared with a conventional strong coupling superconductor.

coupling system such as Pb. The reason for this is that our effective spectral density $\frac{1}{\pi}\tanh(\frac{\omega}{2T})$ is spread out over a large range of frequencies up to $\omega_c$. Also the relatively large value of $2\Delta_o/k_BT_c$ which accompanies this spectrum is due, in part, to the application of a lower cutoff in (3.35) at $\omega = 2\Delta_o$. This entirely cuts out low-lying charge and spin fluctuations with the effect that $2\Delta_o$ is larger relative to $T_c$ than would be expected otherwise. The final curve (long-dashed-short-dashed) in Fig. 4.7 is included only to show that Holstein processes can indeed become more visible when $\omega_c$ is made to be very low. In this case, $\omega_c = 200$ meV and the curve behaves much more like a conventional

strong coupling system. We emphasize however that, when $\omega_c$ is not too small, the phenomenological marginal Fermi liquid model of Varma *et al.* (1989) can yield a large $2\Delta_o/k_BT_c$ without large Holstein structure. Kamarás *et al.* (1990) and Schlesinger *et al.* (1990a) have noted that this is an essential feature of the data in $YBa_2Cu_3O_{7-\delta}$ which cannot be explained within the conventional formalism. This, along with the fact that the absorption starts at $4\Delta_o$ in the clean limit, is one of our important results, and so we emphasize it further in Fig. 4.8. In this figure we show the real part of $\sigma(\omega)$ in the superconducting state normalized to the normal state, $\sigma_{1S}(\omega)/\sigma_{1N}(\omega)$, for the case $2\Delta_o/k_BT_c = 8.5$, $\lambda_\rho = 5.27$, $g = 0.5$ and $\omega_c = 400$ meV (short dashed line). It shows little structure at higher frequencies and does not deviate much in this energy range from the BCS dirty limit (solid curve). The second case, for which $2\Delta_o/k_BT_c = 4.5$, $\lambda_\rho = 1.25$, $g = 0.8$ and $\omega_c = 200$ meV (long dashed curve), shows even less deviation from the solid curve in the Holstein region although the gap ratio and $\lambda$ are not very different from the values for Pb which shows large deviations. This agrees with the experimental data [Kamarás *et al.* (1990); Schlesinger *et al.* (1990a)]. To end we note that for both curves shown in Fig. 4.8 the structure around $\omega/2\Delta_o \simeq 5$ is due to our upper cutoff of the excitation spectrum and could presumably be smoothed out if a gradual cutoff had been used.

In Figs. 4.9a and 4.9b, we study the effect of ordinary impurities (finite value of $t^+$ in Eqs. (3.32) and (3.33)) on the ratio $\sigma_{1S}(\omega)/\sigma_{1N}(\omega)$. The four impurity concentrations used are $t^+ = 0.1$ meV (short dashed curve), $t^+ = 1.0$ meV (long dashed curve), $t^+ = 10.0$ meV (short dashed-dotted curve) and $t^+ = 100.0$ meV (long dashed-dotted curve). The results are also compared with the pure case (solid curve). The most striking feature of these

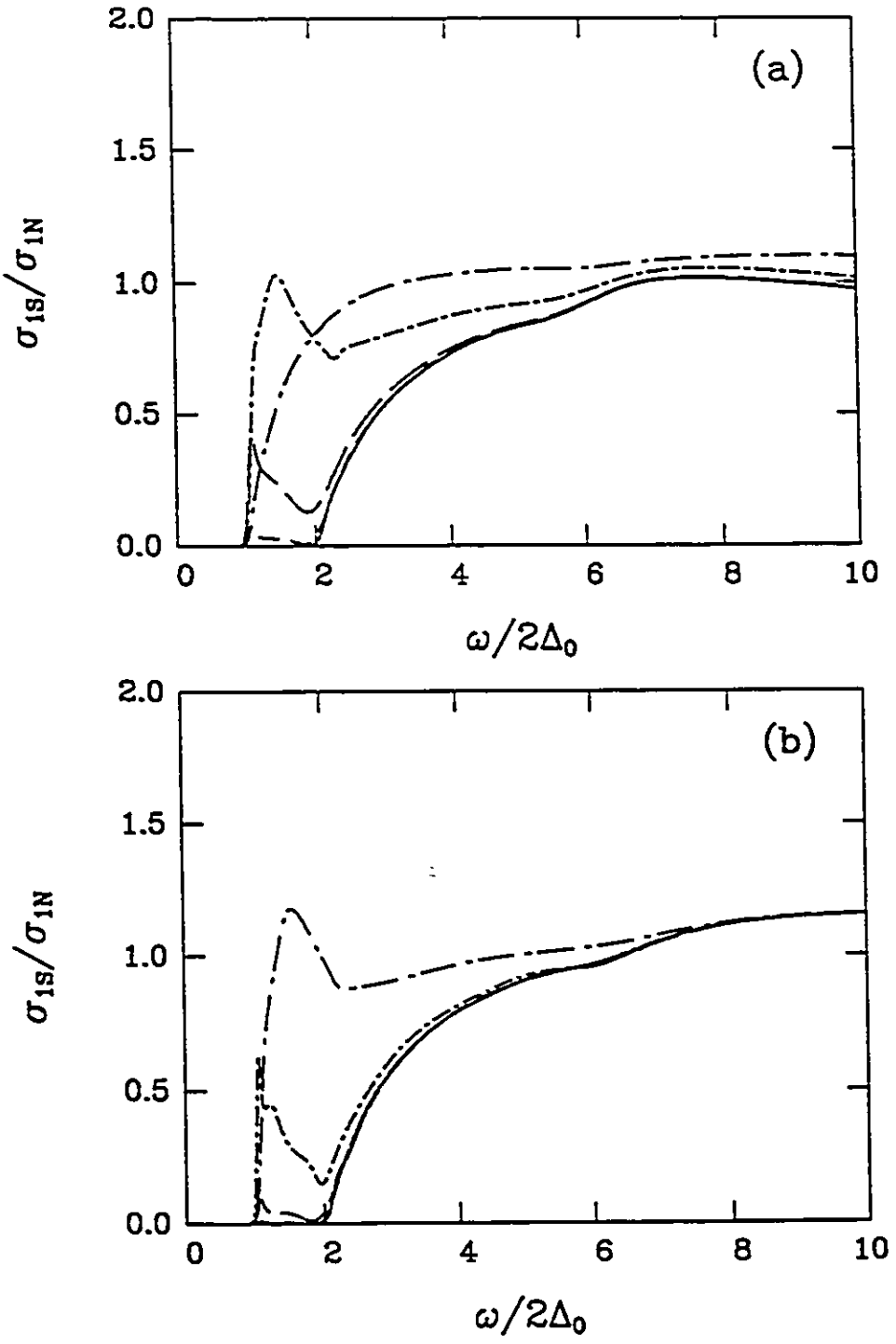


Figure 4.9 The ratio of the real part of the conductivity in the superconducting state to its value in the normal state as a function of frequency in units of twice the zero temperature energy gap $\Delta_o$. For the pure case (solid curve) the absorption starts at $4\Delta_o$ while when impurities are added the onset occurs at $2\Delta_o$ instead. Curves (a) are for the charge fluctuation model with $2\Delta_o/k_BT_c = 4.5$ while curves (b) apply to the case $2\Delta_o/k_BT_c = 8.5$ with other parameters defined in Fig. 4.8 and in the text.

results is that as soon as impurities are introduced the absorption starts at $2\Delta_o$ rather than the $4\Delta_o$ found to occur in the pure case. The momentum can now be transferred to the impurity system. Some remnant of the $4\Delta_o$ threshold does, however, remain even in the $t^+ = 10.0$ meV curve which represents a large amount of impurities but is still far from the dirty limit.

It is of interest to consider the absolute value of the conductivity $\sigma_1(\omega)$ in the frequency range above the absorption edge. To do this the plasma frequency is adjusted to correspond to a value of the dc conductivity of 20,000 $(\Omega\,\mathrm{cm})^{-1}$ at 100K in the normal state which is a typical value for experimental samples. Since $\sigma_{1N}(\omega = 0)$ varies as $1/T$ in the marginal Fermi liquid, this corresponds to a dc conductivity at 10K of 200.000 $(\Omega\,\mathrm{cm})^{-1}$. The normal state conductivity $\sigma_{1N}(\omega)$, as a function of frequency $\omega$, is shown in Figs. 4.10a and 4.10b (dashed curve) for two illustrative model sets of parameters, namely, $2\Delta_o/k_BT_c = 4.5$, $\lambda_\rho = 1.25$, $g = 0.8$ and $\omega_c = 200$ meV (Fig. 4.10a) and $2\Delta_o/k_BT_c = 5.1$, $\lambda_\rho = 0.9$, $g = 0.6$ and $\omega_c = 600$ meV (Fig. 4.10b). In the first case, the width at half maximum comes out to be $1.27k_BT$ and in the second it is $1.0k_BT$ which falls well within the range of experimental values [Kamarás *et al.* (1990)]. Also shown for comparison are the corresponding values for $\sigma_1(\omega)$ in the superconducting state represented by the solid lines. We see that in the region around 2000 $\mathrm{cm}^{-1}$ the conductivity in one case is slightly above 1000 $(\Omega\,\mathrm{cm})^{-1}$ and, in the other, somewhat less than 500 $(\Omega\,\mathrm{cm})^{-1}$. These values are smaller, but of the same order of magnitude, as measured experimentally. Parameters could be varied to obtain better agreement with experiment if one wished. We do not think this to be appropriate at this time and in any case this is not our primary aim here. We believe that before a definitive comparison with experiment can be made it is important

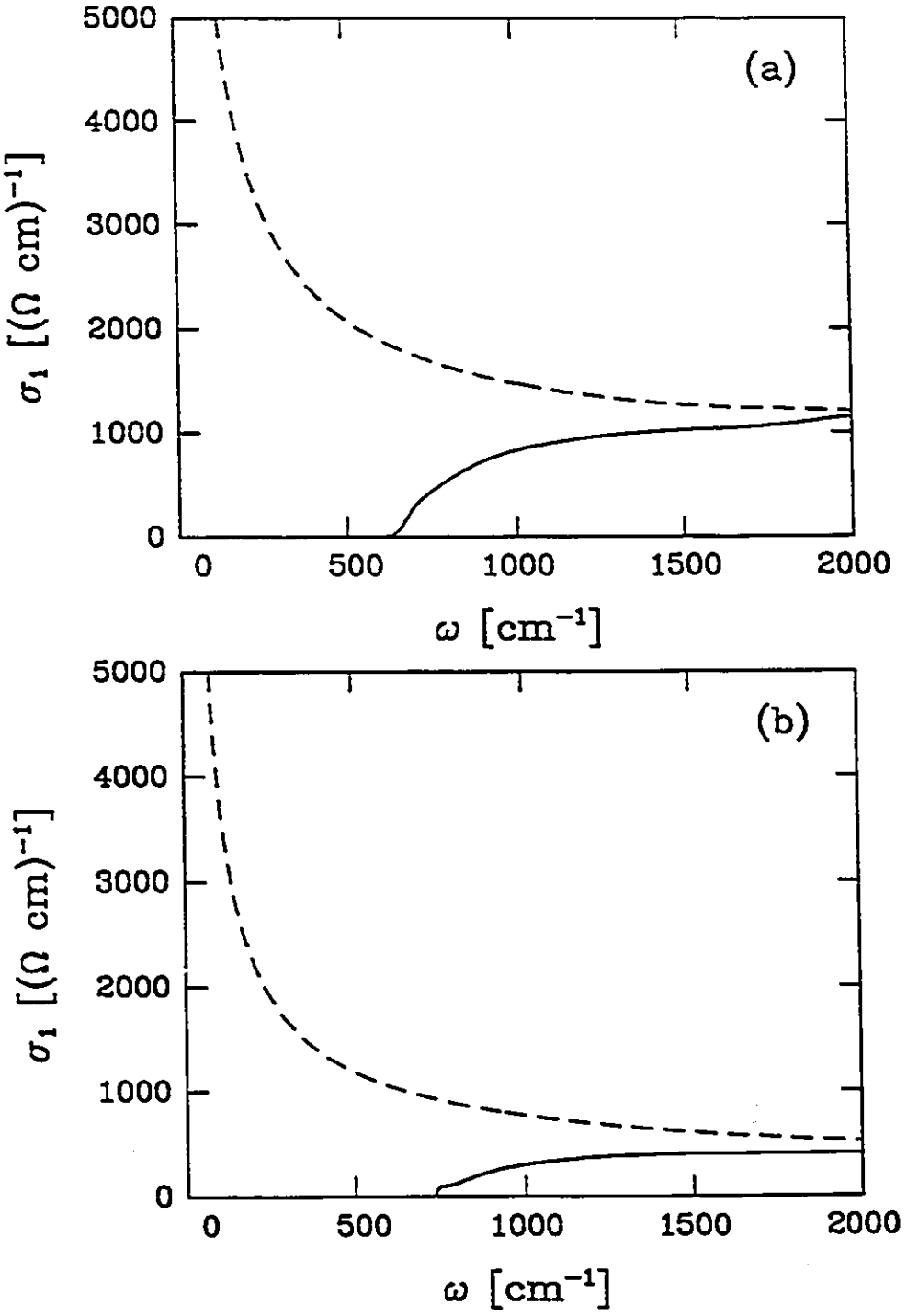


**Figure 4.10** The normal state (dashed curve) and superconducting state (solid curve) conductivity at 10K for two sets of model parameters. The top frame is for $2\Delta_o/k_BT_c = 4.5$, $\lambda_\rho = 1.25$, $g = 0.8$, and $\omega_c = 200$ meV. The lower frame is for $2\Delta_o/k_BT_c = 5.1$, $\lambda_\rho = 0.9$, $g = 0.6$, and $\omega_c = 600$ meV. The plasma frequency has been chosen in both cases to obtain a value of $\sigma_{1,N}(\omega = 0) = 20,000(\Omega\,\mathrm{cm})^{-1}$.

to calculate the complete temperature dependence of the conductivity in the superconducting state from $T_c$ down to low $T$. In this way we could trace the opening up of the gap. This has been done and is presented in Section 4.4. This requires real frequency axis programs because Padé approximants are not reliable at high $T$ near $T_c$. Unfortunately, problems still remain in the interpretation of the experimental conductivity data in the infrared region, precluding any useful comparison between theory and experiment at the present time.

Nevertheless, we can make two statements about experiments. The amount of absorption calculated in the mid-infrared region for the marginal Fermi liquid model is of the same magnitude but smaller than the amount observed and therefore leaves some room for extra absorption processes not accounted for in the model. If this is the case, it might be very hard to see a clear gap in such experiments particularly if one is in the clean limit. Undoubtedly some residual resistivity needs to be added according to sample quality but the amount is not unambiguously known at this point. A very nice feature of the theory is that the dc conductivity scales like $1/T$ with coefficients in front of this variation dependent on the single remaining parameter of the model for a given cutoff.

To conclude, we have studied the behaviour of $\sigma(\omega)$ for the marginal Fermi liquid model and found several important results. First, in the pure limit, absorption can start only at $4\Delta_o$ which is the energy required to form a quasiparticle pair plus the lowest energy in the fluctuation spectrum. When impurities are added, momentum can go into the impurity system, and the absorption starts at $2\Delta_o$. For low impurity concentrations a remnant of the $4\Delta_o$ threshold remains prominent but eventually disappears when $t^+$ is large

enough. Compared with a conventional electron-phonon model, the marginal Fermi liquid model can produce relatively large values for the gap to critical temperature ratio with small associated Holstein structure as required in the experimental data [Kamarás *et al.* (1990); Schlesinger *et al.* (1990)]. The reason for this is two-fold. First, the corresponding electron-boson spectral density is spread out over a large frequency range when the value of the cutoff in the fluctuation spectrum ($\omega_c$) is large. Secondly, the fluctuations become gapped at low frequencies quenching both spin and charge degrees of freedom in this region. This has the net effect of increasing $\Delta_0$ over the value that would be expected if no low energy cutoff was applied.

Finally, when the absolute value of the conductivity is fixed to the measured normal state value at $\omega = 0$ (20,000 $(\Omega\,\mathrm{cm})^{-1}$ typically), with the width at half maximum of $\sigma_{1,N}(\omega)$ of the observed order, 1.0 to 1.5 $k_B T$, its weight in the mid-infrared region is of the same order of magnitude as is observed although, in all the cases considered, it is smaller. This leaves room for some additional absorption process in this region which would add to the direct electronic contribution calculated in this thesis. While we have not attempted a close comparison with experiment, the model does reproduce many of the observed features.

## 4.3 THE QUASIPARTICLE DAMPING RATE

In this section, we present a calculation of the quasiparticle damping rate in both the normal and superconducting state for the phenomenological marginal Fermi liquid model. This quantity shows novel behaviour in this theory and several experiments are presently under way to measure its temperature dependence below $T_c$.

The quasiparticle scattering rate is a fundamental element underlying several properties, such as the optical conductivity. It is given in terms of the imaginary part of the electron self-energy due to fluctuations, such as phonons in the conventional theory. More exactly, the poles of the single particle Green's function give the quasiparticle energy (real part) and the lifetime (imaginary part) [see Section 3.1]. In the superconducting state the quasiparticle damping $\Gamma(\omega,T)$, related to the quasiparticle lifetime $\tau(\omega,T)$ by $\Gamma = 1/(2\tau)$, (note that we use a different sign convention for $\Gamma$ here, than in Section 3.1) is given as [Scalapino (1969); Kaplan *et al.* (1976)]

$$\Gamma(\omega,T) = \frac{Z_2[\omega^2 - \Delta_1^2] - \Delta_1\Delta_2 Z_1}{\omega} \quad . \tag{4.10}$$

Here, $\Delta(\omega) = \Delta_1(\omega) + i\Delta_2(\omega)$ is the complex and frequency-dependent gap function in Eliashberg theory [Scalapino (1969)] and $Z(\omega) = Z_1(\omega) + iZ_2(\omega)$ is the corresponding renormalization function. In the normal state $\Delta = 0$ and we obtain

$$\Gamma(\omega,T) = \omega Z_2 \quad . \tag{4.11}$$

In various limits of zero-temperature or zero frequency, we obtain the well-known limits, for the normal state [Grimvall (1981)],

$$\Gamma(\omega,T=0) = \pi\hbar \int_0^{\omega} \alpha^2F(\omega')d\omega' \tag{4.12}$$

and

$$\Gamma(\omega=0,T) = 2\pi\hbar \int_0^{\omega_{max}} \alpha^2F(\omega')[f(\omega') + n(\omega')]d\omega' \quad , \tag{4.13}$$

where $\alpha^2F(\omega)$ is the electron-phonon spectral density function of Eliashberg theory, $f(\omega)$ and $n(\omega)$ are the Fermi and Bose factors, respectively, and $\omega_{max}$ is the upper frequency in the electron-phonon spectral function.

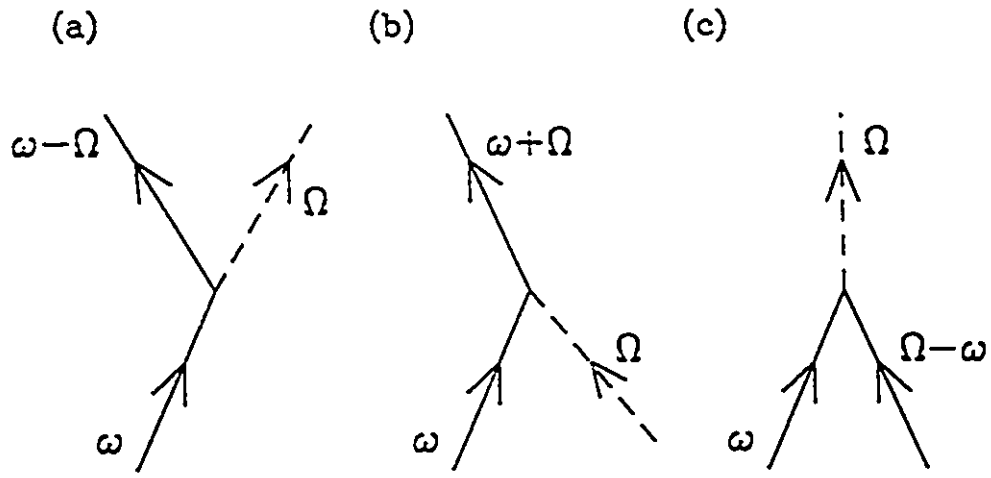


**Figure 4.11** The three scattering processes contributing to the damping of a quasiparticle of frequency $\omega$, representing the three terms in Eq. (4.14), respectively: (a) scattering from $\omega$ to $\omega-\Omega$ (solid line) with the emission of a fluctuation of frequency $\Omega$ (dashed line), (b)scattering from $\omega$ to $\omega+\Omega$ with the absorption of a fluctuation of frequency $\Omega$, and (c) recombination of two quasiparticles of frequency $\omega$ and $\Omega-\omega$ with the emission of a fluctuation of frequency $\Omega$.

A low frequency formula for Eq. (4.10) has been given by Kaplan *et al.* (1976), who also give a very extensive work on quasiparticle lifetimes in conventional superconductors. For frequencies that are small with respect to typical phonon frequencies, they replace the frequency-dependent $\Delta_1(\omega)$ by the temperature dependent energy gap $\Delta(T)$ and write:

$$\Gamma(\omega,T)=\frac{\pi}{[1-f(\omega)]}$$
$$\left[\int_0^{\omega-\Delta} d\Omega\,\alpha^2F(\Omega)N(\omega-\Omega)\left(1-\frac{\Delta^2}{\omega(\omega-\Omega)}\right)[n(\Omega)+1][1-f(\omega-\Omega)]\right.$$
$$+\int_0^{\infty} d\Omega\,\alpha^2F(\Omega)N(\omega+\Omega)\left(1-\frac{\Delta^2}{\omega(\omega+\Omega)}\right)n(\Omega)[1-f(\omega+\Omega)]$$
$$\left.+\int_{\omega+\Delta}^{\infty} d\Omega\,\alpha^2F(\Omega)N(\Omega-\omega)\left(1+\frac{\Delta^2}{\omega(\Omega-\omega)}\right)[n(\Omega)+1]f(\Omega-\omega)\right]. \quad (4.14)$$

where

$$N(\omega) = Re\left(\frac{\omega}{\sqrt{\omega^2 - \Delta^2}}\right) \quad . \tag{4.15}$$

The beauty of this formula is that one can physically see the three different scattering processes involved. The first term represents the scattering of a quasiparticle from state $\omega$ to $\omega - \Omega$ with the emission of a phonon. The second process is the scattering of the quasiparticle from $\omega$ to $\omega + \Omega$ with the absorption of a phonon. And the third process corresponds to recombination of two quasiparticles of $\omega$ and $\Omega - \omega$ with the emission of a phonon. These processes are illustrated in Fig. 4.11. All these processes are weighted by: the available density of states for the other quasiparticle state involved, the Fermi ($f(\omega)$) and Bose ($n(\Omega)$) factors which give the population of available states according to temperature, the electron-phonon spectral density giving the available phonon frequencies and, finally, very important coherence factors that cause enhancement or de-enhancement of processes depending on how the interaction affects time-reversal symmetry [Schrieffer (1964)]. The above formula is good for low frequencies where Kaplan *et al.* (1976) investigated a simple Debye model and the realistic spectra of Pb and Hg.

We have calculated the quasiparticle damping in the marginal Fermi liquid model by first iterating the imaginary axis gap equations, given by Eqs. (3.32)-(3.35), for the Matsubara gaps and renormalized frequencies. We then use the analytical continuation of Marsiglio *et al.* (1988) to obtain the real frequency complex gap function and renormalized energies, $\tilde{\Delta}(\epsilon)$ and $\tilde{\epsilon}(\epsilon) = \epsilon Z(\epsilon)$, respectively, given by the self-consistent solution of:

$$\tilde{\epsilon}(\epsilon) = \epsilon + i\pi T \sum_{m=0}^{\infty} \frac{\tilde{\omega}_m}{\sqrt{\tilde{\omega}_m^2 + \tilde{\Delta}_m^2}} [\lambda^+(\epsilon - i\omega_m) - \lambda^+(\epsilon + i\omega_m)]$$

$$+ i\pi(\lambda_\rho + \lambda_\sigma)\int_{-\infty}^{+\infty} dz \frac{\tilde{z}(\epsilon - z)}{\sqrt{\tilde{z}^2(\epsilon - z) - \tilde{\Delta}^2(\epsilon - z)}}\alpha^2F(z)[N(z) + f(z - \epsilon)]. \tag{4.16}$$

with $\alpha^2F(-z) = -\alpha^2F(z)$, and

$$\tilde{\Delta}(\epsilon) = i\pi T\sum_{m=0}^{\infty}\frac{\tilde{\Delta}_m}{\sqrt{\tilde{\omega}_m^2 + \tilde{\Delta}_m^2}}[\lambda^-(\epsilon - i\omega_m) + \lambda^-(\epsilon + i\omega_m) - 2\mu^*]$$

$$+ i\pi(\lambda_\rho - \lambda_\sigma)\int_{-\infty}^{+\infty} dz \frac{\tilde{\Delta}(\epsilon - z)}{\sqrt{\tilde{z}^2(\epsilon - z) - \tilde{\Delta}^2(\epsilon - z)}}\alpha^2F(z)[N(z) + f(z - \epsilon)]. \tag{4.17}$$

where

$$\lambda^{\pm}(\epsilon) = -(\lambda_\rho \pm \lambda_\sigma)\int_{-\infty}^{+\infty}\frac{d\Omega\alpha^2F(\Omega)}{\epsilon - \Omega + i0^+} \quad . \tag{4.18}$$

with $\alpha^2F(\omega)$ defined in Eq. (3.35) for $2\Delta(T) < \omega < \omega_c$. In these equations, $N(z)$ is the boson occupation $N(z) = 1/(e^{\beta z} - 1)$ and $f(z)$ the fermion occupation $f(z) = 1/(e^{\beta z} + 1)$, with $\beta = \frac{1}{k_BT}$ and $k_B$ is the Boltzmann constant.

The damping rate was calculated from Eq. (4.10). In addition, as a confirmation of our procedure, we also used the low frequency approximate formula of Kaplan *et al.* (1976) to check our full numerical solutions. Excellent agreement between both methods was obtained, except of course, at very high frequencies where the approximations behind Eq. (4.14) break down.

Our results are shown in Fig. 4.12. For comparison we have also calculated the scattering rate for the conventional superconductor Pb and this is presented in Fig. 4.13. The difference in behaviour is quite striking. For the marginal Fermi liquid model we have used the following parameters: $\omega_c = 200$ meV, $g = (\lambda_\rho - \lambda_\sigma)/(\lambda_\rho + \lambda_\sigma) = 0.8$, $T_c = 100$ K, $2\Delta_o/k_BT_c = 4.55$, $\Delta_o = 19.6$ meV, $\lambda \sim 1.3$, and $\mu^* = 0$. [Note that we present the unrenormalized

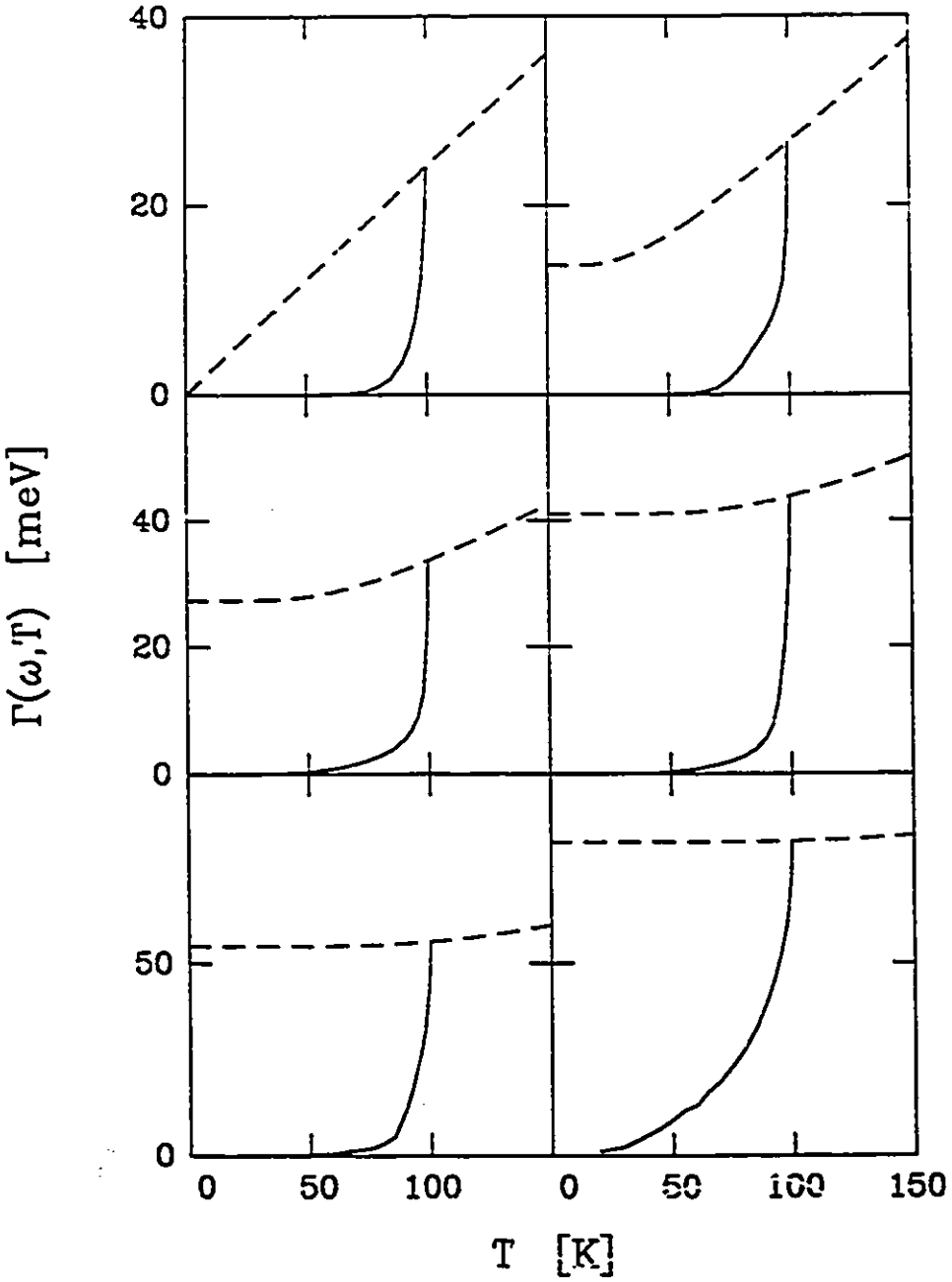


**Figure 4.12** The quasiparticle damping rate $\Gamma(\omega,T)$ in the marginal Fermi liquid model for several frequencies: $\omega = 0$ (top left frame), $\omega = 0.5\Delta_o$ (top right), $\omega = \Delta_o$ (center left), $\omega = 1.5\Delta_o$ (center right), $\omega = 2\Delta_o$ (bottom left), and $\omega = 3\Delta_o$ (bottom right), where $\Delta_o = 19.6$ meV. The dashed curve is the normal state and the solid curve is the superconducting state. The normal state exhibits linear $T$ and $\omega$ behaviour and the superconducting state exhibits a sharp drop in the scattering rate below $T_c$ due to the gap developing in the fluctuation spectrum.

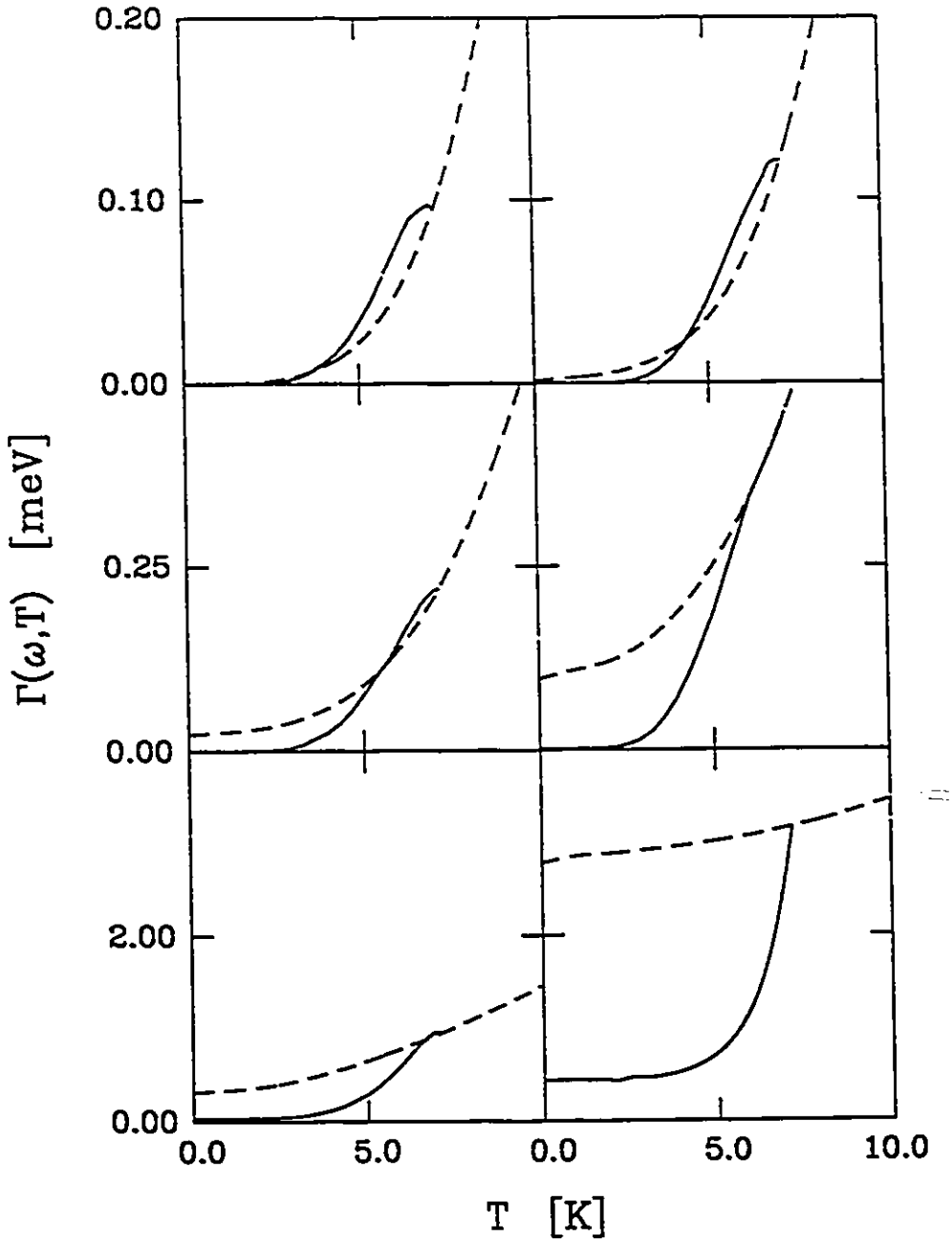


**Figure 4.13** The quasiparticle damping rate $\Gamma(\omega,T)$ for Pb for several frequencies: $\omega = 0$ (top left frame), $\omega = 0.5\Delta_o$ (top right), $\omega = \Delta_o$ (center left), $\omega = 1.5\Delta_o$ (center right), $\omega = 2\Delta_o$ (bottom left), and $\omega = 3\Delta_o$ (bottom right), where $\Delta_o = 1.39$ meV. The dashed curve is the normal state and the solid curve is the superconducting state. The normal state exhibits the characteristic $T^3$ and $\omega^3$ dependence. The superconducting state drops to zero quickly due to the energy gap. However, a coherence peak remains at low frequencies due to quasiparticle recombination.

scattering rate: some authors prefer to present the renormalized quantity $\Gamma/Z_1(0) \approx \Gamma/(1+\lambda)$.] The characteristics of Pb are: $T_c = 7.19$ K, $2\Delta_o/k_BT_c = 4.49$, $\Delta_o = 1.39$ meV, $\lambda = 1.55$, and $\mu^*(6\omega_{max}) = 0.139$. In the figures, there are six frequencies plotted, $\omega = 0$ (top left frame), $\omega = 0.5\Delta_o$ (top right frame), $\omega = \Delta_o$ (center left frame), $\omega = 1.5\Delta_o$ (center right frame), $\omega = 2\Delta_o$ (bottom left frame) and $\omega = 3\Delta_o$ (bottom right frame).

Typically for Pb (Fig. 4.13), the normal state damping rate decays as $T^3$ at $\omega = 0$ as the phonon scattering contribution freezes out at low temperatures. Above approximately $T = \omega_D/10$ the scattering rate takes on a linear dependence in temperature which occurs well above $T_c$. The frequency dependence at zero temperature increases as $\omega^3$. For low frequencies in the superconducting state near $T_c$ there is a coherence peak due to the quasiparticle recombination process being very strong (the temperature is large, the gap is very small and a large number of quasiparticles are excited above the gap). At higher frequencies the coherence peak eventually disappears as the process moves out of the peak in the density of states. At zero temperature and finite frequency there is scattering due to the process of scattering with phonon emission.

In contrast, for the marginal Fermi liquid of Fig. 4.12, the normal state displays a linear $T$ dependence and at finite frequency, a linear $\omega$ dependence *i.e.*, $\Gamma_N = a\omega + bT$. However, the superconducting state displays a sharp drop below $T_c$ with a small tail. This behaviour is due to the fluctuation spectrum, the effective "$\alpha^2F(\omega)$" in Eq. (3.35). In the superconducting state this spectrum is gapped by $2\Delta$ and hence no fluctuations can be absorbed or emitted until the frequency $\omega$ reaches $2\Delta$ as it does in the bottom left frame of Fig. 4.12 and then finally these processes requiring the availability

of fluctuations can begin to occur and in Fig. 4.12 bottom right frame where $\omega = 3\Delta_o$ we see a similar scattering rate as for Pb at $\omega = 3\Delta_o$. The small tail below $T_c$ that occurs in all frames of Fig. 4.12 is due to the gap being nearly zero at $T_c$ and hence some population of the quasiparticle states can occur. In our work we have used a BCS temperature dependence for the gap $\Delta(T)$ for numerical convenience. Typically one solves for the gap self-consistently (which we do at low $T$) but this does not deviate much from the BCS result. A more constant temperature dependence of the gap merely reduces the tail below $T_c$ further. In our work we have used a sharp cutoff at $2\Delta(T)$ in the fluctuation spectrum as there is no microscopic theory to explain exactly how the gap develops. As this is adhoc, the actual shape of the tail near $T_c$ should not be taken as significant at this point, but rather the quick drop in the scattering rate below $T_c$ to zero is the significant result.

In conclusion, we have calculated the quasiparticle damping rate below $T_c$ in both the normal and superconducting state for the marginal Fermi liquid model and have compared it with similar calculations for Pb. We find striking differences. The most notable prediction of the marginal Fermi liquid theory is that the scattering rate should drop precipitously below $T_c$ in the superconducting state. Experiments capable of measuring the frequency dependence, as well as, the temperature dependence of the scattering rate in the superconducting state would be ideal for testing this result. If over a large range of frequencies, the scattering rate dropped sharply below $T_c$ to zero, then this would support this theory. In addition if finally at some frequency, the scattering rate suddenly smeared from a sharp drop, this may be a measure of $2\Delta_o$ and hence a measure of the energy gap in these materials. We believe this to be a definite prediction of marginal Fermi liquid theory

and would encourage experimental investigations of this property. It should be noted that Tanner *et al.* (1991) have recently extracted the scattering rate from their optical data and observe such a drop in the rate just below $T_c$. Impressive additional confirmation of these results has now been obtained by Bonn *et al.* (1991) and is shown in Fig. 4.18 of the next section.

## 4.4 THE TEMPERATURE DEPENDENCE OF THE LOW FREQUENCY CONDUCTIVITY

Within BCS theory, the temperature-dependent low frequency conductivity has type II coherence factors as does the NMR relaxation rate and hence would normally exhibit a coherence peak just below $T_c$, where the superconducting state conductivity is enhanced above the normal state conductivity [Schrieffer (1964)]. Recent work by Akis and Carbotte (1991b) and Marsiglio (1991) has demonstrated that within the strong-coupling theory of superconductivity, the coherence factor can be suppressed: however, normal impurity scattering is shown to enhance the peak. In addition, Akis and Carbotte (1991a) and Allen and Rainer (1991) have shown that a suppression of the coherence peak in the NMR relaxation rate also occurs with increased strong coupling and that the formulae for the NMR and the conductivity are essentially the same, such that the suppression of the peak in one quantity would be accompanied by the suppression of the peak in the other quantity. The observation of the absence of a coherence peak in the NMR experiments [Barrett *et al.* (1990); Takigawa *et al.* (1989)] on the high $T_c$ superconductors can be taken as evidence for strong-coupling effects [Akis and Carbotte (1991a); Allen and Rainer (1991)], anisotropy [Statt (1990)], etc., but the

essential point is that the coherence effects have been suppressed in some manner and hence are likewise suppressed in the conductivity.

In this section, we present results of calculations of the low frequency conductivity in the phenomenological marginal Fermi liquid theory of Varma *et al.* (1989) and find a "coherence-type" peak that is not due to coherence effects but due to the quasiparticle scattering rate. Similar results have been obtained by P.B. Littlewood [Nuss *et al.* (1991)] who has also calculated the NMR relaxation rate in this model and finds an absence of a peak in this latter quantity [Nuss *et al.* (1990); Littlewood and Varma (1991)].

To calculate the optical conductivity, we first solve for the imaginary axis gaps and frequencies and then use the analytic continuation of Marsiglio *et al.* (1988) to obtain the real frequency complex gap function and renormalized energies, $\tilde{\Delta}(\epsilon)$ and $\tilde{\epsilon}(\epsilon) = \epsilon Z(\epsilon)$, respectively, given Eqs. (4.16)-(4.18). We then use these in the formula for the conductivity derived by Lee *et al.* (1989) which is given as:

$$\sigma(\omega,T) = \frac{N(0)e^2v_F^2}{4\pi^2\omega}\int_{-\infty}^{+\infty} d\epsilon \Bigg[ \tanh\left(\frac{\epsilon}{2k_BT}\right) M(\epsilon,\omega)\Big\{g(\epsilon)g(\epsilon+\omega)+h(\epsilon)h(\epsilon+\omega)+\pi^2\Big\}$$

$$-\tanh\left(\frac{\epsilon+\omega}{2k_BT}\right) M^*(\epsilon,\omega)\Big\{g^*(\epsilon)g^*(\epsilon+\omega)+h^*(\epsilon)h^*(\epsilon+\omega)+\pi^2\Big\}$$

$$+\Big\{\tanh\left(\frac{\epsilon+\omega}{2k_BT}\right)-\tanh\left(\frac{\epsilon}{2k_BT}\right)\Big\} L(\epsilon,\omega)\Big\{g^*(\epsilon)g(\epsilon+\omega)+h^*(\epsilon)h(\epsilon+\omega)+\pi^2\Big\}\Bigg], \tag{4.19}$$

where

$$g(\epsilon) = \frac{-\pi\tilde{\epsilon}(\epsilon)}{\sqrt{\tilde{\Delta}^2(\epsilon)-\tilde{\epsilon}^2(\epsilon)}}\quad , \tag{4.20}$$

$$h(\epsilon) = \frac{-\pi\tilde{\Delta}(\epsilon)}{\sqrt{\tilde{\Delta}^2(\epsilon)-\tilde{\epsilon}^2(\epsilon)}}\quad , \tag{4.21}$$

$$M(\epsilon,\omega) = \left\{ \sqrt{\tilde{\Delta}^2(\epsilon+\omega) - \tilde{\epsilon}^2(\epsilon+\omega)} + \sqrt{\tilde{\Delta}^2(\epsilon) - \tilde{\epsilon}^2(\epsilon)} + \frac{1}{\tau} \right\}^{-1} , \qquad (4.22)$$

and

$$L(\epsilon,\omega) = \left\{ \sqrt{\tilde{\Delta}^2(\epsilon+\omega) - \tilde{\epsilon}^2(\epsilon+\omega)} + \sqrt{\tilde{\Delta}^{*2}(\epsilon) - \tilde{\epsilon}^{*2}(\epsilon)} + \frac{1}{\tau} \right\}^{-1} . \qquad (4.23)$$

In Eq. (4.19) $N(0)$ is the single spin electronic density of states at the Fermi surface, $e$ is the electron charge and $v_F$ is the Fermi velocity. The normal impurity scattering time $\tau$ enters Eqs. (4.22) and (4.23). We quote values in terms of $t^+$ where $t^+ = 1/(2\pi\tau)$. The normal state conductivity is obtained by setting the gaps to zero in the above procedure.

In Fig. 4.14, we show the frequency-dependent conductivity for several reduced temperatures $t = T/T_c$: $t = 0.1$ (solid curve), $t = 0.6$ (— - —), $t = 0.7$ (— · —), $t = 0.8$ (- · - ·), $t = 0.9$ (– – –), $t = 0.95$ (— — —), and $t = 1.1$ (- - - -). The marginal Fermi liquid parameters we have used are: $\omega_c = 200$ meV, $g = (\lambda_\rho - \lambda_\sigma)/(\lambda_\rho + \lambda_\sigma) = 0.8$, and $T_c = 100$ K, with $\mu^*$ taken to be zero. This results in $2\Delta_o/k_BT_c = 4.55$, $\Delta_o = 19.6$ meV, and $\lambda \sim 1.3$, where $\lambda$ is taken from $Z_1(\omega = 0) = 1 + \lambda$. In the top frame the conductivity is shown in the clean limit, (*i.e.*, $t^+ = 0$). Notice, at zero temperature, no absorption occurs until $\omega = 4\Delta_0$. As discussed in Section 4.2, this corresponds to $2\Delta_0$ of energy to create an electron-hole pair plus another $2\Delta_0$ of energy to reach the first frequency in the fluctuation spectrum (the creation of another pair), the requirement for conserving both energy and momentum. The $4\Delta_0$ result has been obtained previously by ourselves and other authors [Nicol *et al.* (1991); Littlewood and Varma (1990,1991); Orenstein *et al.* (1990)]. In the bottom frame of Fig. 4.14, $t^+ = 1.0$ meV. While a dip remains at $4\Delta_0$ at low temperatures, impurity-assisted absorption occurs at $2\Delta_0$. Notice that

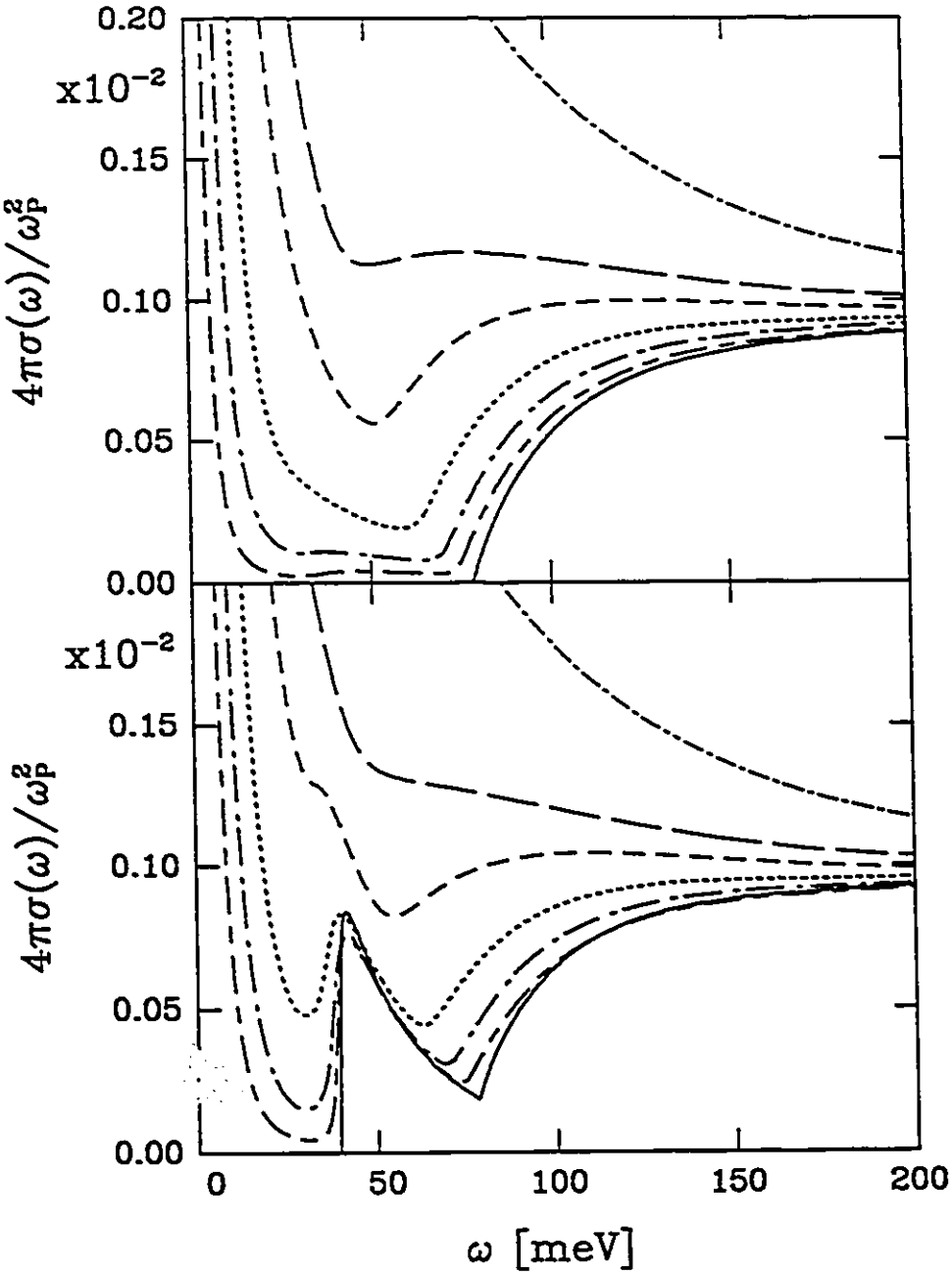


Figure 4.14 The real part of the frequency-dependent conductivity $\sigma(\omega)$ versus frequency $\omega$ for several temperatures below $T_c$. In terms of reduced temperatures $t = T/T_c$ the curves are: $t = 0.1$ (solid curve), $t = 0.6$ (— - —), $t = 0.7$ (— - —), $t = 0.8$ (- - - -), $t = 0.9$ (– – –), $t = 0.95$ (— — —), and $t = 1.1$ (- - - -). The upper frame corresponds to the clean limit (*i.e.*, $t^+ = 0$) and the lower frame corresponds to $t^+ = 1$ meV. The zero-temperature gap $\Delta_o$ is 19.6 meV.

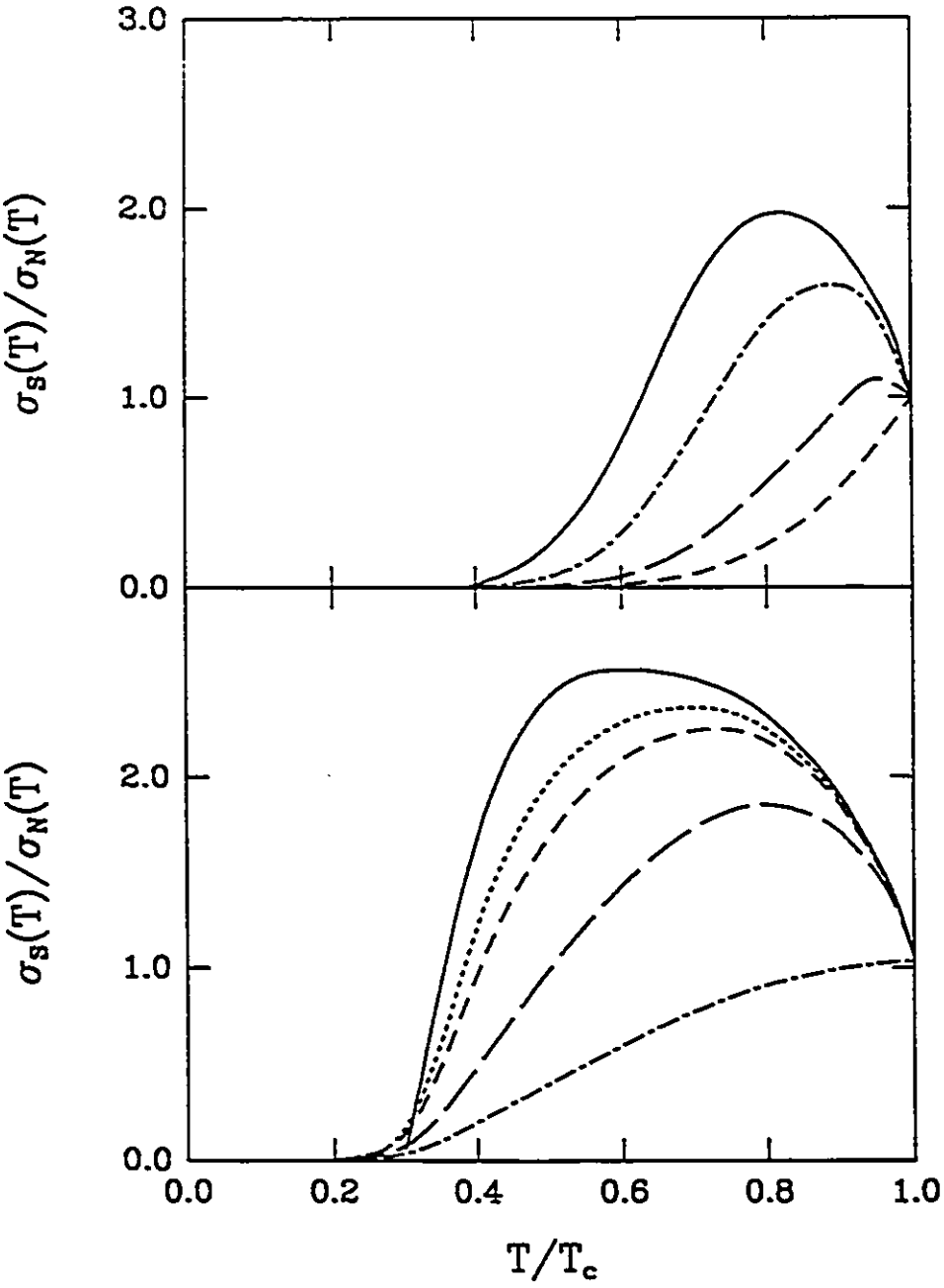


**Figure 4.15** The low-frequency conductivity in the superconducting state normalized by the normal state as a function of temperature. In the upper frame, curves are for the clean limit ($t^+ = 0$) and are drawn for several frequencies: $\omega = 1$ meV (solid curve), $\omega = 2$ meV (- — -), $\omega = 5$ meV (— — —), and $\omega = 10$ meV (– – –). The lower frame shows the effect of normal impurity scattering suppressing the peak. These curves are for $\omega = 0.05$ meV and $t^+ = 0$ meV (solid curve), $t^+ = 0.1$ meV (- - - -), $t^+ = 0.2$ meV (– – –), $t^+ = 1$ (— — —), and $t^+ = 100$ meV (- — - —).

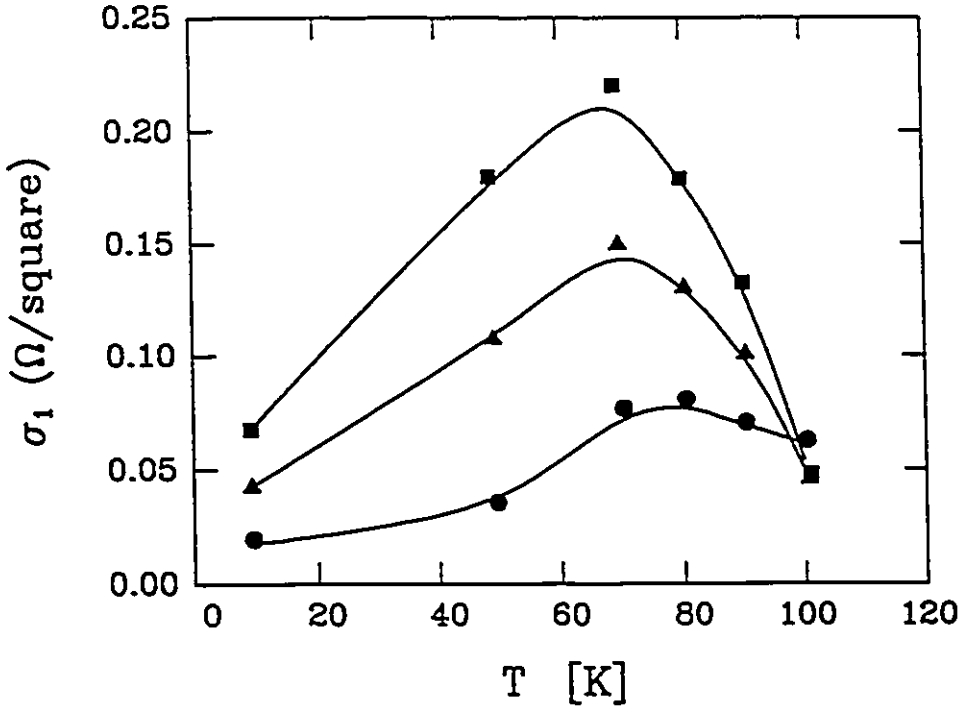


**Figure 4.16** Optical conductivity data of Nuss *et al.* (1991). The points correspond to different frequencies: 0.5 THz (squares), 0.1 THz (triangles), and 2.0 THz (circles). The solid curves are to guide the eye.

the $4\Delta_0$ feature exhibits the temperature-dependence of the gap (taken as BCS here [Nicol and Carbotte (1991a); Section 3.4]) while the dip before the impurity peak fills in with the low frequency absorption due to quasiparticle scattering.

In Fig. 4.15, we plot the low frequency conductivity. The top frame shows the temperature-dependent conductivity for several frequencies: $\omega = 1$ meV (solid curve), $\omega = 2$ meV (- — -), $\omega = 5$ meV (— — —), and $\omega = 10$ meV (– – –). The striking feature is a peak in the conductivity which is not suppressed until rather high frequencies. These curves are for $t^+ = 0$ (the clean limit). Recent experiments have observed such a peak [Nuss *et al.* (1991); Bonn *et al.* (1991); Holczer *et al.* (1991)] and in Fig. 4.16, we reproduce the data of Nuss *et al.* (1991).

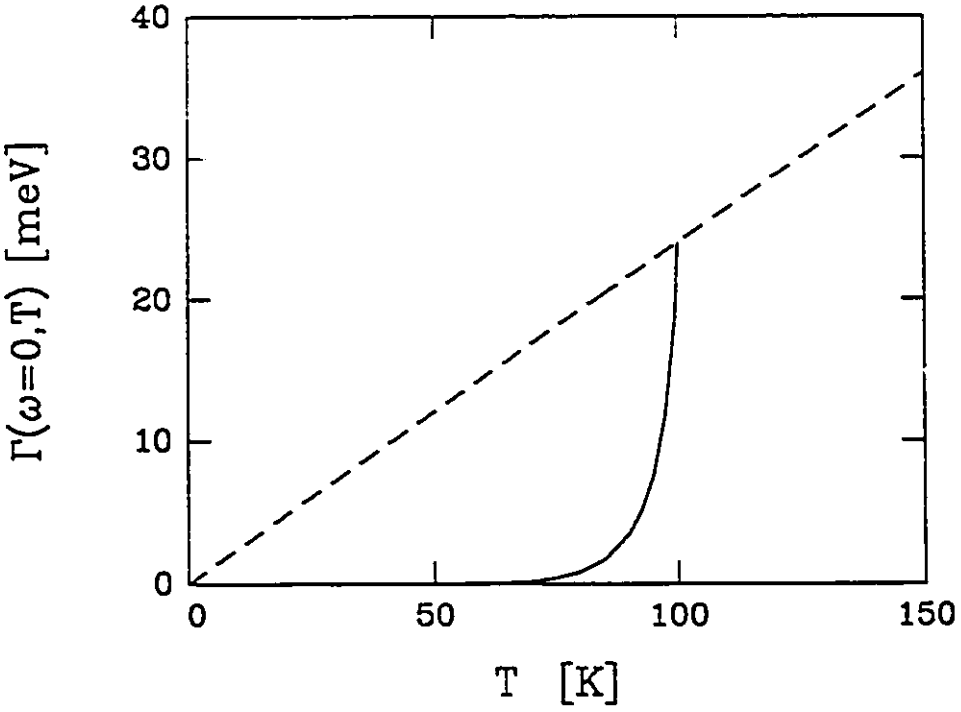


**Figure 4.17** The zero-frequency quasiparticle damping rate as a function of temperature. The dashed curve corresponds to the normal state and the solid curve to the superconducting state. There is a sudden drop in the damping rate just below $T_c$ in the superconducting state, due to a gap opening up in the fluctuation spectrum.

In the lower frame of Fig. 4.15, we exhibit the conductivity as a function of impurity content, at a lower frequency of $\omega = 0.05$ meV, for: $t^+ = 0$ meV (solid curve), $t^+ = 0.1$ meV (· - - -), $t^+ = 0.2$ meV (– – –), $t^+ = 1$ (— — —), and $t^+ = 100$ meV (- — - —). The last curve is essentially the dirty limit and thus for the microwave frequency range, the peak is never suppressed in the near-to-clean limit (the limit in which the high $T_c$ superconductors are thought to be). Note that the behaviour here is completely opposite to what occurs in the conventional strong-coupling case, where increased normal impurity scattering enhances the peak and no peak is observed in the clean limit [Akis and Carbotte (1991b); Marsiglio (1991)].

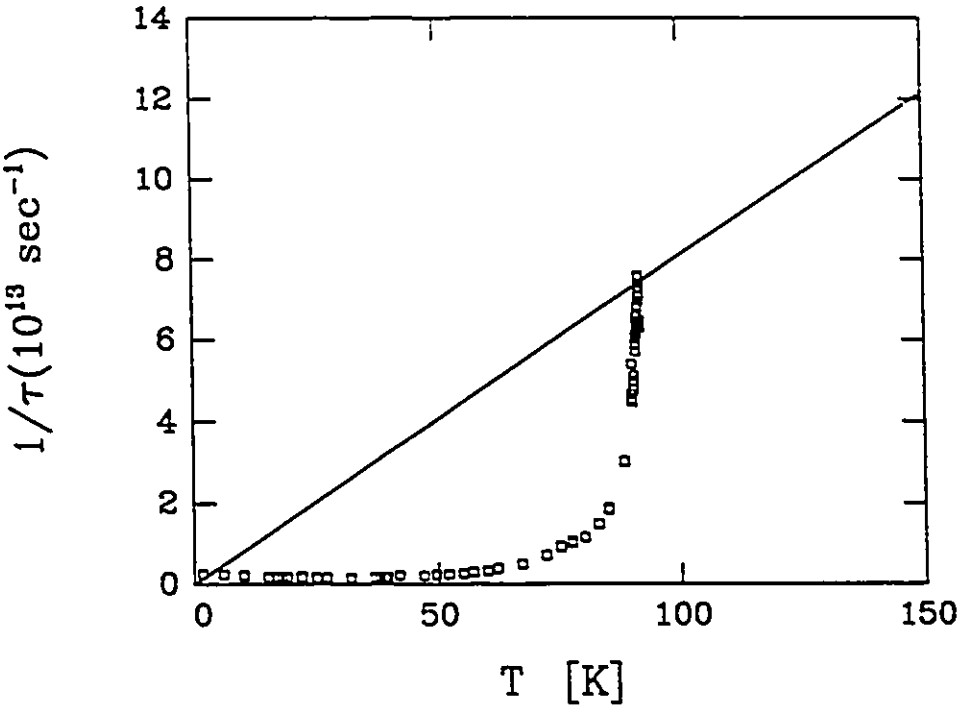


Figure 4.18 Data of Bonn *et al.* (1991) for the scattering rate in $YBa_2Cu_3O_7$. These data are extracted from microwave surface resistance data taken at 2.95 GHz. Due to the method of analysis the authors prefer to trust the data shown here only for temperatures greater than 55K.

These surprising results are not due to coherence effects, which have been suppressed by strong coupling, but rather, they are due to the novel quasiparticle damping rate $\Gamma(\omega,T)$ which is shown in Fig. 4.17. [Nicol *et al.* (1991c)] (see the previous section). Unlike the NMR relaxation rate, the conductivity samples this scattering rate and it is this difference that can produce a peak in the conductivity but not in the NMR. The damping rate depends on the availability of fluctuations for the quasiparticle to emit or absorb when making transitions between states. However, in the marginal Fermi liquid model, such fluctuations are absent for low frequencies and temperatures not near $T_c$, due to the gap of $2\Delta(T)$ in the fluctuation spectrum. It is only very close to $T_c$, where $2\Delta(T)$ is small, that the scattering processes can

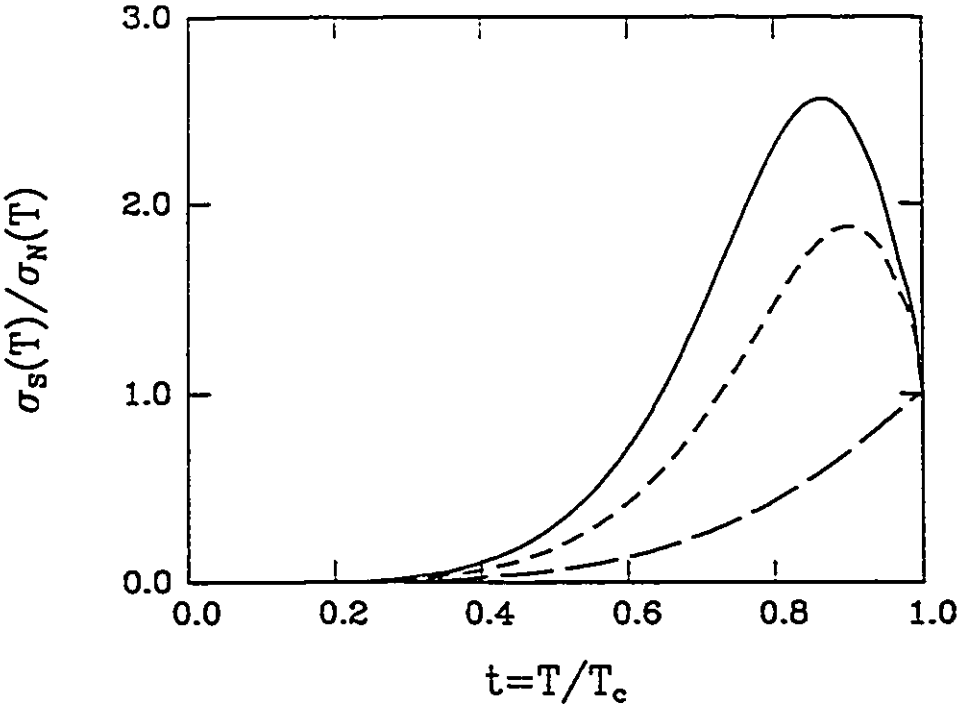


Figure 4.19 A simulation of the low frequency conductivity using a simple two-fluid model as described in the text. These curves are for illustrative purposes only and are not to be taken as quantitatively correct. Curves are drawn for $\omega = 0$ and $t^+ = 1.0$ meV (solid curve), $t^- = 2.0$ meV (– – –), and $t^+ = 100.0$ meV (— — —).

occur. Behaviour, like that shown in Fig. 4.17, has been recently observed experimentally [Tanner *et al.* (1991); Bonn *et al.* (1991)]. In Fig. 4.18, we reproduce the data of Bonn *et al.* (1991).

To aid in visualizing how the peak in the conductivity occurs and how it decreases with increasing impurity scattering, we use a very naive and simplistic model. We take the simple form for the Drude conductivity at zero frequency (as $\omega = 0.05$ meV is quite small relative to $\Delta_o$):

$$\sigma = \frac{ne^2\tau}{m} \quad , \tag{4.24}$$

and make this temperature-dependent by replacing the density of electrons $n$ by the two-fluid model temperature dependence [Schrieffer (1964)] for normal

electrons $n_n^S(T)$ (taking the quasiparticles to be a fluid of normal electrons in the superconducting state) and we also use the temperature dependence of $\tau$ given in Fig. 4.17. Hence,

$$\frac{\sigma_S(T)}{\sigma_N(T)} = \frac{n_n^S(T)[\Gamma_N(T) + \pi t^+]}{[\Gamma_S(T) + \pi t^+]} \quad . \tag{4.25}$$

where we have included the effects of impurity scattering with $\pi t^+ = 1/(2\tau)$. In Fig. 4.19, we show the results of this simple picture and we see the same qualitative shape and behaviour as we find in the full numerical solutions. The curves are drawn for: $t^+ = 1.0$ meV (solid curve), $t^+ = 2.0$ meV (- - -), and $t^+ = 100.0$ meV (— — —). It is the drop in the scattering rate that is causing the peak to appear in the conductivity. Of course, the position and shape of the peak depends on the details of the how the gap forms in the fluctuation spectrum, for which there is no microscopic theory. The curves in Fig. 4.19 are not quantitatively correct and are for illustrative purposes only.

In conclusion, we have calculated the low-frequency conductivity within marginal Fermi liquid theory. Due to the drop in the quasiparticle damping rate, a peak occurs in the microwave conductivity whereas no such peak occurs in the NMR relaxation rate [Nuss *et al.* (1991); Littlewood and Varma (1991)]. With increasing impurity scattering the peak will be reduced. Recent experiments have observed such a peak [Nuss *et al.* (1991); Bonn *et al.* (1991); Holczer *et al.* (1991)] and this model provides a possible explanation for the novel occurrence of a peak in the conductivity with an absence of the same in the NMR relaxation rate.

# Chapter 5

# Paramagnons and Paramagnetic Impurities

*Mainly Optical Properties*

Unlike the previous chapters on thin film critical currents and marginal Fermi liquid theory, which presented ideas and formalism not well-established in the literature, the subject of this chapter has been well developed. The formalism for including paramagnons and paramagnetic impurities in Eliashberg theory has been developed and many results have already been obtained. Our purpose here is merely to adopt this formalism and examine previously uncalculated properties, such as the optical conductivity. Hence, as the background is well-established, we will be brief in our introduction and mainly refer the reader to the literature.

We would also like to point out that the model for paramagnons used in this chapter is formally similar to the form of the Eliashberg equations modified for the marginal Fermi liquid of the previous chapter. Therefore, comparison between results of this chapter and the previous two chapters is useful for illustrating those features of the marginal Fermi liquid model which

are due to the spin fluctuation part of the theory. Likewise, the portion of this chapter dealing with Abrikosov-Gor'kov paramagnetic impurities, which can be seen to be the static limit of spin fluctuations, gives an appropriate introduction to the next chapter on spin glass superconductivity where the resulting equations are formally similar to those for the paramagnetic impurity scattering but with a temperature-dependent scattering rate.

## 5.1 INTRODUCTION

Berk and Schrieffer (1966) have given a model for incorporating paramagnetic spin density fluctuations (paramagnons) into Eliashberg theory. It is based upon capturing the essence of how paramagnetic spin fluctuations are expected to affect spin-singlet pairing in a superconductor. Typically, due to strong Coulomb interactions between electrons in very narrow energy bands, ferromagnetic correlations (for example) may cause spin polarization of the electron cloud (a fluctuation in the spin density), such that an electron seeking to lower its energy by forming a Cooper pair in a spin-singlet state with another electron through the electron-phonon interaction (which is short range in real space), might actually be inhibited or repulsed by this cloud of polarized electrons of the wrong spin [Berk and Schrieffer (1966)]. This forms a repulsive interaction. Allen and Mitrović (1982) have given a loose definition of paramagnons as "interacting electron-hole pairs of spin 1". Paramagnons are typically heavily damped excitations that cause strong renormalization effects [Doniach and Engelsberg (1966); Brinkman and Engelsberg (1968)]. They are more effective at certain frequencies which has been exhibited by functional derivative calculations [Williams (1990)], after the manner of similar calculations for phonons.

In this model, a standard set of Eliashberg equations for both phonons and paramagnons can be written [Berk and Schrieffer (1966); Gladstone *et al.* (1969); Rietschel and Winter (1979); Daams *et al.* (1981); Baquero *et al.* (1981); Mitrović and Carbotte (1982); Zarate and Carbotte (1987); Williams and Carbotte (1991)]. The kernel in these equations is written in terms of the spectral density, $\alpha^2F(\omega)$, for the coupling of the electrons to the phonons and the analogous one for paramagnons, $P(\omega)$. As paramagnons are pair-breaking (or repulsive), they enter the equation for the gap parameter with a negative sign relative to the pair-enhancing phonons. However, in the renormalization equation, $P(\omega)$ enters with a plus sign and hence accentuates strong-coupling effects. The Eliashberg equations for the order parameter and renormalized frequencies of the superconducting state are given as

$$\tilde{\Delta}_n = \pi T \sum_{m=-\infty}^{\infty} [\lambda^-(n-m) - \mu^*\theta(\omega_c - |\,\omega_m\,|)] \frac{\tilde{\Delta}_m}{\sqrt{\tilde{\omega}_m^2 + \tilde{\Delta}_m^2}} \tag{5.1}$$

and

$$\tilde{\omega}_n = \omega_n + \pi T \sum_{m=-\infty}^{\infty} \lambda^+(n-m) \frac{\tilde{\omega}_m}{\sqrt{\tilde{\omega}_m^2 + \tilde{\Delta}_m^2}} \quad , \tag{5.2}$$

where

$$\lambda^{\pm}(n-m) \equiv \lambda(i\omega_m - i\omega_n) \equiv \int_0^{\infty} \frac{2\omega[\alpha^2F(\omega) \pm P(\omega)]}{\omega^2 - (i\omega_m - i\omega_n)^2}\, d\omega \quad , \tag{5.3}$$

and $\tilde{\Delta}_n \equiv \tilde{\Delta}(i\omega_n) = Z(i\omega_n)\Delta(i\omega_n)$ and $\tilde{\omega}_n = Z(i\omega_n)\omega_n$ with $i\omega_n \equiv i\pi T(2n+1)$, $n = 0, \pm1, \pm2, \ldots$, $T$ is the temperature, and $\mu^*$ is the Coulomb pseudopotential. The spin fluctuation spectral density is related to the spin fluctuation propagator by [Allen and Mitrović (1982); Gladstone *et al.* (1969), see Appendix A]:

$$P(\omega) = N(0) \sum_{kk'} \left( -\frac{1}{\pi} \Im m \chi^{+-}(k, k', \omega + i0^+) \right) \delta(\epsilon_k)\delta(\epsilon_{k'}) \Big/ \sum_{kk'} \delta(\epsilon_k)\delta(\epsilon_{k'}) \tag{5.4a}$$

$$= N(0) \int_0^{2k_F} \frac{q\,dq}{2k_F^2} \Im m T(q, \omega) \quad , \tag{5.4b}$$

where $q$ is the momentum transferred and in Eq. (5.4b) we have assumed a spherical Fermi surface. The spin fluctuation propagator is depicted in Fig. 5.1. This is related to the particle-hole $\mathcal{T}$-matrix through the Fourier transform of the transverse susceptibility $\chi^{+-}(q,\omega)$ given by [Doniach and Engelsberg (1966); Doniach and Sondheimer (1974)]:

$$\chi^{+-}(x-x',t-t') = i\theta(t-t')\langle[\sigma^{-}(x,t),\sigma^{+}(x',t')]\rangle \quad , \tag{5.5}$$

where the $\sigma^{\pm}$ are written in terms of the Pauli spin matrices as $\sigma^{\pm} = (\sigma_x \pm i\sigma_y)/2$ and the effect of the product of $\sigma$ operators is to flip a spin up, for instance, at time $t'$ and position $x'$, while flipping a spin down at a later time $t$ and position $x$. Vertex corrections to the diagram in Fig. 5.1 are not considered. Recently, Mitrović and Longo (1988) have proven a Migdal's theorem (analogous to the one for phonons) for the case of an almost full band. This would justify the neglect of vertex corrections. We will not discuss this susceptibility further [for which there exist RPA calculations, *etc.*] but will refer the reader to textbook discussions [see for instance, Doniach and Sondheimer (1974)]. Our starting point will be at an assumed form for $P(\omega)$ and hence details of the microscopic theory beyond this point are unnecessary for our discussion.

The static limit of dynamic paramagnetic spin fluctuations are paramagnetic impurities that spin-flip scatter the electron. These are described in the dilute, non-interacting limit by the theory of Abrikosov and Gor'kov (1961), where interaction between the moments on the magnetic atoms are neglected and single scattering events are assumed such that multiple scattering and the corresponding $\mathcal{T}$-matrix approach need not be considered. Also, the nature of the scattering is assumed to be weak and well described by

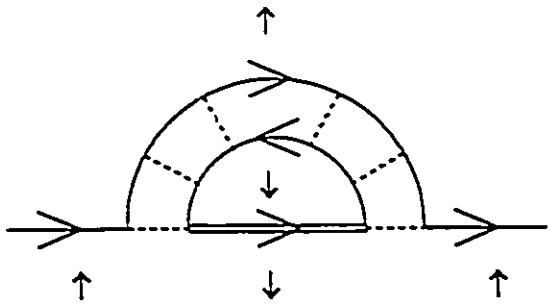

Figure 5.1 The self-energy diagram with the spin fluctuation propagator in the paramagnon model considered here. The spin fluctuation propagator (or paramagnon) consists of an interacting electron-hole pair of spin 1. The dotted lines represent the Coulomb interaction.

the first order diagram in the Born approximation of perturbation theory, as for normal elastic scattering from non-magnetic impurities [see Appendix A]. The strong scattering limit (which allows for the possibility of bound states being formed at the impurity sites) requires the theory of Shiba (1968,1973) and Rusinov (1969), who solved the problem exactly without the use of perturbation theory, but rather used the $T$-matrix. Shiba-Rusinov theory reduces to Abrikosov-Gor'kov theory in the weak scattering limit. Here, we will only consider Abrikosov-Gor'kov theory, which has been examined by many authors [Ambegaokar and Griffin (1965); Skalski *et al.* (1964); Maki (1969); Schachinger *et al.* (1980)]. The case of interacting magnetic impurities will be dealt with in the next chapter. Like paramagnons, as paramagnetic impurities are pair-breaking, they will cause a reduction in $T_c$ over the pure case.

The Eliashberg equations for the Matsubara pairing energy $\tilde{\Delta}(i\omega_n)$ and renormalized frequencies $\tilde{\omega}(i\omega_n)$, incorporating such paramagnetic impurity scattering are given as [Schachinger *et al.* (1980)]:

$$\tilde{\Delta}_n = \pi T \sum_m [\lambda(n-m) - \mu^* \theta(\omega_c - |\omega_m|)] \frac{\tilde{\Delta}_m}{\sqrt{\tilde{\omega}_m^2 + \tilde{\Delta}_m^2}} - \pi t^- \frac{\tilde{\Delta}_n}{\sqrt{\tilde{\omega}_n^2 + \tilde{\Delta}_n^2}} \quad (5.6)$$

and

$$\tilde{\omega}_n = \omega_n + \pi T \sum_m \lambda(n-m) \frac{\tilde{\omega}_m}{\sqrt{\tilde{\omega}_m^2 + \tilde{\Delta}_m^2}} + \pi t^- \frac{\tilde{\omega}_n}{\sqrt{\tilde{\omega}_n^2 + \tilde{\Delta}_n^2}} \quad , \quad (5.7)$$

with the same notation as before. Here, $t^-$ is the magnetic impurity spin-flip scattering rate related to the scattering time $\tau_p$ for paramagnetic impurities by $t^- \equiv 1/(2\pi\tau_p)$. The function $\lambda(n-m)$ is related, in the usual manner, to the electron-phonon spectral density $\alpha^2 F(\Omega)$ by

$$\lambda(n-m) = \int_0^\infty \frac{2\Omega\,\alpha^2 F(\Omega)}{\Omega^2 + (\omega_n - \omega_m)^2}\, d\Omega \quad . \quad (5.8)$$

Eqs. (5.1) and (5.2) reduce in the static limit to the above equations for paramagnetic impurities by choosing for the form of $P(\omega)$:

$$P(\omega) = A_p \omega\, \delta(\omega) \quad . \quad (5.9)$$

We use this in the definition for $\lambda^{\pm}(n-m)$:

$$\lambda_p^{\pm} = \pm 2 \int_0^\infty d\omega \frac{\omega P(\omega)}{\omega^2 + (\omega_n - \omega_m)^2} \quad , \quad (5.10)$$

which for $n = m$ gives

$$\lambda_p^{\pm} = \pm 2 A_p \int_0^\infty d\omega \frac{\omega^2 \delta(\omega)}{\omega^2} \quad ,$$

$$= A_p \quad . \quad (5.11)$$

and for $n \neq m$ yields:

$$\lambda_p^{\pm} = \pm 2A_p \int_0^{\infty} d\omega \frac{\omega^2 \delta(\omega)}{\omega^2 + (\omega_n - \omega_m)^2} \quad .$$

$$= 0 \quad . \tag{5.12}$$

So

$$-\pi T \sum_m \lambda_p(n-m) \frac{\tilde{\Delta}_m}{\sqrt{\tilde{\Delta}_m^2 + \tilde{\omega}_m^2}} = -\pi T A_p \frac{\tilde{\Delta}_n}{\sqrt{\tilde{\Delta}_n^2 + \tilde{\omega}_n^2}} \quad , \tag{5.13}$$

and

$$+\pi T \sum_m \lambda_p(n-m) \frac{\tilde{\omega}_m}{\sqrt{\tilde{\Delta}_m^2 + \tilde{\omega}_m^2}} = +\pi T A_p \frac{\tilde{\omega}_n}{\sqrt{\tilde{\Delta}_n^2 + \tilde{\omega}_n^2}} \quad , \tag{5.14}$$

which make Eqs. (5.1) and (5.2) equivalent to Eqs. (5.6) and (5.7) for $A_p = t^-/T$, at finite $T$.

In this chapter we will present mainly calculations of the optical conductivity for paramagnons and also for paramagnetic impurities. In Section 5.2, we will calculate electromagnetic properties following the model and choice of parameters already defined by Williams and Carbotte (1991) [see also the dissertation of Williams (1990)]. In Section 5.3, we will select certain results in a model of paramagnons and phonons to create a scenario for explaining some of the observed strong coupling features of the high $T_c$ oxides. Finally, in Section 5.4, we will present results for calculations of the optical conductivity at finite frequency and temperature for materials containing paramagnetic impurities. The next chapter on spin glasses, which will be essentially an examination of a form of temperature-dependent paramagnetic impurity scattering, displays results for paramagnetic impurity scattering for several superconducting properties for comparative purposes. The reader is referred to that chapter to see the influence of such impurity scattering on other properties not shown here. We conclude briefly in Section 5.5.

## 5.2 SOME ELECTROMAGNETIC PROPERTIES WITH PARAMAGNONS

In this section, for simplicity, we used Einstein spectra for the form of the spectral densities in Eqs.(5.1)-(5.3). The $\alpha^2F(\omega)$ spectrum is given as

$$\alpha^2F(\omega) = \frac{\lambda_E\omega_E}{2}\delta(\omega - \omega_E) \quad , \tag{5.15}$$

and the paramagnon spectral density is given as

$$P(\omega) = \frac{\lambda_P\omega_P}{2}\delta(\omega - \omega_P) \quad , \tag{5.16}$$

where $\lambda_{E,P}$ is the electron-phonon or paramagnon mass renormalization parameter, respectively, and $\omega_{E,P}$ is the frequency of the corresponding exchange boson. Also, keeping in mind the high temperature superconductors, we follow the choice of parameters given by Williams and Carbotte (1991). They assumed that in the absence of the pair-breaking the material would have an intrinsic $T_c^\circ$ of 200K. To achieve this we take $\omega_E$ to be at high energies (BCS-like) such that $T_c^\circ/\omega_E = 0.05$. Then $T_c^\circ$ was reduced to $T_c = 100$K by the addition of spin fluctuations at some characteristic frequency $\omega_P$. Values that we quote will be in terms of $T_c^\circ/\omega_P$, which is analogous to the strong coupling parameter $T_c/\omega_{\ln}$ identified in Chapter 2. This parameter is a measure of strong coupling effects arising from paramagnons.

Here, we will present results in this model for the London penetration depth, the dc Josephson current, the thin film critical current, and the zero temperature, finite frequency optical conductivity. Williams and Carbotte (1991) have already presented results for the gap ratio, the specific heat jump, the slope of the specific heat jump, the upper critical magnetic field, and the isotope effect [Williams (1990)]. In the next section, we will show

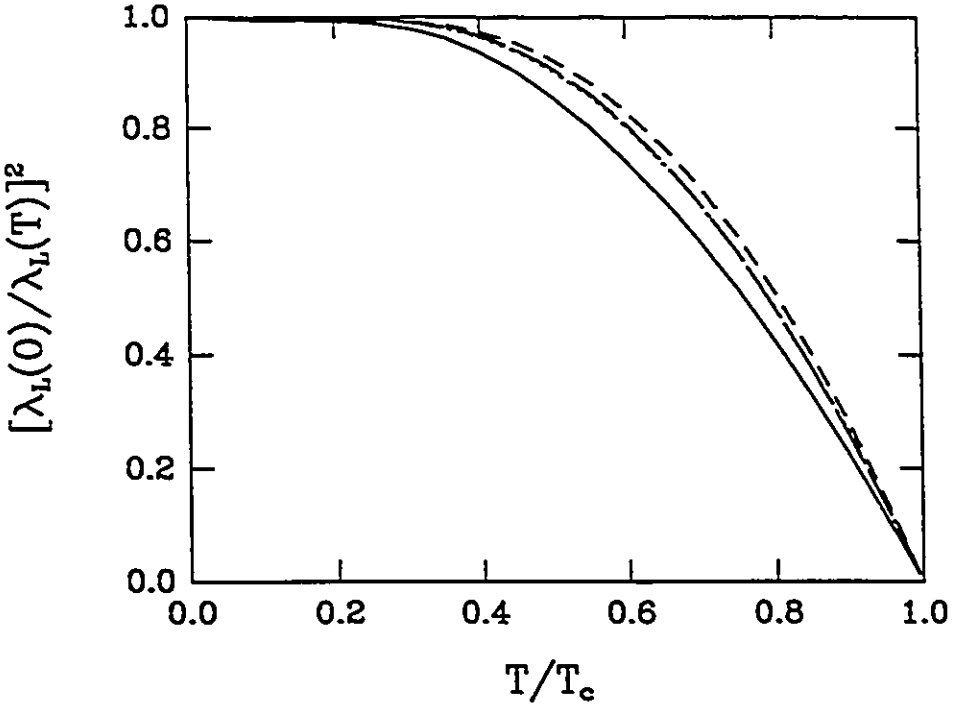


Figure 5.2 The inverse square of the London penetration depth normalized to its zero temperature value as a function of the reduced temperature, $t = T/T_c$. The curves displayed correspond to $T_c^\circ/\omega_p = 0.5$ (solid curve), 1.0 (dotted curve), 2.0 (short dashed curve), 3.0 (long dashed curve). The dotted curve and the long dashed curves are almost on top of each other in this figure.

how this model can be adjusted to provide a possible explanation for the strong coupling effects observed in the high $T_c$ oxides.

To calculate the London penetration depth, we solve Eqs. (5.1)-(5.3) for the model spectra just described (note that we take $\mu^* = 0$ for simplicity). After obtaining the Matsubara gaps and frequencies, we then employ Eq. (3.49) to obtain the London penetration depth. Our results are presented in Fig. 5.2 for several values of the strong coupling parameter $T_c^\circ/\omega_p$. Note that in the weak coupling limit (*i.e.*, $T_c^\circ/\omega_p \to 0$), this quantity is lower in magnitude, but as the coupling is increased the curves shift upwards, and finally they stop increasing and begin to shift downwards again in the extreme

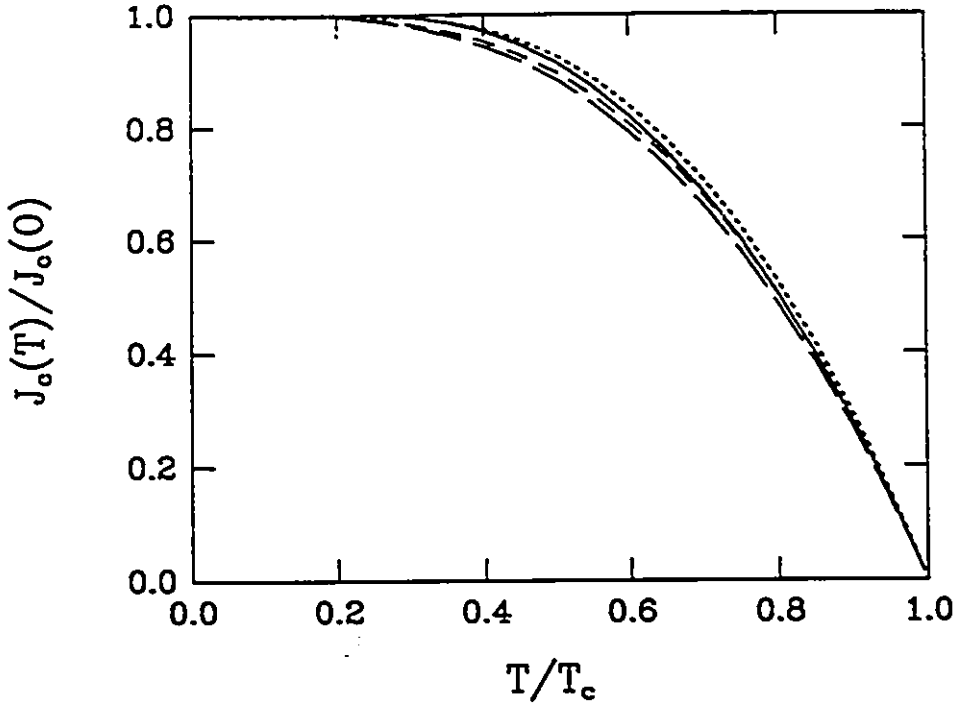


Figure 5.3 The dc Josephson critical current normalized to its zero temperature value as a function $T/T_c$. The curves displayed correspond to $T_c^\circ/\omega_p = 0.5$ (solid curve), 1.0 (dotted curve), 2.0 (short dashed curve), 3.0 (long dashed curve).

strong coupling limit. This is analogous to what occurs when the exchange boson is a phonon [Blezius *et al.* (1988)] and so we conclude that pair-breaking effects from the gap-channel are not important for the temperature dependence of this property, but rather the strong renormalization effects coming from the renormalization channel are important.

The zero-temperature London penetration depth (not shown here), however, is a victim of the pair-breaking effects in the gap equation and hence decreases with increasing coupling strength. [Note that coupling strength increases with reduced $\omega_p$ at fixed $T_c^\circ$.]

In Fig. 5.3, we show the dc Josephson critical current. This was calculated from Eqs. (5.1)-(5.3) and Eqs. (3.51)-(3.52). In this case, modest strong

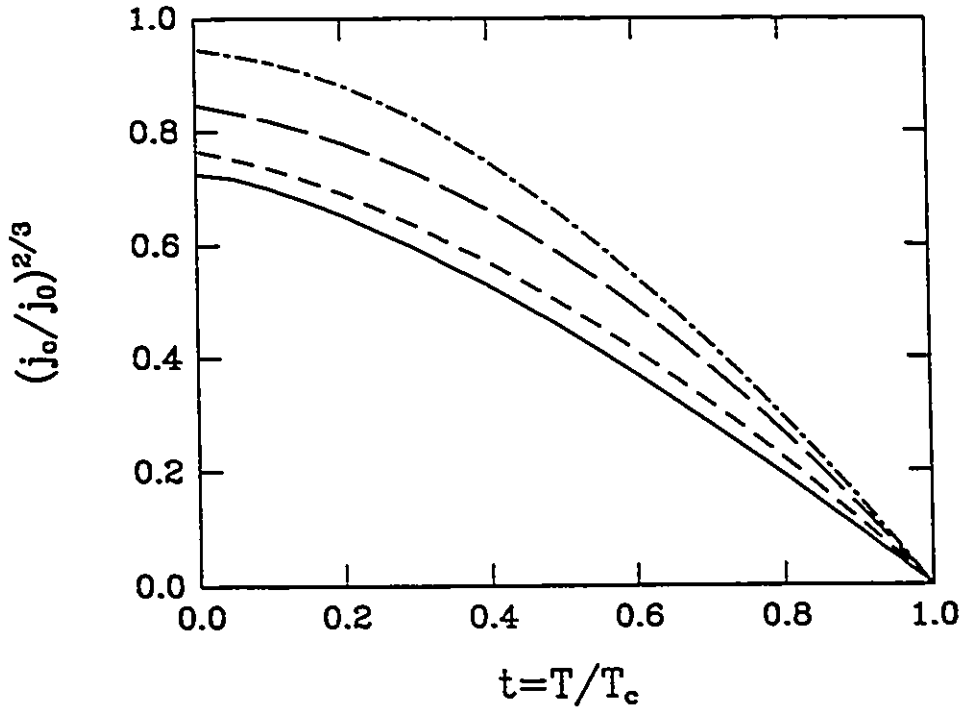


**Figure 5.4** The thin film critical current density normalized to the slope at $T_c$, $(j_o)^{2/3} \equiv -T_c \frac{dj_c^{2/3}}{dT}|_{T_c}$, versus the reduced temperature $t = T/T_c$. Curves are drawn for the BCS limit (solid curve), $T_c^o/\omega_p = 0.5$ (short dashed curve), 1.0 (long dashed curve), and 2.0 (dashed-dotted curve).

coupling strength increases the magnitude of the temperature dependence of this quantity, whereupon, at a lower coupling strength than in the London penetration depth, it reverses it trend and starts to decrease again in the extreme strong coupling limit. This is again similar behaviour to the case of phonons [Akis and Carbotte (1990)]. Note that, overall, deviations in the temperature dependence are small in this quantity.

In Fig. 5.4, we show the thin film critical current, where we use the formalism given in Eqs. (2.5)-(2.8) modified for the kernel as given in Eq. (5.3). It is seen that as in the case of phonons and paramagnetic impurities [Nicol and Carbotte (1991c); Chapter 2], strong coupling increases

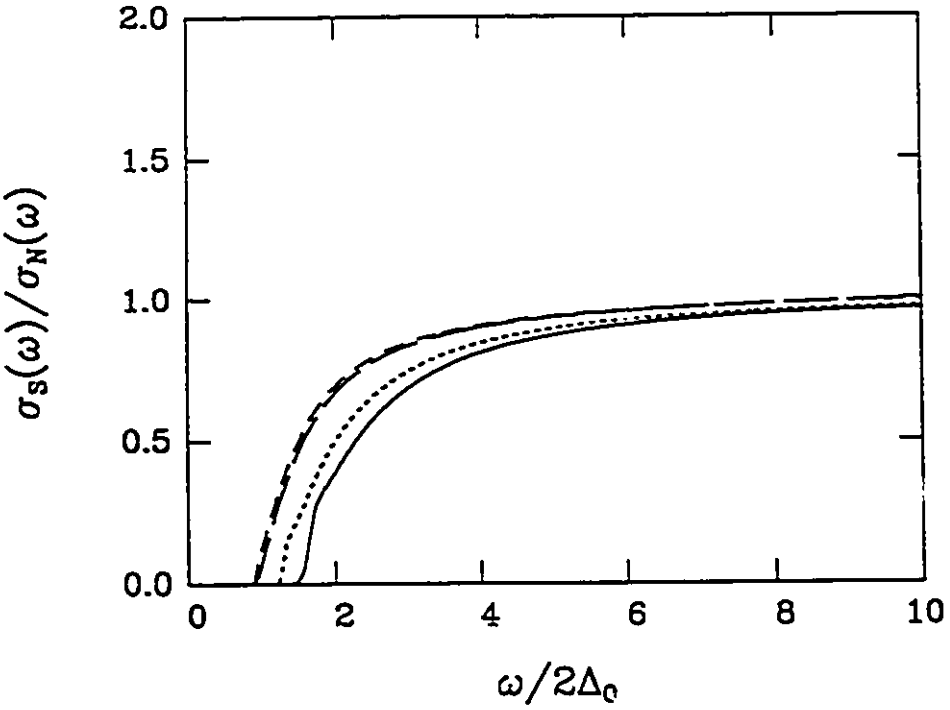


**Figure 5.5** The ratio of the superconducting state to normal state optical conductivity at zero temperature versus the frequency normalized to twice the zero temperature gap value for the model described in the text. Curves are drawn for the strong coupling parameter $T_c^o/\omega_p = 0.5$ (solid curve), 1.0 (dotted curve), 1.5 (short dashed curve), and 2.0 (long dashed curve).

the magnitude of the curves, as a function of temperature, over the weak coupling limit. The largest value examined here was $T_c^o/\omega_p = 2.0$.

Finally, we calculate the zero temperature optical conductivity in the formalism of Bickers *et al.* (1990) given in Eqs. (4.6)-(4.8) but using Eqs. (5.1)-(5.3) for the Matsubara gaps and renormalization function. As the choice of a delta function at $\omega_E$ to give $T_c^o = 200$K will produce unphysical and meaningless structure in this quantity, we have preferred to use here a negative $\mu^*$, which in these equations mimics an electronic attractive interaction, chosen to achieve $T_c^o = 200$K with the phonon part set equal to zero. This allows us to see the effects of the paramagnons alone.

We have done our calculations in the clean limit (*i.e.*, $t^+ = 0$), which should enhance any strong coupling effects [Schlesinger *et al.* (1990)]. Our results are presented in Fig. 5.5, where we have plotted the ratio of the superconducting state conductivity to the normal state $\sigma_s(\omega)/\sigma_n(\omega)$. First, we note as in Chapter 4, that no absorption occurs until $2\Delta$ plus the first fluctuation frequency, which is $2\Delta + \omega_p$ in the delta function model used here. Note that the ratio is smooth and featureless. This is in agreement with experimental observations [Schlesinger *et al.* (1990); Nicol and Carbotte (1991d)]. The minor structure occurring at the low frequency end of the curve of $T_c^\circ/\omega_p = 0.5$ is a result of the paramagnon spectral function in the form of a delta function producing structure in the density of states at $\omega > 2\Delta$ and therefore this is reflected here. This means that high frequency paramagnons in the weak coupling limit will produce structure in the optical conductivity; however, as the renormalization factor of $1 + \lambda_p$ is close to one in this limit, the structure will not be greatly enhanced, contrary to what would normally be expected from strong coupling effects in the clean limit.

In summary, we find the temperature dependence of many of the electromagnetic properties to behave in the same manner whether the exchange boson is a paramagnon rather than a phonon. However, the overall magnitude is reduced due to pair-breaking effects. The frequency dependent optical conductivity ratio is found to be featureless.

## 5.3 STRONG COUPLING EFFECTS FROM PARAMAGNONS IN HIGH $T_c$

While it is acknowledged, from both theoretical and experimental considerations, that the electron-phonon mechanism is not responsible for the

superconductivity in the high-$T_c$ oxides, several experiments remain which exhibit strong-coupling effects. This paradox can be resolved by considering a mechanism for the high-$T_c$ oxides which is mainly electronic in origin but with a small contribution from the electron-phonon interaction and a significant contribution from dynamic spin fluctuations, paramagnons. In such a model, strong coupling effects can arise from the paramagnons. Fixing the electron-phonon contribution to achieve an isotope effect coefficient of 0.05 at a $T_c$ of 96K, we have obtained a large gap ratio, $2\Delta_o/k_BT_c$, a two-fluid model-like temperature dependence for the penetration depth, and a featureless optical conductivity, $\sigma_s/\sigma_N$, in agreement with interpretation of experiment.

To achieve a high $T_c$, we assumed there is a high energy electronic mechanism that would give the material a $T_c^{\infty}$ of 250K. This was modelled by a negative $\mu^*$, the Coulomb pseudopotential in the Eliashberg equations. We then added paramagnons, at frequency $\omega_p$ and renormalization of $\lambda_p$, to reduce $T_c$ down to $T_c^{\circ} = 96$K, the intrinsic $T_c$ of the copper oxides. At the same time, we included an electron-phonon contribution to $T_c$ through $\alpha^2F(\omega)$. The addition of phonons was necessary to achieve an isotope effect, which is experimentally observed in these materials to be small but nonzero.

In Fig. 5.6, we display curves for the London penetration depth, $\lambda_L(T)$, as a function of $t = T/T_c$ for the values of $\omega_p$ as indicated in the figure. It is possible to obtain a two-fluid-like behaviour, *i.e.*, $(1 - t^4)$ for $[\lambda_L(0)/\lambda_L(T)]^2$, for the parameters corresponding to the short-dashed curve, the curve with the strongest coupling. A two-fluid-like temperature dependence of the penetration depth is seen experimentally both in $\mu$SR [Pumpin *et al.* (1990)] and magnetization [Wu and Sridhar (1990)] measurements. For the parameters corresponding to the dashed curve of Fig. 5.6, we display, in

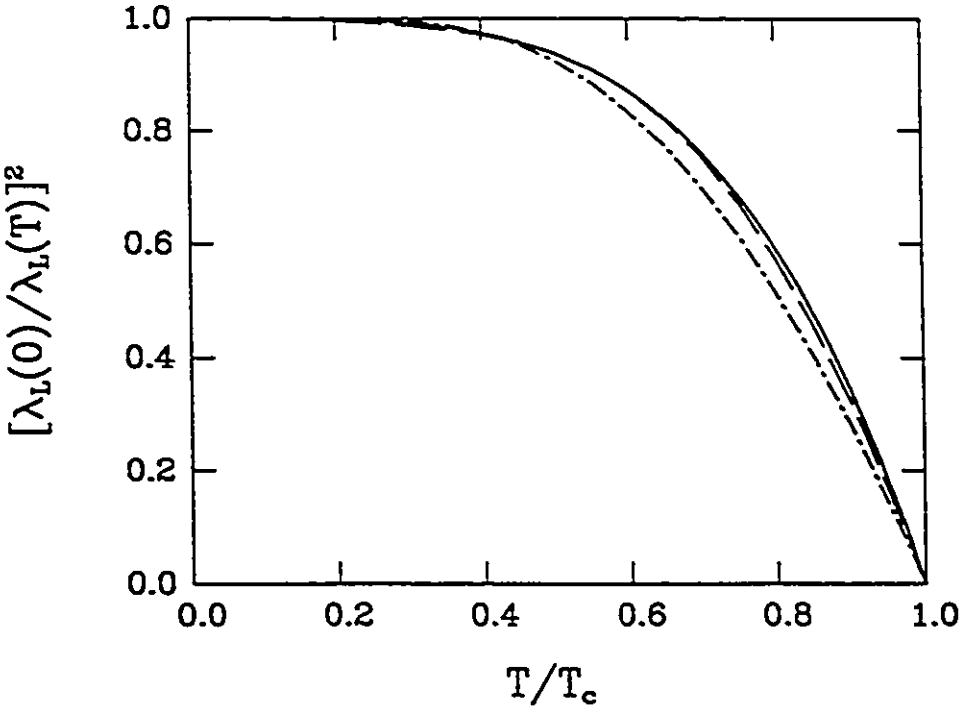


Figure 5.6 The inverse square of the London penetration depth normalized to its zero temperature value as a function of the reduced temperature, $t = T/T_c$. The curves displayed correspond to $\omega_p = 5$ meV (– – –) and $\omega_p = 20$ meV (– · –), with the other parameters given in Table 5.1. The solid line is the phenomenological two-fluid model, $(1 - t^4)$. Curves for $\omega_p = 10$ meV and $\omega_p = 15$ meV fell between the other two curves and are not shown for the purposes of clarity.

Fig. 5.7, the clean limit superconducting state optical conductivity normalized to that in the normal state. Notice that the normalized conductivity is completely featureless, in agreement with the experiments of all infrared spectroscopists [Schlesinger *et al.* (1990); Nicol and Carbotte (1991d)]. The value of the gap ratio $2\Delta_o/k_BT_c$ can be quite large. This is recorded in Table 5.1 for the parameters corresponding to the curves of Fig. 5.6 and two other intermediate cases. No agreement has been reached experimentally on the value of this ratio, but many reports suggest that it can be large, from 4 to 8 [Schlesinger *et al.* (1990); Gurvitch *et al.* (1989)].

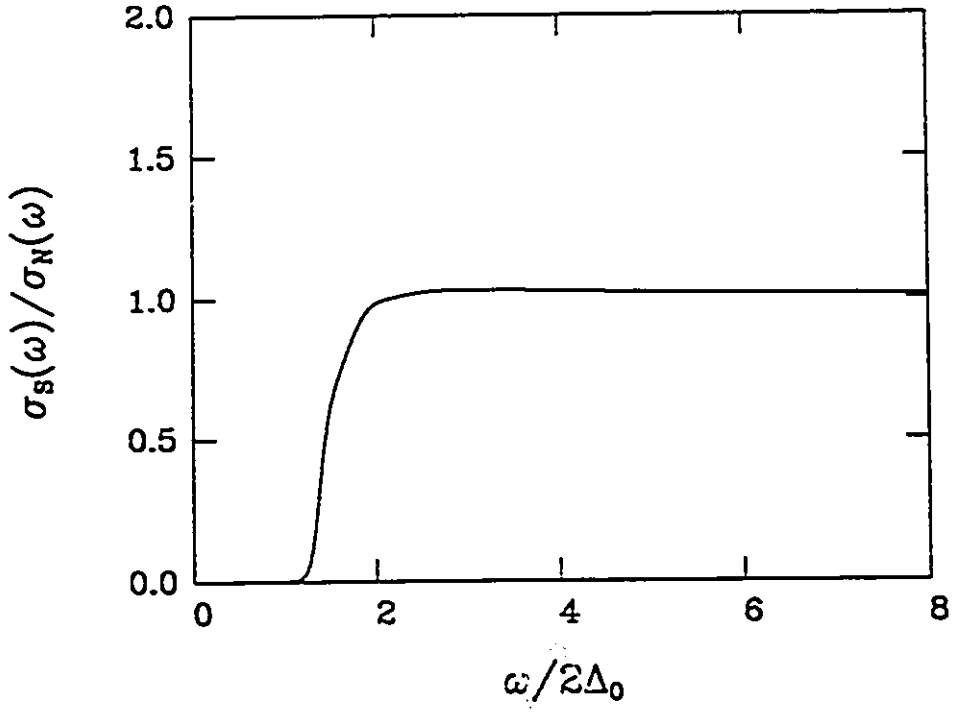


**Figure 5.7** The ratio of the superconducting state to normal state conductivity, in the clean limit, as a function of the frequency $\omega$, for the case of $\omega_P = 5$ meV.

Table 5.1

| $\omega_P$ | $\lambda_P$ | $\omega_E$ | $\lambda_E$ | $2\Delta_o/k_BT_c$ |
|---|---|---|---|---|
| 5 | 0.298 | 20 | 0.225 | 7.06 |
| 10 | 0.285 | 20 | 0.210 | 8.82 |
| 15 | 0.266 | 20 | 0.190 | 5.03 |
| 20 | 0.246 | 20 | 0.175 | 4.49 |

Finally, in Fig. 5.8, we display the isotope effect coefficient defined as $\beta \equiv -d\ln T_c/d\ln M$, corresponding to the stoichiometric compound $YBa_2Cu_3O_7$ with $\beta = 0.05$ and $T_c = 96$K. In this curve, we have increased the paramagnon contribution (which is pair-breaking) to reduce $T_c$ and we find that $\beta$ rises. This is a possible scenario for similar behaviour observed in the Pr doped

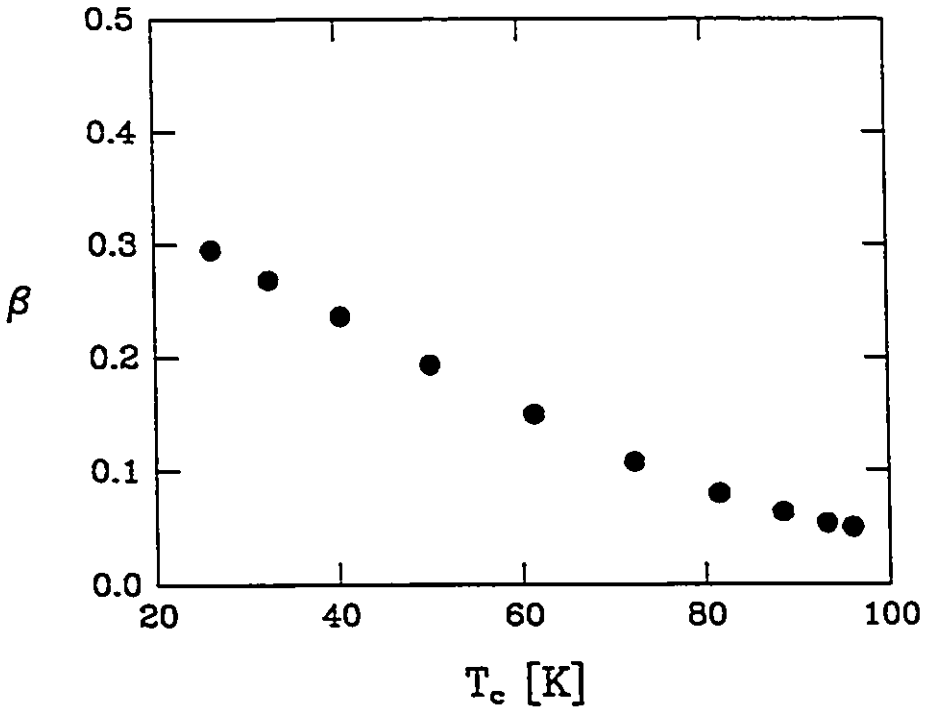


**Figure 5.8** The isotope effect coefficient $\beta$ as a function of the critical temperature $T_c$, for the case of $\omega_p = 5$ meV.

$Y_{1-x}Pr_xBa_2Cu_3O_7$ [J.P. Franck *et al.* (1990)], where magnetic interactions are expected to be important due to Pr.

It should be noted that in all cases reported here, the calculated resistivity is linear with temperature and the corresponding $\lambda \approx \lambda_E + \lambda_p$ does not violate those derived from experimental measurements [Gurvitch and Fiory (1987)]. These calculations are shown in Fig. 5.9, where we have modified Ziman's resistivity formula [Grimvall (1981); Hayman and Carbotte (1971a,b)]:

$$\rho(T) \simeq \frac{4\pi m}{ne^2T}\int_0^\infty \frac{\omega[\alpha^2F(\omega)+P(\omega)]}{\{\exp[\omega/T]-1\}\{1-\exp[-\omega/T]\}}d\omega \quad , \qquad (5.17)$$

in which we have approximated the transport spectral densities by the thermodynamic ones. The linear dependence occurs when the temperature is

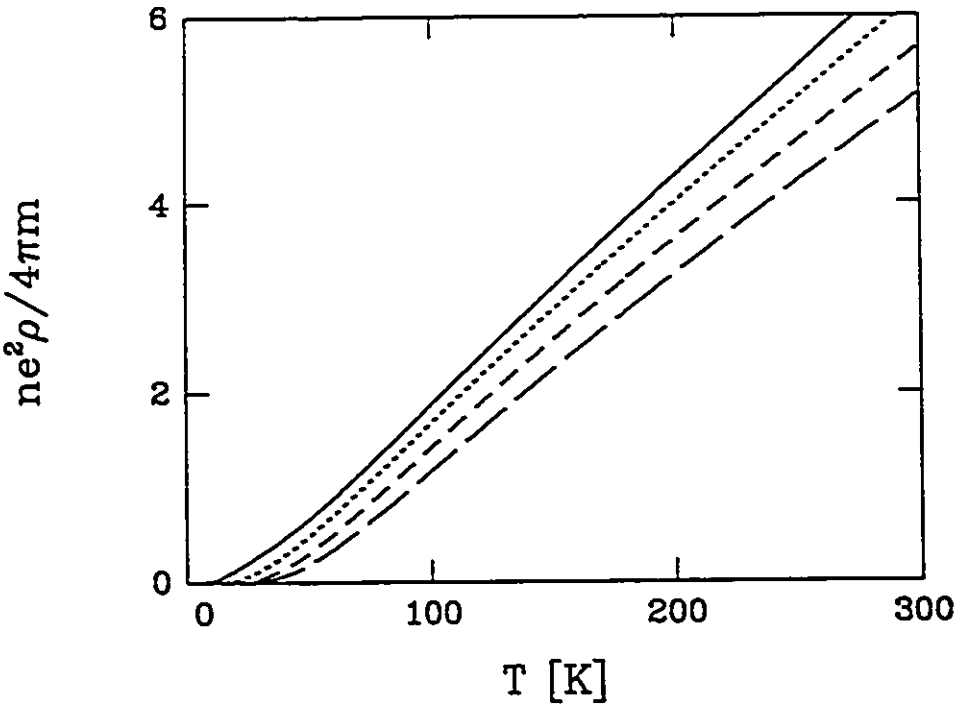


**Figure 5.9** The resistivity $\rho$ normalized to $4\pi m/ne^2$ versus the temperature in Kelvins. The quantity on the y-axis is actually $1/\tau$. Curves are drawn for $\omega_E = 20$ meV and $\omega_p = 5$ meV (solid curve), 10 meV (dotted curve), 15 meV (short dashed curve), and 20 meV (long dashed curve).

greater than about one fifth of the average boson frequency [Lee *et al.* (1989)] and due to the delta functions employed here the scattering is suppressed at low temperatures.

In conclusion, we have calculated the effect of paramagnetic spin fluctuations on the London penetration depth, gap ratio, optical conductivity, dc resistivity, and isotope effect. In all cases, our calculations are either in good agreement with present experiment or, at least, they do not violate present experimental constraints on these properties. Thus, a theory of paramagnons plus some high energy boson can explain the strong coupling effects observed in high $T_c$ oxides. The marginal Fermi liquid model which has a spin fluctuation component will also exhibit this behaviour.

## 5.4 EFFECT OF PARAMAGNETIC IMPURITIES ON OPTICAL PROPERTIES

Nam (1967b) has calculated the finite frequency and temperature optical conductivity within Eliashberg theory and has given numerical results in the BCS limit when magnetic impurities are included in the model of Abrikosov and Gor'kov (1961). This work was done in the dirty limit, for which the mean free path $l$ is smaller than the coherence length $\xi_0$. In the high $T_c$ oxides, it has been argued [Timusk and Tanner (1989); Kamarás *et al.* (1990)] that the clean limit applies because of the very short coherence length observed in these systems. The introduction of Pr substitution for Y in $YBa_2Cu_3O_7$ is known [Ghamaty *et al.* (1991)] to reduce the critical temperature. There is some evidence that this may be due to a reduction in the number of holes in the CuO planes while other evidence supports a strong pair-breaking paramagnetic impurity exchange interaction between the Pr and the conduction holes of the CuO planes. While both mechanisms may well be present it would be of interest to calculate the effect of paramagnetic impurities on the finite frequency conductivity in the clean limit.

In this section, we use the Eliashberg formulation, valid at any temperature and impurity concentration, to calculate the frequency and temperature variation of the conductivity in the clean limit as a function of paramagnetic impurity concentration. The results are also compared with dirty limit results and are found to be very different.

The analytic continuation of the imaginary axis Eliashberg equations using the procedure of Marsiglio *et al.* (1988) was generalized by us to include pair-breaking effects. The real frequency gap and renormalization function

are given as:

$$\tilde{\Delta}(\omega) = i\pi T \sum_{m=0}^{\infty} [\lambda(\omega - i\omega_m) + \lambda(\omega + i\omega_m) - 2\mu^*] \frac{\tilde{\Delta}(i\omega_m)}{\sqrt{\tilde{\omega}^2(i\omega_m) + \tilde{\Delta}^2(i\omega_m)}}$$

$$+ \; i\pi \int_{-\infty}^{+\infty} dz \alpha^2 F(z)[n(z) + f(z - \omega)] \frac{\tilde{\Delta}(\omega - z)}{\sqrt{\tilde{\omega}^2(\omega - z) - \tilde{\Delta}^2(\omega - z)}}$$

$$- i\pi t^- \frac{\tilde{\Delta}(\omega)}{\sqrt{\tilde{\omega}^2(\omega) - \tilde{\Delta}^2(\omega)}} \tag{5.18}$$

and

$$\tilde{\omega}(\omega) = \omega + i\pi T \sum_{m=0}^{\infty} [\lambda(\omega - i\omega_m) - \lambda(\omega + i\omega_m)] \frac{\tilde{\omega}(i\omega_m)}{\sqrt{\tilde{\omega}^2(i\omega_m) + \tilde{\Delta}^2(i\omega_m)}}$$

$$+ i\pi \int_{-\infty}^{+\infty} dz \alpha^2 F(z)[n(z) + f(z - \omega)] \frac{\tilde{\omega}(\omega - z)}{\sqrt{\tilde{\omega}^2(\omega - z) - \tilde{\Delta}^2(\omega - z)}}$$

$$+ i\pi t^- \frac{\tilde{\omega}(\omega)}{\sqrt{\tilde{\omega}^2(\omega) - \tilde{\Delta}^2(\omega)}} \quad , \tag{5.19}$$

where $n(z)$ and $f(z)$ are, respectively, the Bose and Fermi distribution functions, $\alpha^2 F(-z) = -\alpha^2 F(z)$, and

$$\lambda(\omega) = -\int_{-\infty}^{+\infty} \frac{d\Omega \alpha^2 F(\Omega)}{\omega - \Omega + i0^+} \quad . \tag{5.20}$$

The real frequency axis gap $\Delta(\omega)Z(\omega) = \tilde{\Delta}(\omega)$ and the renormalization $\omega Z(\omega) = \tilde{\omega}$ enter directly into the formula of Lee *et al.* (1989) for the conductivity which is given by Eqs. (4.19)-(4.23).

To show that these equations reproduce the results from the Eliashberg equations along the real axis, we have calculated the tunneling density of states of Pb at $T = 0$, which we show in Figs. 5.10 and 5.11. This was done using the tunneling derived $\alpha^2 F(\omega)$ spectrum for Pb in Eqs. (5.6)-(5.8) and reducing $T_c$ from the pure case by the addition of paramagnetic impurities.

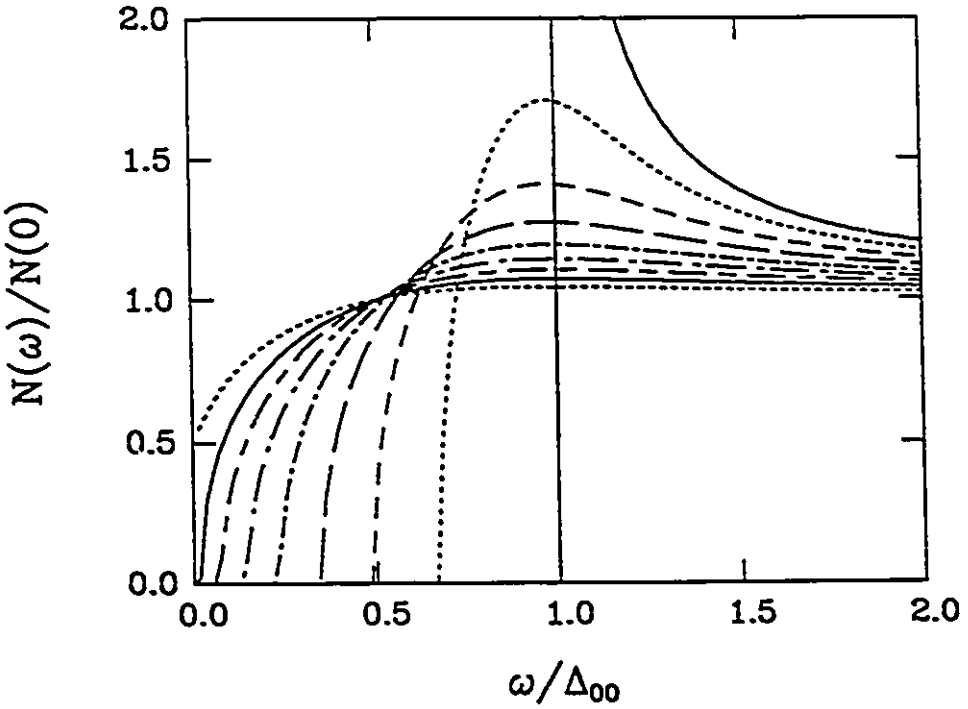


**Figure 5.10** The zero temperature tunneling density of states $N(\omega)$ for Pb normalized to the density of states at the Fermi level, as a function of frequency normalized to the zero temperature gap in the pure case, which is $\Delta_{oo} = 1.39$ meV. Curves are drawn for different reduced $T_c/T_c^\circ$ corresponding to different paramagnetic impurity content. In order of the top to bottom curve on the right hand side of the figure, $T_c/T_c^\circ = 1.0$, 0.9, 0.8, 0.7, 0.6, 0.5, 0.4, 0.3, and 0.2.

We have then used Eqs. (5.18)-(5.20) to analytically continue the Matsubara gaps and renormalization function to the real axis. The tunneling density of states is then given as:

$$\frac{N(\omega)}{N(0)} = \Re e\left\{\frac{|\omega|}{\sqrt{\omega^2 - \Delta^2(\omega)}}\right\} \quad . \tag{5.21}$$

The curves in Fig. 5.10 have already been obtained in BCS theory by Ambegaokar and Griffin (1965) and in particular for Pb by Daams *et al.* (1984). These curves exactly reproduce the curves of Daams *et al.* (1984) which were

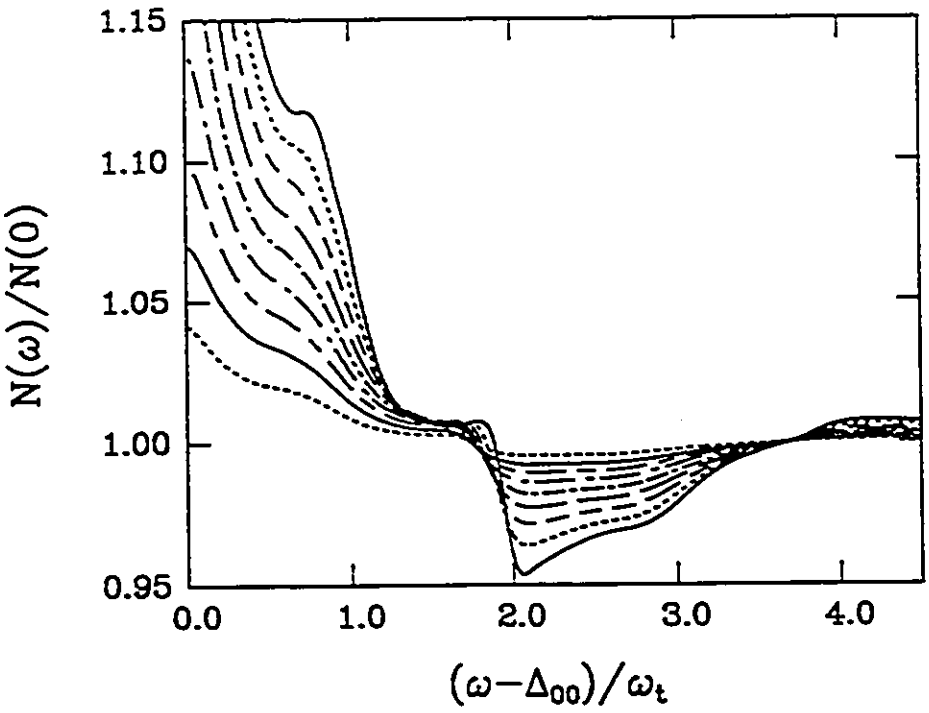


**Figure 5.11** The zero temperature tunneling density of states $N(\omega)$ for Pb normalized to the density of states at the Fermi level, as a function of frequency shifted by the zero temperature gap in the pure case, which is $\Delta_{oo}$ = 1.39 meV, normalized to transverse phonon mode at $\omega_t$ = 4.4 meV. Curves are drawn for different reduced $T_c/T_c^\circ$ corresponding to different paramagnetic impurity content. In order of the top to bottom curve on the far left hand side of the figure, $T_c/T_c^\circ$ = 1.0, 0.9, 0.8, 0.7, 0.6, 0.5, 0.4, 0.3, and 0.2.

calculated with the real axis Eliashberg equations. This is an accurate check that our use of Eqs. (5.18)-(5.20) is correct.

Notice in Fig. 5.11 the phonon structure that appears after the singularity in the density of states at $\Delta_{oo}$. This can not be reproduced by BCS theory and necessitates the full Eliashberg calculations. There are two points that we wish to make about these figures that we will return to in our discussion of the optical results. First, in Fig. 5.10, the density of states fills in at low frequency with increasing paramagnetic impurity scattering and eventually becomes gapless, and the square root singularity is completely

eliminated. In addition, in Fig. 5.11, the phonon structure is also reduced by the addition of spin-flip scattering.

To calculate the optical conductivity with the inclusion of paramagnetic spin-flip scattering, we need only to calculate the imaginary gaps and frequencies from Eqs. (5.6)-(5.8) and analytically continue these quantities to the real frequency axis using the procedure just described. Then the formula given by Lee *et al.* (1989) in Eqs. (4.19)-(4.23) can be applied directly with no further modification. All the necessary information about the paramagnetic impurity scattering is contained in the Matsubara gaps and renormalization function. Normal impurity scattering enters directly into the conductivity formula as it is not included in Eqs. (5.6)-(5.8).

We have solved for the optical conductivity using the Lorentzian spectral function given by Bickers *et al.* (1990) and stated in Eqs.(4.6)-(4.8). For this model the pure $T_c^\circ$ is equal to 67K and $\mu^* = 0$, resulting in the zero temperature gap $\Delta_o = 12$ meV. As $t^-$ is increased the critical temperature is reduced and is denoted by $T_c$.

In Fig. 5.12, we show results for the frequency dependence of the ratio of superconducting to normal state optical conductivity $\sigma_S(\omega)/\sigma_N(\omega)$ at low temperature, namely, $T/T_c = 0.1$. This is sufficiently low for any given sample that it is characteristic of zero temperature. The values of reduced critical temperature used in this figure are $T_c/T_c^\circ = 1.0$ (pure sample) (upper solid curve), 0.9 (dotted curve), 0.8 (short dashed curve), 0.7 (long dashed curve), 0.6 (short dashed-dotted curve), 0.5 (long dashed-dotted curve), 0.4 (long and short dashed curve), 0.3 (lower solid curve). The bottom frame contains our results for the clean limit while the top frame is for comparison and involves the dirty limit, where we define our terminology to be: clean limit

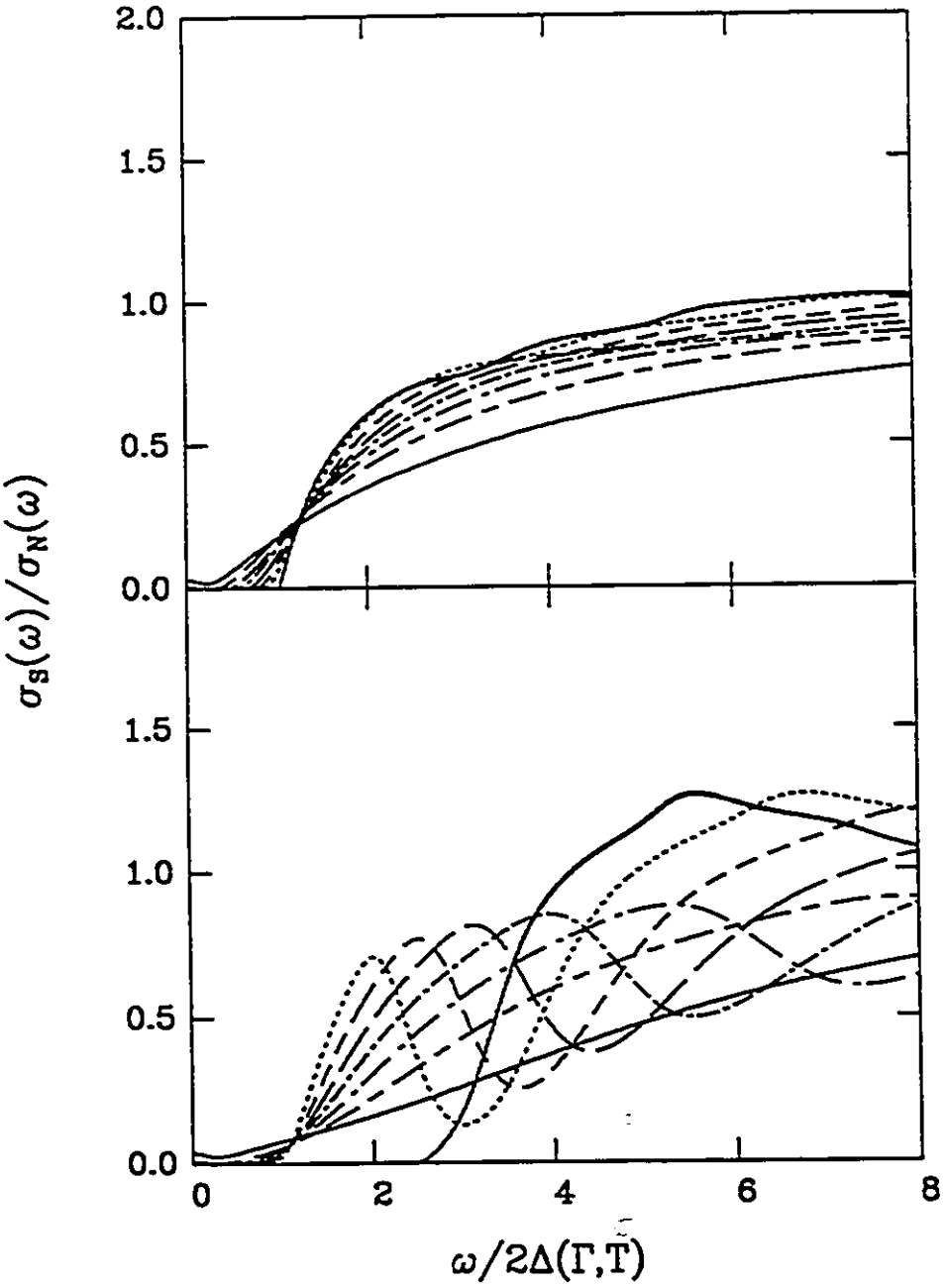


Figure 5.12 The ratio of the real part of the conductivity in the superconducting state to its value in the normal state $\sigma_S(\omega)/\sigma_N(\omega)$ as a function of frequency divided by the gap value of $2\Delta(\Gamma,T)$ for various reduced temperatures $T_c/T_c^o = 1.0$ (pure sample) (upper solid curve), 0.9 (dotted curve), 0.8 (short dashed curve), 0.7 (long dashed curve), 0.6 (short dashed-dotted curve), 0.5 (long dashed-dotted curve), 0.4 (long and short dashed curve), 0.3 (lower solid curve). All curves are for a reduced temperature $T/T_c = 0.1$ which approximates well zero temperature. The top frame is the dirty limit while the lower frame is for the clean limit.

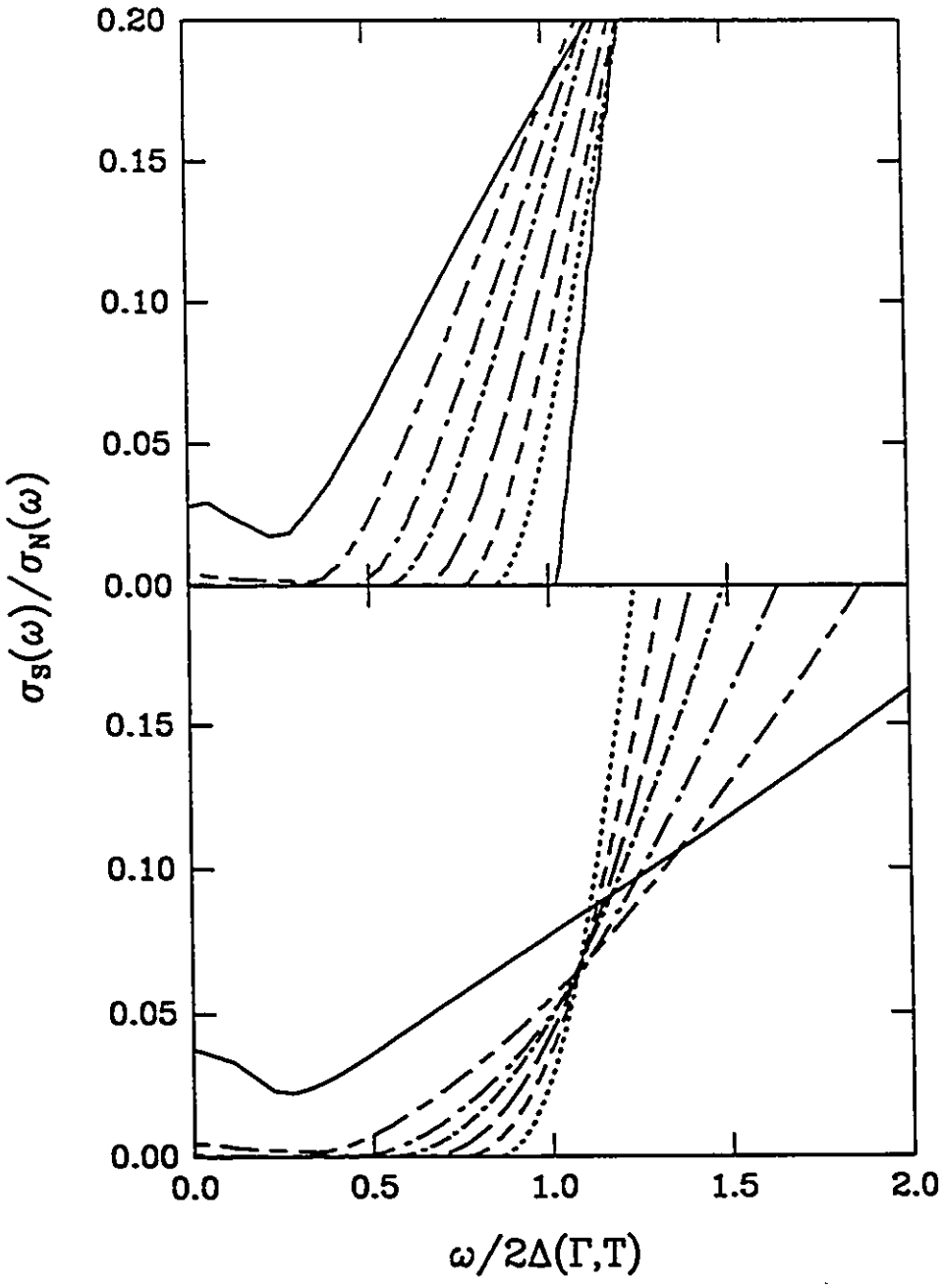


Figure 5.13 Same as for Fig. 5.12 but only the region up to $\omega/2\Delta(\Gamma,T) = 2.0$ is shown for emphasis.

referring to $t^+ = 0$ and dirty limit referring to $t^+ = 100$ meV. The differences between these curves is striking. First we note that absorption in the clean limit with no paramagnetic impurities starts at a frequency equal to twice the gap $\Delta(\Gamma,T) \equiv \Delta(\Gamma = 0, T = 0.1T_c)$, where $\Gamma \equiv 1/(2\tau_p)$, plus the energy of the lowest excitation in our fluctuation spectrum $\alpha^2F(\omega)$. In the dirty limit, by contrast, the absorption starts at $2\Delta(\Gamma,T)$ because the normal impurities now allow for conservation of energy and momentum simultaneously. When magnetic impurities are added to the clean limit, absorption is now possible at $2\Delta(\Gamma,T)$ but this absorption eventually decreases with increasing $\omega$ before the absorption edge corresponding to the solid curve reappears at least for the low $t^-$ curves. As magnetic impurity content is increased further the two peak absorption curve disappears and we arrive at the lower solid curve which shows no structure and is now closer to, although still different from, its dirty limit counterpart.

It is of interest to focus on the filling of the gap region that occurs when $t^-$ is increased from zero. This is shown more clearly in Fig. 5.13 where we show the same results as in Fig. 5.12 but here the scale on $\omega/2\Delta(\Gamma,T)$ extends only until 2.0. The optical absorption below $\omega = 2\Delta(\Gamma,T)$ is a consequence of the filling of the gap in the density of states as was shown in Fig. 5.10 for Pb. Note that the curve for the clean limit with no magnetic impurities does not now appear because it is zero up to a value of $\omega/2\Delta(\Gamma,T) = 2.5$ while even for the equivalent case in the dirty limit the absorption extends down to $\omega/2\Delta(\Gamma,T) = 1.0$. While there is initially a larger zero absorption region in the clean limit than in the dirty limit it is clear that when $T_c/T_c^\circ = 0.3$ (second solid curve) the amount of absorption near $\omega = 0$ in what was originally the gap region is slightly larger for clean limit

than for the dirty case. Of course as $\omega$ is increased toward $\omega/2\Delta(\Gamma,T) \cong 0.5$ and beyond, the dirty limit conductivity ratio is larger than the clean limit. Also as the impurity content is reduced and $T_c/T_c^\circ$ is closer to one, there is considerably less absorption in the gap region in clean as compared to dirty limit.

In Fig. 5.14, we show our results for the frequency dependence of the ratio of $\sigma_S(\omega)/\sigma_N(\omega)$ at various reduced temperatures for a sample with reduced $T_c/T_c^\circ = 0.9$. In Fig. 5.14, the reduced temperatures considered are $T/T_c = 0.9$ (dotted curve), 0.75 (short dashed curve), 0.5 (long dashed curve), 0.25 (short dashed-dotted curve) and 0.1 (solid curve). This last curve is reproduced from the dotted curves of Figs. 5.12 and 5.13. On comparison with the clean (bottom frame) and dirty (top frame) limit results, it is clear that the frequency and temperature variation predicted is completely different. The pattern obtained for the clean limit is very much more complicated and shows an impurity absorption peak at low frequencies before the main absorption at $2\Delta(\Gamma,T)$ plus the phonon energies in our model $\alpha^2F(\omega)$. Similar curves for a sample with a larger concentration of magnetic impurities ($T_c/T_c^\circ = 0.5$) are shown in Fig. 5.15. Here only the reduced temperatures $T/T_c = 0.75$ (short dashed curve), 0.5 (long dashed curve), 0.25 (short dashed dotted curve), and 0.1 (solid curve) are displayed. A similar pattern is observed with a rapid filling of the gap region as $T$ increases toward $T_c$. The differences between clean and dirty limit are still clearly seen but are less prominent than in the previous case. One notable consequence of the previously mentioned washing out of structure in the density of states with increasing paramagnetic impurity content, is the decrease in structure observed in moving from Fig. 5.14 to Fig. 5.15.

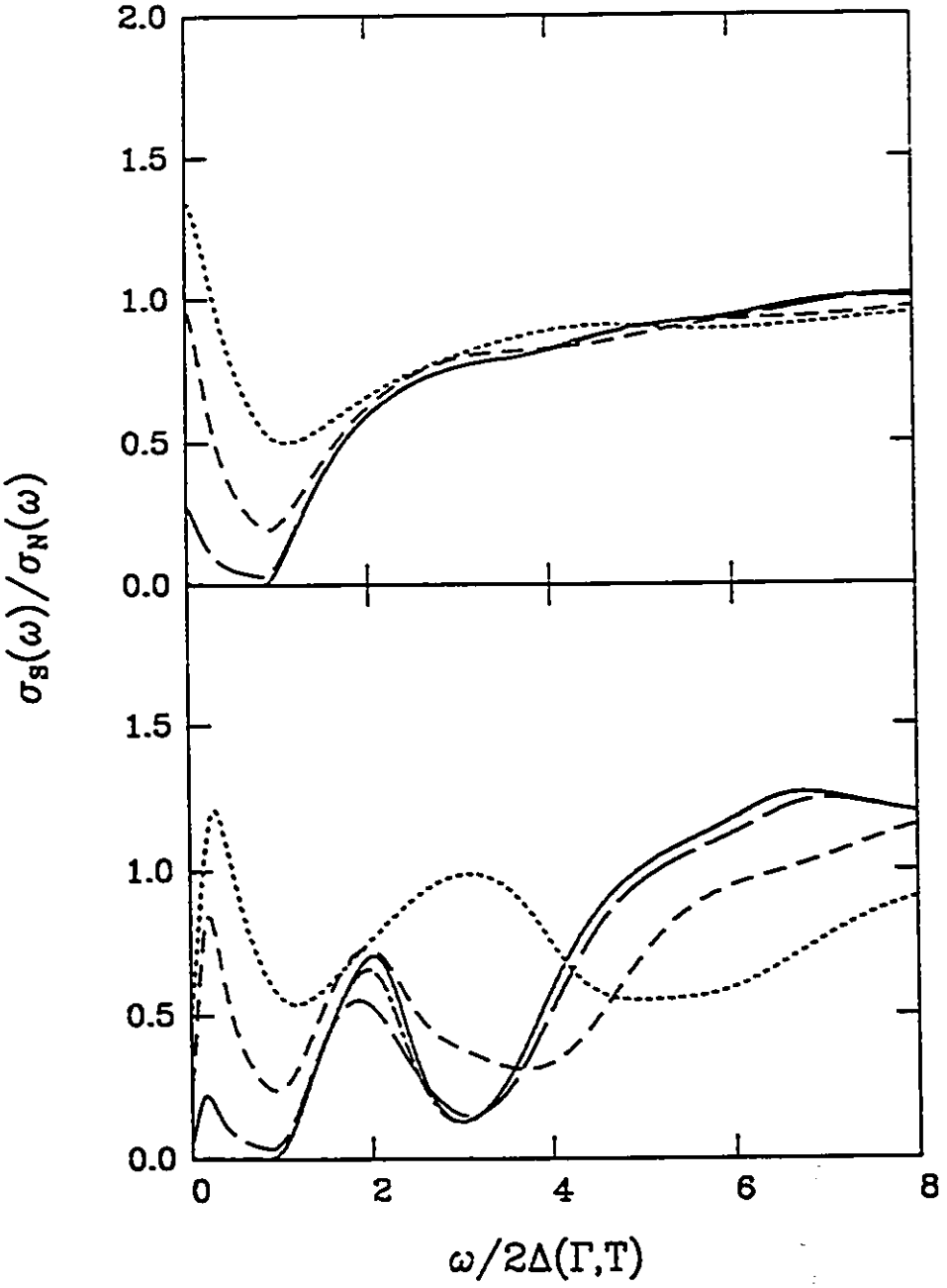


**Figure 5.14** The ratio of the real part of the conductivity in the superconducting state to its value in the normal state $\sigma_S(\omega)/\sigma_N(\omega)$ as a function of frequency divided by the gap value of $2\Delta(\Gamma,T)$ for various reduced temperatures $T/T_c = 0.9$ (dotted curve), 0.75 (short dashed curve), 0.5 (long dashed curve), 0.25 (short dashed-dotted curve), and 0.1 (solid curve). The top frame applies to the dirty limit and the bottom to the clean limit. The reduced critical temperature (due to a finite magnetic impurity concentration) is $T_c/T_c^\circ = 0.9$.

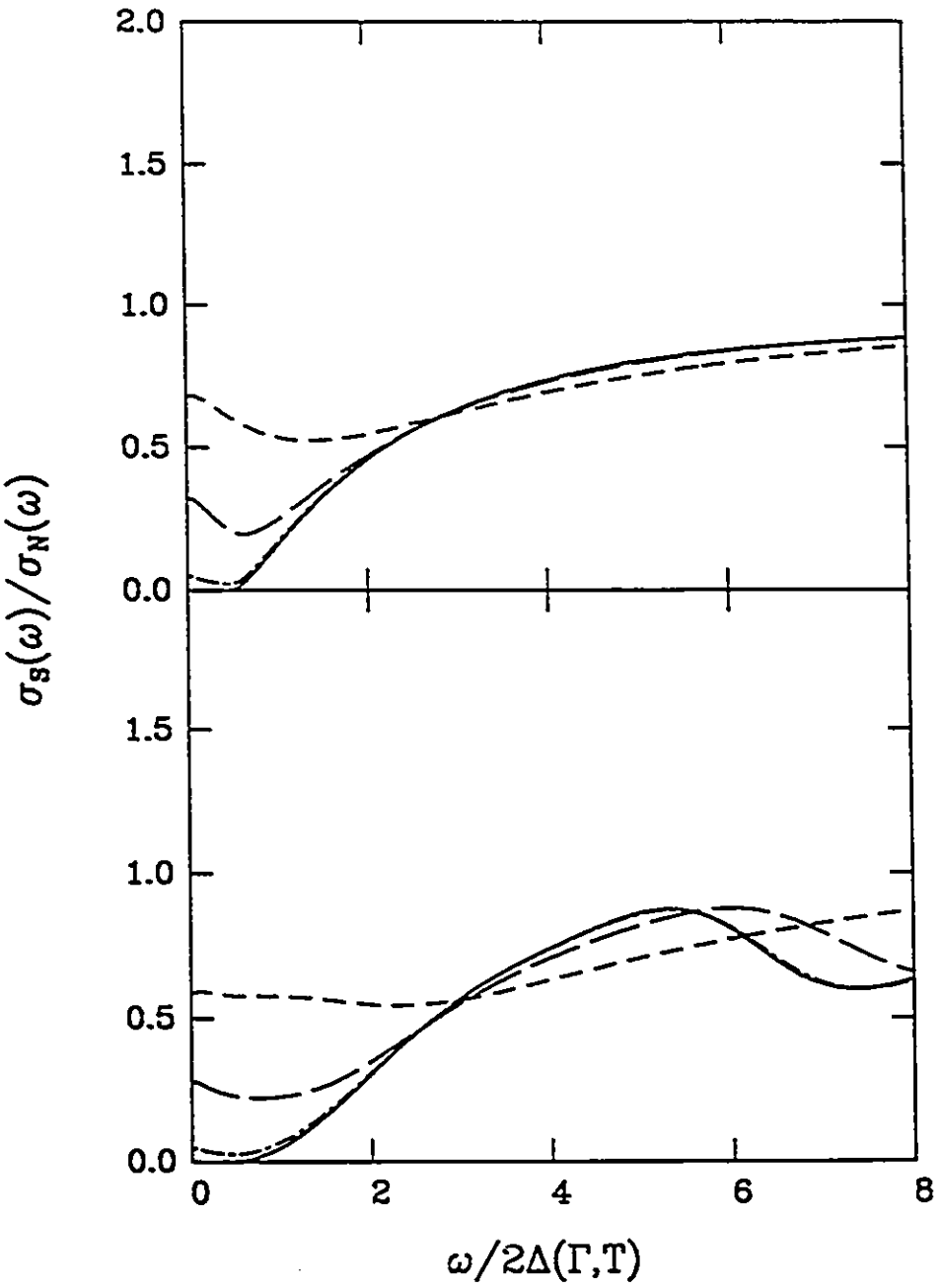


**Figure 5.15** Same as for Fig. 5.14 but now $T_c/T_c^o = 0.5$ and the reduced temperatures are 0.75 (short dashed curve), 0.5 (long dashed curve), 0.25 (short dashed-dotted curve), and 0.1 (solid curve).

In addition to examining the frequency dependent conductivity, we can also look at the low frequency microwave region and examine the temperature dependence at fixed frequency. For these calculations, we used the spectrum of Pb to avoid numerical problems associated with a lack of fluctuations in the low frequency region (which would be unphysical in the case of a phonon spectrum, and hence the truncated Lorentzian spectrum was unsuitable for this calculation).

In Fig. 5.16, we show the temperature dependence of the microwave conductivity as a function of normal impurity content but without paramagnetic impurity scattering, where once again we define our terminology to be: clean limit referring to $t^+ = 0$ and dirty limit referring to $t^+ = 100$ meV. The upper frame is for $\omega = 0.05$ meV and the lower one for $\omega = 0.005$ meV. Normal impurities are seen to enhance the coherence peak while in the clean limit no peak is observed at all. Also the curves quickly saturate towards the dirty limit. By $t^+ = 1$ meV, the curve is almost the same as the one for $t^+ = 100$ meV. The curves are higher in magnitude for the lower frequency as they are sampling more of the "normal" quasiparticle fluid. The opposite behaviour is seen in the clean limit as larger finite frequencies are needed to produce more available phonons for quasiparticle scattering and hence absorption. The nature of the plateau in the clean limit, which is more prominent for the higher frequency, is not understood and could be an artifact of the numerical calculation in the exact clean limit.

In Fig. 5.17, we display curves for $\omega = 0.05$ meV in the clean limit (upper frame) and the dirty limit (lower frame). Here, the curves show the effect of adding paramagnetic impurities. Curves are drawn for $T_c/T_c^\circ = 1$, 0.8, and 0.6. Numerical difficulties prevented us from going further towards

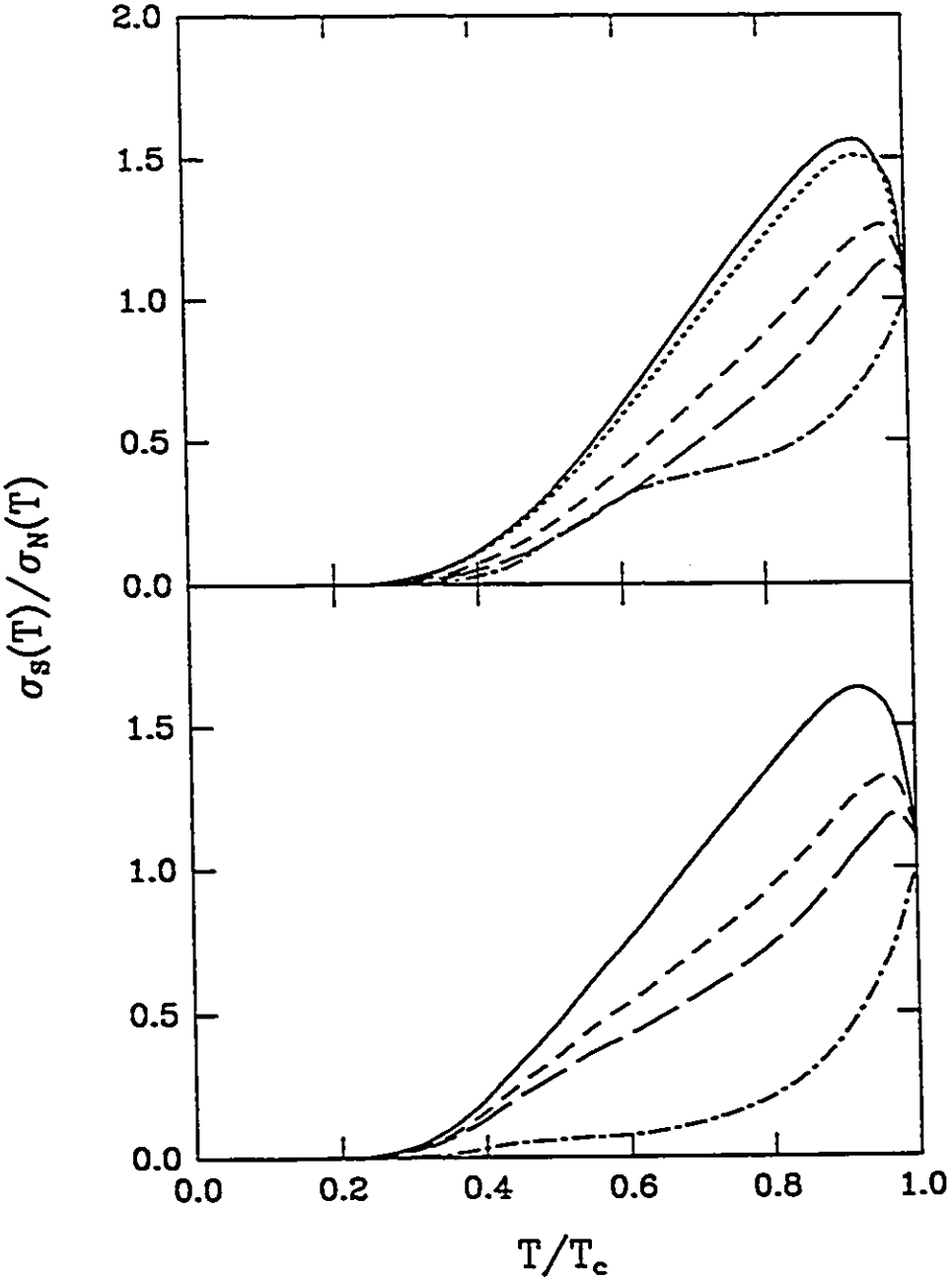


**Figure 5.16** The ratio of the real part of the conductivity in the superconducting state to its value in the normal state $\sigma_S(T)/\sigma_N(T)$ as a function of $T/T_c$ in the pure limit (*i.e.*, $T_c/T_c^\circ = 1$) for several values of the normal impurity scattering rate: $t^+ = 100.0$meV (solid curve), 1.0 meV (dotted curve), 0.2 meV (short dashed curve), 0.1 meV (long dashed curve), and 0.0 (short dashed-dotted curve). The upper frame is for $\omega = 0.05$ and the lower frame is for $\omega = 0.005$.

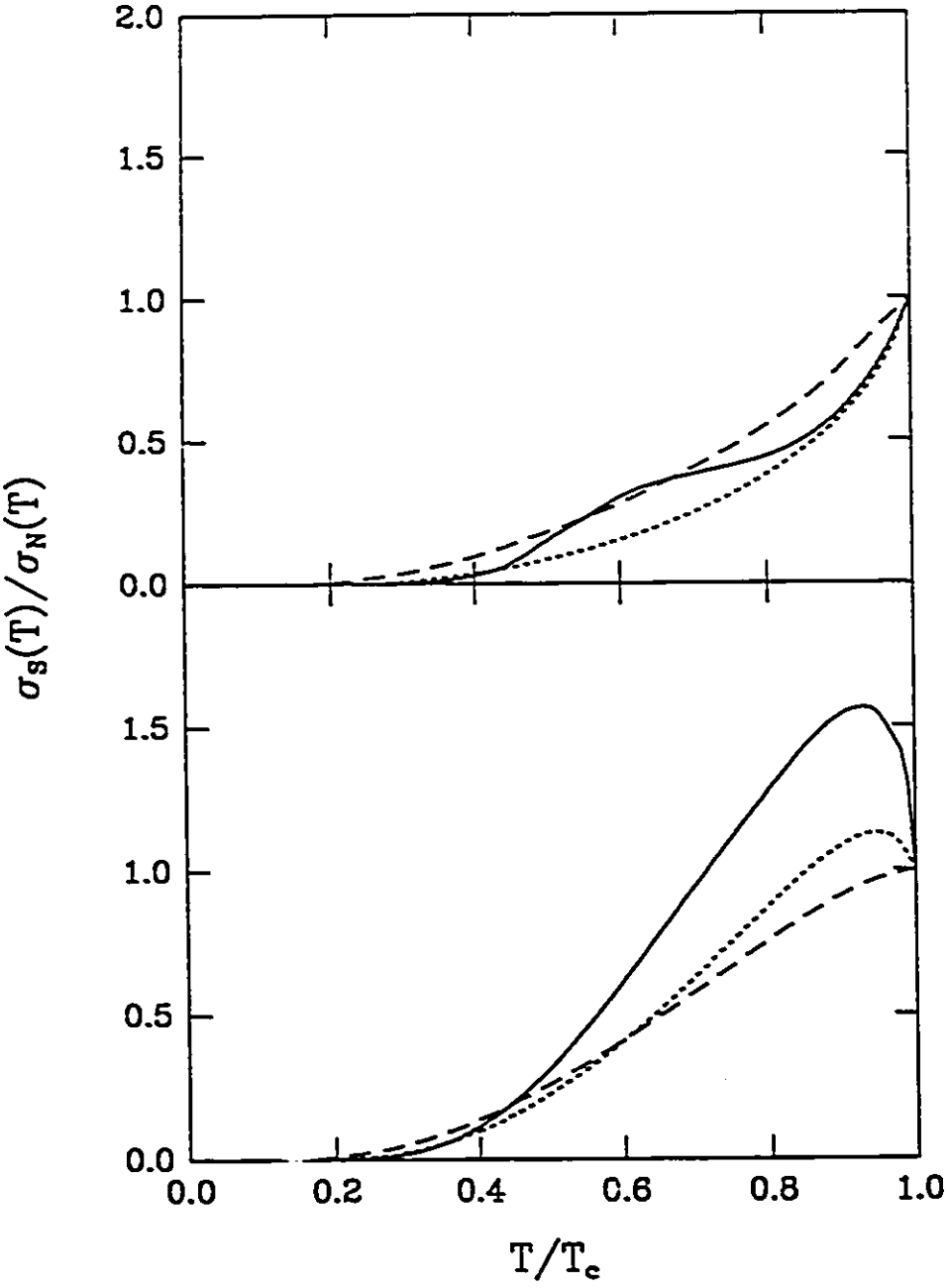


**Figure 5.17** The ratio of the real part of the conductivity in the superconducting state to its value in the normal state $\sigma_S(T)/\sigma_N(T)$ as a function of $T/T_c$ for several values of the paramagnetic impurity scattering rate in the clean and dirty limits: $T_c/T_c^\circ = 1.0$ pure sample (solid curve), 0.8 (dotted curve), and 0.6 (dashed curve). All curves are for $\omega = 0.05$ meV. The top frame is the clean limit while the lower frame is for the dirty limit.

the gapless region, which was unfortunate. However, the trend can be seen clearly. The behaviour here is very different in the clean and dirty limits. In the clean limit, adding paramagnetic impurities acts likes adding normal impurities and serves to increase the magnitude of the curves. However, in the dirty limit, the curves are reduced from the pure limit and the coherence peak is washed out. This is probably due to the paramagnetic impurities smearing out the density of states and thus reducing the available states for the quasiparticle recombination process [see Section 4.3]. Also another notable feature is the lengthening of the absorption tail at lower temperatures. This is a result of the filling in of the gap in the density of states allowing for eventual gaplessness. The exponential function that controls this low temperature behaviour depends on the magnitude of this gap. If we could have reached the gapless regime with our numerical work, we speculate that we would have seen absorption all the way down to zero temperature in these curves. Also note that the $T_c/T_c^\circ = 0.6$ curves in both limits are almost the same.

Finally, in Fig. 5.18, we show the effect of normal impurities on the optical conductivity at different concentrations of paramagnetic impurities. The upper frame is for $T_c/T_c^\circ = 0.8$ and the lower frame is for 0.6. Curves are drawn for $t^+ = 100$, 0.2, 0.1, and 0.0 meV. Again, we notice that the dirty limit coherence peak is reduced with increasing paramagnetic impurity concentration. In addition, the family of curves has tightened up implying that there may eventually be a universal curve for a certain concentration of spin-flip scatterers, with normal impurity scattering no longer having any effect.

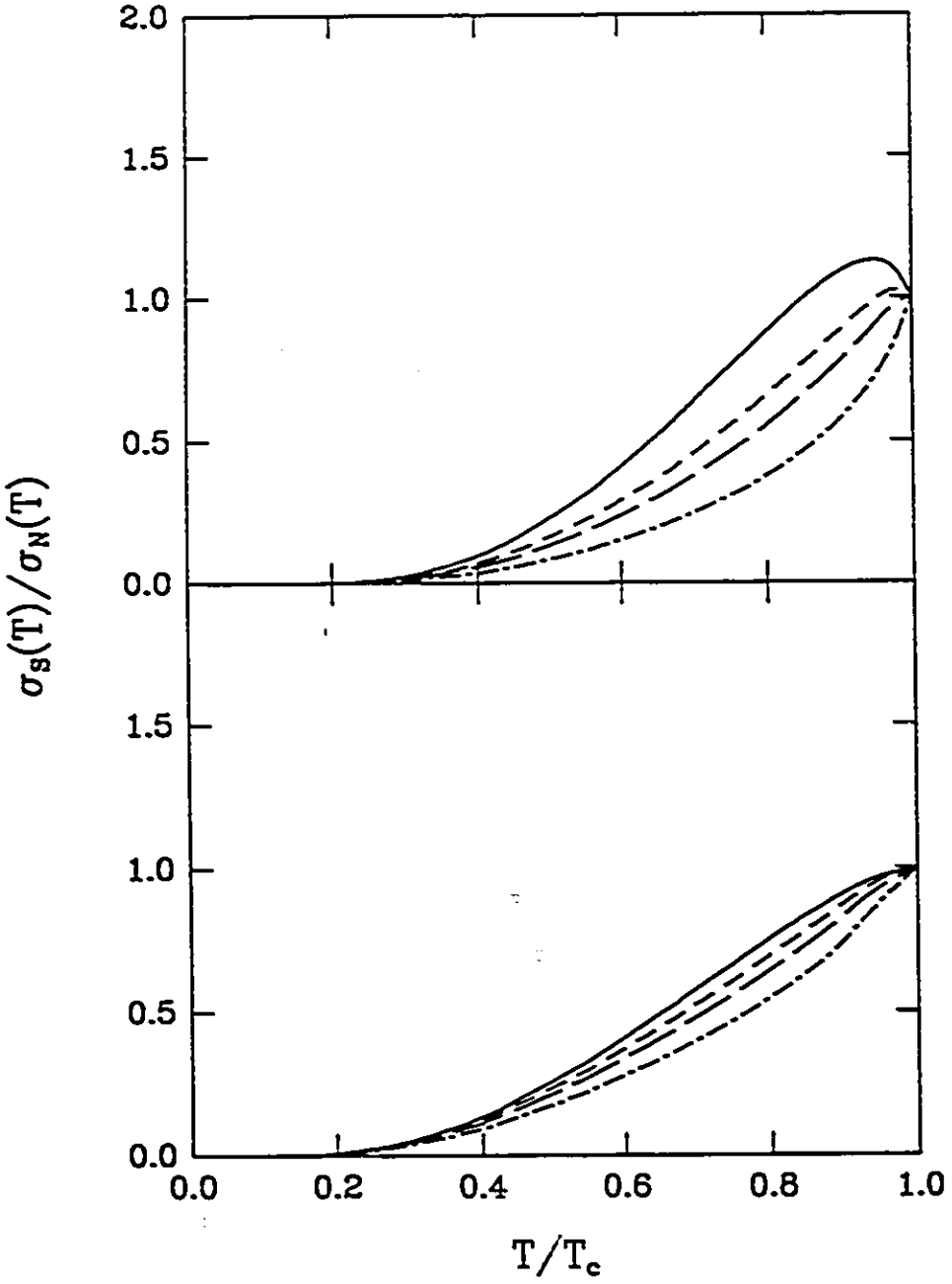


**Figure 5.18** The ratio of the real part of the conductivity in the superconducting state to its value in the normal state $\sigma_s(T)/\sigma_N(T)$ as a function of $T/T_c$ at $\omega = 0.05$ meV for several values of the normal impurity scattering rate: $t^+ = 100.0$ meV (solid curve), 0.2 meV (short dashed curve), 0.1 meV (long dashed curve), and 0.0 (short dashed-dotted curve). The upper frame is for $T_c/T_c^\circ = 0.8$ and the lower frame is for $T_c/T_c^\circ = 0.6$.

In summary, using the real frequency axis Eliashberg formulation of the finite frequency optical conductivity valid for arbitrary impurity concentration and generalized to include the pair-breaking effect of spin-flip scattering off magnetic impurities in the model of Abrikosov and Gor'kov, we have calculated the superconducting state conductivity as a function of frequency and temperature for several magnetic impurity concentrations. Our numerical results are expected to be accurate even near $T_c$ as no approximations in the analytic continuation from Matsubara frequencies to the real axis are used. Comparison of our results in the clean limit, which is expected to be the relevant limit in the high $T_c$ copper oxides, with similar results in the dirty, impurity-dominated limit reveals many important differences. As an example, in the clean limit, with no paramagnetic impurities, absorption at zero temperature starts only at an energy equal to twice the gap value plus the lowest excitation energy in the fluctuation spectrum involved in mediating the superconductivity. By contrast, in the dirty limit absorption starts at twice the gap with a sharp absorption edge. When paramagnetic impurities are added smearing into the gap region is generally more severe for the dirty limit than it is for the clean limit although for low values of $T_c/T_c^o$ the reverse can be true at low frequency *i.e.*, $\sigma_S(\omega)/\sigma_N(\omega)$ at $\omega = 0$ is larger in the clean than in the dirty case. As temperature is increased towards $T_c$, the gap is observed to fill but the details of this filling can be quite different in the clean and dirty limit. For finite paramagnetic impurity concentrations there is an appearance of an impurity absorption edge and peak around the gap value followed by a main absorption peak at higher energy when inelastic processes involving the fluctuation spectra become possible. While these features are most pronounced at zero temperature, they are found to persist even at finite

$T$ near $T_c$. Of course, right at $T_c$ the ratio $\sigma_S(\omega)/\sigma_N(\omega)$ must become flat and take on a value of 1.0.

It is hoped that our detailed prediction can be checked against experiments. The $Y_{1-x}Pr_xBa_2Cu_3O_7$ alloy series may be an appropriate system to investigate if it turns out that a description in terms of pair-breaking is valid. An alternate model for $Y_{1-x}Pr_xBa_2Cu_3O_7$ is the reduction of holes in the CuO planes by the Pr. Optical absorption experiments should be able to help differentiate among these two models.

## 5.5 CONCLUSIONS

To summarize, in this chapter, we have investigated the effect of paramagnons and paramagnetic impurities on various electromagnetic properties, in particular, the optical conductivity. It is found that while paramagnons are pair-breaking, strong coupling effects are observed due to strong renormalization through the Z-channel. This forms a plausible explanation for some of the features observed in the high $T_c$ superconductors and gives support to the marginal Fermi liquid model, which is formally similar.

Paramagnetic impurities smear out phonon structure in the density of states and fill in the gap. This behaviour is reflected in the low frequency absorption below $2\Delta$ in the finite frequency optical conductivity and also in the reduced structure in the Holstein region. Dramatic differences are predicted between the clean and dirty limits for the optical conductivity.

# Chapter 6

# Spin Glass Superconductivity

In this chapter, we will present results of calculations for superconductors which are also intrinsic spin glasses. This is related to the the work on paramagnetic impurities previously discussed and will be formally similar, the only change being a temperature-dependent scattering rate.

## 6.1 INTRODUCTION

In the previous chapter, we discussed paramagnetic impurities in the model of Abrikosov and Gor'kov (1961) for dilute non-interacting impurities that interact with the conduction electrons through spin-flip scattering in the weak scattering limit. Although some materials can be described by such a model, there is a large body of physics devoted to the understanding of localized moments that interact with each other and undergo ordering to states such as ferromagnetism or antiferromagnetism.

Anderson and Suhl (1959) have shown that the coexistence of these ordered states with superconductivity depends on whether the ordered state produces a macroscopic field on the scale of the coherence distance. In the case of ferromagnetism such a net field exists and superconductivity is not able to coexist due to the splitting of the spin-up and spin-down conduction electron bands by the magnetic field. On the other hand, antiferromagnetism and superconductivity are well known to coexist [Maple and Fischer (1982)]; superconductivity is then uninhibited by the magnetic ordering as the net magnetic field of the moments averages to zero.

Another possible magnetic state occurs in substitutionally disordered alloys, where the localized magnetic moments are randomly distributed and interact via the long-range Ruderman-Kittel-Kasuya-Yosida (RKKY) interaction mediated by the conduction electrons. This produces frustration in the magnetic ordering as not all magnetic moments can be simultaneously satisfied in their spin orientation with respect to the others. This leads to an infinite number of random configurations that are degenerate in energy but separated by large energy barriers so that one ground state cannot evolve into another on the laboratory time scale. These materials are known as spin glasses, of which Ag-Mn and Cu-Mn are examples of canonical metallic spin glasses. Coexistence of superconductivity and spin glass ordering has been observed by Davidov *et al.* (1977) in $Gd_xTh_{1-x}Ru_2$, $Gd_xCe_{1-x}Ru_2$, and $Gd_xLa_{3-x}In$.

Associated with the spin glass state is a characteristic temperature $T_f$ (the freezing temperature) below which the spins "freeze" into one of these random configurations. Spin glasses are characterized by a cusp in the magnetic susceptibility at $T_f$, no anomaly at $T_f$ in the specific heat other

than a broad maximum around $T_f$, and no Bragg peaks (which normally indicate long range magnetic order) in neutron scattering experiments.

The first attempt to describe the spin glass phase was by Edwards and Anderson (1975). As in all problems on phase transitions, one tries to identify an appropriate order parameter that will be non-zero in the phase of interest and zero in the disordered phase. Edwards and Anderson (1975) introduced an order parameter $q$ defined as:

$$q = \lim_{t \to \infty} < \vec{S}_i(t) \cdot \vec{S}_i(0) > \quad . \tag{6.1}$$

which is related to the probability that a spin with a given direction at $t = 0$ will have the same direction in the infinite time limit. This order parameter reflects the "frozen" nature of the spin glass state but has no spatial correlations as would be found in other magnetic order parameters. We make use of the temperature dependence of the configuration average of this order parameter in the spin glass model to be described here.

Several reviews and books exist on this topic [Binder and Young (1986); Fischer (1983); Moorjani and Coey (1984)]. Here we will be following a particular model given by Nass *et al.* (1981) and used more recently by Schachinger *et al.* (1988), Stephan and Carbotte (1991), and Perez Gonzalez *et al.* (1991). We will be presenting results which extend the work of Stephan and Carbotte (1991) [see also the dissertation of Stephan (1987)], which was done in the context of BCS theory, to strong coupling theory. In addition, we examine several properties not previously investigated.

Before describing our calculations we will first summarize the necessary theoretical background.

## 6.2 THE THEORETICAL MODEL

Nass *et al.* (1981) [see also Schachinger *et al.* (1988) and Stephan and Carbotte (1991)] have employed the standard form of the Eliashberg equations formulated for paramagnons (see Chapter 5) and have introduced the spin glass nature of the system through their choice of the spectral density for the spin fluctuations $P(\Omega)$.

Following the example of Dzyaloshinskii and Volovik (1978), they model the electron-spin spectral density by a dynamic contribution equivalent to the hydrodynamic limit of a Heisenberg paramagnet [Bennett and Martin (1965); Halperin and Hohenberg (1969); Forster (1975); Fischer (1979)] and a static component in the form of a Dirac delta function at zero frequency which represents spin freezing.

The electron-spin spectral density $P(\Omega)$ that enters the Eliashberg equations is related to the spin spectral density $B(q,\Omega)$ by

$$P(\Omega) = N(0)J^2 \int_0^{2k_F} \frac{q\, dq}{2k_F^2} B(q,\Omega) \quad , \tag{6.2}$$

where $N(0)$ is the single spin density of states at the Fermi momentum and $J$ is the electron magnetic impurity exchange constant, which couples the superconducting electron to the magnetic impurity.

The spin spectral density that Nass *et al.* (1981) suggest is given as

$$B(q,\omega) = B_d(q,\omega) + B_s(q,\omega) \quad , \tag{6.3}$$

where the dynamic part is given as

$$B_d(q,\omega) = \frac{D\chi\omega q^2}{\omega^2 + (Dq^2 - \omega^2\tau)^2} \tag{6.4}$$

and the static part is given by

$$B_s(q,\omega) = \pi(1 - e^{-\beta\omega})\tilde{Q}(T)\delta(\omega) \quad . \tag{6.5}$$

Here, $D$ is the spin diffusion constant, $\chi$ is the static susceptibility, which is taken to be independent of $q$, and $\tau$ is a phenomenological magnetic relaxation time that is used as a cutoff in the sum rules that apply to this spectral density [Nass *et al.* (1981); Stephan and Carbotte (1991); Bennett and Martin (1965); Halperin and Hohenberg (1969)]. In Eq. (6.5), $\tilde{Q}(T)$ is the temperature-dependent Edwards-Anderson order parameter [Edwards and Anderson (1975)]. Two models for the temperature dependence have been suggested for this quantity. Edwards and Anderson (1975) have derived the temperature dependence of this quantity from a mean field solution and find

$$\tilde{Q}(\bar{t}) = S^2(1 - \bar{t}) \quad . \tag{6.6}$$

where $\bar{t} = T/T_f$ and $S$ is the impurity spin. Nass *et al.* (1981) have also suggested the form

$$\tilde{Q}(\bar{t}) = S^2(1 - \bar{t}^2) \quad . \tag{6.7}$$

If the spin glass parameters $\chi$, $D$, and $\tau$ are allowed to vary arbitrarily, unphysical results are found for the tunneling density of states [Nass *et al.* (1981)] and in the transport properties [Fischer (1979)]. Therefore, two sum rules are imposed on the spin spectral density $B(q,\omega)$. The first is the standard $f$-sum rule [Forster (1975)]:

$$\int_{-\infty}^{\infty} \frac{d\omega}{\pi}\omega B(q,\omega) = \frac{\rho_s}{2\kappa}q^2 \quad , \tag{6.8}$$

where the $\kappa$ is the thermal conductivity and $\rho_s$ is the stiffness constant. The left hand side of Eq. (6.8) can be evaluated using Eqs. (6.3)-(6.5) to reduce the above sum rule to

$$D\chi = \frac{\rho_s}{2\kappa}\tau \quad , \tag{6.9}$$

where $D\chi$ is taken to be independent of temperature. The second sum rule comes from the definition of the structure factor [Nass *et al.* (1981)] and is given as:

$$\int_{BZ} d^3q \int_{-\infty}^{\infty} d\omega \frac{2}{1-e^{-\beta\omega}} B(q,\omega) = 2\pi S(S+1) \int_{BZ} d^3q \quad , \tag{6.10}$$

where Nass *et al.* (1981) have used a spherical Brillouin zone ($BZ$) with a radius of $2k_F$. We are not attempting to derive these results here but prefer to refer the reader to the literature [Nass *et al.* (1981); Stephan and Carbotte (1991)].

Keller (1981), in the case of a ferromagnet, and Nass *et al.* (1981) have found that the terms for $\lambda(n-m)$ where $n \neq m$ in the dynamic part of the Eliashberg equations are negligible compared to the the $n = m$ term $\lambda(0)$ and hence it is only necessary to keep the $n = m$ term in the Matsubara frequency sums. Thus, $\lambda_d(0)$ can be evaluated using the sum rules [Stephan and Carbotte (1991)] to be

$$\lambda_d(0) = N(0)J^2\pi\chi \quad . \tag{6.11}$$

It can be shown (as was done in Chapter 5) that the problem has now been reduced from one of dynamic spin fluctuations to one of temperature-dependent static impurity scattering where

$$\frac{1}{2\pi\tau} = T\lambda(0)$$

$$= T[\lambda_d(0) + \lambda_s(0)]$$

$$= N(0)J^2\pi[T\chi + \tilde{Q}(\tilde{t})] \quad . \tag{6.12}$$

Therefore, we are now solving the standard Eliashberg equations modified for Abrikosov-Gor'kov impurities, $\alpha \propto 1/\tau_p$, but now $\alpha$ is temperature-dependent (*i.e.*, $\alpha \rightarrow \alpha(T)$) and is given by

$$\alpha(T) \propto T\lambda(0) \tag{6.13}$$

and the effective scattering rate $t_-^{sg}$ in the spin glass state is reduced from the Abrikosov-Gor'kov scattering rate $t_-^{ag}$ by

$$t_-^{sg} = t_-^{ag}\frac{\alpha(T)}{\alpha(T_c)} \quad . \tag{6.14}$$

Finally, we need a model for the freezing temperature in terms of the concentration of impurities. This is taken from the experimental observation that $T_f$ is proportional to the concentration of impurities:

$$T_f = \frac{n_i}{n_c}RT_c^\circ \quad , \tag{6.15}$$

where $n_i$ is the Abrikosov-Gor'kov impurity concentration and $n_c$ is the critical concentration of Abrikosov-Gor'kov impurities that reduce $T_c$ to zero. $T_c^\circ$ is the $T_c$ in the absence of impurities and $R$ is a dimensionless constant between 0 and 1.

## 6.3 THERMODYNAMIC PROPERTIES

In what follows here, we will be using results previously obtained by Walter Stephan [Stephan and Carbotte (1991); Stephan (1987)] for the temperature-dependent scattering rate. Stephan solved for the temperature

dependence of $\alpha(T)$ for several values of the spin glass parameters $R$, $D$, $\tau$, and either $\tilde{Q}(\tilde{t}) = S^2(1 - \tilde{t})$ or $\tilde{Q}(\tilde{t}) = S^2(1 - \tilde{t}^2)$. We have chosen only two of these cases to illustrate the two possible temperature-dependent scenarios that are likely to occur in this model. For a knowledge of how these quantities might vary with a change in one or the other of the spin glass parameters, the reader should consult the work of Stephan [Stephan and Carbotte (1991); Stephan (1987)]. Stephan used this scattering rate to solve for several superconducting properties in BCS theory. Here, we use this scattering rate to calculate superconducting properties in Eliashberg theory and, in addition, to examine properties not previously investigated by Stephen (1987).

In Fig. 6.1, we show the temperature dependence of the dimensionless diffusion constant $\tilde{D}(\tilde{t}) = D(2k_F)^2/T_f$, the dimensionless susceptibility $\tilde{\chi}(\tilde{t}) = T_f\chi$, and the scattering rate $\alpha(\tilde{t})$ normalized to its infinite temperature limit $\alpha(\infty)$, for two sets of parameters, which we will call Case 1 (solid line) and Case 2 (dashed curve). Here $\tilde{t} = T/T_f$. In Case 1, $\tilde{D}(1) = 1$, $\tilde{Q}(\tilde{t}) = S^2(1 - \tilde{t}^2)$, $R = 0.1$, and $\tilde{\tau} = T_f\tau = 0.2$. In Case 2, $\tilde{D}(1) = 2$, $\tilde{Q}(\tilde{t}) = S^2(1 - \tilde{t})$, $R = 0.4$, and $\tilde{\tau} = 0.2$. These quantities are calculated from the sum rules of Eqs. (6.8)-(6.10) using a numerical subroutine provided by W. Stephan. These curves and many more like them have already been presented by Stephan [Stephan and Carbotte (1991); Stephan (1987)].

In Fig. 6.1, as the diffusion constant is linear in temperature above $T_f$ and the product of $D\chi$ is temperature independent, this implies that the behaviour of the susceptibility above $T_f$ varies as the inverse of $T$, which is just the Curie-Weiss Law. Notice that a cusp in the susceptibility occurs at the freezing temperature $T_f$. The scattering rate reduces from the high temperature limit with significant reduction occurring below $T_f$ as the spins

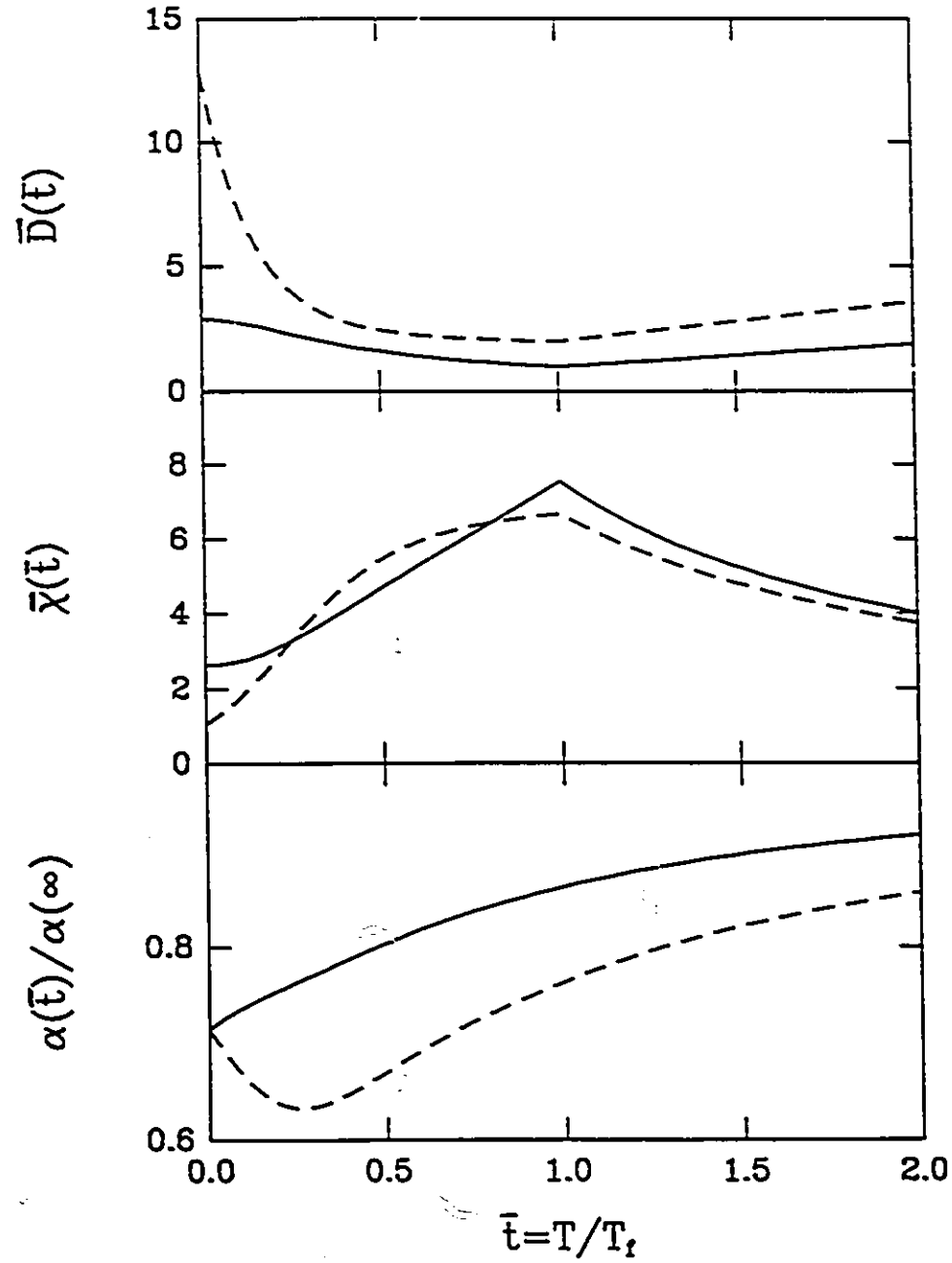


**Figure 6.1** The temperature dependence of the spin glass parameters used in the model in the text. The top frame shows the dependence of the diffusion parameter $\bar{D}(\bar{t})$, the center frame displays the susceptibility $\bar{\chi}(\bar{t})$ and the bottom frame shows the scattering rate $\alpha(\bar{t})$ normalized to its infinite temperature limit. The solid curves correspond to what we call Case 1 and the dashed curves correspond to our notation, Case 2. In Case 1, $\bar{D}(1) = 1$, $\bar{Q}(\bar{t}) = S^2(1 - \bar{t}^2)$, $R = 0.1$, and $\bar{\tau} = 0.2$. In Case 2, $\bar{D}(1) = 2$, $\bar{Q}(\bar{t}) = S^2(1 - \bar{t})$, $R = 0.4$, and $\bar{\tau} = 0.2$.

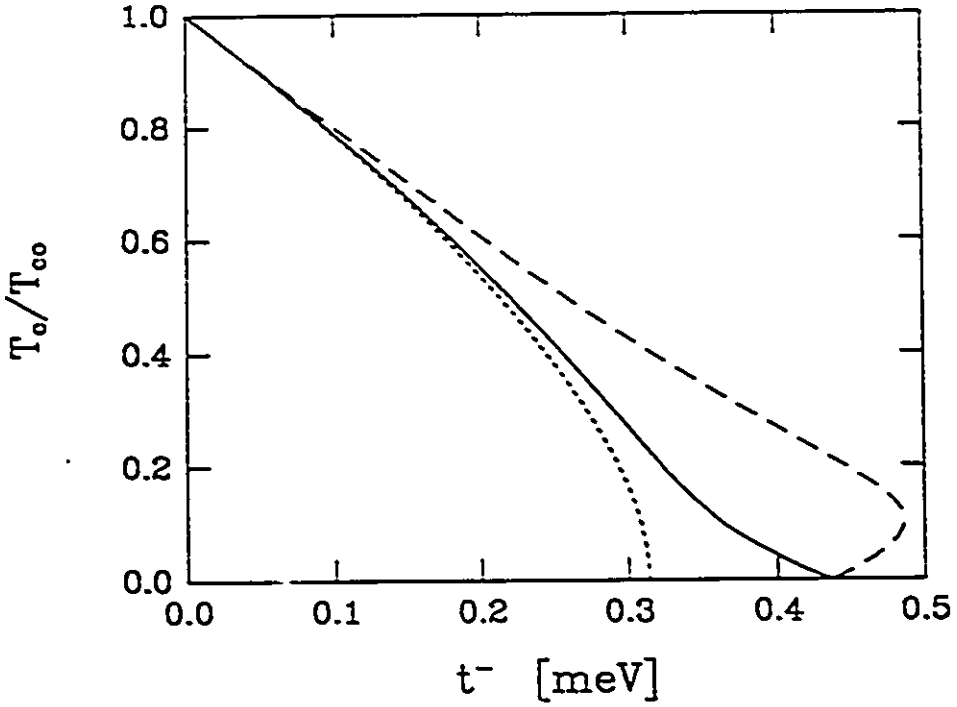


**Figure 6.2** $T_c/T_c^\circ$ versus the magnetic scattering rate $t_-$. The dotted curve is the Abrikosov-Gor'kov result for the phonon model used in the text. The solid curve corresponds to Case 1 in our spin glass model and the dashed curve corresponds to Case 2.

freeze into a random configuration and are unavailable to spin-flip scatter. In Case 2, the rate dips and then recovers producing reentrant phenomena as we will later discuss. The zero temperature limit of the scattering rate is given proportional to $S^2$ whereas the high temperature limit proportional to $S(S+1)$, hence the ratio of $a(\bar{t})/a(\infty)$ approaches $S^2/[S(S+1)]$ at zero temperature. In this work, we have used $S = 5/2$ (keeping Ag-Mn in mind). As a result, these curves approach a value of 0.71428 at $\bar{t} = 0$.

In Fig. 6.2, we show the $T_c$ curves, for these models as a function of impurity scattering concentration $t_-$, which resulted when we solved the Eliashberg equations with the temperature-dependent scattering rate given in the bottom frame of Fig. 6.1. Again, the solid curve corresponds to

Case 1 and the dashed curve to Case 2. The dotted curve is the Abrikosov-Gor'kov curve that results for the same parameters but with no temperature dependence in the impurity scattering (*i.e.*, $\alpha(T) = \alpha(\infty)$ in Eq. (6.14)). Here we have used in the Eliashberg equations a delta function for the electron phonon spectral density $\alpha^2F(\omega) = (\omega_E\lambda_E/2)\delta(\omega-\omega_E)$, with $\omega_E = 10$ meV, $\mu^* = 0$, $T_c^\circ = 11.604\text{K} = 1$ meV, which sets $\lambda_E = 0.9$. One sees the famous Abrikosov-Gor'kov result, that $T_c$ is reduced from its pure value $T_c^\circ$ on addition of magnetic impurities. For small concentrations, the dependence of $T_c$ on $t_-$ is linear. There is also a critical concentration at which the superconductivity is destroyed. In the case of the spin glass, the temperature-dependent scattering rate is reduced from the corresponding Abrikosov-Gor'kov rate as the spins freeze, reducing the effectiveness of the impurity spin to break Cooper pairs through spin-flip scattering. Thus, the spin glass material may sustain a larger concentration of impurities for the same $T_c$. The point at which the critical concentration of spin glass impurities occurs is controlled by the $\bar{t} = 0$ point in the bottom frame of Fig. 6.1 or the ratio $S^2/[S(S+1)]$, with the critical $t_-^{sg}$ equal to $(S+1)/S$ times the critical $t_-^{sg}$.

Note, that for Case 2 (dashed curve) we can expect reentrant phenomena at the lower end of the $T_c$ curve where for the same concentration, two values of $T_c$ exist with a region of superconductivity in between. [Note, that if this diagram were alternatively labelled as a phase diagram with T on the y-axis rather than $T_c$, then the area to the left of a curve would correspond to the superconducting state and the area to the right the normal state.] Reentrant superconductivity is the case where below a temperature $T_{c_1}$ a material becomes superconducting but below an even lower temperature $T_{c_2}$ ($T_{c_2} < T_{c_1}$), the material reenters the normal phase again due to the

Table 6.1

| $T_c/T_c^\circ$ | $t_-^{(1)}$ (meV) | Case 1 $t_-^{(2)}$ (meV) | Case 1 $T_f/T_c$ | Case 2 $t_-^{(2)}$ (meV) | Case 2 $T_f/T_c$ | line type |
|---|---|---|---|---|---|---|
| 1.00 | 0.0000 | 0.0000 | 0.0000 | 0.0000 | 0.0000 | solid line |
| 0.95 | 0.0246 | 0.0247 | 0.0098 | 0.2478 | 0.0195 | - - - - - - |
| 0.80 | 0.0945 | 0.0955 | 0.0445 | 0.0976 | 0.0891 | - - - - - |
| 0.58 | 0.1846 | 0.1893 | 0.1200 | 0.2003 | 0.2400 | — — — |
| 0.34 | 0.2620 | 0.2768 | 0.2005 | 0.3124 | 0.5810 | - - - - - |
| 0.15 | 0.3021 | 0.3409 | 0.7592 | 0.4287 | 1.5183 | — - — - |

Parameters for the curves shown in Figs. 6.2-6.11. Case 1 refers to the spin glass parameters $D = 1$, $\tilde{Q}(\bar{t}) = S^2(1-\bar{t}^2)$ and $R = 0.1$. Case 2 refers to $D = 2$, $\tilde{Q}(\bar{t}) = S^2(1-\bar{t})$ and $R = 0.4$. Parameters used for the pure case are $T_c^\circ = 11.604\text{K} = 1$ meV, $\omega_E = 10$ meV, and $\mu^* = 0$.

formation of magnetic order, such as ferromagnetism, which inhibits the superconductivity. Examples of reentrant superconductors are $ErRh_4B_4$ [Fertig *et al.* (1977)] and $HoMo_6S_8$ [Ishahawa and Fischer (1977)], where their reentrance is due to a ferromagnetic transition occurring at $T_{c_2}$. In Case 2, it is also possible for a spin glass superconductor to exhibit reentrant phenomena, as has been observed in $La_{1-x}Gd_xRu_2$ [Jones *et al.* (1978)].

We will now present results for these two cases for the free energy difference, the thermodynamic critical magnetic field, the deviation function, and the specific heat difference. Similar results have been presented by Stephan and Carbotte (1991) for the critical magnetic field and the deviation function, however, our results will go further by extending the parameters into the reentrant region of the model. In all graphs to be presented from here on, we have plotted our results in three-frame figures with the upper frame displaying the Abrikosov-Gor'kov result, the middle frame showing the analogous results for Case 1 and the bottom frame for Case 2. In addition,

the curves in each figure are given for the same set of parameters; we have listed these in Table 6.1. Curves will be presented for six cases: no magnetic impurities $T_c/T_c^o = 1.00$ (solid line), $T_c/T_c^o = 0.95$ (- - - -), 0.8 (– – –), 0.58 (— — —), 0.34 (- - - -), and 0.15 (— - — -). The corresponding Abrikosov-Gor'kov scattering rate $t_-^{ag}$ and spin glass scattering rate $t_-^{sg}$ for each case are given in Table 6.1. The freezing temperature $T_f$ with respect to $T_c$ is also given for the two spin glass cases.

With our parameters now defined, we will proceed to present results for various thermodynamic quantities: the free energy difference, the thermodynamic critical magnetic field, the deviation function, and the electronic specific heat difference. These results are based upon a calculation of the free energy. The difference in free energy between the superconducting and normal state ($\Delta F = F_s - F_N$) is given in terms of the Matsubara gaps and frequencies, which follow from the solution of the Eliashberg equations modified for the spin glass contribution, by the Bardeen-Stephen formula [Bardeen and Stephen (1964)]:

$$\Delta F = -N(0)\pi T \sum_{n=-\infty}^{\infty} [\sqrt{\omega_n^2 + \Delta_n^2} - |\omega_n|] \left[ Z_S(i\omega_n) - Z_N(i\omega_n) \frac{|\omega_n|}{\sqrt{\omega_n^2 + \Delta_n^2}} \right] , \tag{6.16}$$

where $N(0)$ is the single spin density of states at the Fermi momentum. From this the thermodynamic critical magnetic field $H_c(T)$, which is related to the condensation energy of the superconducting state, is given as

$$H_c(T) = [-8\pi\Delta F]^{1/2} \quad . \tag{6.17}$$

This quantity very closely follows a temperature dependence $(1 - t^2)$, where $t = T/T_c$, and so to differentiate between curves, it is more common to present

the deviation function $D(t)$ defined as

$$D(t) = \frac{H_c(t)}{H_c(0)} - (1 - t^2) \quad . \tag{6.18}$$

Also, the electronic specific heat difference is given in terms of the free energy difference by

$$\Delta C(T) = -T\frac{d^2\Delta F}{dT^2} \quad . \tag{6.19}$$

In Figs. 6.3 and 6.4, we plot the difference in free energy $\Delta F$ and the thermodynamic critical magnetic field $H_c(T)$, respectively. In both cases we normalized these quantities to the zero temperature value in the pure case (solid curve). This reduces the plot to dimensionless quantities but permits the reduction in free energy and the corresponding critical magnetic field due to the magnetic impurities to be seen with clarity. The parameters are given in Table 6.1. Frame (a) shows the Abrikosov-Gor'kov results while frames (b) and (c) show the results of Case 1 and Case 2, respectively, for the spin glass model used here.

Aside from the overall depression in the magnitude of these quantities, we note that at low temperatures in Case 1, there is an upturn in the temperature dependence, whereas, in Case 2 there is a downturn. The upturn in Case 1 reflects the scattering rate steadily decreasing as the temperature is lowered, thus, allowing the superconducting state to lower its energy and become more stable.

On the other hand, in Case 2, the scattering rate begins to recover and grow stronger at lower temperatures, thus, inhibiting the superconducting pairing. Eventually for large spin glass impurity scattering we see reentrant behaviour (best exhibited in (c) of Fig. 6.4), where the sample reverts to the normal state at a reduced temperature around 0.35.

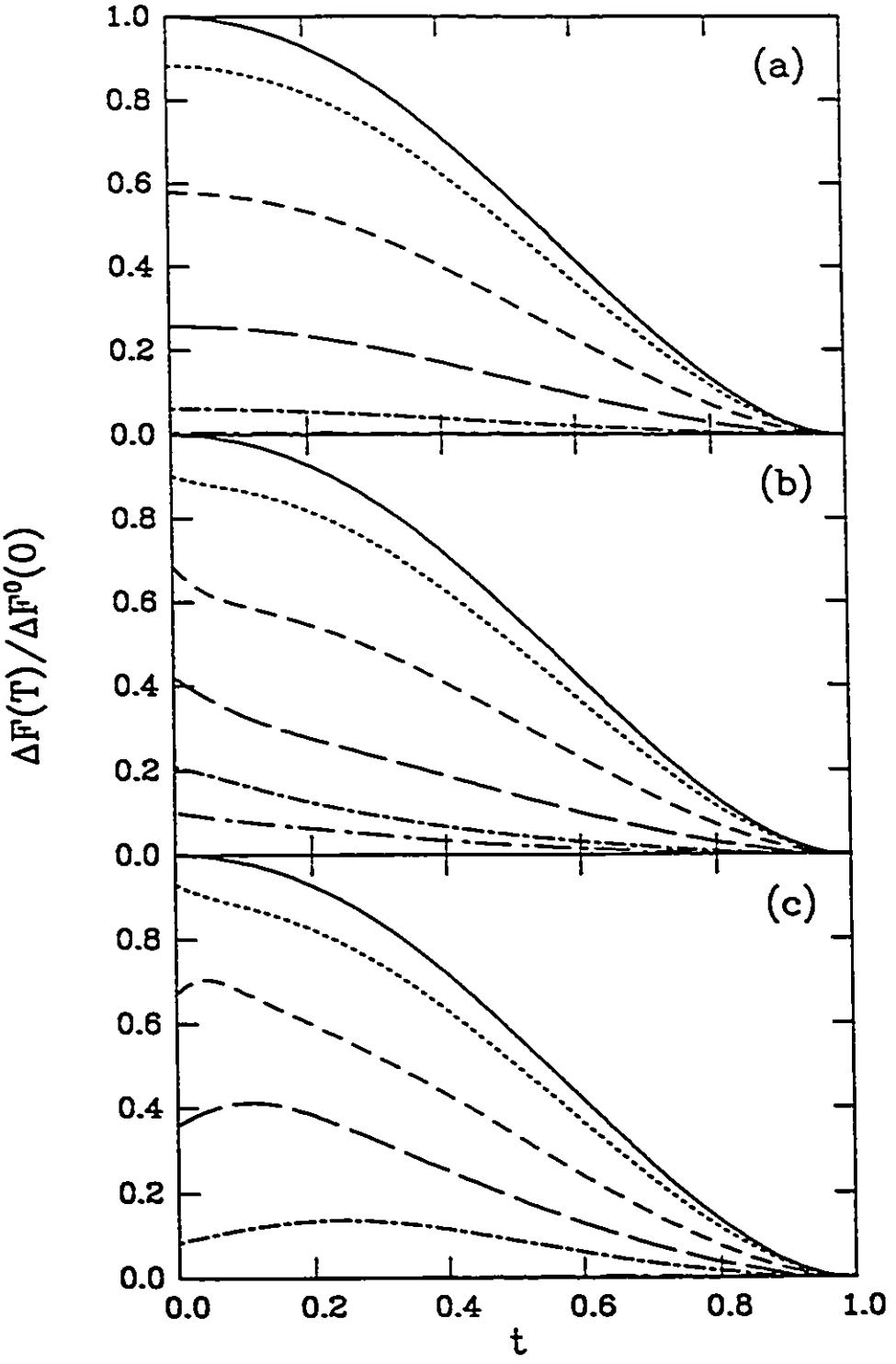


**Figure 6.3** The free energy difference $\Delta F$ normalized to the zero temperature value in the pure case versus the reduced temperature $t = T/T_c$. (a) Abrikosov-Gor'kov impurities. (b) Spin glass impurities for Case 1. (c) Spin glass impurities for Case 2. See Table 6.1 for detail of the parameters.

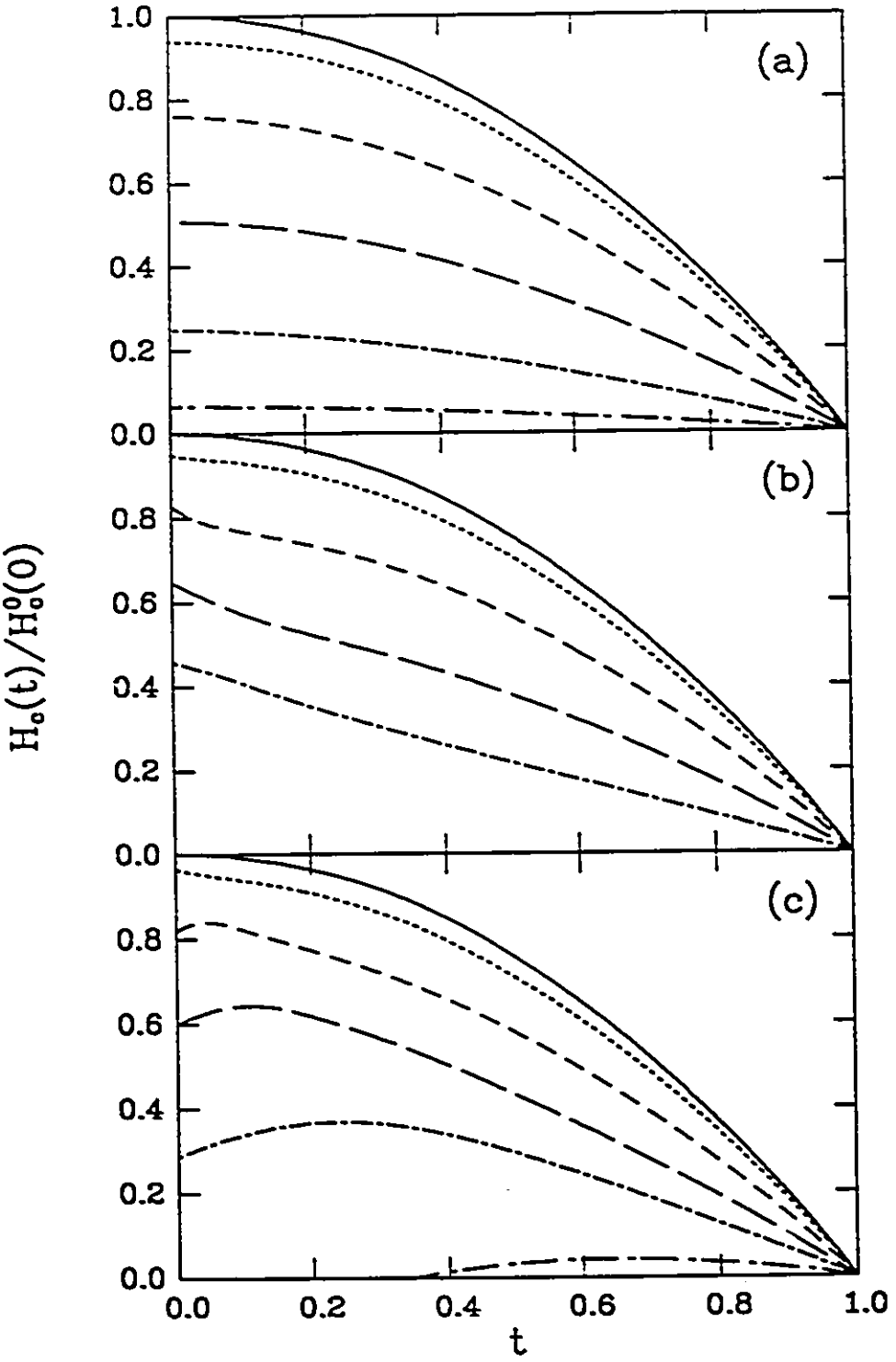


**Figure 6.4** The thermodynamic critical magnetic field $H_c(T)$ normalized to the zero temperature value in the pure case versus the reduced temperature $t = T/T_c$. (a) Abrikosov-Gor'kov impurities. (b) Spin glass impurities for Case 1. (c) Spin glass impurities for Case 2. See Table 6.1 for detail of the parameters.

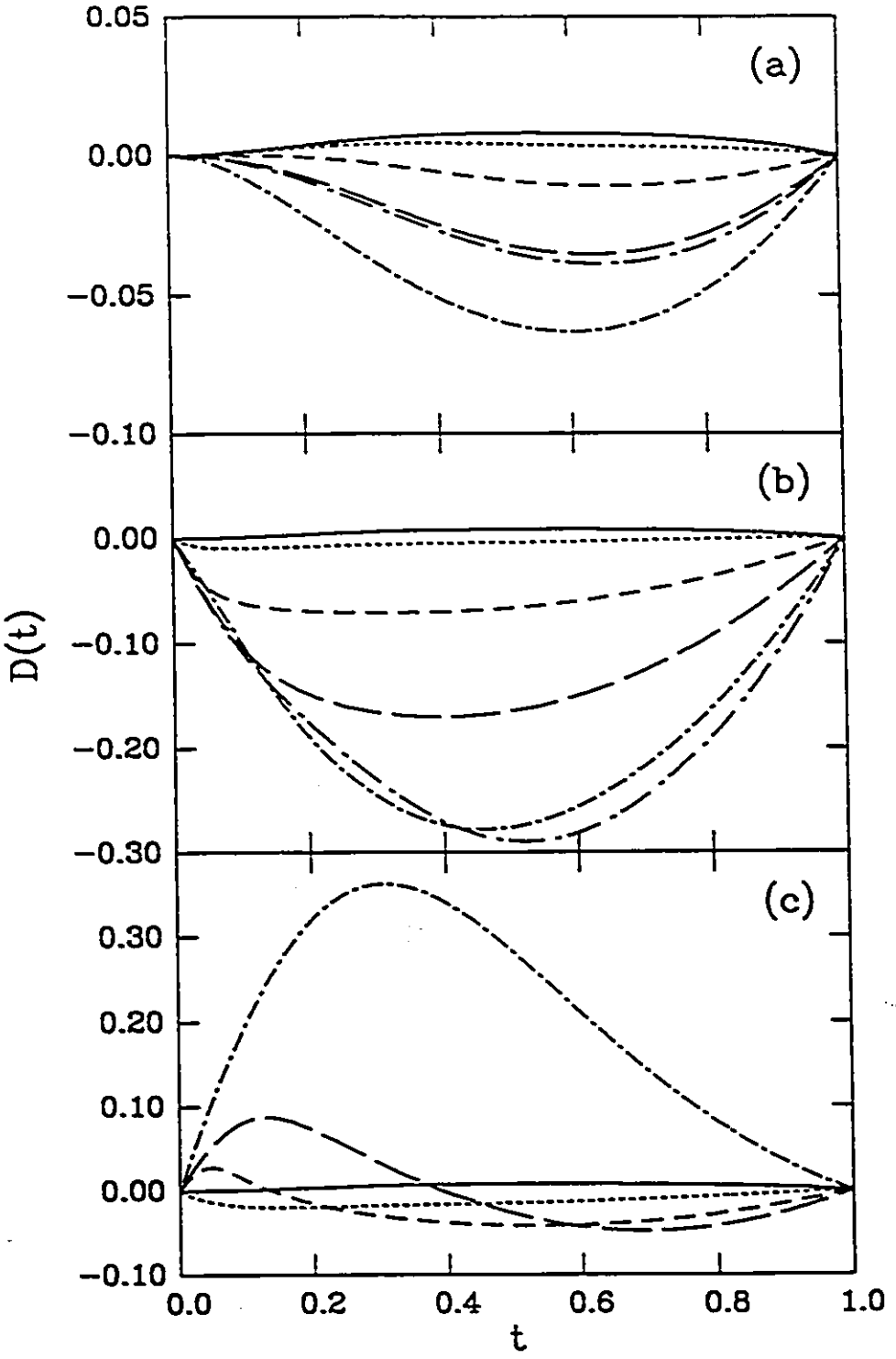


**Figure 6.5** The thermodynamic critical magnetic field deviation function $D(t)$ versus the reduced temperature $t = T/T_c$. (a) Abrikosov-Gor'kov impurities. (b) Spin glass impurities for Case 1. (c) Spin glass impurities for Case 2. See Table 6.1 for detail of the parameters.

To better illustrate the difference in the curvature of the critical magnetic field curves, we plot the deviation function in Fig. 6.5. The curves (b) for the spin glass model corresponding to Case 1 are much deeper than in the Abrikosov-Gor'kov case and show a progressive shift of the minimum to larger negative values and to higher temperatures with increasing impurity content. The curves (c) corresponding to Case 2 show a positive deviation particularly at low temperatures with the maximum shifting to higher temperatures and larger magnitudes with increasing impurity content. On these plots, the features distinguishing Case 1 and Case 2 are quite strong and, in particular, Case 2 has a strong signature with regard to the ordinary Abrikosov-Gor'kov case that should make it observable in experiments.

Finally, in Fig. 6.6. we display results for the calculation of the electronic specific heat difference normalized to the value at $T_c$. Here the curves exhibit a very strong and unusual temperature dependence. The Abrikosov-Gor'kov curves show a shift upwards at higher temperatures with increasing impurity scattering, resulting in the slope of the jump just below $T_c$ decreasing with increased scattering. Overall, the shift in area under the curves reflects the entropy constraint of:

$$\Delta S = \int_0^{T_c} \frac{\Delta C}{T} dT = 0 \quad , \tag{6.20}$$

where $\Delta S$ refers to the difference in entropy between the normal and superconducting states which of course must be zero at $T_c$ (*i.e.*, $\Delta S(T_c) = 0$).

For the two cases considered for the spin glass model there is considerable deviation from the usual temperature dependence with a peak at low temperatures for Case 1 and a dip for Case 2. Notice again the reentrant behaviour in Case 2 where the curve returns to a value of 1 (the normal

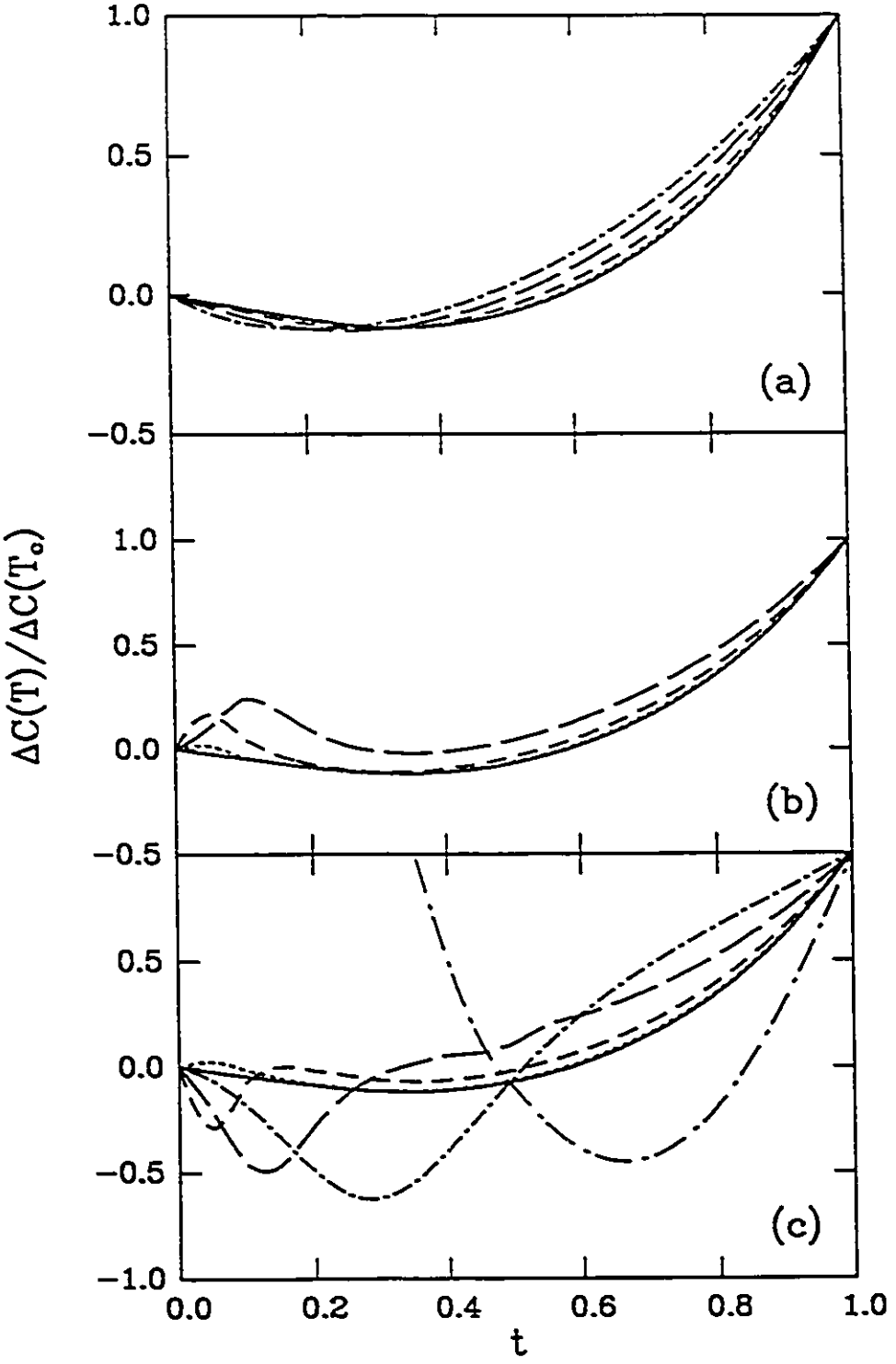


**Figure 6.6** The electronic specific heat difference $\Delta C(T)$ normalized to its value at $T_c$ versus the reduced temperature $t = T/T_c$. (a) Abrikosov-Gor'kov impurities. (b) Spin glass impurities for Case 1. (c) Spin glass impurities for Case 2. See Table 6.1 for detail of the parameters.

state) at $t$ around 0.35. Also, note that the entropy sum rule above cannot possibly be applied. This is due to the fact that the specific heat presented here is the electronic specific heat, whereas, for the sum rule above all the contributions to the specific heat must be included, which in this case would include a large magnetic contribution.

## 6.4 ELECTROMAGNETIC PROPERTIES

In this section, we present calculations for several electromagnetic properties, namely the London, local, and Pippard penetration depths, the electromagnetic coherence length, and finally, the thin film critical current. The local penetration depth has been calculated in this model by Stephan (1987) but is unpublished. Again the reentrant region was never examined.

A discussion of the electromagnetic penetration depth was given in Section 3.6. There are three important limits to the response function given in that section. There we discussed only the London limit and later we discussed the local limit with regard to the dc Josephson current in Section 3.7. Here, for completeness we will present all three.

In the case of a superconductor that is sufficiently dirty such that the mean free path $l$ of the electron is short relative to the zero temperature coherence length $\xi(0)$ because of impurity scattering, the response of the electrons to an external field is local and we have the local penetration depth $\lambda_l$ [Nam (1967a,b)]

$$\lambda_l = \left[\frac{8}{3}\pi N(0)e^2 v_F^2 \tau_N T \sum_{n=1}^{\infty} \frac{\Delta_n^2}{\omega_n^2 + \Delta_n^2}\right]^{-1/2} . \tag{6.21}$$

In Section 3.7, we have related this to the dc Josephson critical current $J_c(T)$ by [Nam (1967a,b)]

$$\frac{J_c(T)}{J_c(0)} = \left[\frac{\lambda_l(0)}{\lambda_l(T)}\right]^2 \quad . \tag{6.22}$$

For non-local effects (as in the case of the clean limit where $l \gg \xi(0)$), there are two limits corresponding to either extreme type I ($\lambda \ll \xi(0)$) or extreme type II ($\lambda \gg \xi(0)$) superconductivity. The type I limit is called the Pippard limit and the type II limit is called the London limit. The formulae for these penetration depths are given in the literature as [Nam (1967a,b)]

$$\lambda_P = \frac{4}{3\sqrt{3}}\left[\frac{3\pi^2}{v_F}\frac{n}{m}e^2T\sum_{n=1}^{\infty}\frac{\Delta_n^2}{\omega_n^2+\Delta_n^2}\right]^{-1/3} \quad , \tag{6.23}$$

for the Pippard penetration depth $\lambda_P$, and

$$\lambda_L(T) = \left[\frac{4}{3}\pi N(0)e^2v_F^2T\sum_{n=1}^{\infty}\frac{\Delta_n^2}{Z_n(\omega_n^2+\Delta_n^2)^{3/2}}\right]^{-1/2} \quad , \tag{6.24}$$

for the London penetration depth $\lambda_L$. The temperature-dependent electromagnetic coherence length $\xi(T)$ is given as [Nam (1967a,b)]

$$\xi(T) = \frac{v_F}{2}\sum_{n=1}^{\infty}\frac{\Delta_n^2}{Z_n(\omega_n^2+\Delta_n^2)^{3/2}}\Bigg/\sum_{n=1}^{\infty}\frac{\Delta_n^2}{\omega_n^2+\Delta_n^2} \quad , \tag{6.25}$$

which can easily be seen to be related to the local and London penetration depths by

$$\xi(T) = l\left(\frac{\lambda_l(T)}{\lambda_L(T)}\right)^2 \quad , \tag{6.26}$$

where $l = v_F\tau$.

In Fig. 6.7, we show the inverse square of the London penetration depth normalized to the value for the pure case at zero temperature. [Please refer to Table 6.1 for the identification of the line types.] Note that in Case 1, (frame (b)), the magnitude of the curves is increased over the corresponding

In Section 3.7, we have related this to the dc Josephson critical current $J_c(T)$ by [Nam (1967a,b)]

$$\frac{J_c(T)}{J_c(0)} = \left[\frac{\lambda_l(0)}{\lambda_l(T)}\right]^2 \quad . \tag{6.22}$$

For non-local effects (as in the case of the clean limit where $l \gg \xi(0)$), there are two limits corresponding to either extreme type I ($\lambda \ll \xi(0)$) or extreme type II ($\lambda \gg \xi(0)$) superconductivity. The type I limit is called the Pippard limit and the type II limit is called the London limit. The formulae for these penetration depths are given in the literature as [Nam (1967a,b)]

$$\lambda_P = \frac{4}{3\sqrt{3}}\left[\frac{3\pi^2}{v_F}\frac{n}{m}e^2T\sum_{n=1}^{\infty}\frac{\Delta_n^2}{\omega_n^2+\Delta_n^2}\right]^{-1/3} \quad . \tag{6.23}$$

for the Pippard penetration depth $\lambda_P$, and

$$\lambda_L(T) = \left[\frac{4}{3}\pi N(0)e^2v_F^2T\sum_{n=1}^{\infty}\frac{\Delta_n^2}{Z_n(\omega_n^2+\Delta_n^2)^{3/2}}\right]^{-1/2} \quad . \tag{6.24}$$

for the London penetration depth $\lambda_L$. The temperature-dependent electromagnetic coherence length $\xi(T)$ is given as [Nam (1967a,b)]

$$\xi(T) = \frac{v_F}{2}\sum_{n=1}^{\infty}\frac{\Delta_n^2}{Z_n(\omega_n^2+\Delta_n^2)^{3/2}}\Bigg/\sum_{n=1}^{\infty}\frac{\Delta_n^2}{\omega_n^2+\Delta_n^2} \quad . \tag{6.25}$$

which can easily be seen to be related to the local and London penetration depths by

$$\xi(T) = l\left(\frac{\lambda_l(T)}{\lambda_L(T)}\right)^2 \quad , \tag{6.26}$$

where $l = v_F\tau$.

In Fig. 6.7, we show the inverse square of the London penetration depth normalized to the value for the pure case at zero temperature. [Please refer to Table 6.1 for the identification of the line types.] Note that in Case 1, (frame (b)), the magnitude of the curves is increased over the corresponding

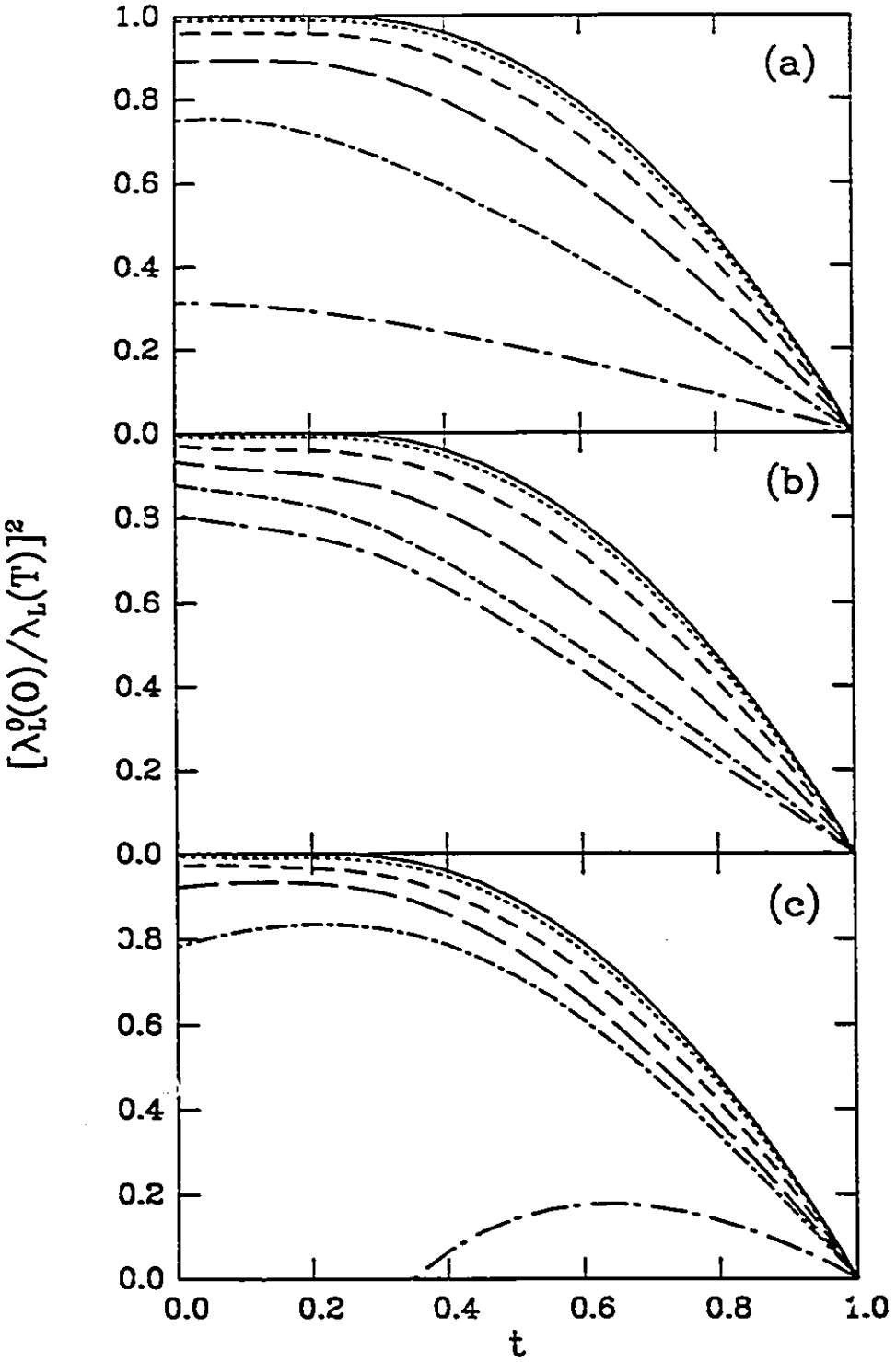


**Figure 6.7** The inverse square of London penetration depth normalized to the value for the pure case at zero temperature versus the reduced temperature $t = T/T_c$. (a) Abrikosov-Gor'kov impurities. (b) Spin glass impurities for Case 1. (c) Spin glass impurities for Case 2. See Table 6.1 for detail of the parameters.

Abrikosov-Gor'kov case, again reflecting the decreased effective scattering rate. Also in Case 2 (frame (c)) the temperature dependence remains even higher due to a more rapid drop in the scattering rate in this model. Note again the reentrant behaviour of the highest concentration case in this figure.

As impurities are added to a system bringing it closer to the dirty limit, the London penetration depth will approach the local limit penetration depth, which already has implicit in it the dirty limit. This is seen upon comparing the dot-long dashed curves in Figs. 6.7 and 6.8, which correspond to the highest impurity concentration used in this model. One cannot see the exact equivalence here as one would in the case of normal impurities, as the concentration of impurities required would be larger than the critical concentration that destroys the superconductivity entirely.

In Fig. 6.8, we display the dc Josephson critical current $J_c(T)$ normalized to its pure limit value at zero temperature. This quantity is also the inverse square of the local limit penetration depth. Again similar discussion applies as in Fig. 6.7, with reentrant behaviour exhibited by Case 2.

In Fig. 6.9, we show the Pippard penetration depth for completeness. Again, it is the inverse square of the penetration depth that is plotted normalized to its zero temperature value in the pure limit. It is not surprising that this figure closely resembles Fig. 6.8 as from Eqs. (6.21) and (6.23), one can see that the formulae are similar with only a slightly different power law. This particular penetration depth is only shown for completeness as it refers to type I superconductors which are usually elemental superconductors such as Al.

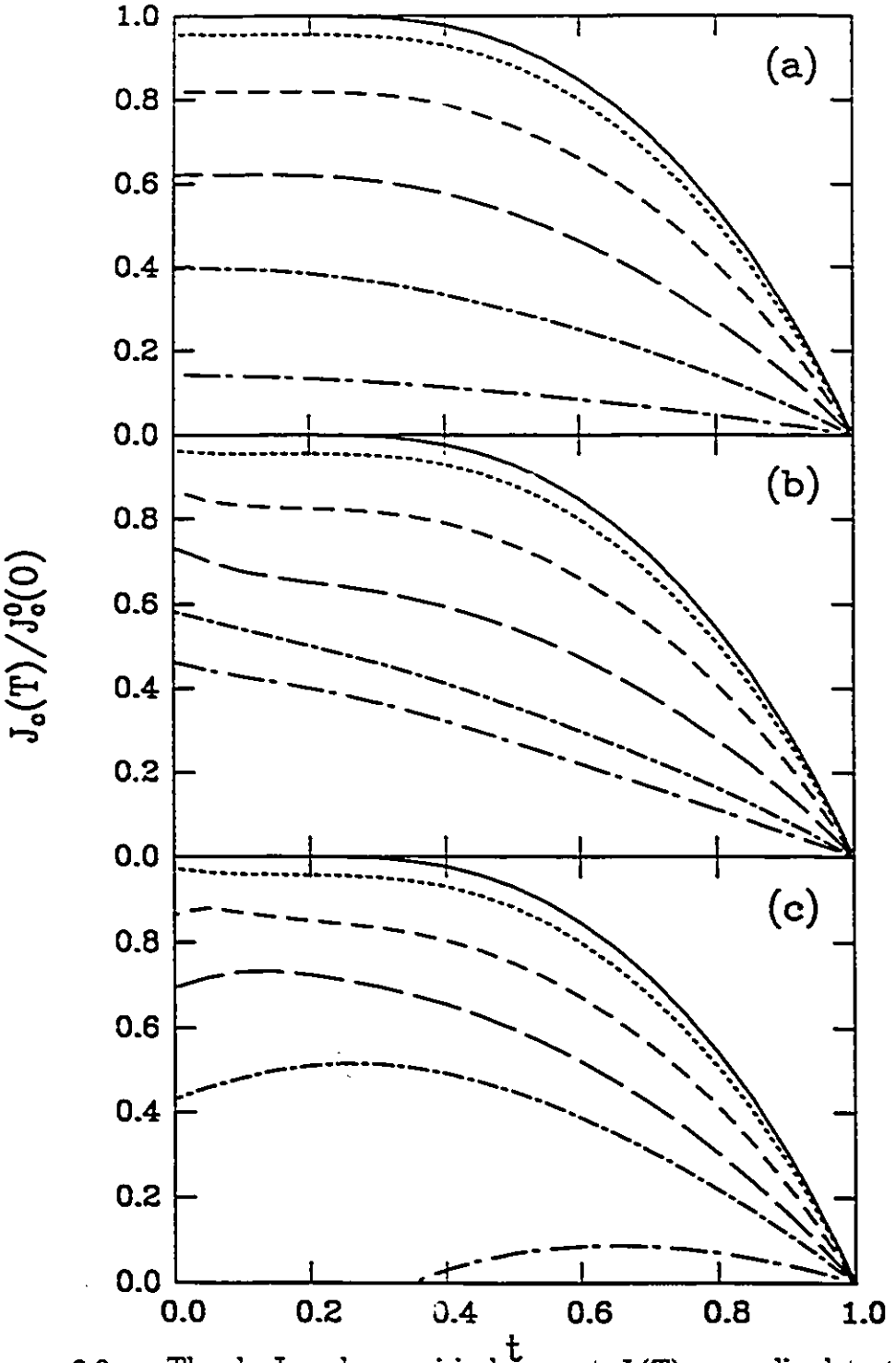


**Figure 6.8** The dc Josephson critical current $J_c(T)$ normalized to the value for the pure case at zero temperature versus the reduced temperature $t = T/T_c$. (a) Abrikosov-Gor'kov impurities. (b) Spin glass impurities for Case 1. (c) Spin glass impurities for Case 2. See Table 6.1 for detail of the parameters.

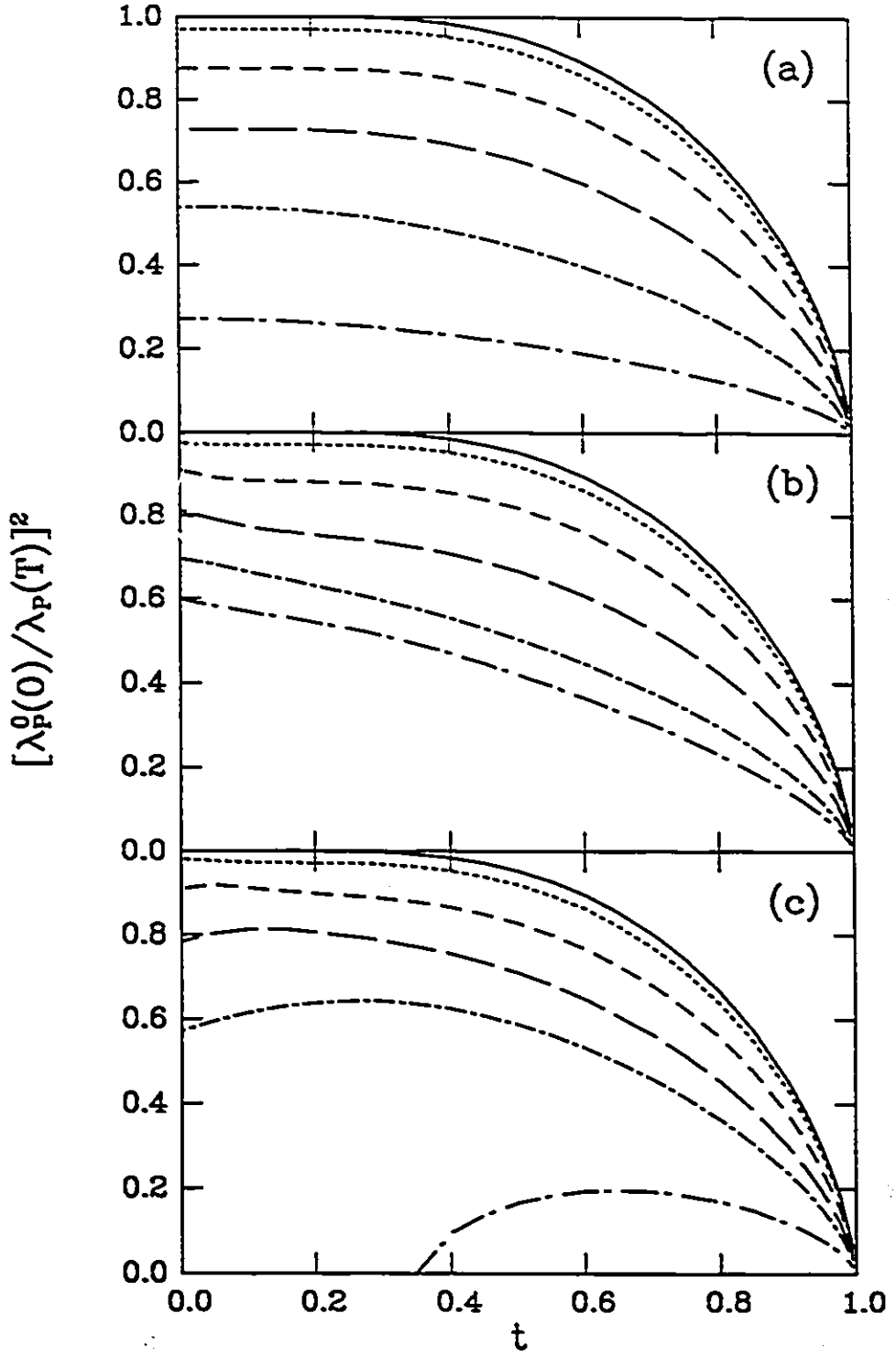


**Figure 6.9** The inverse square of Pippard penetration depth normalized to the value for the pure case at zero temperature versus the reduced temperature $t = T/T_c$. (a) Abrikosov-Gor'kov impurities. (b) Spin glass impurities for Case 1. (c) Spin glass impurities for Case 2. See Table 6.1 for detail of the parameters.

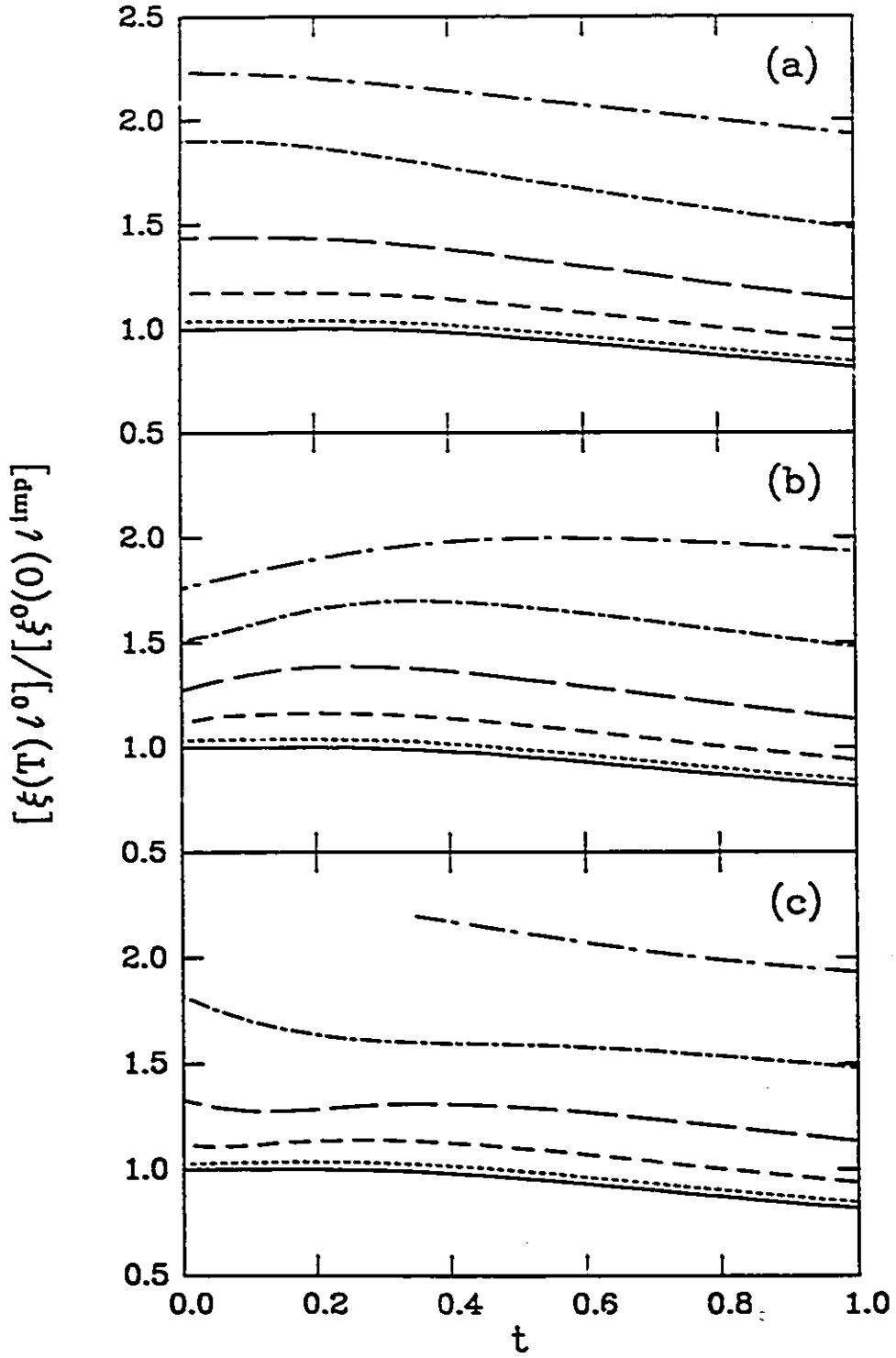


**Figure 6.10** The temperature-dependent coherence length $\xi(T)$ divided by the mean free path $l^{imp}$ normalized to the same quantity at zero temperature in the pure limit, *i.e.*, $\xi(T)l^{\circ}/\xi^{\circ}(0)l^{imp}$, versus the reduced temperature $t = T/T_c$. (a) Abrikosov-Gor'kov impurities. (b) Spin glass impurities for Case 1. (c) Spin glass impurities for Case 2. See Table 6.1 for detail of the parameters.

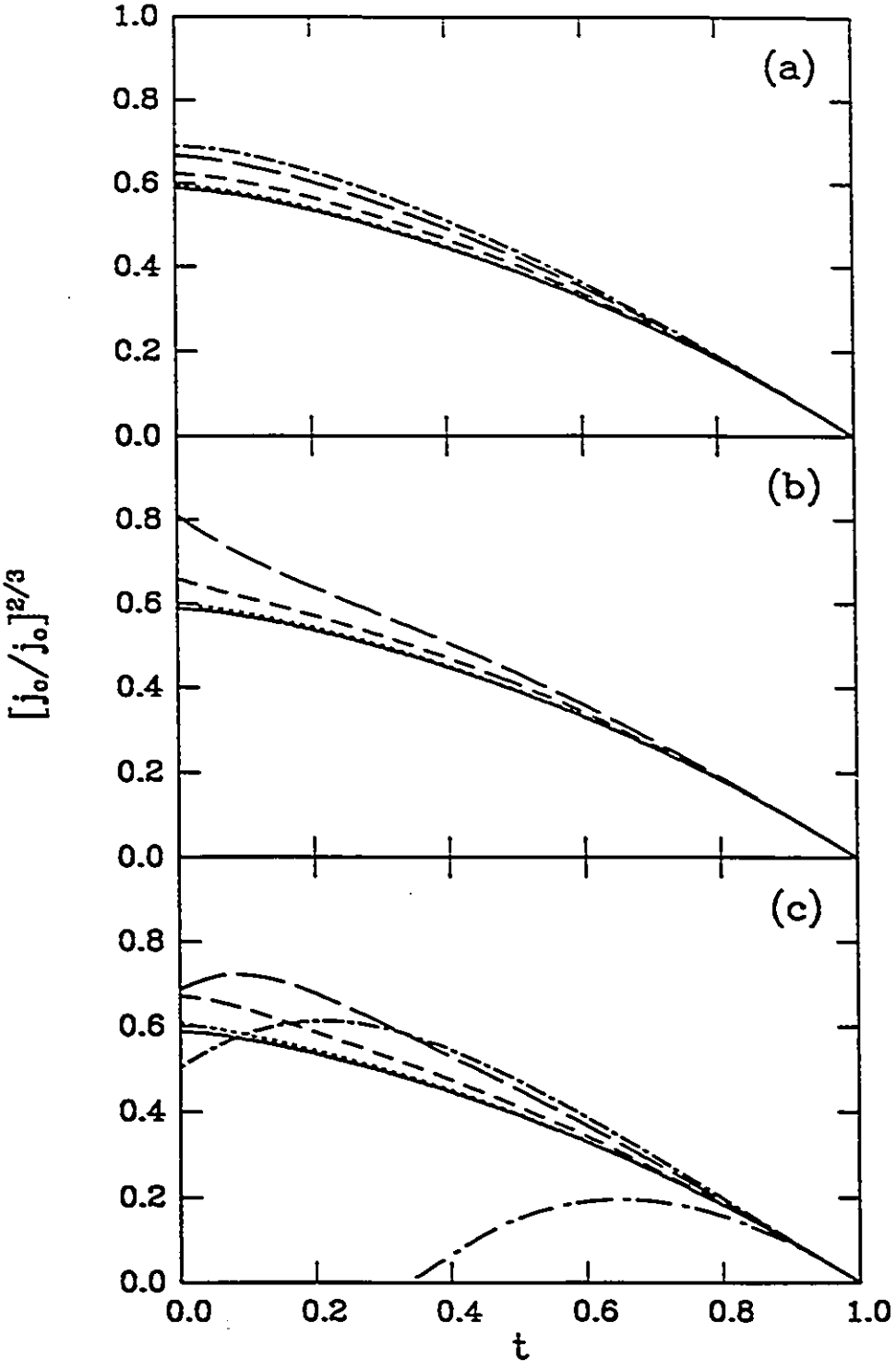


**Figure 6.11** The thin film critical current density normalized to the slope at $T_c$, $(j_o)^{2/3} \equiv -T_c \frac{di_c^{2/3}}{dT}\,|_{T_c}$, versus the reduced temperature $t = T/T_c$. (a) Abrikosov-Gor'kov impurities. (b) Spin glass impurities for Case 1. (c) Spin glass impurities for Case 2. See Table 6.1 for detail of the parameters.

Fig. 6.10 exhibits the temperature-dependent electromagnetic coherence length divided by the mean free path $l^{imp}$ normalized to the same quantity at zero temperature in the pure limit, *i.e.*, $\xi(T)l^{o}/\xi^{o}(0)l^{imp}$. In all cases, magnetic impurity scattering increases the magnitude of this quantity with the temperature dependence once again reflecting the variation in the effective scattering rate. As the mean free path in the impure case will be smaller than in the pure case, these curves would then indicate that the coherence length itself is reduced by magnetic scattering. This appears reasonable as one would expect the coherence length to be smaller in the presence of pair-breaking effects and impurity scattering.

Finally, we present in Fig. 6.11, the thin film critical current plotted as described in Chapter 2. The formalism for calculating this quantity with the addition of paramagnetic impurities has already been given in Chapter 2 and we have merely incorporated the temperature-dependent scattering rate into the procedure. One finds that the temperature dependence in the model for Case 1 is enhanced over the Abrikosov-Gor'kov result in (a) at low temperatures. For Case 2, reentrant behaviour occurs as previously discussed.

## 6.5 CONCLUSIONS

In conclusion, we have calculated thermodynamic and electromagnetic properties for an intrinsic spin glass superconductor in the spin glass model of Nass *et al.* (1981). We have extended the BCS calculations of Stephan and Carbotte (1991) to strong coupling Eliashberg theory, so that the theory is capable of providing quantitative predictions. In addition, we have considered properties not previously investigated within this model.

In general, we find very distinctive behaviour in the temperature dependence of the superconducting properties. These should be observable in experiment if this model has any relevance to spin glass superconductors. In addition, reentrant behaviour is a possible signature of a spin glass state corresponding to Case 2 of the model used here.

# Chapter 7

# Conclusions

As conclusions have been given in each of the preceding chapters, we confine ourselves to a summary of the highlights of the work which has been reported here.

While the mechanism governing the high $T_c$ superconducting oxides is as yet unknown, the results of our work recorded in Chapters 3 and 4 show that the marginal Fermi liquid theory is, at present, one of the most promising candidates. The most exciting results of the thesis are to be found in Figs. 4.15-4.18., where the predictions of the marginal Fermi liquid theory have been dramatically confirmed by experiment. For both the microwave conductivity and the quasiparticle damping rate, our calculations were performed independently of knowledge of experimental results. These appeared shortly after our calculations, the predicted and observed behaviour being completely novel. That a peak in the microwave conductivity can occur when no such peak is observed in the NMR spin lattice relaxation rate, can, at

present, only be explained by the gapping of the excitation spectrum, as occurs in marginal Fermi liquid theory, and not in competing theories. The sudden drop which we found in the quasiparticle damping rate below $T_c$ is also a reflection of this important clue. This work is currently motivating additional efforts to discover other signatures of the gapping in independent properties, and to undertake a systematic comparison of the theory and experiment.

In addition, it has been predicted that the finite frequency optical absorption in the clean limit should exhibit onset of absorption at $4\Delta$ instead of the traditional $2\Delta$. While samples and interpretation of experimental results are still problematic in this area, confirmation of the unusual prediction would be very exciting.

The strong coupling theory of thin film critical currents is presented for the first time, in Chapter 2. This enables us to make quantitative predictions, a luxury not afforded by BCS theory. We have made important predictions which we hope will be experimentally verified. Excellent agreement has been obtained in the past between BCS theory and BCS-type superconductors; therefore, we are confident that strong coupling effects, which enhance the temperature dependence of the critical current, will be confirmed. We have also provided the first predictions for the effect of paramagnetic impurities, paramagnons, and spin glass freezing on this critical current.

Our work on paramagnons serves to add support to the marginal Fermi liquid model which has a spin fluctuation component within its formulation. Predictions for the behaviour of the optical conductivity in the presence of paramagnetic impurities have also been given and could be, in principle, tested in both conventional and high $T_c$ superconductors. Reduced

Holstein structure and absorption below $2\Delta$ should be observed in the clean limit in systems containing paramagnetic impurities.

Finally, we have calculated a series of thermodynamic and electromagnetic properties of spin glass superconductors, predicting unusual temperature dependence and reentrant behaviour. Although experimental work could search for this behaviour, a more promising avenue is to examine proximity effect junctions between superconductors and spin glasses. In such a junction, a thin layer of superconductor is sandwiched with a spin glass material. Superconductivity is then induced in the spin glass material due the Cooper pairs "leaking" across the junction. This would allow for a more systematic investigation of spin glass superconductors through induced superconductivity, as the number of intrinsic spin glass superconductors is small. We are currently working on the theory for such a junction, using the spin glass model presented here.

It is expected that many of the results reported here will not only have theoretical impact but will also provide the fundamental underpinning to both experiments and applications. Knowledge of how different pair-breaking mechanisms can affect superconducting properties allows one to isolate the important processes at work in the materials. Designers of practical superconducting devices and applications can attempt to eliminate the detrimental effects, or use the effects to advantage. The critical current calculated here is the theoretical maximum attainable and hence an important quantity for those interested in high current devices. The dramatic drop in the scattering rate predicted here and observed by Bonn *et al.* (1991), has important implications for high $T_c$ microwave applications requiring very low surface resistance.

# Appendix A

## *Eliashberg Theory*

### A.1 INTRODUCTION

In this appendix, we wish to show the basic derivation of the Eliashberg equations from the electron self-energy. Many books and reviews exist on this topic [see for example, Schrieffer (1964); Allen and Mitrović (1982); Scalapino (1969)]. Our aim here is to show the details of the derivation for the standard equations only and then to show how this derivation is to be modified for several cases presented in this thesis: currents, normal and paramagnetic impurities, and spin fluctuations. Hence, the references should be consulted for a discussion of BCS theory, Green's function formalism, and the background description of the Hamiltonian. We will emphasis the mathematical derivation here for which details are not always present in the reviews. The material in this introduction is a précis of similar material in the review

of Allen and Mitrović (1982) Sections A.2 and A.3 are drawn from notes by Dr. E. Schachinger with his permission.

In BCS theory, it is assumed there is an instantaneous interaction for the pairing between electrons, with no reference to phonons, other than a cutoff of $\omega_D$ on the pairing interaction. No frequency dependence or retardation effects of the response of the phonon system are taken into account, so that in BCS theory, one deals only with the electron Green's functions.

The normal state electron Green's function is defined as

$$G(\vec{k},\tau) \equiv -\langle T_\tau c_{\vec{k}\sigma}(\tau) c^\dagger_{\vec{k}\sigma}(0)\rangle \quad , \tag{A.1}$$

where $T_\tau$ is the Wick time ordering operator. It reorders the operators such that the imaginary time $\tau$ increases from right to left respecting anticommutation relations. The $c^\dagger_{\vec{k}\sigma}$ and $c_{\vec{k}\sigma}$ are the creation and annihilation operators, respectively, in the Heisenberg representation. The thermodynamic average is given as:

$$\langle A\rangle = \frac{\mathrm{Tr}(e^{-\beta\mathcal{H}}A)}{\mathrm{Tr}(e^{-\beta\mathcal{H}})} \quad , \tag{A.2}$$

where $\beta = 1/T$ with $T$ the temperature. The real space version of this Green's function can be seen physically as the propagation of an electron from time $t = 0$ at position $x$ (created) to position $x'$ at time $t$ (annihilated) and hence it is also called a propagator. Once this Green's function is known, anything, in principle, can be calculated about the system. The goal then is to calculate the Green's function.

For non-interacting electrons, the Green's function is easily shown to be given as

$$G_o(\vec{k}, i\omega_n) = \frac{1}{i\omega_n - \epsilon_{\vec{k}}} \quad , \tag{A.3}$$

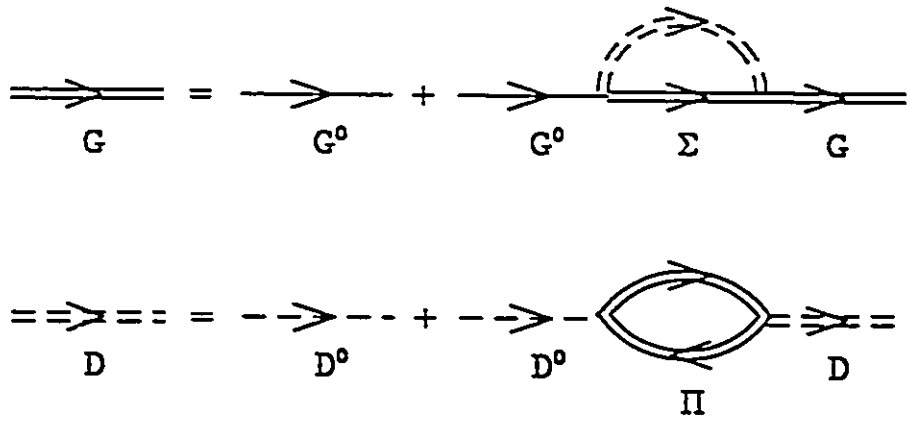


Figure A.1 Dyson's equations for the electron Green's function (top) and the phonon Green's function (bottom).

where we are now using the Matsubara representation. In this case, the Matsubara Green's function is the Fourier coefficient of the Fourier representation of the Green's function in terms of the Matsubara frequencies $\omega_n = \pi T(2n+1)$ with $n = 0, \pm 1, \pm 2, \ldots$. The Matsubara or thermodynamic Green's function contains all the information necessary to calculate the thermodynamics of the system and its analytic continuation to real frequencies allows for the calculation of all transport properties.

For the electron-phonon problem one also needs knowledge of the phonon propagator

$$D_{\alpha\beta}(\vec{q},\tau) = -\langle T_\tau u_{\vec{q}\alpha}(\tau) u_{-\vec{q}\beta}(0)\rangle \quad , \tag{A.4}$$

where $u_{\vec{q}}$ is the bosonic displacement operator:

$$u_{\vec{q}} = \sum_\lambda \left(\frac{\hbar}{2NM\omega_{\vec{q}\lambda}}\right)^{1/2} \hat{\epsilon}_{\vec{q}\lambda}(a_{\vec{q}\lambda} + a^\dagger_{-\vec{q}\lambda}) \quad . \tag{A.5}$$

Our notation here corresponds to $M$, the ion mass, $\lambda$, the branch index, $\vec{q}$, the wave vector, $\hat{\epsilon}_{\vec{q}\lambda}$, the polarization vector, and $a_{\vec{q}\lambda}$ the boson annihilation

operator. In terms of the Fourier representation, this phonon Green's function can be written in terms of bosonic Matsubara frequencies $\nu_n = 2n\pi T$, where $n = 0, \pm 1, \pm 2, \ldots$. For non-interacting phonons

$$D^{\circ}_{\alpha\beta}(\vec{q}, i\nu_n) = \sum_{\lambda} \left( \frac{\hbar}{2NM\omega_{\vec{q}\lambda}} \right) \hat{\epsilon}_{\vec{q}\alpha} \hat{\epsilon}_{-\vec{q}\beta} \left( \frac{1}{i\nu_n - \omega_{\vec{q}}} - \frac{1}{i\nu_n + \omega_{\vec{q}}} \right) \quad . \tag{A.6}$$

As we are interested in the fully interacting system, we require the fully interacting Green's functions which are given in terms of Feynman-Dyson perturbation theory to be:

$$G^{-1}(\vec{k}, i\omega_n) = G_{\circ}^{-1}(\vec{k}, i\omega_n) - \Sigma(\vec{k}, i\omega_n) \tag{A.7}$$

and

$$[D^{-1}(\vec{q}, i\nu_n)]_{\alpha\beta} = [D_{\circ}^{-1}(\vec{q}, i\nu_n)]_{\alpha\beta} - \Pi_{\alpha\beta}(\vec{q}, i\nu_n) \quad , \tag{A.8}$$

where now the problem is shifted to solving for the self-energies $\Sigma(\vec{k}, i\omega_n)$ and $\Pi_{\alpha\beta}(\vec{q}, i\nu_n)$. These Dyson equations are shown diagrammatically in Fig. A.1.

Typically one can obtain the phonon self-energy through its spectral representation which can be measured by inelastic neutron scattering or is known through its coupling to electrons from tunneling experiments. This is considered an input parameter and it is taken from experiment, and in this instance, it will contain all the renormalization effects, and hence we do not need to solve Eq. (A.8) for the phonon propagator.

The Hamiltonian for the electron-phonon system is given by Fröhlich's Hamiltonian:

$$\mathcal{H} = \mathcal{H}_{el} + \mathcal{H}_{L} + \mathcal{H}_{ep} + \mathcal{H}_{c} \quad , \tag{A.9}$$

where the free electron part of the Hamiltonian is given as:

$$\mathcal{H}_{el} = \sum_{\vec{k}\sigma} \epsilon_{\vec{k}} c^{\dagger}_{\vec{k}\sigma} c_{\vec{k}\sigma} \quad , \tag{A.10}$$

with the quasiparticle band energies, $\epsilon_{\vec{k}}$, assumed to be available from band structure calculations. The ion lattice Hamiltonian is given in terms of the harmonic approximation as:

$$\mathcal{H}_L = \sum_{\vec{q}} \hbar\omega_{\vec{q}}(a^\dagger_{\vec{q}}a_{\vec{q}} + \frac{1}{2}) \quad , \tag{A.11}$$

with $\hbar\omega_{\vec{q}}$ coming from experiment. The electron-phonon Hamiltonian is given as

$$\mathcal{H}_{ep} = \sum_{\vec{k}\vec{q}} \langle k+q \mid \nabla_\alpha V \mid k\rangle u_{\vec{q}\alpha} c^\dagger_{\vec{k}+\vec{q}} c_{\vec{k}} \quad . \tag{A.12}$$

with $\nabla_\alpha V$ to be considered as the gradient of the screened electron-ion potential. Finally, the Coulomb Hamiltonian is written as:

$$\mathcal{H}_c = \sum_{\vec{q}\vec{q}'} \frac{4\pi e^2}{\mid \vec{q}+\vec{q}' \mid^2} \rho^\dagger_{\vec{q}+\vec{q}'}\rho_{\vec{q}+\vec{q}'} \quad , \tag{A.13}$$

where the Fourier transform of the charge density is given as:

$$\rho_{\vec{q}+\vec{q}'} \equiv \sum_{\vec{k}\vec{k}'} \langle k' \mid e^{-i(\vec{q}+\vec{q}')\cdot\vec{r}} \mid k\rangle c^\dagger_{\vec{k}'} c_{\vec{k}} \quad . \tag{A.14}$$

Here, $q'$ is a reciprocal lattice vector and $q$ is the momentum transferred, which is to be summed over the FBZ.

In the superconducting state, there are both normal Green's functions ($\langle T_\tau c_{\vec{k}\sigma}(\tau) c^\dagger_{\vec{k}\sigma}(0)\rangle$) and anomalous Green's functions ($\langle T_\tau c^\dagger_{-\vec{k},-\sigma}(\tau) c^\dagger_{\vec{k}\sigma}(0)\rangle$) for the non-zero Cooper pair amplitude. Therefore, both types of fully interacting Green's functions must be found. The added complication of the three-body operator appearing in the interaction term motivated Nambu to introduce two-component spinor operators of the form:

$$\Psi_{\vec{k}} = \begin{pmatrix} c_{\vec{k}\uparrow} \\ c^\dagger_{-\vec{k}\downarrow} \end{pmatrix} \quad \text{and} \quad \Psi^\dagger_{\vec{k}} = \begin{pmatrix} c^\dagger_{\vec{k}\uparrow}, c_{-\vec{k}\downarrow} \end{pmatrix} \quad , \tag{A.15}$$

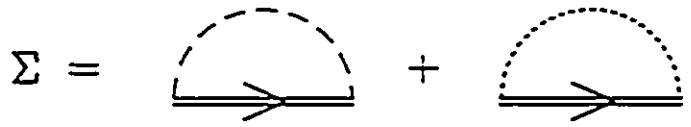

Figure A.2 The electron self-energy due to the electron-phonon interaction (the left diagram) and the Coulomb interaction (the right diagram).

with

$$\{\Psi_{\vec{k}}, \Psi^{\dagger}_{\vec{k}'}\} = \delta_{\vec{k}\vec{k}'}\tau_0, \quad \{\Psi_{\vec{k}}, \Psi_{\vec{k}}\} = 0 \quad . \tag{A.16}$$

Then one can write the Hamiltonian in terms of one-body operators using the Pauli matrices:

$$\tau_0 = \begin{pmatrix} 1 & 0 \\ 0 & 1 \end{pmatrix} \qquad \tau_1 = \begin{pmatrix} 0 & 1 \\ 1 & 0 \end{pmatrix} \qquad \tau_2 = \begin{pmatrix} 0 & -i \\ i & 0 \end{pmatrix} \qquad \tau_3 = \begin{pmatrix} 1 & 0 \\ 0 & -1 \end{pmatrix} \quad . \tag{A.17}$$

So now

$$\mathcal{H}_0 = \sum_{\vec{k}} \epsilon_{\vec{k}} \Psi^{\dagger}_{\vec{k}} \tau_3 \Psi_{\vec{k}} \tag{A.18}$$

$$\mathcal{H}_{ep} = \sum_{\vec{k}\vec{k}'} \langle k' \mid \nabla_\alpha V \mid k \rangle \Psi^{\dagger}_{\vec{k}'} \tau_3 \Psi_{\vec{k}} \; u_{\vec{k}-\vec{k}'\alpha} \tag{A.19}$$

while $\mathcal{H}_c$ remains as given in Eq. (A.13), but the charge density is changed to be:

$$\rho_{\vec{q}+\vec{q}'} = \sum_{\vec{k}\vec{k}'} \langle k' \mid e^{-i(\vec{q}+\vec{q}')\cdot\vec{r}} \mid k \rangle \Psi^{\dagger}_{\vec{k}'} \tau_3 \Psi_{\vec{k}} \quad . \tag{A.20}$$

The Green's function is now a matrix:

$$G(\vec{k},\tau) = -\langle T_\tau \Psi_{\vec{k}}\,(\tau) \Psi^{\dagger}_{\vec{k}}(0) \rangle \tag{A.21}$$

$$= -\begin{pmatrix} \langle T_\tau c_{\vec{k}\uparrow}\,(\tau) c^{\dagger}_{\vec{k}\uparrow}(0) \rangle & \langle T_\tau c_{\vec{k}\uparrow}\,(\tau) c_{-\vec{k}\downarrow}\,(0) \rangle \\ \langle T_\tau c^{\dagger}_{-\vec{k}\downarrow}(\tau) c^{\dagger}_{\vec{k}\uparrow}(0) \rangle & \langle T_\tau c^{\dagger}_{-\vec{k}\downarrow}(\tau) c_{-\vec{k}\downarrow}\,(0) \rangle \end{pmatrix} \quad . \tag{A.21}$$

Now we are ready to proceed with a calculation of the self-energy.

## A.2 THE SELF-ENERGY

The electron self-energy is given diagrammatically in Fig. A.2 and is written according to the Feynman rules as:

$$\Sigma(\vec{k}, i\omega_n) = -\frac{1}{\beta}\sum_{\vec{k}',n'} \tau_3 G(\vec{k}', i\omega_{n'})\tau_3 \{\sum_{\lambda} \mid g_{\vec{k},\vec{k}',\lambda} \mid^2 D_\lambda(\vec{k}-\vec{k}', i\omega_n - i\omega_{n'}) + V(\vec{k}-\vec{k}')\}, \tag{A.22}$$

where the electron-phonon matrix element is defined as:

$$g_{\vec{k},\vec{k}',\lambda} = \left(\frac{\hbar}{2M\omega_{\vec{q}\lambda}}\right)^{1/2} \langle k \mid \hat{\epsilon}_{\vec{q}\lambda} \cdot \nabla V \mid k' \rangle \quad , \tag{A.23}$$

with $\vec{q} = \vec{k} - \vec{k}'$ and $\omega_n = (2n+1)\pi/\beta$; $n = 0, \pm 1, \pm 2, \ldots$ and $\beta = 1/T$. The second term of the self-energy is that due to the Coulomb interaction energy $V$ as a function of momentum transfer. The first term is for the electron-phonon interaction, where the phonon Green's function can be written in terms of a spectral representation as:

$$D_\lambda(\vec{q}, i\nu_n) = \int_0^\infty d\nu B_\lambda(\vec{q}, \nu)\left[\frac{1}{i\nu_n - \nu} - \frac{1}{i\nu_n + \nu}\right] \tag{A.24}$$

$$= \int_0^\infty d\nu \frac{2\nu}{(i\nu_n)^2 - \nu^2} B_\lambda(\vec{q}, \nu) \tag{A.25}$$

$$= -\int_0^\infty d\nu \frac{2\nu}{\nu_n^2 + \nu^2} B_\lambda(\vec{q}, \nu) \quad , \tag{A.26}$$

where $\nu_n = 2n\pi/\beta$, $n = 0, \pm 1, \pm 2, \ldots$. Substituting the spectral function in Eq. (A.24) above, we have for the self-energy

$$\Sigma(\vec{k}, i\omega_n) = -\frac{1}{\beta}\sum_{\vec{k}',n'} \tau_3 G(\vec{k}', i\omega_{n'})\tau_3 \left\{\sum_{\lambda} \mid g_{\vec{k},\vec{k}',\lambda} \mid^2 \int_0^\infty d\nu B_\lambda(\vec{k}-\vec{k}', \nu) \right.$$

$$\left. \times \left[\frac{1}{(i\omega_n - i\omega_{n'}) - \nu} - \frac{1}{(i\omega_n - i\omega_{n'}) + \nu}\right] + V(\vec{k}-\vec{k}')\right\}. \tag{A.27}$$

## A.3 THE ELIASHBERG EQUATIONS ON THE IMAGINARY AXIS

We wish to solve for the Green's function for the superconductor as given by the Dyson equation:

$$G^{-1}(\vec{k}, i\omega_n) = \mathcal{G}_o^{-1}(\vec{k}, i\omega_n) - \Sigma(\vec{k}, i\omega_n) \quad , \tag{A.28}$$

with the matrix Green's function of the non-interacting system:

$$\begin{aligned} G_o(\vec{k}, i\omega_n) &= \frac{1}{i\omega_n \tau_0 - \epsilon_{\vec{k}} \tau_3} \\ &= \frac{i\omega_n \tau_0 + \epsilon_{\vec{k}} \tau_3}{(i\omega_n)^2 - (\epsilon_{\vec{k}})^2} \quad . \end{aligned} \tag{A.29}$$

For the self-energy $\Sigma(\vec{k}, i\omega_n)$ we use the following general ansatz, where we write the self-energy in terms of an expansion using the $\tau$ matrices which form a complete set:

$$\Sigma(\vec{k}, i\omega_n) = i\omega_n[1 - Z(\vec{k}, i\omega_n)]\tau_0 + \chi(\vec{k}, i\omega_n)\tau_3 + \phi(\vec{k}, i\omega_n)\tau_1 + \bar{\phi}(\vec{k}, i\omega_n)\tau_2 \quad . \tag{A.30}$$

The notation for the coefficients is historically rooted in the real-axis derivation, where $\chi$ is the Hartree-Fock energy, $\phi$, the gap parameter, and $Z$ the renormalization function. Using an ansatz is the simplist approach; however, such a form does arise automatically from a Fourier transform during the course of the derivation in the generalized Hartree-Fock scheme [see Schrieffer (1964)]. From this ansatz we obtain for the Green's function:

$$G^{-1}(\vec{k}, i\omega_n) = i\omega_n Z(\vec{k}, i\omega_n)\tau_0 - [\epsilon_{\vec{k}} + \chi(\vec{k}, i\omega_n)]\tau_3 - \phi(\vec{k}, i\omega_n)\tau_1 - \bar{\phi}(\vec{k}, i\omega_n)\tau_2 \quad . \tag{A.31}$$

Forming the inverse of this matrix, we obtain:

$$G(\vec{k}, i\omega_n) = \frac{i\omega_n Z(\vec{k}, i\omega_n)\tau_0 + [\epsilon_{\vec{k}} + \chi(\vec{k}, i\omega_n)]\tau_3 + \phi(\vec{k}, i\omega_n)\tau_1 + \bar{\phi}(\vec{k}, i\omega_n)\tau_2}{[i\omega_n Z(\vec{k}, i\omega_n)]^2 - [\epsilon_{\vec{k}} + \chi(\vec{k}, i\omega_n)]^2 - \phi^2(\vec{k}, i\omega_n) - \bar{\phi}^2(\vec{k}, i\omega_n)} \quad . \tag{A.32}$$

Our procedure for determining $Z$, $\phi$, $\bar{\phi}$, and $\chi$, will be to substitute this expression for the Green's function into the right hand side of Eq. (A.22) and the ansatz for $\Sigma$ from Eq. (A.30) on the left. From this we will eventually obtain two non-linear coupled equations for $\phi$ and $Z$.

We must now elucidate terms of the self-energy. First we start with the phonon contribution. We use for this the result from the previous section:

$$\Sigma^{ph}(\vec{k}, i\omega_n) = -T \sum_{\vec{k}', n'} \tau_3 G(\vec{k}', i\omega_{n'}) \tau_3 \sum_{\lambda} | \bar{g}_{\vec{k},\vec{k}',\lambda} |^2 \int_0^{\infty} d\Omega B_{\lambda}(\vec{k} - \vec{k}', \Omega) \times \left[ \frac{1}{(i\omega_n - i\omega_{n'}) - \Omega} - \frac{1}{(i\omega_n - i\omega_{n'}) + \Omega} \right]. \quad (A.33)$$

Putting $i\omega_{n''} = i\omega_n - i\omega_{n'}$, we can write

$$\Sigma^{ph}(\vec{k}, i\omega_n) = T \sum_{\vec{k}', n''} \tau_3 G(\vec{k}', i\omega_n - i\omega_{n''}) \tau_3 \sum_{\lambda} | \bar{g}_{\vec{k},\vec{k}',\lambda} |^2 \int_0^{\infty} d\Omega B_{\lambda}(\vec{k} - \vec{k}', \Omega) \left[ \frac{2\Omega}{\omega_{n''}^2 + \Omega^2} \right]. \quad (A.34)$$

We change now the summation over $\vec{k}'$ into an integral over the energy; this is done by a series of approximations which greatly simplify the calculation:

(1) $\chi$, which arises from Coulomb scattering, can be shown to be the Hartree-Fock energy which remains unchanged in the normal and superconducting states. Further, $\chi$ is a slowly varying function of $\omega$ on the real frequency axis for $\omega < 10\omega_D$, so that it only depends on $\vec{k}$. Therefore, $\chi$ essentially results in an uninteresting shift of the energy $\epsilon_{\vec{k}}$ and can be absorbed into this quantity, redefined to be $\tilde{\epsilon}_{\vec{k}} = \epsilon_{\vec{k}} + \chi(\vec{k})$.

(2) $Z$ and the $\phi$'s vary with $\vec{k}$ on a scale of order $k_F$ and so we can put $| \vec{k} | = k_F$ in these quantities. Hence, the electron Green's function in Eq. (A.32) depends only on $\omega_n$ and the direction of $k$.

With these simplifications the integration can be carried out explicitly in terms of the phonon interaction energy.

For an isotropic theory, we can introduce the spherically averaged self-energy

$$\Sigma(k, i\omega_n) = \int \frac{d\Omega_{\vec{k}}}{4\pi} \Sigma(\vec{k}, i\omega_n) \quad , \tag{A.35}$$

where the integration is over angular coordinates. We begin with the phonon interaction energy terms:

$$\Sigma^{ph}(k, i\omega_n) = T \sum_{\vec{k}', n''} \tau_3 G(k', i\omega_n - i\omega_{n''}) \tau_3$$

$$\times \sum_{\lambda} \int \frac{d\Omega_{\vec{k}-\vec{k}'}}{4\pi} \mid g_{\vec{k},\vec{k}',\lambda} \mid^2 \int_0^{\infty} d\Omega B_{\lambda}(\vec{k} - \vec{k}', \Omega) \left[ \frac{2\Omega}{\omega_{n''}^2 + \Omega^2} \right] . \tag{A.36}$$

It follows, therefore, that insofar as we are only interested in the energies $\omega \sim \omega_D \ll E_F$, the main contribution to the $\vec{k}'$ integral comes from the states with $\mid \bar{\epsilon}_{\vec{k}'} \mid \sim \omega_D$. Therefore we can replace $k'$ by $k_F$ in $Z$ and $\phi$. This also holds for the last term. Here $\vec{k}$ acts only through the momentum relation $\vec{q} = \vec{k} - \vec{k}_F$ so the anisotropy will disappear. We can therefore change the sum over $\vec{k}'$ into an integral over $\bar{\epsilon}_{\vec{k}'}$, $q \equiv \mid \vec{k} - \vec{k}' \mid$ and the azimuthal angle $\phi$. Therefore,

$$\Sigma_{\vec{k}'} \rightarrow \int \frac{d^3k'}{(2\pi)^3} = \int \frac{1}{(2\pi)^3} k'^2 \sin\theta dk' d\theta d\phi = \frac{m}{(2\pi)^3 k_F} \int d\bar{\epsilon}_{\vec{k}'} q dq d\phi \quad , \tag{A.37}$$

where we have used:

$$\bar{\epsilon}_{\vec{k}'} = \frac{k'^2}{2m} - \frac{k_F^2}{2m} \rightarrow d\bar{\epsilon}_{\vec{k}'} = \frac{2k'dk'}{2m}; \quad dk' = \frac{m d\bar{\epsilon}_{\vec{k}'}}{k'} \tag{A.38}$$

with

$$\sin\vartheta d\theta \approx \frac{dq}{k_F} \quad . \tag{A.39}$$

Since the dominant contribution of the $\bar{\epsilon}_{\vec{k}'}$ integral comes from the range $|\bar{\epsilon}_{\vec{k}'}| \ll \omega_D$, we can extend the limits of integration for this variable to infinity:

$$\int_{-\omega_D}^{\omega_D} d\bar{\epsilon}_{\vec{k}'} \tau_3 G(k', i\omega_n - i\omega_{n''})\tau_3 = \int_{-\infty}^{\infty} d\bar{\epsilon}_{\vec{k}'} \tau_3 G(k', i\omega_n - i\omega_{n''})\tau_3 \quad . \qquad (A.40)$$

We introduce the function $\alpha^2 F(\Omega)$ defined as:

$$\alpha^2 F(\Omega) = N(0) \sum_{\vec{k}\vec{k}'\lambda} |\, g_{\vec{k},\vec{k}',\lambda} \,|^2 \, \delta(\Omega - \omega_{\vec{k},\vec{k}',\lambda}) \delta(\epsilon_{\vec{k}}) \delta(\epsilon_{\vec{k}'}) \Big/ \sum_{\vec{k}\vec{k}'} \delta(\epsilon_{\vec{k}}) \delta(\epsilon_{\vec{k}'})$$

$$= \frac{N(0)}{8\pi k_F^2} \sum_{\lambda} \int d\Omega_{\vec{q}} \int_0^{2k_F} q dq \,|\, g_{\vec{q},\lambda} \,|^2 \, B_\lambda(\vec{q}, \Omega) \quad . \qquad (A.41)$$

where in the last line, we have assumed a spherical Fermi surface. Setting $n'' = n'$ and letting $\bar{\epsilon}_{\vec{k}'} = \epsilon'$:

$$\Sigma^{ph}(\vec{k}, i\omega_n) = T \sum_{n'} \int_{-\infty}^{\infty} d\epsilon' \frac{N(\epsilon')}{N(0)} \int_0^{\infty} d\Omega \alpha^2 F(\Omega) \frac{2\Omega}{\omega_{n'}^2 + \Omega^2} \tau_3 G(\epsilon', i\omega_n - i\omega_{n'})\tau_3$$

$$= T \sum_{n'} \lambda(\omega_{n'}) \int_{-\infty}^{\infty} d\epsilon' \frac{N(\epsilon')}{N(0)} \tau_3 G(\epsilon', i\omega_n - i\omega_{n'})\tau_3 \quad , \qquad (A.42)$$

with $N(\epsilon) = \sum_{\vec{k}} \delta(\epsilon_{\vec{k}} - \epsilon)$ and

$$\lambda(\omega_{n'}) = 2 \int_0^{\infty} d\Omega \alpha^2 F(\Omega) \frac{\Omega}{\omega_{n'}{}^2 + \Omega^2} \quad . \qquad (A.43)$$

For the contribution of the Coulomb interaction potential, we have from Eq. (A.22):

$$\Sigma^c(\vec{k}, i\omega_n) = -\frac{1}{\beta} \sum_{\vec{k}', n'} \tau_3 G(\vec{k}', i\omega_{n'})\tau_3 V(\vec{k} - \vec{k}') \quad , \qquad (A.44)$$

To circumvent the problem of integration associated with the momentum-dependent Coulomb potential, we introduce now the Coulomb pseudopotential $\mu^*$. This development is most easily understood when carried out on the real axis: in this case it restricts the range of the energy integration from

$[0,\infty]$ to a new range $[0,\omega_c]$, where $\omega_c$ is most often chosen to be $6\omega_D$. A rather long derivation on the real axis is used to show that for high frequencies many approximations can be made, such as, $Z(k,\omega) \to 1$ and $\phi^c(k,\omega) \to \phi^c(k)$ for $\omega \gg \omega_D$, since the phonon-electron interaction will be ineffective for $\omega > \omega_D$. Furthermore, $\beta\omega_c = (1/T)\omega_c \gg 1$ for temperatures at which the materials are superconducting ($T \sim 10\text{K} \approx 1$ meV) and we can set $\tanh(\beta\omega'/2)$ (which occurs in the real axis version of $\Sigma^c$) to be $\approx 1$ for $\omega' > \omega_c$. With all this we can simplify the integral from $\omega_c \to \infty$. This results in an integral equation for $\mu^*$, which can be solved for the self-energy in terms of $\mu^*$, providing the energy dependence of $\mu^*$ is neglected. The physical meaning of this parameter is that it describes the contribution of the Coulomb interaction potential which is outside the range $[-\omega_c,\omega_c]$. On the imaginary axis, analogous approximations are used: above the cutoff, $\phi(k,i\omega_n) \approx \phi_\infty(k)$ and $Z(k,i\omega_n) \approx 1$, and $\mu^*$ is similarly found to satisfy an integral equation, which can be solved for by neglecting the frequency dependence. This quantity on the imaginary axis does not analytically continue to a sharp cutoff on the real axis. Hence, the $\mu^*$ used here is to be considered as a parameter to be fit to the experimental value of $T_c$.

We therefore can write:

$$\Sigma_c(i\omega_n) = -T\sum_m \mu^*(\omega_c)\theta(\omega_c - |\omega_m|)\int_{-\infty}^{\infty} d\epsilon' \frac{N(\epsilon')}{N(0)}\tau_3 G^{od}(\epsilon', i\omega_m)\tau_3 \quad . \quad (A.45)$$

Here we will consider only the off diagonal (od) contribution as it will be reasonable to assume that the diagonal contributions are identical for both the normal and superconducting states and have already been absorbed into the band structure. For ordinary superconductors we can set $N(\epsilon') = N(0)$.

The fully interacting Green's function is then given by:

$$G^{-1}(\epsilon, i\omega_n) = G_o^{-1} - T\left\{\sum_m \lambda(\omega_n - \omega_m)\int_{-\infty}^{\infty} d\epsilon' \tau_3 G(\epsilon', i\omega_m)\tau_3 - \sum_m \mu^*(\omega_c)\theta(\omega_c - |\omega_m|)\int_{-\infty}^{\infty} d\epsilon' \tau_3 G^{od}(\epsilon, i\omega_m)\tau_3\right\}. \quad (A.46)$$

or,

$$i\omega_n Z(\vec{k}, i\omega_n)\tau_0 - \bar{\epsilon}_{\vec{k}}\tau_3 - \phi(\vec{k}, i\omega_n)\tau_1 - \bar{\phi}(\vec{k}, i\omega_n)\tau_2 =$$
$$= i\omega_n\tau_0 - \bar{\epsilon}_{\vec{k}}\tau_3 - T\left\{\sum_m \lambda(\omega_n - \omega_m)\int_{-\infty}^{\infty} d\epsilon' \tau_3 \left[\frac{P(\vec{k}, i\omega_n)}{H(\vec{k}, i\omega_n)}\right]\tau_3 - \sum_m \mu^*(\omega_c)\theta(\omega_c - |\omega_m|)\int_{-\infty}^{\infty} d\epsilon' \tau_3 \left[\frac{P^{od}(\vec{k}, i\omega_n)}{H(\vec{k}, i\omega_n)}\right]\tau_3\right\}, \quad (A.47)$$

with

$$P(\vec{k}, i\omega_n) = i\omega_n Z(\vec{k}, i\omega_n)\tau_0 + \bar{\epsilon}_{\vec{k}}\tau_3 + \phi(\vec{k}, i\omega_n)\tau_1 - \bar{\phi}(\vec{k}, i\omega_n)\tau_2 \quad (A.48)$$

and

$$P^{od}(\vec{k}, i\omega_n) = i\omega_n Z(\vec{k}, i\omega_n)\tau_0^{od} + \bar{\epsilon}_{\vec{k}}\tau_3^{od} + \phi(\vec{k}, i\omega_n)\tau_1^{od} - \bar{\phi}(\vec{k}, i\omega_n)\tau_2^{od} \quad (A.49)$$

and

$$H(\vec{k}, i\omega_n) = [i\omega_n Z(\vec{k}, i\omega_n)]^2 - \bar{\epsilon}_{\vec{k}}^2 - \phi^2(\vec{k}, i\omega_n) - \bar{\phi}^2(\vec{k}, i\omega_n)$$
$$= -\{\omega_n^2 Z^2(\vec{k}, i\omega_n) + \bar{\epsilon}_{\vec{k}}^2 + \phi^2(\vec{k}, i\omega_n) + \bar{\phi}^2(\vec{k}, i\omega_n)\}. \quad (A.50)$$

From the properties of the spin matrices we have:

$$\tau_3\tau_0\tau_3 = \tau_0 \qquad \tau_3\tau_3\tau_3 = \tau_3 \qquad \tau_3\tau_1\tau_3 = -\tau_1 \qquad \tau_3\tau_2\tau_3 = -\tau_2 \quad (A.51)$$

Therefore, by comparison we obtain:

$$i\omega_n Z(i\omega_n) = i\omega_n - T\left\{\sum_m \lambda(\omega_n - \omega_m)\int_\infty^\infty d\epsilon' \frac{i\omega_m Z(i\omega_m)}{H(i\omega_m)}\right\}. \quad (A.52)$$

$$\phi(i\omega_n) = T\left\{\sum_m [\lambda(\omega_n - \omega_m) - \mu^*\theta(\omega_c - |\omega_m|)]\int_{-\infty}^\infty d\epsilon' \frac{-\phi(i\omega_m)}{H(i\omega_m)}\right\}. \quad (A.53)$$

$$\bar{\phi}(i\omega_n) = T\left\{\sum_m [\lambda(\omega_n - \omega_m) - \mu^*\theta(\omega_c - |\omega_m|)]\int_{-\infty}^\infty d\epsilon' \frac{-\bar{\phi}(i\omega_m)}{H(i\omega_m)}\right\}. \quad (A.54)$$

For $\phi$ and $\bar{\phi}$ identical defining equations are found. These functions can only be distinguished from each other by a proportionality factor, therefore, any scaling of the kind that preserves $\phi^2 + \bar{\phi}^2$ results in equally good solutions. We therefore propose to set $\bar{\phi} = 0$ and obtain:

$$\omega_n Z(i\omega_n) = \omega_n + T\left\{\sum_m \lambda(\omega_n - \omega_m)\int_{-\infty}^\infty d\epsilon' \frac{\omega_m Z(i\omega_m)}{\omega_m^2 Z^2(i\omega_m) + \epsilon'^2 + \phi^2(i\omega_m)}\right\} \quad (A.55)$$

$$\phi(i\omega_n) = T\sum_m [\lambda(\omega_n - \omega_m) - \mu^*\theta(\omega_c - |\omega_m|)]\int_{-\infty}^\infty d\epsilon' \frac{\phi(i\omega_m)}{\omega_m^2 Z^2(i\omega_m) + \epsilon'^2 + \phi^2(i\omega_m)} \quad (A.56)$$

with $\omega_n = \pi T(2n+1)$, the usual Matsubara frequencies. The integral that appears here can immediately be worked out:

$$\int_{-\infty}^\infty d\epsilon \frac{1}{\omega^2 Z^2 + \phi^2 + \epsilon^2} = \pi \frac{1}{\sqrt{\omega^2 Z^2 + \phi^2}} \quad . \quad (A.57)$$

We further introduce the symbols $\tilde{\omega}_n = \omega_n Z(i\omega_n)$ and $\tilde{\Delta}_n = \phi(i\omega_n)$ and obtain the usual form of the Eliashberg equations on the imaginary axis:

$$\tilde{\omega}_n = \omega_n + \pi T\sum_m \lambda(\omega_n - \omega_m)\frac{\tilde{\omega}_m}{\sqrt{\tilde{\omega}_m^2 + \tilde{\Delta}_m^2}} \quad (A.58)$$

$$\tilde{\Delta}_n = \pi T\sum_{m=-N}^{N} [\lambda(\omega_n - \omega_m) - \mu^*]\frac{\tilde{\Delta}_m}{\sqrt{\tilde{\omega}_m^2 + \tilde{\Delta}_m^2}}, \quad \omega_c = \pi T(2N+1) \quad (A.59)$$

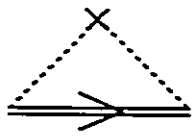

Figure A.3 The electron self-energy due to impurity scattering.

From these equations we can obtain the critical temperature $T_c$. One makes use of the fact that as $T \to T_c$, the gap $\tilde{\Delta}$ goes to zero. We therefore have the linearized equations for $T_c$:

$$\tilde{\omega}_n = \omega_n + \pi T \sum_m \lambda(\omega_n - \omega_m)\mathrm{sign}\omega_m \tag{A.60}$$

$$\tilde{\Delta}_n = \pi T_c \sum_{m=-N}^{N} [\lambda(\omega_n - \omega_m) - \mu^*]\frac{\tilde{\Delta}_m}{|\tilde{\omega}_m|}, \quad \omega_c = \pi T(2N+1) \tag{A.61}$$

There are two input parameters for this theory: $\alpha^2 F(\Omega)$ and $\mu^*$. One can apply the data from inelastic neutron scattering to determine $F(\Omega)$; further, the IV characteristic of superconducting tunnelling experiments gives information concerning $\alpha^2 F(\Omega)$. On the imaginary axis, $\mu^*$ is chosen to give the experimentally observed $T_c$.

## A.4 MODIFICATION FOR MAGNETIC AND NONMAGNETIC IMPURITY SCATTERING

The self-energy diagram for normal impurity scattering is given in Fig. A.3. In this case, perturbation theory is well-behaved and for a dilute concentration of impurities, the concentration $n_i$ forms a small expansion parameter. We can therefore treat the scattering in lowest order of the Born

approximation, corresponding to Fig. A.3. The self-energy can be written for this diagram as:

$$\Sigma^N(\vec{k}, i\omega_n) = n_N \sum_{\vec{k}'} |\langle k \mid V_N \mid k' \rangle|^2 S_N(\vec{k}' - \vec{k}) \tau_3 G(\vec{k}', i\omega_n) \tau_3 \quad , \qquad (A.62)$$

where the structure factor is given as

$$S_N(\vec{Q}) = \sum_a e^{-i\vec{Q}\cdot\vec{R}_a} \quad , \qquad (A.63)$$

with $\vec{R}_a$ the impurity location and $V_N$ the alteration of the crystal potential due to the presence of the impurity. There is no time dependence associated with impurity scattering and hence there is no frequency sum here.

The normal impurity scattering rate $1/\tau_N$ is then given as

$$\frac{1}{\tau_N} = \frac{2\pi}{\hbar} n_N N(0) \langle\langle |V_N|^2 \rangle\rangle_{FS} \quad , \qquad (A.64)$$

where $\langle\langle\rangle\rangle_{FS}$ denotes the averaging of the impurity potential over the Fermi surface. Once the self-energy has been specified, we can redo the algebra of Section A.3 with Eq. (A.62) added to Eq. (A.22).

The self-energy for paramagnetic impurities is also given by the diagram of Fig. A.3. However, the interaction now includes the impurity spin which brings in another two degrees of freedom. It is therefore more natural in this case to extend the Nambu notation from a $2 \times 2$ notation to a $4 \times 4$ notation. Pauli matrices are retained but there are two sets $\sigma_i$ and $\rho_i$, acting on the spin and particle-hole spaces separately. In this notation, we have:

$$\Psi_{\vec{k}} = \begin{pmatrix} c_{\vec{k}\uparrow} \\ c_{\vec{k}\downarrow} \\ c^\dagger_{-\vec{k}\uparrow} \\ c^\dagger_{-\vec{k}\downarrow} \end{pmatrix} \quad \text{and} \quad \Psi^\dagger_{\vec{k}} = \left( c^\dagger_{\vec{k}\uparrow}, c^\dagger_{\vec{k}\downarrow}, c_{-\vec{k}\uparrow}, c_{-\vec{k}\downarrow} \right) \quad , \qquad (A.65)$$

and tensor products are defined as

$$\rho_3\sigma_1 = \begin{pmatrix} \sigma_1 & 0 \\ 0 & -\sigma_1 \end{pmatrix} \quad . \tag{A.66}$$

Hence,

$$G_0(\vec{k}, i\omega_n) = \frac{i\omega_n\rho_0\sigma_0 + \epsilon_{\vec{k}}\rho_3\sigma_0}{(i\omega_n)^2 - (\epsilon_{\vec{k}})^2} \tag{A.67}$$

and Eq. (A.30) is written as

$$\Sigma(\vec{k}, i\omega_n) = i\omega_n[1 - Z(\vec{k}, i\omega_n)]\rho_0\sigma_0 + \chi(\vec{k}, i\omega_n)\rho_3\sigma_0 + \phi(\vec{k}, i\omega_n)\rho_1\sigma_2 + \bar{\phi}(\vec{k}, i\omega_n)\rho_2\sigma_2 \quad . \tag{A.68}$$

The self-energy is then written as

$$\Sigma^P(\vec{k}, i\omega_n) = n_P \sum_{k'} |\langle k \mid V_P \mid k' \rangle|^2 \frac{S(S+1)}{12} \vec{\alpha} G(\vec{k}', i\omega_n) \cdot \vec{\alpha} \quad . \tag{A.69}$$

with $S$ the impurity spin, $V_P$ the alteration of the crystal potential due to the presence of the impurity, and the vector matrix $\vec{\alpha}$ defined by $\vec{\alpha} = (\rho_3\sigma_1, \rho_0\sigma_2, \rho_3\sigma_3)$. There is no time dependence associated with impurity scattering to this order in the perturbation expansion and hence again there is no frequency sum here. The paramagnetic impurity scattering rate $1/\tau_P$ is defined as

$$\frac{1}{\tau_N} = \frac{2\pi}{\hbar} n_P S(S+1) N(0) \langle\langle |V_P|^2 \rangle\rangle_{FS} \quad . \tag{A.70}$$

Once again, we can repeat the procedure in Section A.3, in this expanded notation. The final result is given in summary in Section A.7.

## A.5 MODIFICATION FOR SPIN FLUCTUATIONS

For spin fluctuations, if one assumes an exchange coupling $J$ between the conduction electrons and the local moments (a quantity analogous to

the electron-phonon coupling $g$) then the self-energy resembles the electron-phonon self-energy, the only modification being the inclusion of the vector matrix $\vec{\alpha}$, as in the case of paramagnetic impurities:

$$\Sigma^{sf}(\vec{k}, i\omega_n) = -\frac{J^2}{\beta}\sum_{m\vec{k}'} \vec{\alpha}G(\vec{k}', i\omega_m)\cdot\vec{\alpha}D(\vec{k}-\vec{k}', i\omega_n - i\omega_m) \quad . \qquad (A.71)$$

The spin fluctuation propagator has the spectral representation

$$D(\vec{q}, i\nu_n) = \int_0^\infty \frac{d\Omega}{\pi} B(\vec{q}, \Omega)\frac{2\Omega}{(i\nu_n)^2 - \Omega^2} \quad . \qquad (A.72)$$

with the spectral density given, as usual, in terms of the Fourier transform of the spin-spin correlation function:

$$B(\vec{q}, \Omega) = \frac{1 - e^{-\beta\Omega}}{2}[S(\vec{q}, \Omega) + \pi\langle\vec{S}(\vec{q})\rangle\cdot\langle\vec{S}(-\vec{q})\rangle\delta(\Omega)] \quad , \qquad (A.73)$$

where $\vec{S}(\vec{q})$ is the Fourier transform of the spin density operator [Doniach and Sondheimer (1974)] and $S(\vec{q}, \Omega)$ is the spin-spin correlation function:

$$\begin{aligned} S(\vec{q}, \Omega) &= \int_{-\infty}^{\infty} dt \int \frac{d^3r}{V} e^{i(\Omega t - \vec{k}\cdot\vec{r})} S(\vec{r}, t) \quad , \\ &= \int_{-\infty}^{\infty} dt\; e^{i\Omega t}\,[\langle\vec{S}(\vec{q}, t)\cdot\vec{S}(-\vec{q}, 0)\rangle - \langle\vec{S}(\vec{q}, 0)\cdot\vec{S}(-\vec{q}, 0)\rangle] \quad . \qquad (A.74) \end{aligned}$$

With this self-energy defined, the procedure of Section A.3 can be followed to obtain the modified form of the Eliashberg equations, summarized in Section A.7, written in terms of the paramagnon spectral density

$$P(\Omega) = N(0)I^2\int_0^{2k_F} \frac{qdq}{2k_F^2} B(q, \Omega) \quad . \qquad (A.75)$$

## A.6 MODIFICATION FOR CURRENTS

Likewise, under the application of an applied current there is a shift in the energies due to a term $\vec{v}\cdot\vec{q}_s$. This enters the Green's function in the tensor notation as:

$$G_0(\vec{k},i\omega_n)=\frac{(i\omega_n-\vec{v}\cdot\vec{q}_s)\rho_0\sigma_0+\epsilon_{\vec{k}}\rho_3\sigma_0}{(i\omega_n-\vec{v}\cdot\vec{q}_s)^2-(\epsilon_{\vec{k}})^2} \tag{A.76}$$

and

$$\Sigma(\vec{k},i\omega_n)=i\omega_n[1-Z(\vec{k},i\omega_n)]\rho_0\sigma_0-\vec{v}\cdot\vec{q}_s\rho_0\sigma_0+\chi(\vec{k},i\omega_n)\rho_3\sigma_0$$
$$+\phi(\vec{k},i\omega_n)\rho_1\sigma_2+\bar{\phi}(\vec{k},i\omega_n)\rho_2\sigma_2 \tag{A.77}$$

With these definitions, the derivation proceeds in the same fashion as before. Note that in Chapter 2, our notation is to take $\rho_0=1$ and $\sigma_0=1$.

## A.7 GENERAL FORM OF THE ELIASHBERG EQUATIONS

Here we state the final form of the Eliashberg equations when all the modifications mentioned in this appendix are included.

$$\tilde{\Delta}_n=\pi T\sum_{m=-\infty}^{\infty}[\lambda^-(n-m)-\mu^*\theta(\omega_c-|\omega_m|)]\int_{-1}^{1}\frac{dz}{2}\frac{\tilde{\Delta}_m}{\sqrt{(\tilde{\omega}_m-isz)^2+\tilde{\Delta}_m^2}}$$
$$+\pi(t^+-t^-)\int_{-1}^{1}\frac{dz}{2}\frac{\tilde{\Delta}_n}{\sqrt{(\tilde{\omega}_n-isz)^2+\tilde{\Delta}_n^2}} \tag{A.78}$$

and

$$\tilde{\omega}_n=\omega_n+\pi T\sum_{m=-\infty}^{\infty}\lambda^+(n-m)\int_{-1}^{1}\frac{dz}{2}\frac{\tilde{\omega}_m-isz}{\sqrt{(\tilde{\omega}_m-isz)^2+\tilde{\Delta}_m^2}}$$
$$+\pi(t^++t^-)\int_{-1}^{1}\frac{dz}{2}\frac{\tilde{\omega}_n-isz}{\sqrt{(\tilde{\omega}_n-isz)^2+\tilde{\Delta}_n^2}}\ . \tag{A.79}$$

Where,

$$\lambda^{\pm}(n-m) \equiv \lambda(i\omega_m - i\omega_n) \equiv \int_0^\infty \frac{2\omega[\alpha^2 F(\omega) \pm P(\omega)]}{\omega^2 - (i\omega_m - i\omega_n)^2}\, d\omega \quad , \tag{A.80}$$

and $\tilde{\Delta}_n \equiv \tilde{\Delta}(i\omega_n) = Z(i\omega_n)\Delta(i\omega_n)$ and $\tilde{\omega}_n = Z(i\omega_n)\omega_n$. The normal impurity scattering rate, $t^+$, is defined as $1/(2\pi\tau_N)$ and the paramagnetic impurity scattering rate, $t^-$, is defined as $1/(2\pi\tau_P)$, where $\tau_P$ is the spin-flip lifetime and $\tau_N$ is the normal impurity scattering time. Here, $s = v_F q_s$ where $q_s$ is the magnitude of the applied momentum of the current. The electron-phonon and paramagnon spectral densities are $\alpha^2 F(\omega)$ and $P(\omega)$, respectively.

# Appendix B

## *jc.c: Program and Documentation*

### B.1 THEORETICAL EQUATIONS

In Chapter 2, we discussed results of calculations of the critical current of a thin film, type I superconductor. Numerical solution of Eqs. (2.5)-(2.7) was required and, in this appendix, we discuss the realization of this procedure in greater detail.

Restating the coupled equations we wish to solve, we have for the superfluid current density $\vec{j}_s$ [Eq. (2.5)]:

$$\vec{j}_s = \frac{3eN}{2k_F}\pi T \sum_{n=-\infty}^{\infty} \int_{-1}^{1} dz \frac{i(\tilde{\omega}_n - isz)z}{\sqrt{(\tilde{\omega}_n - isz)^2 + \tilde{\Delta}_n^2}} \hat{q}_s \quad , \qquad (B.1)$$

where $\varepsilon = v_F q_s = k_F q_s/m$, $\hat{q}_s$ is a unit vector in the direction of $\vec{q}_s$, $N$ the electronic density and $k_F$ the Fermi momentum. The Eliashberg equations for the order parameter and renormalized frequencies of the superconducting

state, modified by the presence of the current, are given as [Eqs. (2.6) and (2.7)]:

$$\tilde{\Delta}_n = \pi T \sum_{m=-\infty}^{\infty} [\lambda(n-m) - \mu^*\theta(\omega_c - |\omega_m|)] \int_{-1}^{1} \frac{dz}{2} \frac{\tilde{\Delta}_m}{\sqrt{(\tilde{\omega}_m - isz)^2 + \tilde{\Delta}_m^2}} + \pi(t^+ - t^-) \int_{-1}^{1} \frac{dz}{2} \frac{\tilde{\Delta}_n}{\sqrt{(\tilde{\omega}_n - isz)^2 + \tilde{\Delta}_n^2}} \qquad (B.2)$$

and

$$\tilde{\omega}_n = \omega_n + \pi T \sum_{m=-\infty}^{\infty} \lambda(n-m) \int_{-1}^{1} \frac{dz}{2} \frac{\tilde{\omega}_m - isz}{\sqrt{(\tilde{\omega}_m - isz)^2 + \tilde{\Delta}_m^2}} + \pi(t^+ + t^-) \int_{-1}^{1} \frac{dz}{2} \frac{\tilde{\omega}_n - isz}{\sqrt{(\tilde{\omega}_n - isz)^2 + \tilde{\Delta}_n^2}} \quad . \qquad (B.3)$$

Where [Eq. (2.8)],

$$\lambda(n-m) \equiv \lambda(i\omega_m - i\omega_n) \equiv \int_0^{\infty} \frac{2\nu\alpha^2 F(\nu)}{\nu^2 - (i\omega_m - i\omega_n)^2} d\nu \qquad (B.4)$$

and $\tilde{\Delta}_n \equiv \tilde{\Delta}(i\omega_n) = Z(i\omega_n)\Delta(i\omega_n)$ and $\tilde{\omega}_n = Z(i\omega_n)\omega_n$ with $i\omega_n \equiv i\pi T(2n-1)$, $n = 0, \pm 1, \pm 2, \ldots$. As before, the normal impurity scattering rate, $t^+$, is defined as $1/(2\pi\tau_N)$ and the paramagnetic impurity scattering rate, $t^-$, is defined as $1/(2\pi\tau_P)$, where $\tau_P$ is the spin-flip lifetime and $\tau_N$ is the normal impurity scattering time.

We can further manipulate these equations into a form which is more convenient for numerical solution. Performing the integrals over $z$ and writing $\bar{\Delta}_n = \tilde{\Delta}_n / |\tilde{\omega}_n|$ and $\bar{s}_m = s/|\tilde{\omega}_m|$, we find that Eqs. (*B*.2) and (*B*.3) can be written as

$$|\tilde{\omega}_n| \bar{\Delta}_n = \pi T \sum_{m=-\infty}^{\infty} [\lambda(m-n) - \mu^*] \frac{\bar{\Delta}_m}{\bar{s}_m} \arctan\frac{y_m}{x_m} + \pi(t^+ - t^-) \frac{\bar{\Delta}_n}{\bar{s}_n} \arctan\frac{y_n}{x_n} \qquad (B.5)$$

and

$$\tilde{\omega}_n = \pi T\{2n+1+\sum_{m=-\infty}^{\infty}\lambda(m-n)\mathrm{sgn}(\omega_m)\frac{\mathrm{imf}[m]}{\bar{s}_m}\}+\pi(t^+ + t^-)\mathrm{sgn}(\omega_n)\frac{\mathrm{imf}[n]}{\bar{s}_n} \quad , \tag{B.6}$$

where we have defined the following notation:

$$x_{pm} = 1-\bar{s}_m^2+\bar{\Delta}_m^2 \quad , \tag{B.7}$$

$$y_{pm} = 2\bar{s}_m \quad , \tag{B.8}$$

$$\rho_m = \sqrt{x_{pm}^2+y_{pm}^2} \quad , \tag{B.9}$$

$$\mathrm{imf}[m] = \sqrt{(\rho_m - x_{pm})/2} \quad , \tag{B.10}$$

$$\mathrm{ref}[m] = \sqrt{(\rho_m + x_{pm})/2} \quad , \tag{B.11}$$

$$x_m = 1+\mathrm{ref}[m] \quad , \tag{B.12}$$

$$y_m = \bar{s}_m + \mathrm{imf}[m] \quad . \tag{B.13}$$

Using the symmetries of the gaps, $\bar{\Delta}_{-n} = \bar{\Delta}_{n-1}$, and $\omega_{-n} = -\omega_{n-1}$ to fold the sums to the $[0,\infty]$ domain:

$$|\,\tilde{\omega}_n\,|\,\bar{\Delta}_n = \pi T\sum_{m=0}^{N}[\lambda(m-n)+\lambda(m+n+1)-2\mu^*]\frac{\bar{\Delta}_m}{\bar{s}_m}\arctan\frac{y_m}{x_m}$$

$$+\pi(t^+ - t^-)\frac{\bar{\Delta}_n}{\bar{s}_n}\arctan\frac{y_n}{x_n} \quad , \tag{B.14}$$

and

$$\tilde{\omega}_n = \pi T\{2n+1+\sum_{m=0}^{N}[\lambda(m-n)-\lambda(m+n+1)]\frac{\mathrm{imf}[m]}{\bar{s}_m}\}$$

$$+\pi(t^+ + t^-)\frac{\mathrm{imf}[n]}{\bar{s}_n} \quad . \tag{B.15}$$

These equations can easily be shown to reduce to the usual nonlinear Eliashberg equations in the limit of $s \to 0$:

$$|\tilde{\omega}_n|\tilde{\Delta}_n = \pi T \sum_{m=0}^{N}[\lambda(m-n)+\lambda(m+n+1)-2\mu^*]\frac{\tilde{\Delta}_m}{\sqrt{1+\tilde{\Delta}_m^2}} + \pi(t^+ - t^-)\frac{\tilde{\Delta}_n}{\sqrt{1+\tilde{\Delta}_n^2}} \qquad (B.16)$$

and

$$\tilde{\omega}_n = \pi T\{2n+1+\sum_{m=0}^{N}[\lambda(m-n)-\lambda(m+n+1)]\frac{1}{\sqrt{1+\tilde{\Delta}_m^2}}\} + \pi(t^+ + t^-)\frac{1}{\sqrt{1+\tilde{\Delta}_n^2}} \quad . \qquad (B.17)$$

In a similar manner, the current density can be shown to be:

$$j_s \propto \sum_{n=0}^{\infty}\frac{1}{\tilde{s}_n^2}\{\tilde{s}_n \mathrm{ref}[n] + \tilde{\Delta}_n^2 \arctan\frac{y_n}{x_n}\} \quad , \qquad (B.18)$$

where $t$ is the reduced temperature $T/T_c$.

We now solve Eqs. (*B*.14)-(*B*.15) and Eq. (*B*.18). The procedure is to search for a value of $s$ which maximizes $j_s$. In section II, we summarize the essential points of the subroutines in a non-rigorous fashion. The subroutines are listed in the order in which they appear in the program; after the main subroutine, this is alphabetical. Section III contains some general comments about the program, particularly in the running of the code. Section IV contains the program listing.

## B.2 SUBROUTINES

(i) `void main(argc,argv)`

This is the main part of the program that primarily calls subroutines that execute the real working code. Defined in /home/physun/ewald/util.c are `Time()` and `Date()` and these simply store the present time and date at the beginning of the program in the character arrays `datum` and `ttime`, to be printed in the output listing.

g_screen is a switch to be used externally when running the program. It is set to one in the global variable list. In the statement

```
g_screen = stparg(argc,argv,"-s") == (char *)NULL;
```

if there is a `-s` after the command to execute the program then g_screen = 0 and all print statements that start with `if (g_screen)` will not be printed. That is, there will be no printing to the screen. Note that `*stparg` is also defined in util.c.

The next few statements read the current logged directory from which the program is being run and appends this to the listing file. The name of the listing file will depend on whether the `-l` option (programmed in these statements) has been used, *i.e.*, using `-ltest` when executing the program means that the listing file will be test.lst on the directory from which the program was run. If this is not given, the default `LISTE` is used which in this case is in the definitions as jc.lst. The `MakeFile` command which attaches the logged directory, listing filename and ".lst" together is defined in util.c.

The subroutine `input()` is called to read in any necessary input parameters. `page1()`, `page2()`, `page3()` print output information to the listing file.

Next there is a loop with counter inrun that is a temperature loop. For each iteration it sets the reduced temperature to be the one from the array s_tc[inrun] (which may either be the standard temperature set or specific temperatures read into the program - see input()).

In the call if(it_init(inrun)), the routine it_init is called to initialize all the parameters that must be changed for the new temperature. If something fails here, it returns a value of one and the program exits.

Then the call Titer(inrun) is executed which does the iterative calculation for $j_c$ at the temperature g_t. The summary values of the temperature $t$, $(j_c/j_o)^{2/3}$, and $j_c/j_{GL}$, where $j_{GL}$ = chi() * $(1-t)^{3/2}$, are stored in the array g_summ[][].

If the input was not a delta function and functional derivatives have been asked for (g_fder = 1) then the subroutine funder() that calculates the functional derivatives is called. The inrun loop finishes here.

jc_0() is a subroutine to find the $T = 0$ value of $(j_c/j_o)^{2/3}$. jc_end() prints the contents of jc_rec to a binary output file for use by another program such as tunnel.c. g_save must be set to one for this to occur. summary() lists the contents of the g_summ array in columns.

**(ii) double bdelta (nn,cc)**

This subroutine has been taken from fbelow.c program to calculate an initial set of starting gaps and frequencies at a temperature $T$ with no applied momentum (ie. $v = 0$). This is the usual iteration of the nonlinear Eliashberg equations:

$$|\tilde{\omega}_n|\tilde{\Delta}_n = \pi T \sum_{m=0}^{N} [\lambda(m-n) + \lambda(m+n+1) - 2\mu^*] \frac{\tilde{\Delta}_m}{\sqrt{1+\tilde{\Delta}_m^2}}$$

$$+\pi(t^+ - t^-)\frac{\tilde{\Delta}_n}{\sqrt{1+\tilde{\Delta}_n^2}} \qquad (B.19)$$

and

$$\tilde{\omega}_n = \pi T\{2n+1+\sum_{m=0}^{\mathcal{N}}[\lambda(m-n)-\lambda(m+n+1)]\frac{1}{\sqrt{1+\tilde{\Delta}_m^2}}\}$$
$$+\pi(t^+ + t^-)\frac{1}{\sqrt{1+\tilde{\Delta}_n^2}} \quad . \qquad (B.20)$$

where $\bar{\Delta}_n = \tilde{\Delta}_n / \mid \tilde{\omega}_n \mid$. In this piece of code, bc is equal to $\mid \tilde{\omega}_n \mid \bar{\Delta}_n/\pi T$ and wwmw is $\tilde{\omega}_n/\pi T$. nn is the gap index and cc is a factor multiplying $\Delta$ which is used by the calling subroutine jciter to iterate quickly for a self-consistent solution (see jciter). jcdelta is used by jciter to call bdelta.

(iii) double chi()

The impurity-dependent prefactor in the BCS Ginzburg-Landau theory near $T_c$ is given as:

$$\chi(\rho) = \frac{8}{7\zeta(3)}\sum_{n=0}^{\infty}\frac{1}{(2n+1)^2}\frac{1}{2n+1+\rho} \quad , \qquad (B.21)$$

where $\rho = (2\pi T_c\tau)^{-1}$ and $\zeta(3)$ is the Riemann zeta function ($\zeta(3) = 1.202$). This routine calculates this prefactor. It is necessary for the normalization of $j_c$ by $j_{GL}$ and can be called at the end of the subroutine Titer, but this is not done in the present program listing of section IV.

(iv) double current(sbar)

This subroutine calculates the current $j_s$ from the formula

$$j_s = \text{CONST}*t\sum_{n=0}^{\infty}\frac{1}{\bar{s}_n^2}\{\bar{s}_n \text{ref}[n] + \tilde{\Delta}_n^2 \arctan\frac{y_n}{x_n}\} \quad , \qquad (B.22)$$

where these quantities have been globally passed from jcdelta. The subroutine jcdelta should be consulted for the definition of the above variables. CONST is defined in the program listing.

(v) `void funder()`

This routine calculates the functional derivatve of $j_c$ with respect to $\alpha^2F(\omega)$ for a particular temperature $t$. The functional derivative is given as:

$$\frac{\delta j_c^{2/3}}{\delta \alpha^2 F(\Omega)} = \lim_{\epsilon \to 0} \frac{j_c^{2/2}[\alpha^2 F(\omega) + \epsilon\delta(\omega - \Omega)] - j_c^{2/3}[\alpha^2 F(\omega)]}{\epsilon} \qquad (B.23)$$

One frequency bin in the $\alpha^2F(\omega)$ spectrum at a frequency $\Omega$ is augumented by a delta function of infinitesimal weight $\epsilon$ and the change in the property $j_c$ is computed and analogous to the usual derivative, the difference between the perturbed and unperturbed $j_c$ divided by $\epsilon$ in the limit of $\epsilon$ going to zero is the functional derivative. This derivative is a measure of which frequencies enhance or de-enhance the superconducting property.

The routine is called by the `main()` routine after $j_c$, for a particular temperature, has been found and only if functional derivatives have been requested (*i.e.*, if `g_fder = 1`). Also, this can only be done for a real $\alpha^2F(\omega)$ spectrum and not a delta function spectrum. The first few lines request an output filename for the functional derivative data and creates the file using the `MakeFile` routine defined in util.c. The value of $j_c$ is stored in `s_jc` and also `g_full` is stored and then set to zero so that there is no iteration output (an entire calculation for $j_c$ is done for each frequency bin which would increase the amount of useless output by a factor corresponding to the number of bins in the $\alpha^2F(\omega)$ spectrum). Next, a loop is run where, for each iteration, one bin in the $\alpha^2F(\omega)$ is stored in `savbin` and a new bin is defined at this frequency which is greater by five percent. The $\epsilon$ in this case then is the area of this added piece or `eeps = 0.05*savbin*g_dw/tomeg`. Note that the `jc_rec.a2f` array is actually $\omega\alpha^2F(\omega)$ and hence we have to divide by the frequency here, which is `tomega`. The `epplus[i]` have to be recalculated

for the new $\alpha^2F(\omega)$ spectrum, as is done in the `it_init` routine by calling `rlambda`. `norm()` also is called again to recalculate the exact normal state $\omega$-channel. We are essentially reinitializing everything for the new modified spectrum. Then `Titer()` is called to iterate for the new $j_c$ and the functional derivative at that point is calculated as `djda[ifunc] = (g_jc-s_jc)/eeps`. The frequency is stored in the array `omeg[]` and the original value of the modified frequency bin is replaced into `jc_rec.a2f`. The step size starts with one frequency bin at a time to carefully describe the shape of the derivative, however, as the derivative levels off at higher frequencies fewer points are necessary to describe the curve and so the next few lines simply increase the step size to save time and unnecessary calculations. When the step size has incremented to the number of bins available, the program jumps out of the loop. Then there is the usual writing to the listing file of the arrays containing the frequencies and derivatives. And these are also written in column form into output files for use in plotting. `g_full` is restored to its original value.

(vi) `void input()`

This routine asks a lot of questions. See the sample jc.run file in section III to see typical input values. First it reads input from the data file (must be binary output from the ftcrit.c program and produced on the same machine (*i.e.*, MIPS/SPARC or physun); the two types are not compatible). Note `MakeFile` is defined in util.c. The structure for the input file is `Jcrec`, which is defined in the global variable list. If binary output is required at the end, a file is created.

This subroutine uses `ReadReal()` and `ReadChar()` which are both defined in util.c.

(vii) `it_init (inrun)`

This subroutine is very similar to the same routine in fbelow.c and is called by the `main` routine at the beginning of each temperature to initialize the number of Matsubara gaps, frequencies and $\lambda_n$'s. This number is assigned to `jc_rec.jcp1`. (For anyone who is familiar with the FORTRAN code for fbelow.c, as the arrays in C start at zero, there is no need to add one to this number as is done in the old FORTRAN version of fbelow.c. However, when calculating the $\lambda_n$'s the `for` loop ends with `2*ng+1` to compensate for both the loop starting at zero and the fact that ng is one less than the FORTRAN version.)

The `rlambd` routine is called to calculate the $\lambda_n$'s and `norm` is called to calculate the correction to the $\omega$-channel due to F. Marsiglio. Finally, if the temperature is too small such that the redimensioning of the arrays is greater than the dimension of the array, as defined in the global variable list, then the routine prints an error message and returns a one instead of a zero to the `main` routine and this causes `main` to exit the program.

(viii) `double jcdelta (nn,cc,sbar)`

This subroutine is called by `jciter()` to calculate $\tilde{\Delta}_n$ and $\tilde{\omega}_n$ for one iteration of the Eliashberg equations. If `sbar = 0` (note that $s$ is called `sbar` here), then the routine does this by calling the `bdelta` routine which is the usual fbelow.c version. Here `nn` refers to the gap or frequency index $n$.

For nonzero `sbar`, the equations for the Matsubara gaps and frequencies are used:

$$|\tilde{\omega}_n| \tilde{\Delta}_n = \pi T \sum_{m=0}^{N} [\lambda(m-n) + \lambda(m+n+1) - 2\mu^*] \frac{\tilde{\Delta}_m}{\tilde{s}_m} \arctan \frac{y_m}{x_m}$$

$$+\pi(t^+ - t^-)\frac{\bar{\Delta}_n}{\bar{s}_n}\arctan\frac{y_n}{x_n} \quad . \tag{B.24}$$

and

$$\tilde{\omega}_n = \pi T\{2n+1+\sum_{m=0}^{N}[\lambda(m-n)-\lambda(m+n+1)]\frac{\mathrm{imf}[m]}{\bar{s}_m}\}$$

$$+\pi(t^+ + t^-)\frac{\mathrm{imf}[n]}{\bar{s}_n} \quad . \tag{B.25}$$

where

$$x_{pm} = 1 - \bar{s}_m^2 + \bar{\Delta}_m^2 \quad , \tag{B.26}$$

$$y_{pm} = 2\bar{s}_m \quad , \tag{B.27}$$

$$\rho_m = \sqrt{x_{pm}^2 + y_{pm}^2} \quad , \tag{B.28}$$

$$\mathrm{imf}[m] = \sqrt{(\rho_m - x_{pm})/2} \quad , \tag{B.29}$$

$$\mathrm{ref}[m] = \sqrt{(\rho_m + x_{pm})/2} \quad , \tag{B.30}$$

$$x_m = 1 + \mathrm{ref}[m] \quad , \tag{B.31}$$

$$y_m = \bar{s}_m + \mathrm{imf}[m] \quad , \tag{B.32}$$

and $\bar{\Delta}_n = \tilde{\Delta}_n / \mid \tilde{\omega}_n \mid$ and $\bar{s}_n = s / \mid \tilde{\omega}_n \mid$. In this piece of code, `bc` is equal to $\mid \tilde{\omega}_n \mid \bar{\Delta}_n/\pi T$ and `wwmw` is $\tilde{\omega}_n/\pi T$. The `norm()` routine should be cross-referenced here to understand the slight differences associated with the $\omega$-channel that come about from summing from the cutoff to infinity using the the normal state $\omega$-channel.

(ix) `double jcder (x,y)`

This routine calculates the derivative $dj/dv$ by fitting a second order polynomial $a + bx + cx^2$ to three points of $j$ versus $v$ passed in the arrays `y[]` and `x[]`, respectively. The derivative $b + 2cx$ is evaluated at the middle point $x =$ `x[1]` and passed back to the calling routine `Titer`.

(x) `void jc_end()`

If `g_save = 1` (see `input()`), then a file is opened that has been given a name in `input()` and `jc_rec` of the structure `Jcrec` is written to the file in binary to be read by another program that uses the same structure, such as tunnel.c.

(xi) `void jciter (sbar,itsw)`

This routine is adapted from the `iteration` routine of fbelow.c. It is the control routine for iterating for a self-consistent set of Matsubara frequencies and gaps for a particular velocity $v$ (or `sbar` here). It is called by `Titer` and calls `jcdelta` which calculates the gaps and frequencies from the nonlinear Eliashberg equations for $v \neq 0$ or by in turn calling `bdelta` for the case of $v = 0$.

For `nn = 0` and `s = 0` a gap is iterated for using a fast iteration where a guess for $\Delta_0$ is given as $c\Delta_0$ and a $\Delta_0^{new}$ is calculated. Three of these are found and a Newton iteration procedure is used to quickly find the self-consistent solution.

Otherwise, for $s \neq 0$, a slow iteration occurs where the old gaps and frequencies are used on the righthand side of the equations to calculate a new set and the procedure repeated until self-consistency is achieved.

(xii) `void jc_0()`

If reduced temperatures have been calculated that are less than or equal to $t = 0.2$, then `jc_0` uses the last four values of $(j_c/j_o)^{2/3}$ and their corresponding $t$'s to fit a cubic polynomial using `inv(x,y)` defined in util.c,

where

$$y[i] = a + bx[i] + cx^2[i] + dx^3[i] \qquad (B.33)$$

and the $T = 0$ value is simply $a$. After matrix inversion, this has been returned in the array y[], where $a$ =y[0], $b$ =y[1], $c$ =y[2], and $d$ =y[3]. $a$ is assigned to g_jc0.

(xiii) `void jc_slope()`

This subroutine calculates the slope $dj_c^{2/3}/dT$ at $T_c$ by fitting a polynomial, as described above in `jc_0()`, to the four points around $T_c$, taking the derivative of this polynomial and evaluating it at $T_c$.

(xiv) `void norm()`

This subroutine is called by `it_init()` and `funder()` after the calculation of the epplus[]. The output global array `wwmnorm[]` is used in `bdelta()` and `jcdelta()`. This routine was added to the programs for hc2, fbelow, and ftcrit by F. Marsiglio to sum the $\omega$-channel more accurately. In this routine the exact normal state $\tilde{\omega}_n/\pi T$ is calculated and this is `wwmnorm[n]`. This is given as:

$$\frac{\tilde{\omega}_n}{\pi T} = 2n + 1 + \lambda(0) + 2\sum_{m=1}^{n} \lambda(m) \qquad (B.34)$$

for $\omega_n = \pi T(2n+1)$. Thus, in the calculation of the $\omega$-channel for the superconducting state (done in `bdelta` and `jcdelta`), the sum is not to infinity but to a cutoff and the rest of the sum from the cutoff to infinity is approximated not as zero (as in the old versions) but with the normal state contribution. So if `wwmnorm`$\equiv \tilde{\omega}_N^{exact}$ and `wwm` is $\tilde{\omega}_S^{approx} - \tilde{\omega}_N^{approx}$ then

$$\tilde{\omega}_S = \tilde{\omega}_S^{approx} + (\tilde{\omega}_N^{exact} - \tilde{\omega}_N^{approx}) \quad , \qquad (B.35)$$

where $\omega_S$ corresponds to the `jc_rec.wwww[]` and $N$ refers to normal state and $S$ refers to superconducting state. Here *approx* refers to it being summed to a cutoff and *exact* refers to it being summed to infinity. One should cross reference with `bdelta` and `jcdelta` to see this.

(xv) `void page1(), void page2(), void page3()`

These three subroutines print out input data, preprocessed data, and output from the iteration procedure, respectively, to the listing file. The static character lists exhibit clearly what is being printed. The input data is read in by the `input()` subroutine. The preprocessed data is read in from the binary file produced by the ftcrit.c program. This includes the Matsubara gaps. Any significant data of the system is printed with `pag ()` and all three pages are appended together in the output listing. If the full protocol switch, `full_p`, is set to 1, then `page3()` also starts a new page with the `fputc('\f',pr)` command and the output from the iteration procedure is recorded.

`W_C_String()` for centering character strings and `print_arr()` for printing arrays, are defined in util.c.

(xvi) `double rlambd (b2,iel)`

This routine is called by `funder()` and `it_init()` to calculate the electron-phonon mass enhancement parameter given as

$$\lambda_n = 2\int d\omega \frac{\omega\alpha^2F(\omega)}{\omega^2+\omega_n^2} \quad . \tag{B.36}$$

If the spectrum is a delta function, $A\omega_E/(\omega_E^2+\omega_n^2)$ is returned. Note that `we`, `we2`, `awe`, and `dw` are defined in the `input` subroutine. If it is a real spectrum, the above formula is used and, as the $\alpha^2F(\omega)$ bin at $\omega = 0$ is zero, the sum

starts with the second bin. Please note that the $\alpha^2F(\omega)$ spectrum is passed from the ftcrit.c program NOT as $\alpha^2F(\omega)$ but rather as $\omega\alpha^2F(\omega)$.

(xvii) `void summary()`

This prints to the listing file a tabulation of final results as stored in the array `g_summ[] []`. The column headings are `run`, `T/Tc`, `jc^2/3`, and `jc`. At the end, the time and date are checked and printed again to have a feel for the amount of time the program takes to run (it usually takes a lot!). The listing file is closed and the `LoggedDir` is freed. Again, `W_C_String` is defined in util.c.

(xviii) `void Titer(inrun)`

This is the main subroutine called by the `main` program to iterate u to find $j_c$ at a fixed temperature $t$.

Because for each temperature the dimension of the arrays for the gaps and frequencies changes, the `malloc` (memory allocation) and `memcpy` (memory copy) C routines are used to create memory allowance as it is required (consult a C manual).

In the first few lines, the amount of memory required for ten arrays, needed further on, is allocated in the arrays `del[i]` and `wwmw[i]`, `i` $= 0, 1, 2, 3, 4$.

Then if it is the beginning of a temperature iteration (*i.e.*, `inrun == 0`), `jciter` is called with `sbar = 0` and `itsw = 1` to iterate the usual nonlinear Eliashberg equations using `bdelta`. This is necessary to have an initial set of gaps and frequencies to start with as a first guess. The contents of the `jc_rec.del0` and `jc_rec.wwmw` arrays are copied into the arrays `del` and `wwmw` for initial starting values.

The ijk loop now iterates for $u_c$ and $j_c$. Five values of $u_i$ are used, four of which are slightly larger or smaller than the main value of $u$ of interest. These are assigned to the array x[i]. Then for each value of $u_i$, jciter is called to iterate for a self-consistent set of gaps and frequencies for that value of $u_i$ and current is called to calculate the corresponding $j_s$. Now to find the maximum of $j_s$ with respect to $u$, the jcder() routine is called three times to get three values of $dj_s/du$ from which a Newtonian iteration is used calling by corr() to correct for $u$ until $dj_s/du = 0$. If the five values of $u_i$ are taken in groups of three, ie. $(u_0, u_1, u_2)$, $(u_1, u_2, u_3)$, and $(u_2, u_3, u_4)$, then each set of three points with their corresponding set of $j_s$'s stored in y[i] can be used to calculate $dj_s/du\ |_{u_1}$, $dj_s/du\ |_{u_2}$, and $dj_s/du\ |_{u_3}$, respectively, and these three derivatives are used by the Newtonian procedure.

Note, that in the i loop the stored values in the array del[i] and wwmw[i] are copied into the working arrays jc_rec.del0 and jc_rec.wwmw and after the iteration the working arrays are copied back into the storage arrays to be used as an initial guess for the next iteration.

When $u_c$ is found, the storage arrays del[2] and wwmw[2] corresponding to this value are copied into the working arrays to iterate one last time for the gaps and frequencies and to calculate $j_c$. The storage array memory is freed with the free command.

## B.3 GENERAL COMMENTS

Several routines have been defined by Ewald Schachinger and are to be found in a utility file /home/physun/ewald/util.c. This file is compiled and linked to the program through the makef command which also compiles the program. To compile the program, one would type

```
/home/physun/ewald/makef jc
```

The makef command requires that a file called jc.amak exists on the directory. The jc.amak file contains the following:

```
jc.ann: jc.c /home/physun/ewald/util.a.o
    cc jc.c /home/physun/ewald/util.a.o -o jc.ann -lm -lcurses -
ltermlib
/home/physun/ewald/util.a.o: /home/physun/ewald/util.c
    cc -c /home/physun/ewald/util.c -o /home/physun/ewald/util.a.o
```

After the makef command has been successfully executed, the executable code is now under the name of jc.ann. The program may now be run interactively by typing jc.ann or it may be run with an input file that contains all the required answers for the input subroutine. The typical command to run the program in background with the screen switched off and requiring the output listing file to be named jcpb.lst is

```
jc.ann -s -ljcpb.lst < jcpb.run &
```

where the jcpb.run file contains the input values and is shown below:

```
jcpb
none
18        /* number of temperatures     */
y         /* standard temperatures?     */
0.0       /* inv. tau for normal imps.  */
600       /* max. no. iter. for gaps    */
25        /* max. no. iter. for u       */
1.0e-8    /* iteration accuracy         */
1.0e-6    /* iteration accuracy for u   */
0.002     /* gridsize for u             */
f         /* full or minimum output     */
0.0       /* iteration damping for u    */
0.0       /* iteration damping for gaps */
0.4       /* estimate for u             */
n         /* functional derivatives?    */
```

Here, none indicates that no binary output file is required. jcpb is the binary file created by the /home/physun/ewald/ftcrit.c program.

Some general comment about the organization of the program:

- Aside from the main routine, all the subroutines are in alphabetical order.

- All constants, etc. defined at the beginning of the program are in upper-case letters.

- Most of the global variables have g_ in front of them to remind one that they are global.

- In C all arrays start at zero instead of one as in FORTRAN.

- The ordering of the `include` statements is important for the program to compile and run correctly on the MIPS machine.

- The machines are not compatible. The program must be recompiled if running on the SUN workstations, the physun, the MIPS or the SPARCs. Also the ftcrit.c program, in most cases, must be run on the same machine, otherwise the binary output file from that program cannot be read by jc.c.

- The material aluminum is difficult to run. It requires some damping, an increase of the grid size for the five values of u and a reduction in the accuracy of `korr`. It will also take more than a week to run through eighteen temperatures.

## B.4 JC.C: PROGRAM LISTING

Here follows the program listing and documentation for calculating the critical current for a strong coupling superconductor. It was written in the C programming language.

```
/* Critical Current - Strong Coupling */

#include <sys/param.h>
#include <memory.h>
#include <curses.h>
#include <ctype.h>
#include <string.h>
#include <math.h>
#include "/home/physun/ewald/utils.h"

#define STR64   64
#define GAPDIM  2500
#define MAXBIN  170
#define LISTE   "jc.lst"
#define CONST   3.26328
#define BOLTZ   11.605
#define DATEXT  ".dat"
#define NUL     0.0
#define ONE     1.0
#define TWO     2.0
#define THREE   3.0
#define TOL     1.0E-8
#define OUTR    1.0E-8
#define DDERV   1.0E-5
#define ACCUR   1.0E-6
#define OUTS    1.0E-11
#define GRID    0.002
#define LENGTH  85
#define MAXTEMP 21
#define MAXIT   20
#define MAXFUND 50

#define  SQR(x)     ((x)*(x))

struct Jcrec {
   int jcp1,na,iel;
   char Comment[LENGTH];
   double nw,tc00,tc0,ctau,ctaum,mu,wmax,a,lambda,sa,slambda,con,aco,
  a2f[MAXBIN],del0[GAPDIM],wwmw[GAPDIM],gog;
};
struct Jcrec jc_rec;
```

```
double g_t,g_consum,g_sdamp,g_summ[21][3],wtfac,g_jc0,g_jc,
       epplus[GAPDIM*2+1],del1[GAPDIM],g_uaccur,g_gridsize,
       we,we2,awe,wes,wes2,g_dw,wc,g_out,mu2,sawes,g_condif,
       wwmnorm[GAPDIM],imf[GAPDIM],ref[GAPDIM],invtan[GAPDIM],
       tmev,tpi,g_damp,u,g_jcslope;
double s_tc[] = {0.95,0.9,0.85,0.8,0.75,0.7,0.65,0.6,0.55,0.5,0.45,
                 0.4,0.35,0.3,0.25,0.2,0.15,0.1,0.05,0.01};
int    g_nrun,g_screen=1,g_delta,g_niter,g_full,g_iter,g_fder=0,
       g_save;
char   LoggedDir[MAXPATHLEN];
char   datum[11],ttime[11],ListFile[STR64],JcFile[STR64],
       OutFile[STR64];
FILE   *pr;

/*********************************************************************/
void main(argc,argv)
/*********************************************************************/
int  argc;
char *argv[];
{
   int    inrun;
   char   *stparg(),*f;
   void   Time(),Date(),summary(),page1(),page2(),page3(),
          input(),jc_0(),funder(),Titer(),jc_end(),jc_slope();

   Time(ttime);
   Date(datum);
   g_screen = stparg(argc,argv,"-s") == (char *)NULL;
   if (getwd(LoggedDir) == NULL) {
      perror("pwd");
      exit(1);
   }
   strcat(LoggedDir,"/");
   if ((f = stparg(argc,argv,"-l")) != (char *)NULL)
      strcpy(ListFile,f);
   else
      strcpy(ListFile,LISTE);
   MakeFile(ListFile,LoggedDir,".lst");
   if ((pr = fopen(ListFile,"w")) == NULL) {
      perror(ListFile);
      exit(1);
   }

   input();
   page1();
   page2();
   page3();

   for (inrun=0; inrun<=(g_nrun-ONE); inrun++) {
      g_t = s_tc[inrun];
```

```
      if (g_screen)
         printf("t= %lf, u= %lf, t+ = %lf\n",g_t,u,jc_rec.ctau);
      if (it_init(inrun)) {
         summary();
         exit(0);
      }
      Titer(inrun);
      g_summ[inrun][0] = g_t;
      g_summ[inrun][1] = pow(g_jc,0.6666667);
      g_summ[inrun][2] = g_jc/pow(ONE-g_t,1.5);
      if (g_screen)
         printf("t: %lf, jc^2/3: %lf\n\n",g_t,g_summ[inrun][1]);
      fprintf(pr,"t: %lf, jc^2/3: %lf\n\n",g_t,g_summ[inrun][1]);
      if (!g_delta && g_fder) funder();
   } /* end of inrun loop */
   jc_0();
   jc_slope();
   jc_end();
   summary();
}
/*************************************************************************/
double bdelta (nn,cc)   /* calculates the gaps without the current*/
/*************************************************************************/
int nn;
double cc;
{
   double xx,wwm,bc,fac,delsq[GAPDIM];
   static double cca;
   int i,k1s,k2s;

   if (!nn) {
      cca = cc*cc;
      for (i=0; i<=jc_rec.jcp1; i++) {
         xx = jc_rec.del0[i];
         delsq[i] = ONE/sqrt(ONE+cca*xx*xx);
      }
   }
   xx = delsq[nn];
   wwm = g_consum*xx;
   bc = g_condif*jc_rec.del0[nn]*xx;
   for (i=0; i<=jc_rec.jcp1; i++) {
      fac = i==jc_rec.jcp1 ? wtfac : ONE;
      k1s = abs(nn-i);
      k2s = nn+i+1;
      xx = delsq[i];
      wwm += (epplus[k1s]-epplus[k2s])*(xx-ONE)*fac;
      bc += (epplus[k1s]+epplus[k2s]-mu2)*xx*jc_rec.del0[i]*fac;
```

```
   }
   jc_rec.wwmw[nn] = wwm+wwmnorm[nn];
   return(bc);
}
/*************************************************************************/
double chi() /* impurity-dependent prefactor in GL theory near Tc */
/*************************************************************************/
{
   double diff,sum,sumold,wn;
   int    n;

   if (jc_rec.ctau <= 10.0) {
      diff = ONE;
      sum = NUL;
      sumold = NUL;
      for (n=0; diff>=TOL; n++){
         sumold = sum;
         wn = TWO*(double)n+ONE;
         sum +=  ONE/wn/wn/(wn+jc_rec.ctau/jc_rec.tc0);
         diff = fabs((sum-sumold)/sum);
      }
      return (8.0*sum/7.0/1.202);
   } else
      return (M_PI*M_PI*(jc_rec.tc0/jc_rec.ctau/7.0/1.202));
}
/*************************************************************************/
double current(sbar)                    /* calculates the current j */
/*************************************************************************/
double sbar;
{
   double j,js,xx,yy,term1,term2,term3;
   int    i;

   j = NUL;
   for (i=0; i<=jc_rec.jcp1;i++){
      xx = jc_rec.del0[i];
      yy = jc_rec.wwmw[i];
      term1 = invtan[i]*xx*xx;
      term2 = -sbar*ref[i]/yy;
      term3 = imf[i];
      j += (term1+term2+term3)*yy*yy/sbar/sbar;
   }
   js = CONST*g_t*j;
   return (js);
}
/*************************************************************************/
void funder()                  /* calculates functional derivatives */
/*************************************************************************/
{
   char rd,ReadChar(),fname[STR64];
```

```
static int ifunc= -1,kstep=1;
int    iadd,i_save,s_summp,i;
double x,s_jc,eeps,tomeg,rlambd(),y,savbin;
static double djda[MAXFUND],omeg[MAXFUND];
void   prt_arr(),ncrm();
FILE   *fder;
static char
   *t01 = "Number of frequencies                                    ",
   *t02 = "Save functional derivatives on file     ";

rd = 'Y';
do
   if (g_screen)
      printf("Do you want functional derivatives? (def.: y) > ");
while ((rd = ReadChar(rd)) != 'Y' && rd != 'N');
if (rd == 'Y') {
   if (g_screen)
      printf("Save functional derivatives on file
              (def.: %s????%s) > ",LoggedDir,DATEXT);
   fgets(fname,STR64,stdin);
   fname[strlen(fname)-1] = '\0';
   if (!(i_save = strlen(fname)==0 || !strcmp(fname,"none"))) {
      MakeFile(fname,LoggedDir,DATEXT);
      if ((fder = fopen(fname,"w")) == NULL) {
         perror(fname);
         exit(1);
      }
   }
   s_jc=g_jc;
   s_summp = g_full;
   g_full = 0;
   ifunc = -1;
   kstep = 1;
   while (ifunc < MAXFUND) {
      fprintf(pr,"\nFreq. no.: %d\n\n",ifunc+1);
      if (g_screen) printf("\nFreq. no.: %d\n\n",ifunc+1);
      tomeg = g_dw*(double)kstep;
      savbin = jc_rec.a2f[kstep];
      jc_rec.a2f[kstep] = savbin*1.05;
      eeps = 0.05*savbin*g_dw/tomeg;
      x = TWO*M_PI*tmev;
      for (i=0; i<=2*jc_rec.jcp1+1; i++) {
         y = x*(double)i;
         epplus[i] = rlambd(y*y,jc_rec.iel);
       }
      norm();
      Titer(1);
      omeg[++ifunc] = tomeg;
      djda[ifunc] = (pow(g_jc,0.6666667)-pow(s_jc,0.6666667))/eeps;
      jc_rec.a2f[kstep] = savbin;
```

```
         if ((tomeg /= jc_rec.tc0) > 40.0) break;
         iadd = tomeg > 9.0 ? (int)(1.6*jc_rec.tc0/g_dw) :
                tomeg > 1.0 ? (int)(0.8*jc_rec.tc0/g_dw) : 1;
         kstep += iadd ? iadd : 1;
         if (kstep > jc_rec.na) break;
      }
      putc('\f',pr);
      W_C_String("Functional Derivatives",pr,80);
      W_C_String("======================",pr,80);
      fprintf(pr,"\n%s\n\n",jc_rec.Comment);
      fprintf(pr,"Day and Time of Run: %s//%s\n\n\n\n",datum,ttime);
      fprintf(pr,"    %s%10d  ( ifunc)\n",t01,ifunc);
      if (!i_save)
         fprintf(pr,"    %s%s\n\n",t02,fname);
      fputs("\n\nFrequencies [meV]:\n\n",pr);
      prt_arr(pr,omeg,0,ifunc,"%12.6lf",6,0);
      for (iadd=0; iadd<=ifunc; iadd++)
         omeg[iadd] /= jc_rec.tc0;
      fputs("\n\nFrequencies/Tc:\n\n",pr);
      prt_arr(pr,omeg,0,ifunc,"%12.6lf",6,0);
      fputs("\n\nFunctional Derivative for added isotropic delta
                function:\n\n",pr);
      prt_arr(pr,djda,0,ifunc,"%12.6lf",6,0);
      if (!i_save) {
         for (i=0; i<=ifunc; i++)
            fprintf(fder,"%12.7f %12.7f\n",omeg[i],djda[i]);
         fclose(fder);
      }
      g_full = s_summp;
   }
}
/*************************************************************************/
void input()                              /* queries for input values */
/*************************************************************************/
{
   double ReadReal();
   int    i;
   char   rd,ReadChar();
   FILE   *fp;

   do {
      if (g_screen)
         printf("Read the input data from file (def.: %s?????%s) > ",
                LoggedDir,DATEXT);
      fgets(JcFile,STR64,stdin);
      JcFile[strlen(JcFile)-1] = '\0';
   } while (!strlen(JcFile) || !strcmp(JcFile,"none"));
   MakeFile(JcFile,LoggedDir,DATEXT);
   if ((fp = fopen(JcFile,"rb")) == NULL) {
      perror(JcFile);
```

```
      exit(2);
   }
   fread((char *)&jc_rec,sizeof(struct Jcrec),1,fp);
   fclose (fp);
   if (g_screen)
      printf("Save results for the gaps on file (def.: %s????%s) > ",
             LoggedDir,DATEXT);
   fgets(OutFile,STR64,stdin);
   OutFile[strlen(OutFile)-1] = '\0';
   if (g_save = strlen(OutFile)!=0 && strcmp(OutFile,"none"))
      MakeFile(OutFile,LoggedDir,DATEXT);
   g_nrun = MAXTEMP;
   do
      if (g_screen)
         printf("Enter number of temperatures (def.: %d) > ",
                g_nrun);
   while ((g_nrun = ReadInt(g_nrun)) < 1 && g_nrun > MAXTEMP);
   rd = 'Y';
   do
      if (g_screen)
         printf("Do you want the standard temperatures? (def.:y) > ");
   while((rd = ReadChar(rd)) != 'Y' && rd != 'N');
   if (rd == 'N')
      for (i=0; i<g_nrun; i++)
         do
            if (g_screen)
               printf("Enter %2d. value for T/Tc (def.: %6.3lf) > ",
                      i+1,s_tc[i]);
         while ((s_tc[i] = ReadReal(s_tc[i]))<=NUL && s_tc[i]>=0.995);
   do
      if (g_screen)
         printf("Enter value for ctau (def.: %6.1le) > ",
                jc_rec.ctau);
   while ((jc_rec.ctau = ReadReal(jc_rec.ctau)) < NUL);
   g_niter = MAXIT;
   do
      if (g_screen)
         printf("Enter max. number of iterations for gaps
                (def.: %d) > ",g_niter);
   while ((g_niter = ReadInt(g_niter)) <= 0);
   g_iter = MAXIT;
   do
      if (g_screen)
         printf("Enter max. number of iterations per temperature
                (def.: %d) > ",g_iter);
   while ((g_iter = ReadInt(g_iter)) <= 0);
   g_out = OUTR;
   do
      if (g_screen)
         printf("Enter iteration accuracy for gaps (def.: %6.1le) >
```

```
                ",g_out);
while ((g_out = ReadReal(g_out)) < NUL);
g_uaccur = ACCUR;
do
   if (g_screen)
      printf("Enter iteration accuracy for u (def.: %6.1le) > ",
             g_uaccur);
while ((g_uaccur = ReadReal(g_uaccur)) < NUL);
g_gridsize = GRID;
do
   if (g_screen)
      printf("Enter gridsize for u (def.: %6.1le) > ",
             g_gridsize);
while ((g_gridsize = ReadReal(g_gridsize)) < NUL);
rd = 'M';
do
   if (g_screen)
      printf("Do you want f(ull) output or m(inimum) output?
             (def.:m) > ");
while ((rd = ReadChar(rd)) != 'F' && rd != 'M');
g_full = rd == 'F';
g_sdamp = NUL;
do
   if (g_screen)
      printf("Iteration damping for u loop (def.:= %6.3lf) > ",
             g_sdamp);
while ((g_sdamp = ReadReal(g_sdamp)) < 0);
g_damp = NUL;
do
   if (g_screen)
      printf("Iteration damping for gaps (def.:= %6.3lf) > ",
             g_damp);
while ((g_damp = ReadReal(g_damp)) < 0);
u = NUL;
do
   if (g_screen) printf("Enter estimate for the velocity u > ");
while ((u = ReadReal(u)) <= NUL);
rd = 'N';
do
   if (g_screen)
      printf("Do you want functional derivatives? (def.: n) > ");
while ((rd = ReadChar(rd)) != 'Y' && rd != 'N');
g_fder = rd=='Y';
mu2 = TWO*jc_rec.mu;
g_delta = jc_rec.na == 0;
if (g_delta) {
   we = TWO*jc_rec.a/jc_rec.lambda;
   we2 = we*we;
   awe = TWO*jc_rec.a*we;
} else
```

```
      g_dw = jc_rec.wmax/(double)(jc_rec.na-1);
   wc = jc_rec.nw*jc_rec.wmax;
}
/*********************************************************************/
it_init (inrun)     /* initializes parameters for new temperature */
/*********************************************************************/
int inrun;
{
   double x,wcs,y,rlambd();
   int ng,i,itin;
   void norm();

   itin = 0;
   tmev = jc_rec.tc0*s_tc[inrun];
   x = TWO*M_PI*tmev;
   g_consum = (jc_rec.ctau+jc_rec.ctaum)/tmev;
   g_condif = (jc_rec.ctau-jc_rec.ctaum)/tmev;
   tpi = M_PI*tmev;
   ng = (int)(0.5+wc/x);
   if (ng <= GAPDIM) {
       wcs = ((double)ng+0.5)*x;
       wtfac = ONE+(wc-wcs)/x;
       if (jc_rec.tc00 == jc_rec.tc0) {
           for (i=0; i<=ng; i++)
              if (i <= jc_rec.jcp1)
                 jc_rec.del0[i] /= 15.0;
              else
                 jc_rec.del0[i] = jc_rec.del0[jc_rec.jcp1];
       } else {
           for (i=jc_rec.jcp1+1; i<=ng; i++) {
              jc_rec.del0[i] = jc_rec.del0[jc_rec.jcp1];
              jc_rec.wwmw[i] = jc_rec.wwmw[jc_rec.jcp1];
   }
       }
       jc_rec.jcp1 = ng;
       jc_rec.tc00 = tmev;
       for (i=0; i<=2*ng+1; i++) {
          y = x*(double)i;
          epplus[i] = rlambd(y*y,jc_rec.iel);
       }
       norm();
       if (g_screen) {
          printf("Beginning of the %2d. temperature = %10.6lf K\n",
                 inrun+1,tmev*BOLTZ);
          printf("-------------------------------------------------
                 \n\n");
          printf("T/Tc = %10.6lf  number of matsubara frequencies =
                  %4d",s_tc[inrun],ng+1);
          printf("  wtfac = %10.7lf\n",wtfac);
       }
```

```
      if (g_full) {
         if (inrun > 0)
            fputs("\n\n",pr);
         fprintf(pr,"Beginning of the %2d. temperature = %10.6lf K\n",
                 inrun+1,tmev*BOLTZ);
         fprintf(pr,"-----------------------------------------
                    ---\n\n");
         fprintf(pr,"T/Tc = %10.6lf \n",s_tc[inrun]);
         fprintf(pr,"Number of matsubara frequencies = %4d  wtfac =
                    %10.6lf\n",ng+1,wtfac);
      }
   }  else  {
      itin = 1;
      fprintf(stderr,"Temperature too small -> increase array
                     dimensions! -- cancel\n");
   }
   return(itin);
}
/*********************************************************************/
double jcdelta (nn,cc,sbar) /* calculate gaps with influence of v */
/*********************************************************************/
int nn;
double cc, sbar;
{
   double xx,yy,wwm,bc,xp,yp,rho,x,y,fac,bdelta();
   static double cca;
   int    i,k1s,k2s;

   if (sbar == NUL)
      bc = bdelta(nn,cc);
   else {
      if (!nn) {
         cca = cc*cc;
         for (i=0; i<=jc_rec.jcp1; i++) {
            xx = jc_rec.del0[i];
            yy = jc_rec.wwmw[i];
            xp = ONE-sbar*sbar/yy/yy+cca*xx*xx;
            yp = TWO*sbar/yy;
            rho = sqrt(yp*yp+xp*xp);
            imf[i] = sqrt((rho-xp)/TWO);
            ref[i] = sqrt((rho+xp)/TWO);
            x = ONE + ref[i];
            y = sbar/yy + imf[i];
            invtan[i] = atan(y/x);
         }
      }
      wwm = g_consum*imf[nn]*jc_rec.wwmw[nn]/sbar;
      if (nn == jc_rec.jcp1)
         wwm -= TWO*(ONE-wtfac);
      bc = g_condif*jc_rec.del0[nn]*invtan[nn]*jc_rec.wwmw[nn]/sbar;
```

```
      for (i=0; i<=jc_rec.jcp1; i++) {
         fac = i==jc_rec.jcp1 ? wtfac : ONE;
         k1s = abs(nn-i);
         k2s = nn+i+1;
         yy = jc_rec.wwmw[i];
         wwm += (epplus[k1s]-epplus[k2s])*(imf[i]*yy/sbar-ONE)*fac;
         bc += (epplus[k1s]+epplus[k2s]-mu2)*jc_rec.del0[i]*
               invtan[i]*yy*fac/sbar;
      }
      jc_rec.wwmw[nn] = wwm+wwmnorm[nn];
   }
   return(bc);
}
/*************************************************************************/
double jcder (x,y)          /* calculates the derivative: dj/dv */
/*************************************************************************/
double x[],y[];
{
   double s,x21,x31,y21,y31,xq21,xq31,c,b;

   x21 = x[1]-x[0];
   x31 = x[2]-x[0];
   y21 = y[1]-y[0];
   y31 = y[2]-y[0];
   xq21 = x[1]*x[1]-x[0]*x[0];
   xq31 = x[2]*x[2]-x[0]*x[0];
   c = (y31*x21-y21*x31)/(xq31*x21-xq21*x31);
   b = (y21-c*xq21)/x21;
   s = b+2.0*c*x[1];
   return (s);
}
/*************************************************************************/
void jc_end()                    /* saves jc_rec on binary file */
/*************************************************************************/
{
   FILE *fp;

   if (g_save) {
      if ((fp = fopen(OutFile,"wb")) == NULL) {
         perror(OutFile);
         exit(2);
      }
      fwrite((char *)&jc_rec,sizeof(struct Jcrec),1,fp);
      fclose(fp);
   }
}
/*************************************************************************/
void jciter (sbar,itsw)        /* control loop for gap iteration */
/*************************************************************************/
double sbar;
```

```
int    itsw;
{
   double korr,cc,ddel,xx,yy,minus,c[3],bc[3],jcdelta(),corr();
   int iter,i,olddif,newdif,jtsw;

   olddif = newdif = 1;
   jtsw = itsw;
   cc = ONE;
   iter = 0;
   while ((olddif || newdif) && (iter <= g_niter)) {
      olddif = newdif;
      if (jtsw) {                /*  start fast iteration mode   */
         c[0] = ONE-DDERV;
         c[1] = ONE;
         c[2] = ONE+DDERV;
         for (i=0; i<=2; i++)
            bc[i] = jcdelta(0,c[i],sbar)/jc_rec.wwmw[0]/jc_rec.del0[0];
         korr = corr(ONE,c,bc);
         cc = ONE-korr;
         cc = ONE+(cc-ONE)/(ONE+g_damp);
      }
      for (i=0; i<=jc_rec.jcp1; i++)
                  del1[i] = jcdelta(i,cc,sbar)*cc/jc_rec.wwmw[i];
      ddel = NUL;
      minus = del1[0] < NUL ? -ONE : ONE;
      for (i=0; i<=jc_rec.jcp1; i++) {
         xx = minus*del1[i];
         yy = jc_rec.del0[i];
         ddel += fabs((xx-yy)/yy);
         jc_rec.del0[i] = itsw ? xx : (xx+g_damp*jc_rec.del0[i])/
                                      (ONE+g_damp);
      }
      newdif = ddel > g_out;
      iter++;
      if ((ddel <= OUTS) || !newdif) {
         jtsw = 0;
         cc = ONE;
      }
   }
   if (g_full) {
      fprintf(pr,"After %6d iters change in gaps = %14.6le, del0[0]
                  = %14.7le\n",iter,ddel,jc_rec.del0[0]);
 }
   if (g_screen) {
      printf("After %6d iters change in gaps = %14.6le, del0[0]=
              %14.7le\n",iter,ddel,jc_rec.del0[0]);
   }
}
```

```
/*************************************************************************/
void jc_0()                    /* calculates the t=0 value of jc^2/3 */
/*************************************************************************/
{
   double x[4],y[4];
   int    i,j;
   void inv();

   j = g_nrun-1;
   if (g_summ[j][0] <= 0.2) {  /* calculate jc(0) */
      for (i=0; i<4; i++) {
         x[i] = g_summ[j-3+i][0];
         y[i] = g_summ[j-3+i][1];
      }
      inv(x,y);
      g_jc0 = y[0];
      if (g_screen)
         printf("\n\njc(0) = %12.5lf\n",g_jc0);
   }
}
/*************************************************************************/
void jc_slope()            /* calculates the slope of jc^2/3 at Tc */
/*************************************************************************/
{
   double x[4],y[4];
   int    i,j;
   void inv();

   x[0] = 1.0;
   y[0] = 0.0;
   for (i=1; i<4; i++) {
      x[i] = g_summ[i-1][0];
      y[i] = g_summ[i-1][1];
   }
   inv(x,y);
   g_jcslope = y[1]+TWO*y[2]+THREE*y[3];
   if (g_screen)
      printf("\n\nslope at Tc = %12.5lf\n",g_jcslope);
}
/*************************************************************************/
void norm()     /* Frank's more accurate summing of the w-channel */
/*************************************************************************/
{
   double sum;
   int    n,m;

   wwmnorm[0] = epplus[0]+ONE;
   for (n=1; n<=jc_rec.jcp1; n++) {
      sum = NUL;
      for (m=1; m<=n; m++)
```

```
 sum += epplus[m];
      wwmnorm[n] = wwmnorm[0]+TWO*(sum+(double)n);
   }
}
/*********************************************************************/
void page1()                              /* a summary of input data */
/*********************************************************************/
{
   static char
      *t01 = "Critical Current for a Superconductor",
      *t02 = "====================================",
      *t03 = "    Input data:\n",
      *t04 = "    Number of temperatures                              ",
      *t05 = "    Number of iterations per temperature                ",
      *t06 = "    Value of t+ (meV)                                   ",
      *t07 = "    Initial estimate for u                              ",
      *t08 = "    Number of iterations per velocity                   ",
      *t09 = "    Accuracy for gaps                                   ",
      *t10 = "    Functional derivatives (=Y yes/=N no)               ",
      *t11 = "    Read starting values from file                      ",
      *t12 = "    Iteration damping for u (=0 / no damping)           ",
      *t13 = "    Iteration damping for gaps (=0 / no damping)        ",
      *t14 = "    Full protocol (=M  minimum/=F  full)                ",
      *t15 = "    Save results for tunneling on file                  ",
      *t16 = "    Accuracy for u                                      ",
      *t17 = "    Gridsize for u                                      ";
   void prt_arr();

   W_C_String(t01,pr,80);
   W_C_String(t02,pr,80);
   fprintf(pr,"\n%s\n\n",jc_rec.Comment);
   fprintf(pr,"Day and Time of Run: %s//%s\n\n\n",datum,ttime);
   fputs(t03,pr);
   fprintf(pr,"%s%10d  (g_nrun)\n",t04,g_nrun);
   fprintf(pr,"%s%10d  (g_niter)\n",t08,g_niter);
   fprintf(pr,"%s%10d  (g_iter)\n",t05,g_iter);
   fprintf(pr,"%s%10.6lf  ( ctau )\n",t06,jc_rec.ctau);
   fprintf(pr,"%s%10.6lf  (   u  )\n",t07,u);
   fprintf(pr,"%s%10.6lf  (g_sdamp)\n",t12,g_sdamp);
   fprintf(pr,"%s%10.6lf  (g_damp)\n",t13,g_damp);
   fprintf(pr,"%s         %c  (g_full)\n",t14,g_full?'F':'M');
   fprintf(pr,"%s         %c  (g_fder)\n",t10,g_fder?'Y':'N');
   fprintf(pr,"%s%10.1le  ( g_out)\n",t09,g_out);
   fprintf(pr,"%s%10.1le  (g_uaccur)\n",t16,g_uaccur);
   fprintf(pr,"%s%10.6lf  (g_gridsize)\n\n",t17,g_gridsize);
   fprintf(pr,"    Reduced temperatures for this run, s_tc[i],i=1,%d:
            \n",g_nrun);
   prt_arr(pr,s_tc,0,g_nrun-1,"%12.6lf",6,0);
   if (g_save == 1) fprintf(pr,"\n%s%s\n",t15,OutFile);
   fprintf(pr,"\n%s%s\n",t11,JcFile);
```

```
}
/*************************************************************************/
void page2()                        /* a summary of preprocessed data */
/*************************************************************************/
{
   static char
      *t01 = "\n\n    Preprocessed data:\n",
      *t02 = "    Critical temperature [K]                              ",
      *t03 = "    Actual temperature [K]                                ",
      *t04 = "    Inv. lifetime of normal scat. imp. [meV]              ",
      *t05 = "    Inv. lifetime of param. scat. imp. [meV]              ",
      *t06 = "    Define type of A2F:\n",
      *t07 = "      (=0 one or two delta functions                  )\n",
      *t08 = "      (>0 defined by spectral function with na bins)",
      *t09 = "    Mu - star                                             ",
      *t10 = "    Cutoff frequency = nw*wmax                            ",
      *t11 = "    Debye frequency  [meV]                                ",
      *t12 = "    System with inelastic scattering? (=T yes/=F no)",
      *t13 = "    Concentration of inelastic scatterers                 ",
      *t14 = "    Parameter gog                                         ";
   void prt_arr();

   fputs(t01,pr);
   fprintf(pr,"%s%10.6lf  (  tc0 )\n",t02,jc_rec.tc0*BOLTZ);
   fprintf(pr,"%s%10.6lf  ( tc00 )\n",t03,jc_rec.tc00*BOLTZ);
   fprintf(pr,"%s%10.6lf  ( ctau )\n",t04,jc_rec.ctau);
   fprintf(pr,"%s%10.6lf  ( ctaum)\n",t05,jc_rec.ctaum);
   fputs(t06,pr);
   fputs(t07,pr);
   fprintf(pr,"%s%10d  (  na  )\n",t08,jc_rec.na);
   fprintf(pr,"%s%10.6lf  (  mu  )\n",t09,jc_rec.mu);
   fprintf(pr,"%s%10d  (  nw  )\n",t10,(int)jc_rec.nw);
   fprintf(pr,"%s%10.6lf  ( wmax )\n",t11,jc_rec.wmax);
   if (jc_rec.gog != ONE)
      fprintf(pr,"%s%10.5lf  (  gog )\n",t14,jc_rec.gog);
   fprintf(pr,"%s         %c  (  iel )\n",t12,jc_rec.iel?'T':'F');
   if (jc_rec.iel)
      fprintf(pr,"%s%10.6lf  (  con )\n",t13,jc_rec.con);
   fprintf(pr,"\nMatsubara gaps jc_rec.del0[i],i:=1,%d:\n",
          jc_rec.jcp1+1);
   prt_arr(pr,jc_rec.del0,0,jc_rec.jcp1,"%12.6lf",6,0);
}
/*************************************************************************/
void page3()      /* listing of signif. data and iteration output */
/*************************************************************************/
{
   static char
     *t01 = "Siginificant Data of the System",
     *t02 = "==============================",
     *t03 = "    Area under A2F                                        ",
```

```
    *t04 = "    Mass enhancement factor                              ",
    *t05 = "    Lambda(Tc)                                           ",
    *t06 = "    Electronic part of the spec. heat [J/mole/K] ",
    *t07 = "    Sommerfeld constant gamma [J/g-at/K**2]              ",
    *t08 = "Iteration of the nonlinear Eliashberg Equations",
    *t09 = "=============================================";

  fputc('\n',pr);
  fputc('\n',pr);
  W_C_String(t01,pr,80);
  W_C_String(t02,pr,80);
  fprintf(pr,"%s%10.5lf  (   a  )\n",t03,jc_rec.a);
  fprintf(pr,"%s%10.5lf  (lambda)\n",t04,jc_rec.lambda);
  if (g_full) {
     fputc('\f',pr);
     W_C_String(t08,pr,80);
     W_C_String(t09,pr,80);
     fprintf(pr,"\n%s\n\n",jc_rec.Comment);
     fprintf(pr,"Day and Time of Run: %s//%s\n\n\n",datum,ttime);
  }
}
/*************************************************************************/
double rlambd (b2,iel)                          /* calculates lambda */
/*************************************************************************/
double b2;
int iel;
{
  double w,ep,rlam;
  int i;

  if (g_delta) {
      rlam = awe/(we2+b2);
      if (iel)
        rlam = rlam+sawes/(wes2+b2);
      return(rlam);
  }  else  {
     ep = w = NUL;
     for (i=1; i<jc_rec.na; i++) {
        w += g_dw;
        ep += jc_rec.a2f[i]/(w*w+b2);
     }
     rlam = ep*g_dw*TWO;
     if (iel)
 rlam += sawes/(b2+wes*wes);
     return(rlam);
  }
}
```

```
/*************************************************************************/
void summary()                    /* a tabulation of final results */
/*************************************************************************/
{
   int i,j;
   void Time(),Date();

   putc ('\f',pr);
   W_C_String("Summary",pr,80);
   W_C_String("=======",pr,80);
   putc ('\n',pr);
   fprintf (pr,"\n\n\n\n");
   fprintf (pr,"  run     T/Tc       jc^2/3        jc");
   putc ('\n',pr);
   putc ('\n',pr);
   for (i=0; i<=(g_nrun-ONE); i++) {
      fprintf (pr,"%4d",i+1);
      for (j=0; j<=2; j++)
         fprintf (pr,"%12.6lf",g_summ[i][j]);
      putc ('\n',pr);
   }
   if (g_summ[g_nrun-1][0] <= 0.2) {
      fprintf (pr,"%4d",g_nrun+1);
      fprintf (pr,"%12.6lf%12.6lf%12.6lf",NUL,g_jc0,pow(g_jc0,1.5));
      putc ('\n',pr);
   }
   fprintf (pr,"\n\n\nSlope of j_c^2/3 at Tc= %12.6lf",g_jcslope);
   putc ('\n',pr);
   Time(ttime);
   Date(datum);
   fprintf (pr,"\n\nDay and Time of Ending: %s//%s\n\n\n\n",datum,
            ttime);
   fclose (pr);
   free(LoggedDir);
}
/*************************************************************************/
void Titer(inrun)       /* iterates u to find jc at temperature t */
/*************************************************************************/
int  inrun;
{
   double corr(),jcder(),current(),yy[3],korr,x[5],y[5],chi(),
          *del[5],*wwmw[5];
   int    ijk,olddif,newdif,i,m_jcp1;
   void   jciter(),summary();

   m_jcp1 = (jc_rec.jcp1+1)*sizeof(double);
   for (i=0; i<=4; i++) {
      del[i] = (double *)malloc((unsigned)m_jcp1);
      wwmw[i] = (double *)malloc((unsigned)m_jcp1);
      if (del[i] == NULL || wwmw[i] == NULL) {
```

```
            fprintf(stderr,"insufficient storage\n");
            exit(1);
         }
      }
      if (inrun == 0)
         jciter(NUL,1);
      for (i=0; i<=4; i++) {
         memcpy((char *)del[i],(char *)jc_rec.del0,m_jcp1);
         memcpy((char *)wwmw[i],(char *)jc_rec.wwmw,m_jcp1);
      }
      olddif = newdif = 1;
      for (ijk=1; ijk<=g_iter && (olddif || newdif); ijk++) {
         olddif = newdif;
         x[0] = u*(ONE-TWO*g_gridsize);
         x[1] = u*(ONE-g_gridsize);
         x[2] = u;
         x[3] = u*(ONE+g_gridsize);
         x[4] = u*(ONE+TWO*g_gridsize);
         for (i=0; i<=4; i++) {
            memcpy((char *)jc_rec.del0,(char *)del[i],m_jcp1);
            memcpy((char *)jc_rec.wwmw,(char *)wwmw[i],m_jcp1);
            jciter (x[i],0);
            y[i] = current(x[i]);
            memcpy((char *)del[i],(char *)jc_rec.del0,m_jcp1);
            memcpy((char *)wwmw[i],(char *)jc_rec.wwmw,m_jcp1);
         }
         yy[0] =jcder(x,y);
         yy[1] =jcder(x+1,y+1);
         yy[2] =jcder(x+2,y+2);
         korr = corr(NUL,x+1,yy);
         newdif = fabs(korr) > g_uaccur;
         if (korr < -ONE)
            u += ONE;
         else
            u = (u-korr+g_sdamp*u)/(ONE+g_sdamp);
         if (g_screen)
            printf("i= %d, u= %lf, korr= %14.7le\n",ijk,u,korr);
         fprintf(pr,"i= %d, u= %lf, korr= %14.7le\n",ijk,u,korr);
      } /* end of ijk loop */
      memcpy((char *)jc_rec.del0,(char *)del[2],m_jcp1);
      memcpy((char *)jc_rec.wwmw,(char *)wwmw[2],m_jcp1);
      for (i=0; i<=4; i++) {
         free((char *)del[i]);
         free((char *)wwmw[i]);
      }
      jciter (u,0);
      g_jc = current(u);
}
```

# Bibliography


Abrikosov, A.A. and L.P. Gor'kov, *Sov. Phys. JETP* 12, 1243 (1961).

Abrikosov, A.A., L.P. Gor'kov, and I.E. Dzyaloshinski, Methods of Quantum Field Theory in Statistical Physics (Prentice Hall, Englewood Cliffs, 1963).

Akis, R. and J.P. Carbotte, *Phys. Rev. B* 42, 920 (1990).

Akis, R. and J.P. Carbotte, *Solid State Comm.* 78, 393 (1991).

Akis, R. and J.P. Carbotte, *Solid State Comm.* 79, 577 (1991).

Allen, P.B. and R.C. Dynes, *Phys. Rev. B* 12, 905 (1975).

Allen, P.B. and B. Mitrović, *Solid State Phys.* 37, 1 (1982).

Allen, P.B. and D. Rainer, *Nature* 34, 396 (1991).

Anderson, P.W. and H. Suhl, *Phys. Rev.* 116, 898 (1959).

Anderson, P.W., *Science* 235, 1196 (1987).

Anderson, P.W., *Phys. Rev. Lett.* 64, 1839 (1990).

Andratskii, V.P., L.M. Grundel, V.N. Gubankov, and N.B. Pavlov, *Sov. Phys. JETP* 38, 794 (1974).

Anlage, S.M., B.W. Langley, G. Deutscher, J. Halbritter, and M.R. Beasley, (preprint, 1991).

Ambegaokar, V. and A.A. Griffin, *Phys. Rev.* 137, A1151 (1965).

Arko, A.J. *et al.* , *Phys. Rev. B* 40, 2268 (1989).

Ashcroft, N.W. and N.D. Mermin, Solid State Physics (Holt, Rinehart and Winston, Philadelphia, 1976).

Baquero, R., J.M. Daams, and J.P. Carbotte, *J. Low Temp. Phys.* 42, 585 (1981).

Bardeen, J., L.N. Cooper, and J.R. Schrieffer, *Phys. Rev.* 108, 1175 (1957).

Bardeen, J., *Rev. Mod. Phys.* 34, 667 (1962).

Bardeen, J. and M. Stephen, *Phys. Rev.* 136, A1485 (1964).

Barrett, S.E., D.J. Durand, C.H. Pennington, C.P. Slichter, T.A. Freidmann, J.P. Rice, and D.M. Ginsberg, *Phys. Rev. B* 41, 6283 (1990).

Batlogg, B., R.J. Cava, A. Jagaraman, R.B. van Dover, G.A. Kourouklis, C. Sunshine, D.W. Murphy, L.W. Rupp, H.S. Chen, A. White, K.T. Short, A.M. Majsce, and E.A. Reitman, *Phys. Rev. Lett.* 58, 2333 (1987).

Bednorz, J.G. and K.A. Müller, *Z. Physik* B64, 189 (1986).

Benitez, E.L., J.J. Lin, S.J. Poon, W.E. Farneth, M.K. Crawford, and E.M. McCarron, *Phys. Rev. B* 38, 6690 (1989).

Bennett, H.S. and P. C. Martin, *Phys. Rev.* 13B, A608 (1965).

Berk, N.F. and J.R. Schrieffer, *Phys. Rev. Lett.* 17, 433 (1966).

Bickers, N.E., D.J. Scalapino, R.T. Collins, and Z. Schlesinger, *Phys. Rev. B* 42, 67 (1990).

Binder, K. and A. P. Young, *Rev. Mod. Phys.* 58, 801 (1986).

Blaschke, R., and R. Blocksdorf, *Z. Physik* B49, 99 (1982).

Blezius, J., R. Akis, F. Marsiglio, and J.P. Carbotte, *Phys. Rev. B* 38, 179 (1988).

Bonn, D.A., P. Dosanjh, R. Liang, W.N. Hardy, preprint (to be submitted to *Phys. Rev. Lett.*).

Bourne, L.C., M.F. Crommie, A. Zettl, H.C. zur Loye, S.W. Keller, K.L.Leary, A.M. Stacy, K.J. Chang, M.L. Cohen, and D.E. Morris, *Phys. Rev. Lett.* 58, 2337 (1987).

Bourne, L.C., A. Zettl, T.W. Barbee III, and M.L. Cohen, *Phys. Rev. B* 36, 3990 (1987).

Brinkman, W.F. and S. Engelsberg, *Phys. Rev.* 169, 417 (1968).

Campuzano, J.C. *et al.* , *Phys. Rev. Lett.* 64, 2308 (1990).

Carbotte, J.P., F. Marsiglio, and B. Mitrović, *Phys. Rev. B* 33, 6135 (1986).

Carbotte, J.P., *Rev. Mod. Phys.* 62, 1027 (1990).

Carbotte, J.P., M. Greeson, and A. Perez-Gonzalez, *Phys. Rev. Lett.* 66, 1789 (1991).

Carbotte, J.P. and E.J. Nicol, to be published in the Proceedings of the M²S-HTSC Conference(Kanazawa, Japan, July, 1991).

Chaudhari, P., D. Dimos and J. Mannhart, *IBM J. Res. Develop.* 33, 299 (1989).

Collins, R.T., Z. Schlesinger, F. Holtzberg, and C. Field, *Phys. Rev. Lett.* **63**, 422 (1989).

Cooper, L.N., *Phys. Rev.* **104**, 1189 (1956).

Crawford, M.K., M.N. Kunchur, W.E. Farneth, E.M. McCarron III, and S.J. Poon, *Phys. Rev. B* **41**, 283 (1990).

Daams, J.M., PhD. Thesis, McMaster University, 1979 (unpublished)

Daams, J.M. and J.P. Carbotte, *J. Low Temp. Phys.* **43**, 263 (1981).

Daams, J.M., B. Mitrović, and J.P. Carbotte, *Phys. Rev. Lett.* **46**, 65 (1981).

Daams, J.M., H.G. Zarate, and J.P. Carbotte, *Phys. Rev. B* **30**, 2577 (1984).

Davidov, D., K. Baberschke, J. A. Mydosh, and G. J. Nieuwenhuys, *J. Phys. F: Metal Phys.* **7**, L47 (1977).

Deutscher, G., *IBM J. Res. Develop.* **33**, 293 (1989).

Doniach, S. and S. Engelsberg, *Phys. Rev. Lett.* **17**, 750 (1966).

Doniach, S. and E.H. Sondheimer, Green's Functions for Solid State Physicists (Benjamin, Inc, Reading, Mass., 1974).

Dzyaloshinskii, I.E. and G. E. Volovik, *Jour. de Phys.* **39**, 693 (1978).

Edwards, S.F. and P. W. Anderson, *J. Phys. F: Metal Phys.* **5**, 965 (1975).

Eilenberger, G., *Z. Physik* **214**, 195 (1968).

Eliashberg, G.M., *Sov. Phys.-JETP* **11**, 696 (1960).

Ferrell, R.A. and R.E. Glover, *Phys. Rev.* **109**, 1398 (1958).

Fertig, W.A., D. C. Johnston, L. E. DeLong, R. W. McCallum, M. B. Maple, B. T. Matthias, *Phys. Rev. Lett.* **38**, 387 (1977).

Fetter, A.L. and J.D. Walecka, Quantum Theory of Many-particle Systems (McGraw-Hill, New York, 1971).

Fischer, K.H., *Z. Phys.* **B34**, 45 (1979).

Fischer, K.H., *Phys. Stat. Sol.* **(B) 166**, 357 (1983).

Forster, D., Hydrodynamic Fluctuations, Broken Symmetry, and Correlation Functions (W. A. Benjamin, Reading, Massachusetts, 1975).

Franck, J.P., J. Jung, G.J. Salomons, W.A. Miner, M.A.K. Mohamed, J. Chrzanowski, S. Gygax, J.C. Irwin, D.F. Mitchell, I. Sproule, *Physica C* **162-164**, 753, (1990).

Franck, J.P., J. Jung, M.A.K. Mohamed, S. Gygax, and G.I. Sproule, *Physica B* **165-166**, 697 (1990).

Fröhlich, H., *Phys. Rev.* **79**, 845 (1950).

Ghamaty, S., B.W. Lee, J.J. Neumeier, G. Nieva, and M.B. Maple, *Phys. Rev. B* **43**, 5430 (1991).

Ginzburg, V.L. and L.D.J. Landau, *Sov. Phys. JETP* **20**, 1064 (1950).

Ginzburg, V.L., *Sov. Phys. Dokl.* **3**, 102 (1956).

Gladstone, G., M.A. Jensen, and J.R. Schrieffer, in Superconductivity, edited by R.D. Parks (Dekker, New York, 1969), p.665.

Glover, III, R.E. and H.T. Coffey, *Rev. Mod. Phys.* **36**, 299 (1964).

Gor'kov, L.P., *Sov. Phys. JETP* **9**, 1364 (1959).

Gor'kov, L.P., *Sov. Phys. JETP* **10**, 593 (1960).

Gorter, C.J. and H.B.G. Casimir, *Phys. Z.* **35**, 963 (1934).

Gorter, C.J. and H.B.G. Casimir, *Z. Techn. Phys.* **15**, 539 (1934).

Grimvall, G., The Electron-Phonon Interaction in Metals (North-Holland, Amsterdam, 1981).

Gurvitch, M. and A.T. Fiory, *Phys. Rev. Lett.* **59**, 1337 (1987).

Gurvitch, M., J.M. Valles, Jr., R.C. Dynes, A.M. Cucolo, J.P. Garno, L.F. Schneemeyer, and J.V. Vaszczak, *Phys. Rev. Lett.* **63**, 1008 (1989).

Halperin, B.I. and P. C. Hohenberg, *Phys Rev.* **188**, 898 (1969).

Hayman, B. and J.P. Carbotte, *Can. J. Phys.* **49**, 1952 (1971).

Hayman, B. and J.P. Carbotte, *J. Phys. F* **1**, 828 (1971).

Hidaka, T., T. Matsui, and X. Nakagawa, *Jpn. J. Appl. Phys.* **27**, L553 (1988).

Hoen, S., W.N. Creager, L.C. Bourne, M.F. Crommie, T.W. Barbee III, M.L. Cohen, and A. Zettl, *Phys. Rev. B* **39**, 2269 (1989).

Holczer, K., L. Forro, L. Mihály, and G. Grüner, *Phys. Rev. Lett.* **67**, 152 (1991).

Hunt, T.K., *Phys. Rev.* **151**, 325 (1966).

Imer, J.M. *et al.* , *Phys. Rev. Lett.* **262**, 336 (1989).

Ishahawa, M., and O. Fischer, *Solid State Comm.* **23**, 37 (1977).

Jones, T.E., J. F. Kwak, E. P. Chock and P. M. Chaikin, *Solid State Comm.* **27**, 209 (1978).

Josephson, B.D., *Phys. Letters* **1**, 251 (1962).

Josephson, B.D., *Advan. Phys.* **14**, 419 (1965).

Kamarás, K., S.L. Herr, C.D. Porter, N. Tache, D.B. Tanner, S. Etemad, T. Venkatesan, E. Chase, A. Inam, X.D. Wu, M.S. Hegde, and B. Dutta, *Phys. Rev. Lett.* **64**, 84 (1990).

Kaplan, S.B., C.C. Chi, D.N. Langenberg, J.J. Chang, S. Jafarey, and D.J. Scalapino, *Phys. Rev. B* **14**, 4854 (1976).

Katayama-Yoshida, H., *et al.* , *Physica C* **156**, 481 (1988).

Keller, J., in Ternary Superconductors, edited by G. K. Shenoy, B.D. Dunlap, and F. Y. Fradin (Elsevier-North Holland, New York, 1981).

Kittel, C., Introduction to Solid State Physics (John Wiley and Sons, New York, 1986).

Kirtley, J.R., *Int. J. Mod. Phys. B* **4**, 201 (1990).

Kupriyanov, M. Yu. and V.F. Likichev, *Sov. J. Low Temp. Phys.* **6**, 210 (1980).

Kuroda, Y. and C.M. Varma, *Phys. Rev. B* **42**, 8619 (1990).

Landau, L.D.J., *Sov. Phys. JETP* **30**, 1058 (1956).

Landau, L.D.J., *Sov. Phys. JETP* **32**, 59 (1957).

Laughlin, R.B., *Phys. Rev. Lett.* **60**, 2677 (1988).

Leary, K.J., H.C. zur Loye, S.W. Keller, T.A. Faltens, W.K. Ham, J.N. Michaels, and A. Stacy, *Phys. Rev. Lett.* **59**, 1236 (1987).

Leavens, C.R. and D.S. Ritchie, *Solid State Comm.* **53**, 137 (1985).

Lee, W., D. Rainer, and W. Zimmermann, *Physica C* **159**, 535 (1989).

Lemberger, T.R. and L. Coffey, *Phys. Rev. B* **38**, 7058 (1988).

Lichti, R.L., K.C.B. Chan, D.W. Cooke, and C. Boekema, *J. Appl. Phys. Lett.* 54, 2361 (1989).

Littlewood, P.B., C.M. Varma, S. Schmitt-Rink, and E.A. Abrahams, *Phys. Rev. B* 39, 12371 (1989).

Littlewood, P.B. and C.M. Varma, to be published in the Proceedings of the International Seminar on Theory of High-$T_c$, Dubna, USSR, July 1990

Littlewood, P.B. and C.M. Varma, *J. Appl. Phys.* 69, 4979 (1991).

London, F., *Phys. Rev.* 24, 562 (1948).

London, F., Superfluids, Vol. 1 (John Wiley and Sons, New York, 1950)

Luttinger, J.M. and P. Nozières, *Phys. Rev.* 127, 1423 (1962).

Luttinger, J.M. and P. Nozières, *Phys. Rev.* 127, 1431 (1962).

Mahan, G.D., Many-particle Physics (Plenum, New York, 1981).

Maki, K., *Progr. Theor. Phys.* 29, 333 (1963).

Maki, K., *Progr. Theor. Phys.* 31, 731 (1964).

Maki, K., in Superconductivity, edited by R.D. Parks (Dekker, New York, 1969), p.1035.

Mannhart, J., P. Chaudhari, D. Dimos, C.C. Tsuei, and T.R. McGuire, *Phys. Rev. Lett.* 61, 2476 (1988).

Manzke, R., T. Buslaps, R. Classen, and J. Fink, *J. Europhys. Lett.* 9, 477 (1989).

Maple, M.B. and O. Fischer, in Superconductivity in Tenary Compounds II, edited by M. B. Maple and O. Fischer (Springer- Verlag, Berlin, 1982).

Marsiglio, F. and J.P. Carbotte, *Phys. Rev. B* 33, 6141 (1986).

Marsiglio, F., M. Schossmann, and J.P. Carbotte, *Phys. Rev. B* 37, 4965 (1988).

Marsiglio, F., Ph.D. thesis, McMaster University, 1988 (unpublished)

Marsiglio, F., P.J. Williams, and J.P. Carbotte, *Phys. Rev. B* 39, 9595 (1989).

Marsiglio, F., J.P. Carbotte, and P.J. Williams, *Phys. Rev. B* 41, 4484 (1990).

Marsiglio, F. and J.P. Carbotte, *Phys. Rev. B* 41, 11114 (1990).

Marsiglio, F., preprint (submitted to *Phys. Rev. B*).

Mattis, D.C. and J. Bardeen, *Phys. Rev.* 111, 412 (1958).

Maxwell, E., *Phys. Rev.* 78, 477 (1950).

Meissner, W. and R. Ochsenfeld, *Naturwiss.* 21, 787 (1933).

Migdal, A.B., *Sov. Phys.-JETP* 34, 996 (1958).

Mitrović, B., MSc. Thesis, McMaster University, 1979 (unpublished)

Mitrović, B., PhD. Thesis, McMaster University, 1981 (unpublished)

Mitrović, B. and J.P. Carbotte, *Solid State Comm.* 41, 695 (1982).

Mitrović, B., H.G. Zarate, and J.P. Carbotte, *Phys. Rev. B* 29, 184 (1984).

Mitrović, B. and J.P. Longo, *Solid State Comm.* 67, 935 (1988).

Moorjani, K. and J. M. D. Coey, Magnetic Glasses, (Elsevier, Amsterdam, 1984).

Morris, E., R.M. Kuroda, A.G. Markelz, J.H. Nickel, and J.T.T. Wei, *Phys. Rev. B* 37, 5936 (1988).

Nagaosa, N. and P.A. Lee, *Phys. Rev. Lett.* 64, 2450 (1990).

Nam, S.B., *Phys. Rev.* 156, 470 (1967).

Nam, S.B., *Phys. Rev.* 156, 487 (1967).

Nass, M.J., K. Levin, and G. S. Grest, *Phys. Rev.* B23, 1111 (1981).

Nicol, E.J., J.P. Carbotte, and T. Timusk, *Solid State Comm.* 76, 937 (1990).

Nicol, E.J., J.P. Carbotte, and T. Timusk, *Phys. Rev. B* 43, 473 (1991).

Nicol, E.J., and J.P. Carbotte, *Phys. Rev. B* 43, 1158 (1991).

Nicol, E.J. and J.P. Carbotte, *Solid State Comm.* 78, 55 (1991).

Nicol, E.J., and J.P. Carbotte, *Phys. Rev. B* 43, 10210 (1991).

Nicol, E.J., and J.P. Carbotte, *Solid State Comm.* 79, 835 (1991).

Nicol, E.J., J.P. Carbotte, and T. Timusk, submitted to *Phys. Rev. Lett.*

Nuss, M.C., P.M. Mankiewich, M.L. O'Malley, E.H. Westerwick, and P.B. Littlewood, *Phys. Rev. Lett.* 66, 3305 (1991).

Olsen, C.G. *et al.* , *Science* 245, 731 (1989).

Onnes, H.K., *Leiden Comm.*, 1206 (1911).

Orenstein, J., S. Schmitt-Rink, and A. Ruckenstein, in Electronic Properties of High-Tc Superconductors and Related Compounds, edited by H. Kuzmany, M. Mehring, and J. Fink (Springer, Berlin, 1990), p.254.

Palmer, L.H. and M. Tinkham, *Phys. Rev.* 165, 588 (1968).

Parameter, R.H., *RCA Rev.* 23, 323, (1962)

Parameter, R.H., and L.J. Berton, *RCA Rev.* 25, 596, (1964)

Parks, R.D., Ed. Superconductivity (Dekker, New York, 1969).

Perez Gonzalez, A., E.J. Nicol, and J.P. Carbotte, submitted to *Phys. Rev. B.*

Phillips, J.C., Physics of High-$T_c$ Superconductors, (Academic Press, Boston, 1989) p. 168.

Phillips, J.C., *Phys. Rev. B* 43, 6257 (1991).

Phillips, J.C. (preprint)

Pines, D. and P. Nozières, The Theory of Quantum Liquids (W.A. Benjamin, New York, 1966).

Plakida, N.M., in the Proceedings of the First CINVESTAV-Superconductivity Symposium, edited by R. Baquero (World Scientific).

Pumpin, B. *et al.*, *Phys. Rev. B* 42, 8019 (1990).

Quan, L. *et al.*, *Solid State Comm.* 65, 869 (1988).

Rainer, D. and G. Bergmann, *J. Low Temp. Phys.* 14, 501 (1974).

Renker, B., F. Gompf, E.Gering, N. Nüker, D. Ewert, W. Reichhardt, and H. Rietschel, *Z. Phys.* B67, 15 (1987).

Renker, B., F. Gompf, E.Gering, G. Roth, W. Reichhardt, D. Ewert, H. Rietschel, and H. Mutka, *Z. Phys.* B71, 437 (1988).

Reynolds, C.A., B. Serin, W.H. Wright, and L.P. Nesbitt, *Phys. Rev.* 78, 487 (1950).

Rickayzen, G., Theory of Superconductivity (Wiley, New York, 1965).

Rickayzen, G., Green's Functions and Condensed Matter (Academic Press, Toronto, 1980).

Rietschel, H., and H. Winter, *Phys. Rev. Lett.* 43, 1256 (1979).

Rogers, K.T., Ph.D. thesis, University of Illinois, 1960 (unpublished).

Romijn, J., T.M. Klapwijk, M.J. Renne, and J.E. Mooij, *Phys. Rev. B* **26**, 3648 (1982).

Rusinov, A.I., *Sov. Phys.-JETP* **29**, 1101 (1969).

Ruvalds, J. and A. Virosztek, *Phys. Rev. B* **43**, 5498 (1991).

Scalapino, D.J., in Superconductivity R.D. Parks, editor, (Dekker, New York, 1969), p. 449.

Schachinger, E., J.M. Daams, and J.P. Carbotte, *Phys. Rev. B* **22**, 3194 (1980).

Schachinger, E., W. Stephan, and J.P. Carbotte, *Phys. Rev. B* **37**, 5003 (1988).

Schachinger, E., M.G. Greeson, and J.P. Carbotte, *Phys. Rev. B* **42**, 406 (1990).

Schlesinger, Z., R.T. Collins, D.L. Kaiser, and F. Holtzberg, *Phys. Rev. Lett.* **59**, 1958 (1987).

Schlesinger, Z., R.T. Collins, F. Holtzberg, C. Field, N.E. Bickers, and D.J. Scalapino, *Nature* **343**, 242 (1990).

Schlesinger, Z., R.T. Collins, F. Holtzberg, C. Field, G. Koren, and A. Gupta, *Phys. Rev. B* **41**, 11237 (1990).

Schmitt-Rink, S., C.M. Varma, and A.E. Ruckenstein, *Phys. Rev. Lett.* **63**, 445 (1989).

Scholten, P.D., J.D. Lejeune, W.M. Saslow, and D.G. Naugle, *Phys. Rev. B* **16**, 1068 (1977).

Schrieffer, J.R., Theory of Superconductivity (Addison-Wesley, New York, 1964)

Schrieffer, J.R., X.-G. Wen, and S.-C. Zhang, *Phys. Rev. Lett.* **60**, 944 (1988).

Schutzmann, J. *et al.* , *J. Europhys. Lett.* **8**, 679 (1989).

Shiba, H., *Prog. Theor. Phys.* **40**, 435 (1968).

Shiba, H., *Prog. Theor. Phys.* **50**, 50 (1973).

Skalski, S.S., O. Betbeder-Matibet, and P.R. Weiss, *Phys. Rev.* **136**, A1500 (1964).

Skocpol, W.J., *Phys. Rev. B* **14**, 1045 (1976).

Statt, B.W., *Phys. Rev. L* **42**, 6805 (1990).

Stephen, W., PhD. Thesis, McMaster University, 1987 (unpublished)

Stephan, W. and J.P. Carbotte, *J. Low Temp. Phys.* **83**, 131 (1991).

Takigawa, M., P.C. Hammel, R.H. Heffner, and Z. Fisk, *Phys. Rev. B* **39**, 7371 (1989).

Tanner, D.B., D B. Romero, K. Kamarás, G.L. Carr, L. Forro, D. Mandrus, L. Mihaly, and G.P. Williams, to be published in the Proceedings of the Miami Workshop on Electronic Structure and Mechanisms for High Temperature Superconductivity, G. Vezzoli *et al.* , Eds. (Plenum Publishing Corp., 1991).

T. Timusk, M. Reedyk, R.A. Hughes, D.A. Bonn, J.D. Garrett, J.E. Greedan, C.V. Stager, D.B. Tanner, Feng Gao, S.L. Herr, K. Kamarás, G.A. Thomas, S.L. Cooper, J. Orenstien, L.K. Schneemeyer, and A.J. Millis, *Physica C* **162-164**, 841 (1989).

Timusk, T. and D.B. Tanner, in Physical Properties of High Temperature Superconductors I, D.M. Ginsberg, editor (World Scientific, Singapore, 1989) p.339.

Tinkham, M. and R.A. Ferrell, *Phys. Rev. Lett.* **2**, 331 (1959).

Tinkham, M., Superconductivity, (McGraw-Hill Inc., New York, 1975).

Tsuei, C.C., D.M. Newns, C.C. Chi, and P.C. Pattnaik, *Phys. Rev. Lett.* **65**, 2724 (1990).

Varma, C.M., S. Schmitt-Rink, and E.A. Abrahams, *Solid State Comm.* **62**, 681 (1987).

Varma, C.M., *Int. J. Mod. Phys. B* **3**, 2083 (1989).

Varma, C.M., P.B. Littlewood, S. Schmitt-Rink, E. Abrahams, and A. Ruckenstein, *Phys. Rev. Lett.* **63**, 1996, (1989); **64**, 497 (1990) (E).

Vasiliev, B.V. and V.I. Luschikiov, *Physica C* **153-155**, 261 (1988).

Vasiliev, B.V., V.I. Luschikiov, and V.V. Sikolenko, *Pis'ma Zh. Eksp. Teor. Fiz.* **48**, 276 (1988) [*JETP Lett.* **48**, 252 (1988)].

Vidberg, H.J. and J.W. Serene, *J. Low Temp. Phys.* **29**, 179 (1977).

Virosztek, A. and J. Ruvalds, *Phys. Rev. B* **42**, 4064 (1990).

Wasserman, A., M. Springford, and F. Han, *J. Phys.: Condens. Matter* **3**, 5335 (1991).

Wilkins, J.W., in Electrons at the Fermi Surface, edited by M. Springford (Cambridge University Press, Cambridge, 1980).

Williams, P., PhD. Thesis, McMaster University, 1990 (unpublished)

Williams, P. and J.P. Carbotte, *Phys. Rev. B* **43**, 7960 (1991).

Yvon, P.J., R.B. Schwarz, C.B. Pierce, L. Bernardez, A. Conners, and R. Meisenheimer, *Phys. Rev. B* **39**, 6690 (1989).

Wu, D.-H. and S. Sridhar, *Phys. Rev. Lett.* **65**, 2074 (1990).

Zarate, H.G. and J.P. Carbotte, *J. Low Temp. Phys.* **57**, 291 (1984).

Zarate, H.G. and J.P. Carbotte, *Phys. Rev. B* **35**, 3256 (1987).

Zimanyi, G.T. and K.S. Bedell, *Phys. Rev. Lett.* **66**, 228 (1991).